

# Development of an advanced tilt actuator for tilt-to-length coupling investigations

Von der QUEST-Leibniz-Forschungsschule  
der Gottfried Wilhelm Leibniz Universität Hannover  
zur Erlangung des Grades

**Doktor der Naturwissenschaften**  
- Dr. rer. nat. -

genehmigte Dissertation von

**M.Sc. Yongho Lee**

2021

*Referent:* Prof. Dr. Gerhard Heinzl  
(AEI, Hannover)

*Korreferent:* Prof. Dr. Benno Willke  
(AEI, Hannover)

*Korreferent* Prof. Dr. Claus Braxmaier  
(DLR Institute for Quantum Technologies, Universität Ulm)

*Tag der Promotion* 05.July.2021

---

# Abstract

A coupling between angular jitter of satellite and length readout, called tilt-to-length coupling, is one of the major noise sources in space-based laser interferometers such as LISA and GRACE Follow-On. With comprehensive knowledge of its characteristics and reduction, experimental investigations are an indispensable gateway to develop future space laser interferometers. A recurring difficulty in tilt-to-length coupling experiments is the motion errors of the actuators used to generate the tilting beam. This motion error then couples into the path length readout and cannot be distinguished from the tilt-to-length coupling under investigation.

Within this thesis, an optical testbed named advanced tilt actuator(ATA) was developed in order to provide a tilted beam and reduce the actuator's parasitic longitudinal displacement, thereby enabling the characterisation of the tilt-to-length coupling. The actuator employed in the ATA can produce a motion in three degrees of freedom for yaw and pitch and a displacement and is used for tilting a beam needed in tilt-to-length experiments. The vertices of retroreflectors attached to the rear of the actuator are traced by dedicated interferometers, such that the actuator's motion could be measured.

Although potential misalignments during the construction of the ATA endeavoured to be minimised through the devised alignment techniques, residual misalignment may degrade the advanced tilt actuator's performance. Based on analytical and numerical analyses of the various misalignment effects, possible readouts errors that may appear in a real experiment were simulated. For counteracting the readout error due to misalignments, a calibration method enabling suppressing the longitudinal displacement readout error was established, and its validity was verified through numerical simulations.

As the purpose of the ATA, an optical breadboard for examining tilt-to-length coupling effects was constructed, aiming to experimentally demonstrate that the imaging system enables mitigating the tilt-to-length coupling. Prior to this experiment, suppressing the ATA's longitudinal displacement readout error caused by various misalignments was performed through the calibration method. In the main experiment, we measured two path length readouts with and without the imaging system, applying the calibration enabling the suppression of linear and hysteresis error. The best experimental result with the imaging system showed tilt-to-length coupling of about  $2\ \mu\text{m}/\text{rad}$ , which is a significantly better performance than the  $25\ \mu\text{m}/\text{rad}$  required for LISA. Additionally, the ATA's angular readouts were compared with differential wavefront sensing signals measured on the optical breadboard, showing the measurement error in the order of a micro-radian within the rotation angle of  $\pm 200\ \mu\text{rad}$ .

Keywords: tilt-to-length coupling, LISA, actuator, space laser interferometer



# Contents

<b>Terms and abbreviations</b>	<b>xi</b>
<b>1 Introduction</b>	<b>1</b>
1.1 Ground-based gravitational wave detectors . . . . .	1
1.2 Laser Interferometer Space Antenna . . . . .	3
1.3 Space interferometry for geodesy mission . . . . .	5
1.4 About this thesis . . . . .	7
<b>2 Interferometric signals and Tilt-to-length coupling</b>	<b>11</b>
2.1 Interferometric signals . . . . .	11
2.1.1 Heterodyne interferometry . . . . .	11
2.1.2 Alignment signals . . . . .	15
2.2 Tilt-to-length coupling in space interferometers . . . . .	17
2.2.1 Tilt to length coupling in LISA . . . . .	17
2.2.2 Tilt to length coupling in GRACE-Follow-On . . . . .	21
2.3 Characteristic of tilt-to-length coupling . . . . .	23
2.3.1 Geometric tilt-to-length coupling . . . . .	23
2.3.2 Non-geometric tilt-to-length coupling . . . . .	24
2.4 Suppression of tilt-to-length coupling . . . . .	28
2.4.1 Special conditions for reduction of TTL coupling . . . . .	28
2.4.2 Imaging systems . . . . .	28
2.5 Summary . . . . .	32
<b>3 Advanced-Tilt-Actuator</b>	<b>35</b>
3.1 Motivation of Advanced-Tilt-Actuator . . . . .	35
3.1.1 Longitudinal displacement error in the ordinary actuator . . . . .	35
3.1.2 previous tilt-to-length coupling experiments . . . . .	36
3.1.3 Concept of advanced-tilt-actuator . . . . .	40
3.2 Development of advanced-tilt-actuator . . . . .	40
3.2.1 Retroreflectors in the ATA . . . . .	43
3.2.2 Actuation platform . . . . .	43
3.2.3 Multiple interferometers . . . . .	46
3.2.4 Working principle of ATA . . . . .	48
3.3 Alignment campaign . . . . .	52
3.3.1 Measurement of vertices for the retroreflectors . . . . .	52
3.3.2 Alignment for four beams . . . . .	54
3.3.3 Limitations of alignment campaigns and future works . . . . .	63
<b>4 Optical simulations</b>	<b>67</b>
4.1 Analysis of misalignment effect in the ATA . . . . .	68
4.1.1 Misalignment of beam reflection point . . . . .	68
4.1.2 Lateral misalignment of retroreflector . . . . .	71

4.1.3	Incident beam angle to retroreflector . . . . .	77
4.1.4	Dihedral angle error of retroreflector . . . . .	83
4.1.5	Relevance of the various misalignments . . . . .	89
4.2	Simulation for more realistic scenario . . . . .	91
4.2.1	Simulation conditions . . . . .	91
4.2.2	Simulation result . . . . .	96
4.3	Calibration strategy for the ATA readout . . . . .	105
4.3.1	Calibration based on counteracting . . . . .	109
4.4	Summary of optical simulation . . . . .	120
<b>5</b>	<b>Measurement campaign</b>	<b>123</b>
5.1	Experimental setup . . . . .	123
5.1.1	Modulation Bench . . . . .	123
5.1.2	The ATA testbed . . . . .	126
5.1.3	TTL coupling experiment . . . . .	126
5.1.4	Electronics . . . . .	129
5.2	Preliminary test . . . . .	132
5.2.1	Beam walk on QPD by temperature effect . . . . .	132
5.2.2	Beam parameter measurement . . . . .	135
5.3	Experimental result . . . . .	138
5.3.1	Longitudinal displacement calibration . . . . .	138
5.3.2	TTL coupling and its reduction with imaging system . . . . .	141
5.3.3	Comparison between the ATA's angular readout and the DWS signal . . . . .	155
5.4	Summary . . . . .	160
<b>6</b>	<b>Summary and discussion</b>	<b>163</b>
6.1	Summary . . . . .	163
6.2	Discussion . . . . .	164
<b>A</b>	<b>Ray tracing analysis for the retroreflector</b>	<b>167</b>
	<b>References</b>	<b>173</b>
	<b>Acknowledgments</b>	<b>179</b>

## List of Figures

1.1	Photographs of LIGO and the first detected gravitational wave signal.	3
1.2	Illustration for the LISA orbit and triangular constellation. . . . .	4
1.3	Illustration of GRACE Follow-On. . . . .	6
2.1	Simplified schematic of a heterodyne interferometer. . . . .	12
2.2	Quadrant photodiode and labels of each segment. . . . .	15
2.3	Illustration of differential wavefront sensing (DWS). . . . .	17
2.4	Illustration of a single arm of LISA. . . . .	18
2.5	Simplified illustration of the test mass interferometer with the angular misalignment between two beams. . . . .	19
2.6	Illustration of an telescope for LISA. . . . .	20
2.7	Layout of the LRI in GRACE Follow-On. . . . .	21
2.8	Mismatch between the spacecraft's centre of mass and the TMA's vertex. . . . .	22
2.9	Illustration of the lever-arm effect. . . . .	24
2.10	Depiction of the piston effect. . . . .	24
2.11	IfoCAD simulation results for TTL coupling in different scenarios. . .	25
2.12	Influence of unequal wavefronts on TTL coupling. . . . .	26
2.13	Examples of imaging systems designed for reducing the TTL coupling.	29
2.14	Illustration of spatial constraints in designing imaging systems. . . .	30
2.15	Ray trace for two-lens imaging system via a commercial optical software called Zemax. . . . .	31
2.16	Comparison of the path length variation with and without the two-lens imaging system. . . . .	32
3.1	Schematic of the simplified TTL coupling testbed with a conventional actuator. . . . .	36
3.2	Schematic of the first AEI TTL coupling experiment testbed. . . . .	37
3.3	Schematic of the second AEI TTL coupling experiment testbed. . . .	38
3.4	Concept of LISA optical bench testbed. . . . .	39
3.5	Concept of the advanced tilt actuator for the TTL coupling experiment.	41
3.6	CAD model of the advanced tilt actuator. . . . .	42
3.7	Hollow retroreflector used for the ATA. . . . .	44
3.8	Actuation platform of the ATA. . . . .	45
3.9	Schematic of the voltage amplifier used for the ATA's actuation. . . .	46
3.10	Beam path for respective interferometers in the ATA. . . . .	47
3.11	Illustration of the ATA-plane determined by the vertices of three retroreflectors. . . . .	49
3.12	Photograph of a coordinate-measurement-machine (CMM) . . . . .	53
3.13	Illustration of the procedure to measure the vertices of the four retroreflectors. . . . .	54
3.14	Illustration of cosine error of a retroreflector. . . . .	55
3.15	Schematic of a setup for the beam parallel alignment in the ATA. . .	56

3.16	Photograph of the aperture plate and the large mirror used for beam parallel alignment. . . . .	58
3.17	Naked eyes test for the flatness of a mirror surface. . . . .	59
3.18	Irregular mirror surface versus flat mirror surface for the parallel beam alignment. . . . .	60
3.19	Schematic of setup for beam perpendicular alignment. . . . .	62
3.20	Picture of a new large mirror for future alignment. . . . .	64
3.21	A different setup for aligning beams parallel. . . . .	64
4.1	Illustration of beam reflection point offset in the ATA setup. . . . .	69
4.2	Additional displacement of the ATA due to the BRP's lateral offset .	72
4.3	IfoCAD simulation for the ATA's readout errors without the lateral misalignment of the retroreflectors. . . . .	75
4.4	The ATA's readout errors due to the lateral misalignment of the vertex positions. . . . .	78
4.5	Three different distances while the ATA-plane tilts. . . . .	79
4.6	Three different distances with oblique incident beam angle towards retroreflector. . . . .	81
4.7	Displacement readout error for a single retroreflector under the rotation of the ATA, depending on incident beam angle. . . . .	82
4.8	Geometry of a retroreflector. . . . .	86
4.9	Dihedral angle deviation's influence to path length error for ATA's rotation. . . . .	88
4.10	The ATA's 3-DOF motion measured in an experiment was applied to the IfoCAD simulations in Chapter 4.2 and 4.3. . . . .	93
4.11	ATA's 3-DOF readout errors under the perfect alignment. . . . .	98
4.12	Characterising the TTL coupling with the ATA. . . . .	100
4.13	Illustrations of the ATA's difference rotations corresponding to the two TTL couplings. . . . .	101
4.14	The ATA's 3-DOF readout deviations due to the misalignments. . . . .	103
4.15	Path length readout with the imaging system and the ATA's displacement readout under multiple misalignments. . . . .	105
4.16	Variation of yaw readout error under the different ATA's motion. . . . .	108
4.17	Difference between two longitudinal displacement readout for the fourth retroreflector's vertex. . . . .	112
4.18	Reducing the error of $z_{\text{mea}}^{123}$ by tuning the measurement point $x_{\text{mea}}$ and $y_{\text{mea}}$ . . . . .	113
4.19	Cancelling out the linear and hysteresis error in path length readout. . . . .	115
4.20	Comparison of the path length signal after the calibration with the original TTL coupling signal. . . . .	116
4.21	Residual TTL couplings via the calibration method for each misalignment. . . . .	118
5.1	Schematic of the experimental setup. . . . .	124
5.2	Picture of the experimental setup on an optical table. . . . .	125
5.3	Mounting modules for the imaging system. . . . .	128
5.4	Alignment procedure for the two-lens imaging system. . . . .	130



---

5.5	Schematic of the three testbeds with electronic devices. . . . .	131
5.6	Test setup to measure beam walk on a QPD due to the air temperature variation. . . . .	133
5.7	Test result for correlation between beam walk and air temperature variation. . . . .	134
5.8	Beam parameter measurement for the TTL coupling experiment. . . . .	136
5.9	The ATA's two longitudinal displacements measured in the experiment. . . . .	139
5.10	Mitigating hysteresis of $z_{\text{mea}}^{123}$ by tuning the measurement point's y-value. . . . .	140
5.11	Reduction of residual linear error of $z_{\text{mea}}^{123}$ . . . . .	140
5.12	Final $z_{\text{mea}}^{123}$ error after calibration. . . . .	141
5.13	The ATA's motion in 3-DOF for this TTL coupling experiment. . . . .	143
5.14	The measured DPS and DWS signals at QPD1 and QPD2. . . . .	144
5.15	Measured path length signals before and after subtracting the ATA's longitudinal displacement. . . . .	145
5.16	The path length slopes and comparison with the LISA requirement. . . . .	147
5.17	Further reduction of TTL coupling through longitudinally shifting the second lens of the imaging system. . . . .	149
5.18	TTL coupling comparison between experimental results and IfoCAD simulation. . . . .	152
5.19	Best result in the TTL coupling experiment. . . . .	154
5.20	The ATA's angular readouts and DWS signal. . . . .	157
5.21	Illustration of mismatch between the QPD's slit lines and the ATA's orthogonal two axes. . . . .	158
5.22	Comparison between the ATA's angular readout and calibrated DWS. . . . .	158
5.23	The measured difference between the ATA's yaw readout and horizontal DWS signal. . . . .	159
5.24	IfoCAD simulation result for angular readout comparison. . . . .	160
5.25	Comparison of the DWS signal's non-linearity between the experimental result and IfoCAD simulation result for the ATA's rotation angle. . . . .	161



---

## List of Tables

2.1	Lists of parameters of the IfoCAD simulations for TTL coupling plotted in Figure 2.11. . . . .	27
2.2	Parameters of the two-lens imaging system. . . . .	31
3.1	Measured vertex positions of the four retroreflectors by using the Coordinate Measuring Machine. . . . .	55
3.2	Measurement of the power of four beams returning through the aperture plate in the beam alignment. . . . .	61
4.1	IfoCAD simulation parameters for a case without lateral misalignment of retroreflector. . . . .	73
4.2	Lateral shift of each retroreflector in IfoCAD simulation. . . . .	76
4.3	IfoCAD simulation parameters for incident beam angle effect. . . . .	81
4.4	Simulation parameters for the rotation of the imperfect retroreflector. . . . .	87
4.5	Vertex positions for three retroreflectors and their lateral shifts in simulations . . . . .	94
4.6	Simulation parameters for the incident beams' angle and direction in the ATA. . . . .	94
4.7	Parameter for modelling imperfect retroreflectors with dihedral angles in the simulation. . . . .	95
4.8	Beam reflection point's lateral offset in the IfoCAD simulation. . . . .	96
4.9	IfoCAD simulation Parameters for beams and photodiodes in the ATA. . . . .	96
5.1	Beam parameters for the TTL coupling experiment . . . . .	137
5.2	Applied parameters in the IfoCAD simulation for comparison with measured TTL couplings. . . . .	151
5.3	IfoCAD simulation parameters for angular readout comparison. . . . .	160



## List of Terms

**ADC** Analog to Digital Converter

**AEI** Albert Einstein Institute

**AOM** acousto-optic modulator

**AP** actuation platform

**ATA** Advanced Tilt Actuator

**BRP** beam's reflection point

**BS** beam splitter

**CM** centre-of-mass

**CMM** coordinate measurement machine

**CP** compensation plate

**DAC** Digital to Analog Converter

**DOF** degrees-of-freedom

**DPS** differential power sensing

**DWS** differential wavefront sensing

**EMRIs** extreme mass-ratio inspirals

**ESA** European Space Agency

**FI** Faraday Isolator

**FPGA** Field Programmable Gate Array

**GRACE** Gravity Recovery And Climate Experiment

**GRACE-FO** GRACE Follow-On

**GRS** gravitational reference sensor

**HW** half-wave plate

**KBR** K-Band Ranging

**LIGO** Laser Interferometer Gravitational-Wave Observatory

**LINT** L-shaped interferometer

**LISA** Laser Interferometer Space Antenna

**LPF** LISA Pathfinder

**LRI** Laser Ranging Interferometer

**MB** Modulation Bench

**NGGM** Next Generation Gravity Missions

**OPL** optical path length

**PBS** polarisation beam splitter

**PLL** phase-lock loop

**QPD** quadrant photodiode

**QW** quarter-wave plate

**SEPD** Single Element Photo Diode

**SMBH** supermassive black hole

**TIA** transimpedance-amplifier

**TMA** Triple Mirror Assembly

**TS** telescope simulator

**TTL** tilt-to-length

# 1 Introduction

Laser Interferometer Space Antenna (LISA) is a space laser interferometer to detect gravitational waves in the low-frequency regime between 0.1 mHz and 100 mHz that cannot be covered by ground-based gravitational-wave observatories [24, 25]. Forming extremely long arms with a few million kilometres by three satellites, it would measure the variation of its arm-length due to gravitation waves in picometre precision.

GRACE Follow-On (GRACE-FO), the successor of Gravity Recovery And Climate Experiment (GRACE), is the space mission for Earth gravity field recovery, consisting of two identical satellites orbiting around the Earth [8, 48, 50, 51]. The most noticeable difference of GRACE-FO with its predecessor is the Laser Ranging Interferometer (LRI) that improves the sensitivity on measuring the distance variation between the two satellites [31].

In the both space laser interferometers above, one of the critical noise source is tilt-to-length (TTL) coupling, which originates from a cross-coupling between tilt of spacecraft and length measurement [21, 63]. Based on understanding the TTL coupling's properties, investigating methods to mitigate its effect is essential to developing future space laser interferometers. However, one difficulty in TTL coupling experiments is the actuator's motion error that introduces a parasitic longitudinal displacement into length readout, intervening to measure the initial TTL coupling signals.

The main topic of this thesis is the development of an optical breadboard, named Advanced Tilt Actuator (ATA), to provides a measurable tilted beam needed to be used in TTL coupling experiments. Equipping an actuator that produces a motion in three degrees-of-freedom, the ATA measures the actuator's motion. This measurement enables decoupling of the actuator's longitudinal displacement that interrupts characterising TTL couplings.

The following sections begin with introducing ground-based laser interferometers for gravitational-wave detection. Then, a brief overview of LISA and GRACE-FO will be followed. In the last section of this chapter, an outline of this thesis with the ATA's motivation is given.

## 1.1 Ground-based gravitational wave detectors

Gravitational-waves are the ripple of the spacetime caused by the acceleration of mass and propagate throughout the universe at the speed of light [11, 27, 62]. Albert Einstein believed the existence of gravitation wave. However, he was sceptical about experimentally proving the existence of the gravitational wave because the change of the spacetime is too tiny when a gravitational wave reaches the Earth. Suppose a gravitation wave generated by an astrophysical event, for instance, a binary black hole. Its amplitude is expected to be in the order of  $10^{-21}$ . The amplitude in here refers to the relative change  $\Delta L/L$  corresponding to the length  $L$  due to the

gravitational wave. Taking a running race track with 100 m length as an example, its length variation is just about  $10^{-19}$  m when the gravitational wave reaches the Earth. At that time being with Einstein, a sensitive instrument capable of measuring the tiny length variation was barely conceivable.

Nonetheless, an experimental attempt for gravitational wave detection was initiated by Joseph Weber in the 1960s [60, 61]. He developed a resonant bar detector which is based on an aluminium cylindrical rod with a length of 1.5 m and a diameter of 0.6 m and has high resonance at the frequency of about 1600 Hz [61]. Its measurement principle is to monitor the electric signal from piezoelectric crystals, which is caused by the vibration of the aluminium rod induced by a gravitational wave. A variety of advanced resonant bar detectors beyond Weber's detectors had been developed, such as ALLEGRO, NAUTILUS, AURIGA, and EXPLORER [14, 15, 19, 35].

Meanwhile, scientists conceived another concept on developing a gravitational wave detector, based on laser interferometry [9, 42]. One of the laser interferometers, Laser Interferometer Gravitational-Wave Observatory (LIGO), refers to twin Michelson interferometers with 4 km long arm length. The twin interferometers shown in the photographs of Figure 1.1 are located in the eastern (Livingstone) and western (Handford) of the United States, respectively [6, 9].

After long term wait for hunting gravitational waves since its construction was finished in 1999, LIGO succeed the first detection of a gravitational wave on September 14, 2015 (named 'GW150915'), which was generated by merging of a pair of black holes [5]. After verifying the data for several months, the first gravitational wave detection was officially announced on February 11, 2016, through an official press conference and published in [5]. The gravitational wave GW150915 was detected in both twin interferometers of LIGO, and its simultaneous measurement enhanced the credibility of the gravitation wave detection. Unfortunately, the other gravitational waves detectors could not detect the event, because the VIRGO detector (in Italy) was under the upgrading phase and GEO 600 (German-British gravitational wave detector) was not sensitive enough to detect the event.

In August 2017, two significant detections widened gravitational wave astronomy; GW170814 and GW170817 [2, 3]. VIRGO in Italy had been upgraded and resumed its operation on August 1, 2017. Two weeks later, the gravitational wave GW170814 was detected by three detectors, including not only the twin interferometers of LIGO but also VIRGO [2]. This detection was significant in the aspect of that the network between the three laser interferometers enhanced not only the credibility of gravitational wave detection but also the accuracy to capture the position of the origin of the gravitational wave. Three days later, another gravitational wave GW170817 was detected by the three detectors again, which was a remarkable event that triggers the first multiple-messenger observations [1, 3, 4]. Comparing to the GW170814 generated by a pair of merging black holes, the GW170817 was caused by two merging neutron stars, which entails signals of electromagnetic wave. The Fermi space telescope, which orbited the earth in space, detected a gamma-ray burst (named GRB170817A) 1.7 second after when LIGO and VIRGO detected the gravitational wave GW170817 [4, 28]. Subsequently, over seventy observatories



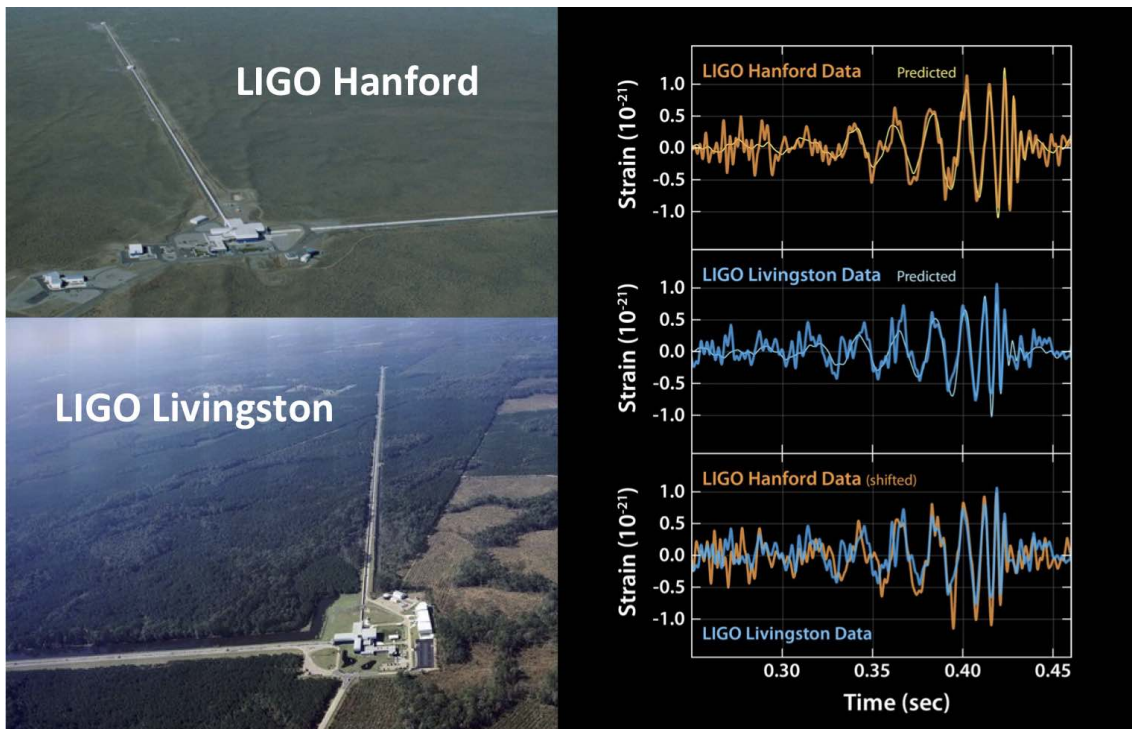


Figure 1.1: Photographs of LIGO and the first detected gravitational wave signals. The twin LIGO detectors are respectively located in the east and west of the US, which are based on long arm Michelson interferometer with 4 km arm length. On the right-hand side, the plots indicate the gravitation wave signal detected by LIGO in 2015, where the  $x$ -axis is time, and  $y$ -axis stands for the strain. The twin detectors of LIGO simultaneously detected the gravitational wave. Credit: Caltech/MIT/LIGO Lab

around the world observed electromagnetic signals in the multi-spectral range [1]. These two gravitation waves that were detected in August 2017 signified an importance of the network between gravitation wave detectors, as well as its contribution to mark the beginning of multi-messenger astronomy.

Beyond gravitational waves mentioned above, many gravitation wave events have been detected [7]. In February 2020, KAGRA detector in Japan began its operation [10], and LIGO-India is planned to be constructed. When they begin their operation in the future together with existing detectors, plentiful discoveries are foreseen to be yielded by the reinforced network between detectors.

## 1.2 Laser Interferometer Space Antenna

A variety of gravitational wave sources exist in a wide frequency range. However, the ground-based laser interferometers are capable of measuring gravitation wave sources in the frequency range about between about 10 Hz and 1000 Hz [24]. Detecting

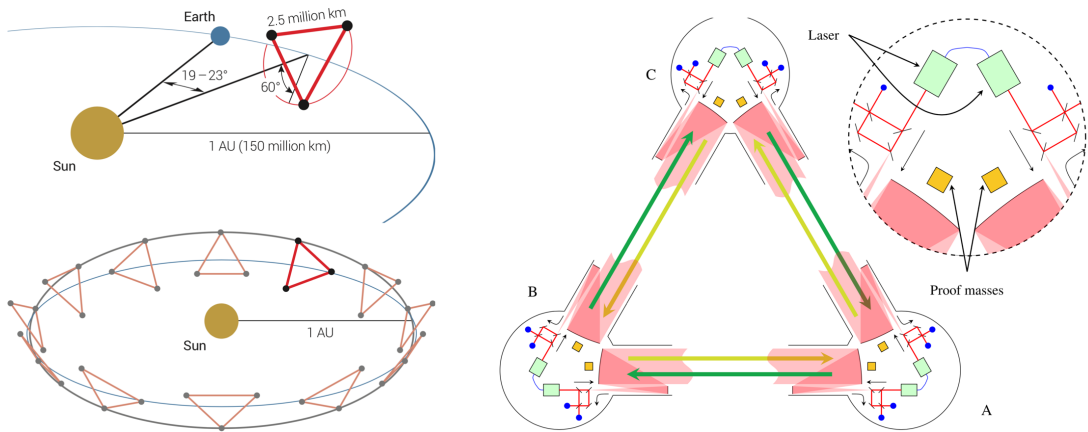


Figure 1.2: *Illustration for the LISA orbit and triangular constellation. Left figure is taken from [25], and right figure from [39], Courtesy of LISA Mission Consortium*

gravitational wave in the lower frequency range is limited due to the seismic noise caused by Earth’s activity [30]. A way to measure gravitational waves without the influence by the seismic noise is to build a laser interferometer in space.

Laser Interferometer Space Antenna (LISA), which will be the first gravitation wave observatory in space, is expected to be launched in around 2034. The proposal for the LISA mission was accepted as the third-large class mission (L3 mission) by the European Space Agency (ESA) in June 2017 [25]. LISA consists of three identical satellites, and its orbit would be an Earth-trailing helio-centric orbit about 50 million kilometres from Earth which is about  $20^\circ$  in the Earth orbit, as depicted in Figure 1.2 [25]. The separation distance between each satellite is approximately 2.5 million kilometres. Gravitational waves detected by LISA would be in the frequency range of 0.1 mHz to 1 mHz, which are limited to be detected by the ground-based laser interferometers; for instance merging of supermassive black hole (SMBH), extreme mass-ratio inspirals (EMRIs), and many others [24]. LISA mutually complementary with the ground-based laser interferometers and other observatories is expected to unveil novel observations and enhance multi-messenger astronomy.

As depicted on the right-hand side of Figure 1.2, LISA consists of three satellites forming a triangular constellation, and each satellite carries two test masses as notated by ‘proof mass’ in the figure. The test mass is a cubic made of gold-platinum alloy and acts as a reference object as if a mirror at the end of the arm in the ground-based laser interferometers. The distance between two test masses (one is from a remote satellite, another is in a local satellite), which defines the arm length of LISA, is 2.5 million kilometres. In order to form the laser links between two test masses, each satellite of LISA equips two telescopes with 30 cm diameter and two optical benches that contain multiple interferometers. The measurement principle of LISA is based on tracking the distance variation between the two test masses when a gravitation wave passes.

Ideally, the the triangular constellation formed by the several test masses is desired to be stable as much as possible. For this reason, each test mass is enclosed by an inertial sensor situated inside the satellite, and the satellite protects the test mass against external forces such as solar radiation. In contrast, the satellite undergoes the external force resulting in a change of its posture and the longitudinal displacement between the test mass and satellite. To counteract the influences due to the external force, the readouts for the displacement and rotation angle, which are measured by the optical bench, are fed back to the micro-thruster system onboard satellite, such that the nominal position of the satellite can be maintained.

Aiming for validating the required crucial technologies prior to launching LISA into space, a technology demonstrator, called LISA Pathfinder (LPF), had been developed and was launched at the end of 2015 [12, 13, 57]. Unlike LISA that consists of three satellites, LPF is a single satellite containing two free-floating test masses 37 cm apart. The goal in the LPF mission was set to measure the distance variation between two test masses with picometre precision through interferometric readouts and achieve the differential acceleration noise of two test masses below  $30 \text{ fm s}^{-1} \text{ Hz}^{-1/2}$  by reducing external and internal disturbances to free-floating test masses [57]. As a result of the test for about a year and a half, the measured acceleration noise surpassed not only the initial goal of the LPF mission but also the requirement for LISA mission [12].

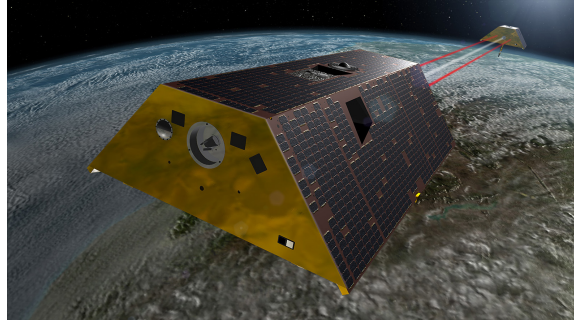
### 1.3 Space interferometry for geodesy mission

In addition to LISA, there are other space laser interferometers, for instance, GRACE-FO. Unlike LISA for detecting gravitational waves, GRACE-FO aimed to recover the Earth's gravitational field. The Laser Ranging Interferometer (Laser Ranging Interferometer (LRI)) onboard the spacecraft tracks the distance variation between two spacecraft, employing similar technologies applied to the laser interferometry of LISA. Thus, it plays a role in fulfilling the purpose of GRACE-FO and a technology demonstrator for LISA.

#### **Gravity Recovery and Climate Experiment (GRACE)**

Gravity Recovery And Climate Experiment (GRACE), the predecessor of GRACE-FO, was a joint space mission between the United States and Germany to monitor the changes in the Earth's gravitational field [51]. GRACE consisted of two identical satellites about 200 km apart and orbited around the Earth at the height of about 500 km from the Earth's surface. The K-Band Ranging (KBR) system was employed for measuring the distance variation of two satellites. Orbiting around the Earth through the South and the North Pole with approximately 90 minutes period, GRACE covered whole Earth over a month, exploiting GPS that tracks the location of GRACE satellites on the orbit. By using the data for the location and distance variation of GRACE, the global map for Earth's gravitational field could be monthly yielded. Furthermore, GRACE mission had contributed to observing

Figure 1.3: *Illustration of GRACE Follow-On. GRACE Follow-On consists of two identical satellites in a low Earth orbit and measures distance variation between two satellites via the KBR system but also the LRI for monitoring Earth's gravity anomalies. Courtesy NASA/JPL-Caltech.*



and understanding changes in the Earth's global environment such as variations of ice mass, global (local) surface water levels, global sea-level rise and others [20, 49, 55].

## GRACE Follow-On

Since GRACE launched in March 2002, it had successfully performed its mission for about 15 years until October 2017, exceeding far beyond its initially expected life span of 5 years. GRACE-FO, developed as a mission succeeding GRACE, was launched in May 2018. Compared to its predecessor GRACE, the most notable difference in GRACE-FO is the Laser Ranging Interferometer (LRI) onboard the satellite. Although the KBR system is still the main instrument in GRACE-FO for tracking the displacement between two spacecraft, the LRI is capable of enhancing the precision on the displacement measurement based on laser interferometry. Moreover, the LRI also serves as a technology demonstrator for future space laser interferometers like LISA [8].

Due to the KBR system situated at the front-centre of the spacecraft, the LRI adopted the design forming a racetrack configuration. One of the main components that enable establishing the racetrack configuration of the LRI is the Triple Mirror Assembly (TMA) which is a retroreflector consisting of three mirrors at 90 degree angle to each other [31, 48]. By placing the TMA's vertex on the centre of mass of the satellite, the LRI is not sensitive to the attitude of the satellite for the displacement measurement between two satellites.

Regarding the measurement performance, the LRI targeted to achieve sensitivity below  $80 \text{ nm}/\sqrt{\text{Hz}}$  for the displacement measurement, which is almost two orders of magnitude below the KBR's performance in GRACE [8]. It was reported that the measurement sensitivity of the LRI reached approximately  $10 \text{ nm}/\sqrt{\text{Hz}}$  at the frequency of 40 mHz and  $300 \text{ pm}/\sqrt{\text{Hz}}$  at 1 Hz [8]. Besides, analysing the LRI's performance in the lower frequency band below 40 mHz is currently in progress [8].

There are ongoing discussions for future geodesy missions beyond GRACE-FO; for instance, ESA's Next Generation Gravity Missions (NGGM) [29, 37]. Although specific design concepts for the future mission have not been established yet, the technologies of laser interferometry as applied to LISA or GRACE-FO may be adopted as the main instrument.

## 1.4 About this thesis

As described in **Chapter 2**, despite minimising internal and external disturbances to maintain the nominal attitude of the satellite, the residual angular jitter of the satellite or test mass couples into the length readout. This effect, named tilt-to-length (TTL) coupling, is one of the significant noise sources in LISA as well as the LRI of GRACE-FO. Studies to understand the tilt-to-length (TTL) coupling's characteristics and mitigate this effect have been ongoing [22, 23, 43, 54, 56]. Especially for future space laser interferometers employing test masses, several studies demonstrated that imaging systems could suppress the TTL coupling caused by the angular misalignment between two beams [43, 44].

One challenge to experimentally investigate TTL coupling effects and the imaging systems is establishing an actuation system capable of providing a pure tilted beam without a longitudinal displacement. Why do we need such actuation system that produces only pure tilt? Due to the inherent characteristic of the TTL coupling that is indistinguishable from the longitudinal displacement, the actuator's longitudinal displacement should be eliminated or measurable in order to characterise the TTL coupling in the experiment. However, ordinary actuators generally produce undesired longitudinal motion that disturbs to characterise the TTL coupling. As demonstrated in **Chapter 3**, the optical testbed named ATA, was developed to serve a measurable tilted beam for TTL coupling experiments. It consists of two main parts; an actuating platform and several interferometers. The actuation platform driven by three piezo produces a motion in three degrees-of-freedom (DOF), hosting four retroreflectors in the rear. The several interferometers, tracking the retroreflectors' longitudinal displacement, enable measuring the actuation platform's 3-DOF motion. One critical issue is the ATA's readouts are affected by various misalignments. For these reasons, possible misalignments during the construction of the ATA were attempted to be minimised by employing devised alignment tactics.

Although the attempts to mitigate the misalignment as much as possible, residual misalignment are likely appeared in the ATA, degrading the ATA's performance. The consequence of this, therefore, leads to the necessity of calibration for the ATA's readout. One importance prior to conceiving a calibration strategy is that the characteristic of the ATA's readout error should be understood and analysed. In **Chapter 4**, potential misalignments and their influences on the ATA's readout are examined via analytical and numerical analyses. Beyond individual analysis for each misalignment, a realistic scenario was mimicked in a numerical simulation to predict possible readout errors, which could be a basis of establishing calibration method. From these analyses, a few calibration methods are discussed. In particular, the calibration method cancelling out the longitudinal displacement readout error, which is the ATA's most important readout for the TTL coupling experiment, will be demonstrated.

As the initial motivation for the development of the ATA, an optical breadboard, called TTL coupling experiment, was constructed to investigate TTL coupling effects experimentally. **Chapter 5** demonstrates the results from three experiments

performed in this thesis. In the first experiment, the calibration method cancelling out the longitudinal displacement readout error, discussed in Chapter 4, is applied. Its experimental result shows that the residual error on the longitudinal displacement readout could be reduced in the order of a few hundred picometres. In the second experiment, the suppression of the TTL coupling via a two-lens imaging system was experimentally performed, comparing two TTL couplings measured with and without the imaging system. As a result of that, the TTL coupling suppressed by the imaging system was in the order of about  $2\ \mu\text{m}/\text{rad}$ , fully satisfying the LISA requirement that the TTL coupling should be below  $25\ \mu\text{m}/\text{rad}$  within the beam angle of  $\pm 300\ \mu\text{rad}$ . In the third experimental campaign, the ATA's angular readouts were compared to the DWS signal measured in the TTL coupling experiment, which is a preliminary experiment to future experiments, such as co-measurement between the ATA and other interferometers.

Finally, **Chapter 6** provides a summary of this thesis and an outlook for future investigations.







## 2 Interferometric signals and Tilt-to-length coupling

This chapter covers basic knowledge of laser interferometry relevant to LISA and GRACE-FO, as well as the characteristics of the tilt-to-length (TTL) coupling. Firstly of all, techniques for heterodyne interferometry and various interferometric signals are demonstrated in this chapter. Also, the mechanisms of TTL coupling in the LISA and GRACE-FO are explained. Focusing on the TTL coupling due to the angular misalignment between two interfering beams, its characteristics and suppression by an optical imaging system are described.

### 2.1 Interferometric signals

Ground-based gravitational wave detectors have ultra-stable arm length and adopt a homodyne detection technique for sensing length variation of its two arms. On the other hand, the distance between satellites in LISA or GRACE-FO varies at a speed of few metres per second. Thus, the homodyne detection technique is inadequate in space-based laser interferometers. To cover a wide range of displacements, LISA and GRACE-FO employ heterodyne interferometry using two frequency-shifted laser beams. The heterodyne technique is utilised to not only the space laser interferometers but also the interferometers developed in this thesis, which will be explained in Chapter 5. Basics regarding heterodyne readout technique and readout signals are described in the following sections, based on literature in [43, 56, 59].

#### 2.1.1 Heterodyne interferometry

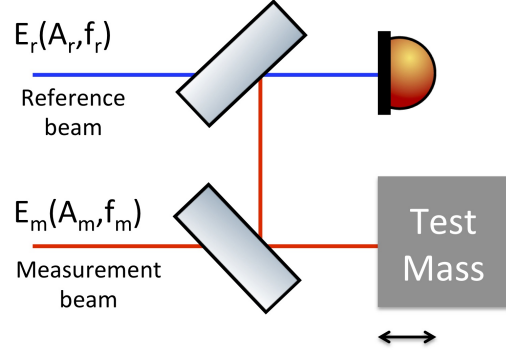
Figure 2.1 depicts a simplified scheme for a heterodyne interferometer. The blue line and red line represent the reference and the measurement beam, respectively. The two beams have a slightly different frequency to each other. Assuming that the two beams are fundamental Gaussian beams, their electric field propagating in the  $z$ -direction is expressed, as

$$E(r, z, t) = E_0 \frac{w_0}{w(z)} \exp\left(\frac{-r^2}{w(z)^2}\right) \exp\left(\frac{-ikr^2}{2R(z)} + i\eta(z) - ikz\right) \exp(i2\pi ft), \quad (2.1)$$

where  $w_0$  is the waist radius,  $w(z)$  denotes the radius of the beam at the longitudinal position  $z$  along the beam,  $f$  is the frequency of beam,  $r = \sqrt{x^2 + y^2}$ ,  $R(z)$  and  $\eta(z)$  are respectively the radius of curvature of the beam wavefront and the Gouy phase, given by the longitudinal position  $z$  and the Rayleigh range  $z_R = \pi w_0^2 / \lambda$ , as

$$R(z) = z \left[ 1 + \left( \frac{z_R}{z} \right)^2 \right] \quad (2.2)$$

Figure 2.1: *Simplified schematic of a heterodyne interferometer. A measurement beam and reference beam are drawn by a red line and blue line, respectively. The two interfering beams with a slightly different frequency measure a displacement of a moving test mass.*



$$\eta(z) = \arctan\left(\frac{z}{z_R}\right). \quad (2.3)$$

Equation (2.1) can be simplified as

$$E(r, z, t) = A(r, z) \exp(i2\pi ft - i\Phi), \quad (2.4)$$

where  $A(r, z)$  is the local amplitude, and  $\Phi(r, z)$  is local phase, given by

$$A(r, z) = E_0 \frac{w_0}{w(z)} \exp\left(\frac{-r^2}{w(z)^2}\right), \quad (2.5)$$

$$\Phi(r, z) = \frac{kr^2}{2R(z)} - \eta(z) + kz. \quad (2.6)$$

By following the expression of Equation (2.4), electric fields for the reference and measure beam are notated by

$$\begin{aligned} E_R(r, z, t) &= A_R(r, z) \exp(i2\pi f_R t - i\Phi_R(r, z)) \\ E_M(r, z, t) &= A_M(r, z) \exp(i2\pi f_M t - i\Phi_M(r, z)), \end{aligned} \quad (2.7)$$

where  $f_R$  and  $f_M$  are the frequency of each beam,  $\Phi_R(r, z)$  and  $\Phi_M(r, z)$  are local phases for the reference and measurement beam, respectively. For the sake of simplification of math expression, the functional dependency of  $r$  and  $z$  in the notation of  $A_{R/M}(r, z)$  and  $\Phi_{R/M}(r, z)$  is omitted in the following expressions. The local intensity as a result of two-beam interference is calculated like

$$\begin{aligned} I &= |A_R \exp(i2\pi f_R t - i\Phi_R) + A_M \exp(i2\pi f_M t - i\Phi_M)|^2 \\ &= A_R^2 + A_M^2 + 2A_R A_M \cos(2\pi \underbrace{(f_R - f_M)}_{f_{\text{het}}} t - \underbrace{(\Phi_R - \Phi_M)}_{\Delta\Phi}) \\ &= A_R^2 + A_M^2 + 2A_R A_M \cos(\omega_{\text{het}} t - \Delta\Phi), \end{aligned} \quad (2.8)$$

where  $f_{\text{het}}$  signifies the heterodyne frequency,  $\omega_{\text{het}} = 2\pi f_{\text{het}}$ , and  $\Delta\Phi$  is the local phase difference. The intensity in Equation (2.8) can be rearranged as

$$\begin{aligned}
 I &= (A_R^2 + A_M^2) \cdot \left[ 1 + \frac{\overbrace{2A_R A_M}^{c_I}}{A_R^2 + A_M^2} \cos(\omega_{\text{het}} t - \Delta\Phi) \right] \\
 &= \bar{I} [1 + c_I \cos(\omega_{\text{het}} t - \Delta\Phi)],
 \end{aligned} \tag{2.9}$$

where  $\bar{I} = A_R^2 + A_M^2$ , and  $c_I$  is the local contrast. The power sensed on a photodiode of surface  $S$  is given by

$$P = \int I dS = \int \bar{I}(r) [1 + c_I(r) \cos(\omega_{\text{het}} t - \Delta\Phi(r))] dS, \tag{2.10}$$

and its general form for arbitrary fields and detectors can be expressed as

$$P = \bar{P} \cdot [1 + c \cos(\omega_{\text{het}} t - \Delta\varphi)], \tag{2.11}$$

where  $\bar{P}$  is the mean power,  $c$  is the contrast, and  $\Delta\varphi$  is the phase of the power signal resulting from the interference.

Note that the phase  $\Delta\varphi$  in Equation (2.11) is different from the local phase  $\Delta\Phi(r)$  used in Equation (2.10).  $\Delta\varphi$  is the phase of power signal detected by a photodiode, which is dependent on not only the longitudinal path length but also the wavefront curvature of the beam and the Gouy phase. The longitudinal path length (or the phase  $\Delta\varphi$ ) is the most interested information from the interferometer, which corresponds to the displacement of the test mass. Analytically, it also contains small contributions of the beam curvature and the Gouy phase. In most cases when two beams are well aligned, their contributions to the phase  $\Delta\varphi$  is small as can be negligible. Thus, the contribution of the longitudinal path length to the phase is dominant, and their relations are given by

$$\Delta\varphi \approx k \cdot \Delta s_m = \frac{2\pi}{\lambda} \Delta s_m, \tag{2.12}$$

where  $\Delta s_m$  is the measured longitudinal path length.

## Phase demodulation

The power signal sensed on a photodiode as a result of the interference oscillates with the angular frequency  $\omega_{\text{het}}$  and contains the phase  $\Delta\varphi$  expressed in Equation (2.11). The photodiode generates electric current proportional to the beam power. The current delivered to a transimpedance-amplifier (TIA) is converted to voltage and transmitted to a phasemeter. The phasemeter digitalises the transmitted voltage signal and extracts the phase through the phase demodulation technique [18, 47]. Detailed theories and techniques regarding the phase extraction process are beyond the scope of this thesis. Instead, the analytical calculation to extract the phase is presented based on previous research literature [43, 56].

In order to extract the phase  $\Delta\varphi$  contained in the power signal in Equation (2.11), the powers multiplied by the cosine and sine are respectively integrated, as

$$\begin{aligned}
 \text{Int1} &= \frac{1}{\pi} \int_0^{2\pi} d(\omega_{\text{het}}t) \cos(\omega_{\text{het}}t) \cdot P(\omega_{\text{het}}t) \\
 &= \frac{1}{\pi} \int_0^{2\pi} d(\omega_{\text{het}}t) \cos(\omega_{\text{het}}t) \cdot \bar{P}[1 + c \cos(\omega_{\text{het}}t - \Delta\varphi)]
 \end{aligned} \tag{2.13}$$

$$\begin{aligned}
 \text{Int2} &= \frac{1}{\pi} \int_0^{2\pi} d(\omega_{\text{het}}t) \sin(\omega_{\text{het}}t) \cdot P(\omega_{\text{het}}t) \\
 &= \frac{1}{\pi} \int_0^{2\pi} d(\omega_{\text{het}}t) \sin(\omega_{\text{het}}t) \cdot \bar{P}[1 + c \cos(\omega_{\text{het}}t - \Delta\varphi)].
 \end{aligned} \tag{2.14}$$

By solving the integrals of Equation (2.13) and (2.14) as calculated in [43], they can be simplified, as

$$\text{Int1} = \bar{P}c \cos(\Delta\varphi), \tag{2.15}$$

$$\text{Int2} = \bar{P}c \sin(\Delta\varphi). \tag{2.16}$$

Using Equation (2.15) and Equation (2.16), the complex amplitude of the power signal can be notated by

$$a := \text{Int1} + i \text{Int2} = \bar{P}c \exp(i\Delta\varphi). \tag{2.17}$$

The phase  $\Delta\varphi$ , therefore, can be extracted by

$$\Delta\varphi = \arctan\left(\frac{\text{Int2}}{\text{Int1}}\right) = \arg(a). \tag{2.18}$$

For a quadrant photodiode (QPD) which consists of four segments, as shown in Figure 2.2, four phases from each segment are extracted. In this case, one way to define a phase for the QPD is to average the four individual phases as

$$\Delta\varphi_{\text{AP}} = \frac{\Delta\varphi_1 + \Delta\varphi_2 + \Delta\varphi_3 + \Delta\varphi_4}{4}. \tag{2.19}$$

Another way to extract a phase in the QPD can be implemented by computing the argument of the summed up complex amplitudes from the four segments, as

$$\Delta\varphi_{\text{LPF}} = \arg(a_A + a_B + a_C + a_D), \tag{2.20}$$

which was used in LISA Pathfinder (LPF) phasemeter. More detailed explanations for each phase definition can be found in [58, 59].

In this section, the procedure on the phase extraction is derived analytically using the calculation of integration for the continuous-time signal. In experiments, the phase extraction is implemented by using the summation of digitised power, and its computation procedure is explained in [18, 47].

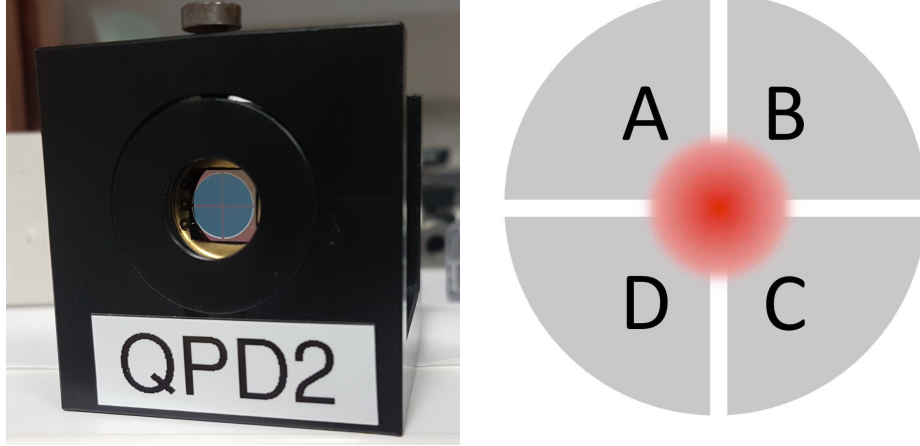


Figure 2.2: *Photograph of a quadrant photodiode and labels of each segment. A quadrant photodiode (QPD) consists of four segments which sense a beam individually. The QPD is utilised to measure a lateral shift or rotation of a beam. The illustration on the right-hand side shows the labelling of each segment with a beam on the centre. Note that one can define positions of the labels differently.*

### 2.1.2 Alignment signals

QPDs are widely used for various purposes such as beam alignments, measuring a beam position or an object's lateral displacement. Each segment in the QPD is symmetrically arrayed on the horizontal and vertical axis with a gap (also called QPD slit). Signals sensed in each segment are transmitted to a phasemeter that measures the powers and phases for each segment. By using the measured powers and phases, not only path length but also the alignment of the beam can be measured.

#### 2.1.2.1 Differential power sensing signal

The differential power sensing (DPS) signal, based on comparing the powers sensed from each segment of the QPD, is utilised for checking the beam alignment, measuring beam lateral shift or beam rotation. Figure 2.2 shows a picture of a QPD and labels of each segment with a beam on the centre of the QPD. By comparing the sensed beam powers between the right and left (or upper and lower) segments of the QPD, two DPS signals are defined here, as

$$\text{DPS}_h = \frac{\bar{P}_{\text{left}} - \bar{P}_{\text{right}}}{\bar{P}_{\text{total}}} = \frac{\bar{P}_A + \bar{P}_D - \bar{P}_B - \bar{P}_C}{\bar{P}_A + \bar{P}_B + \bar{P}_C + \bar{P}_D}, \quad (2.21)$$

$$\text{DPS}_v = \frac{\bar{P}_{\text{upper}} - \bar{P}_{\text{lower}}}{\bar{P}_{\text{total}}} = \frac{\bar{P}_A + \bar{P}_B - \bar{P}_C - \bar{P}_D}{\bar{P}_A + \bar{P}_B + \bar{P}_C + \bar{P}_D}, \quad (2.22)$$

where the ‘h’ and ‘v’ subscripts of DPS stand for horizontal and vertical respectively. Note that one can also use a different convention to define the DPS signal, like the right-hand side (or lower) segments minus the left-hand side segments (or upper). The  $\text{DPS}_h$  and  $\text{DPS}_v$  signals measure the horizontal and vertical beam walk on the QPD. If a fundamental Gaussian beam, which is circularly symmetrical, is placed on the centre of the QPD surface, the beam powers sensed by each segment are equal, resulting in the DPS signals of zero. However, when the beam deviates from the QPD’s centre, the powers measured by each segment are out of balance, leading to a change in the DPS signals. The DPS signal is dependent on the beam parameters and geometric parameters of the QPD, such as its diameter and slit width. For the fundamental Gaussian beam, the DPS signal appears in the form of the **error function** (also called the **Gauss error function**) to the lateral shift of a beam on the QPD surface [33, 56]. Within a small range of lateral shift of a beam, the DPS signal has a linear characteristic against the beam’s lateral offset or tilt angle, which is beneficial for aligning the beam to the QPD. A more detailed explanation regarding the DPS signal can be found in [56].

### 2.1.2.2 Differential wavefront sensing signal

Similar to the DPS signal comparing the sensed power between the segments, the differential wavefront sensing (DWS) technique is based on comparing the phases between the segments of the QPD. It is useful in particular for measuring the tilt angle of beam with higher sensitivity in comparison with the DPS signal. Suppose one beam tilts with respect to the other beam, as illustrated in Figure 2.3. In that case, the tilt of the wavefront in the interference leads to a phase change in each segment, specifically a phase difference between the left and right (or upper and lower) segments. The DWS signals are defined as

$$\text{DWS}_h = \varphi_{\text{left}} - \varphi_{\text{right}} = \frac{\varphi_A + \varphi_D}{2} - \frac{\varphi_B + \varphi_C}{2}, \quad (2.23)$$

$$\text{DWS}_v = \varphi_{\text{upper}} - \varphi_{\text{lower}} = \frac{\varphi_A + \varphi_B}{2} - \frac{\varphi_C + \varphi_D}{2}, \quad (2.24)$$

averaging two phases readouts in each side.

In general, the DWS signal is sensitive to angular misalignment rather than a lateral shift of the beam. Within a small range, the DWS signal is linear to the rotation angle of the beam, and its value is dependent on the beam parameters and QPD’s geometry. In experiments, the DWS signal requires a calibration process to be employed for beam angle measurement. More details regarding DWS signals can be found in [56, 59].

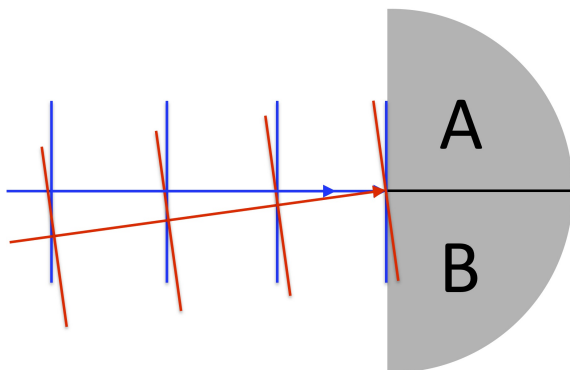


Figure 2.3: *Illustration of differential wavefront sensing (DWS). If one of two interfering beams (red line) is tilted with respect to the other, it results in different phase readouts between the left and right (or upper and lower) segments of the QPD. Subtracting the different phase readouts yields the DWS signal, which can be used for measuring the tilted beam's angle. Note that the two beams' wavefront, illustrated by lines perpendicular to the beams' propagating direction, are simplified as plane-waves.*

## 2.2 Tilt-to-length coupling in space interferometers

In space laser interferometers for detecting gravitational waves or measuring the Earth gravity field, the most important readout is the longitudinal displacement variation between reference points; the centre of mass of test masses for LISA, the centre of mass of satellite for GRACE-FO. However, unintended tilt motions of satellites or test masses couple into length readout, disturbing LISA and GRACE-FO's longitudinal displacement measurement. This effect, called tilt-to-length (TTL) coupling, is treated as one of the critical noise sources in both missions. This section introduces mechanisms of the TTL couplings in LISA and GRACE-FO.

### 2.2.1 Tilt to length coupling in LISA

LISA consists of three satellites, forming an equilateral triangle constellation. The distance between each satellite is approximately 2.5 million kilometres. Each satellite contains two cubic test masses made of a gold-platinum alloy, which are regarded as reference objects for detecting gravitational waves. Gravitational waves passing through the LISA's constellation oscillate the distance between two test masses (one from a local satellite and the other one from a remote satellite), and its distance variation is measured by laser interferometry.

As illustrated in Figure 2.4, the laser link between the two test masses (denoted by TM 1 and TM 2) is accomplished by means of two telescopes and two optical benches. The link can be split into three sub-links whose length variations are measured by independent interferometers; a test mass interferometer (TM interferometer) for measuring the distance between the TM 1 and the satellite 1 (sub-link 1), a long-arm interferometer for measuring the distance between the two satellites (sub-link 2) and another TM interferometer for measuring the distance between the TM 2 and satellite 2 (sub-link 3).

In the sub-link 1, the TM interferometer, using two Gaussian beams generated

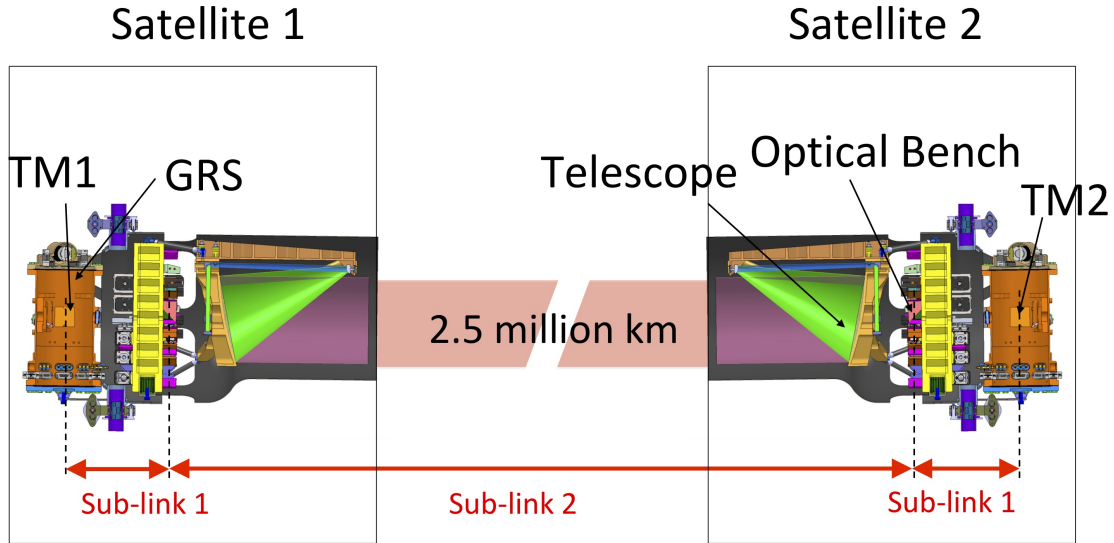


Figure 2.4: *Illustration of a single arm of LISA. The laser-link between two test masses enclosed by gravitation reference sensors (GRS) consists of three sub-links; The test mass interferometer measures the displacement between test mass 1 and satellite 1 (sub-link 1), a long-arm interferometer measures the distance variation between two satellites (sub-link 2). Another test mass interferometer measures the displacement between test mass 2 and satellite 2 (sub-link 3). The optical bench onboard each satellite hosts multiple interferometers. Receiving and transmitting beams between satellites are achieved by means of identical telescopes. Figure from [25], Credit: Airbus Defence and Space GmbH, Friedrichshafen, Sept. 2011*

on the optical bench that is rigidly mounted to the satellite, measures the distance variation and the rotation angle between the TM 1 and satellite 1.

In the sub-link 2, two telescopes are a critical instrument for the link between the two satellite. Each satellite equips two telescopes, and a total of six telescopes are used to form the triangular constellation of LISA. The telescope in LISA is an afocal beam expander that magnifies the collimated 2.2 mm diameter beam generated on the optical bench to 300 mm diameter beam. The large beam expanded through the telescope propagates 2.5 million kilometres to the remote satellite. Although the telescope is designed to generate collimated beams, the beam's divergence is inevitable, which leads to a giant beam at the remote satellite (its beam radius will be over few kilometres) as a result of the propagation of a few million kilometres. The identical telescope mounted on the remote satellite 2 receives only a small fraction (the telescope's diameter is 300 mm) of the giant beam having a few kilometres in diameter, resulting in a very weak power of beam with a few hundreds of picowatt. The clipped beam is delivered to the optical pupil of the telescope. The delivered beam, which is a top-hat beam, interferes with a local Gaussian beam on the optical bench to measure the distance variation between two satellites.



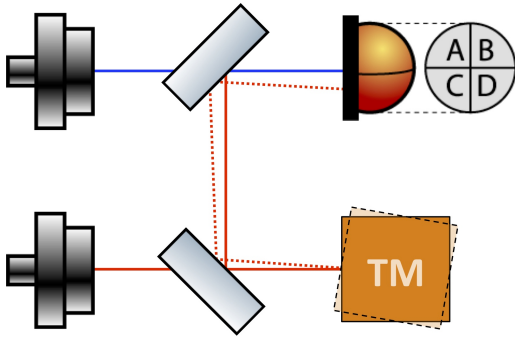


Figure 2.5: *Simplified illustration of the test mass interferometer with the angular misalignment between two beams. The angular misalignment between the reference (blue line) and measurement beam (red line) due to the jitter of the test mass couples to the length measurement.*

For the sub-link 3, another TM interferometer on the optical bench of satellite 2 measures the distance variation between satellite 2 and TM 2, similar to the TM interferometer in satellite 1.

During LISA’s mission operation, it will be necessary to keep the three measurements aligned as much as possible except the distance variation along the optical axis. However, undesired residual jitter of the satellite or test mass results in a coupling between the angular motion and the length measurement.

### Tilt-to-length coupling in the test mass interferometer

The LISA satellite protects the test mass floating freely against external disturbance such as solar radiation pressure. The TM interferometer measures the tilt angle and longitudinal displacement of the test mass with respect to the satellite, cooperating with the capacitive sensor of the GRS. The interferometric readouts and the GRS capacitive sensor’s readout are used to maintain the satellite’s nominal position relative to the test mass against external disturbances. Nonetheless, the residual jitter of the satellite or test mass causes an angular misalignment between interfering beams as illustrated in Figure 2.5, which couples into the length readout.

### Tilt-to-length coupling in the long-arm interferometer

The TTL coupling in the long-arm interferometer is also introduced by an angular misalignment between two beams, due to the spacecraft’s jitter. Figure 2.6 shows an example of the telescope with ray tracing. The telescope clips a small portion of the giant beam propagated a few million kilometres and transforms the clipped beam with a diameter of 300 mm to a collimated beam with a diameter of approximately 2.2 mm [25, 41]. The compressed beam is delivered to the optical bench through an aperture called ‘RX-clip’ that is one of the optical pupils of the telescope (In some literature, the RX-clip is also defined as ‘internal pupil’) [41].

While the received beam is compressed with a ratio of 300 mm to 2.2 mm by the telescope, the tilt angle of the beam delivered to the optical bench is magnified with an inverse ratio of the beam’s compression at the RX-clip. That means that the jitter of the spacecraft or the beam pointing angle toward the spacecraft magnifies the tilt angle of the beam on the optical bench. This beam angle magnification is depicted in Figure 2.6. Blue rays represent a nominal beam, and green rays illustrate a beam entering into the telescope with a small angle. In the Figure, the

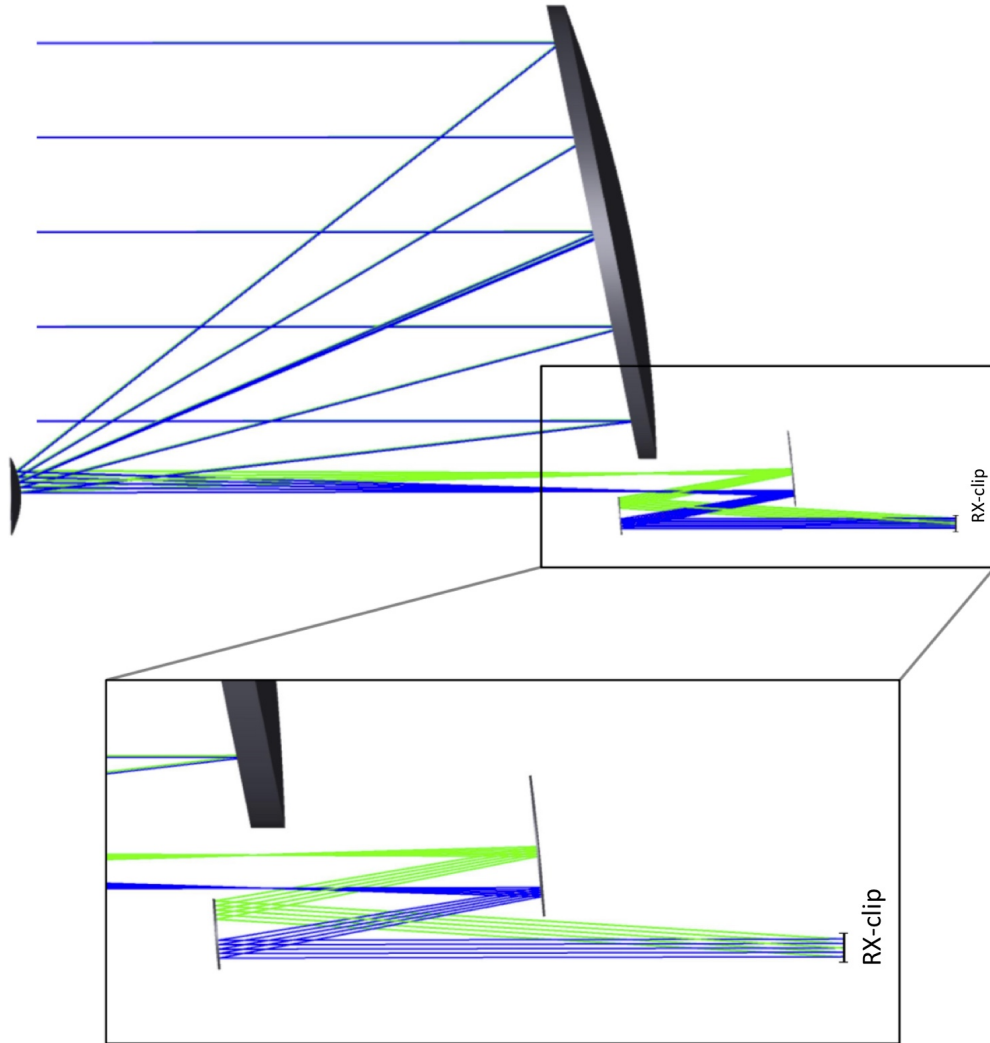


Figure 2.6: *Illustration of an example of LISA telescope. The LISA telescope clips a small portion of the giant beam propagated from a remote satellite. It also delivers the clipped beam to the optical bench through an aperture called RX-clip, which is one of the telescope's optical pupils. The telescope is an afocal system that compresses the clipped beam of 300 mm diameter to a beam of approximately 2.2 mm. Blue rays depict a nominal beam before rotation, and green rays represent a tilted beam. By following the telescope's magnification, the tilt angle of the delivering beam at the RX-clip is amplified in the ratio of around 300 mm/2.2 mm. Credit: This telescope design was provided by the Jeff Livas and the NASA LISA Telescope team, and used with their permission. Figure is taken from [43]*

angle between two beams at the entrance of the telescope is small as two beams are barely distinguishable. In contrast, the beam angle of the green rays at the RX-clip is magnified as explained above.

The beam transmitted through the RX-clip to the optical bench interferes with a local beam, and the angular misalignment between the two beams eventually causes the TTL coupling.

### 2.2.2 Tilt to length coupling in GRACE-Follow-On

The Laser Ranging interferometer (LRI) instrument onboard GRACE-FO measures the distance variation between two spacecraft based on laser interferometry, complementing to the KBR system. Since the line of sight between the centre-of-mass of each satellite is blocked by the KBR system located at the centre-front of each spacecraft, the LRI was designed in a race-track configuration. The Triple-Mirror-Assembly (TMA), a type of retroreflector consisting of three mirrors whose reflection surfaces are orthogonal to each other, is one of the critical components that enable the LRI's race track configuration.

The scheme of the LRI is illustrated in Figure 2.7. Lasers used in the LRI are Nd: YAG nonplanar ring oscillators of 1064 nm wavelength [8]. Denoting the left and right spacecraft by SC 1 and SC 2, the beam transmitted through the optical fibre (LO beam1) in SC 1 is reflected from the steering mirror to the beam splitter whose split ratio between reflectance and transmittance is 90:10. The reflected beam enters into the TMA after passing through an optical window called the compensation plate (CP) [48]. The beam entering into the TMA undergoes internal reflections, then it propagates toward the distant spacecraft (SC 2). The beam received by SC 2 (RX beam in SC 2) is clipped (order of nW) by the RX-aperture of 8 mm diameter and interferes with the local laser (LO beam) of SC 2. The local laser of SC 2 is

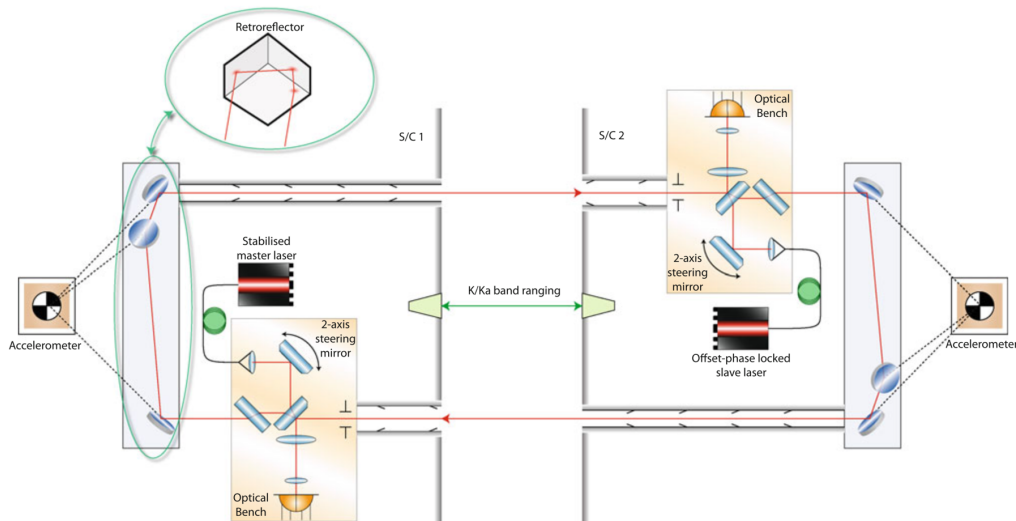


Figure 2.7: *Layout of the LRI in GRACE Follow-On. Since the KBR systems are placed at the front-centre of each spacecraft, the LRI is designed in a race-track configuration. Figure is taken from [48]*

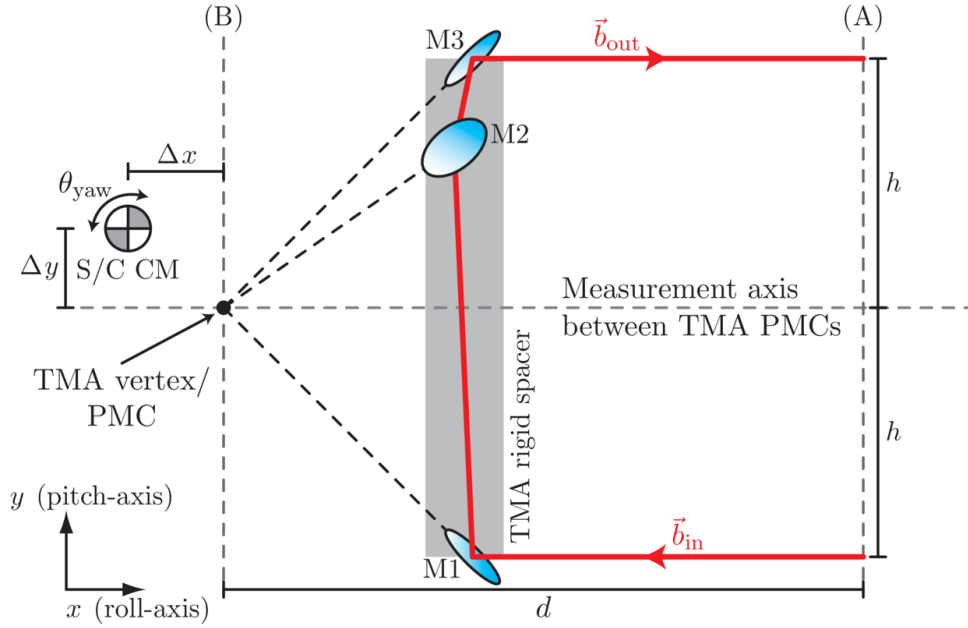


Figure 2.8: *Mismatch between the spacecraft's centre of mass (labelled 'S/C CM') and the TMA's vertex. The ideal condition is a perfect match between S/C CM and the TMA's vertex so that the spacecraft's jitter does not influence the length readout. However, the offset between the two points leads to a length readout error. Credit of picture: Daniel Schütze-AEI, [46]*

phase-locked with a fixed 10 MHz frequency offset with respect to the RX beam and propagates to SC 1 after undergoing the same routine as the LO beam 1 experienced. The beam that propagated from SC 2 to SC 1 is clipped by the RX-aperture and interferes with LO beam 1. The phase readout as a result of the interference contains information of the relative distance change between the two spacecraft.

The primary TTL coupling in the LRI originates from the mismatch between the TMA's vertex point and the spacecraft's centre-of-mass (CM), as illustrated in Figure 2.8. The TMA has some unique properties. Firstly, the incident and reflected beam are parallel regardless of the TMA's rotation or the incident beam's angle. Secondly, the optical path length does not vary when the TMA rotates around its vertex point. These two properties enable the LRI to be designed in the race-track configuration and to be insensitive against the spacecraft's jitter while measuring the displacement between the two spacecraft. Unlike the ideal situation that the TMA's vertex point and spacecraft's CM coincide, there is an offset in the order of 100 micrometres between the two points [63]. Consequently, the rotation of the vertex point around the CM leads to the length readout error.

In addition, there is another TTL coupling that occurs when the beam passing through the beam splitter becomes tilted, which leads to a variation of path length. However, this effect is mitigated by adding the compensation plate (CP) made from the same material as the main beamsplitter but rotated by 90 degrees [8, 31]. This

TTL coupling has relatively less influence than the aforementioned TTL coupling. Further information regarding TTL couplings in the LRI of GRACE-FO can be found in [46, 63]

## 2.3 Characteristic of tilt-to-length coupling

This section focuses on characteristics of the TTL coupling caused by the angular misalignment between two beams. As discussed in Chapter 2.2, the TTL couplings in LISA and GRACE-FO are based on different mechanisms. However, future geodesy missions beyond GRACE-FO may adopt a test mass and similar interferometric techniques of LISA, meaning that the TTL coupling due to the beam angular misalignment may be regarded as an important issue in future geodesy missions as well. In this context, the TTL coupling discussed in this section is not confined to only the LISA mission.

The TTL coupling discussed in this section is categorised by geometric and non-geometric effects. The following section will describe mechanisms and characteristics of both effects, based on previous literature [43, 56].

### 2.3.1 Geometric tilt-to-length coupling

#### Lever-arm effect

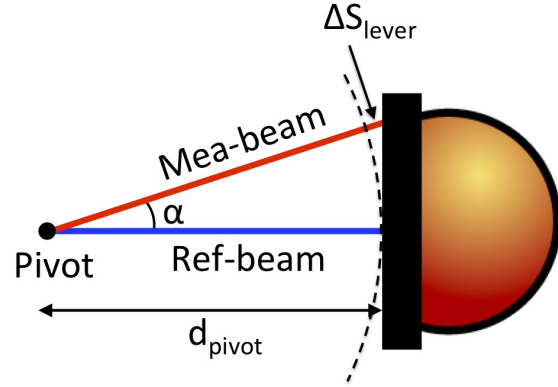
The lever-arm effect is introduced by the increment of optical path length when one of two beams becomes tilted. Figure 2.9 depicts a simplified scheme of angular misalignment between two interfering beams. Blue and red line represent a reference and measure beam, respectively. For the sake of simplicity, optical components are omitted in the figure. Suppose that the two beams are initially well aligned. If the measurement beam rotates around the pivot point, it acquires an additional path length  $\Delta S_{\text{lever}}$  as indicated in Figure 2.9. This additional optical path length, called lever-arm TTL coupling, can be calculated as

$$\Delta S_{\text{lever}} = \left( \frac{1}{\cos(\alpha)} - 1 \right) d_{\text{pivot}} \approx \frac{\alpha^2}{2} d_{\text{pivot}}, \quad (2.25)$$

where  $\alpha$  denotes the angle between the two beams, and  $d_{\text{pivot}}$  is the longitudinal distance from the pivot point to the photodiode.

In a case that two plane-waves interferes, it was analytically proved that the path length variation due to one beam's rotation follows this lever-arm effect as presented in Equation (2.25) [45]. However, the beam's rotation in the Gaussian-Gaussian beam interference yields an additional TTL coupling to the lever-arm effect, which will be discussed in Chapter 2.3.2.

Figure 2.9: *Illustration of the lever-arm effect. Red and blue lines represent a measurement and reference beam, respectively. The measurement beam is rotated by an angle  $\alpha$  around the pivot point where is longitudinally offset by  $d_{\text{pivot}}$  from a photodiode. The rotated beam acquires an additional path length of  $\Delta S_{\text{lever}}$*



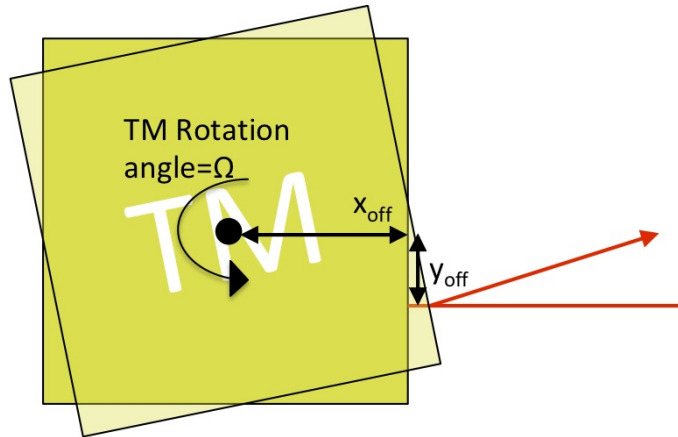
### Piston effect

The piston effect is introduced by the offset between the beam's reflection point and the pivot point of test mass. Figure 2.10 illustrates a beam that is reflected by a test mass rotating around its centre of mass. Suppose a longitudinal and lateral offset between the pivot of the test mass and the beam's reflection point. When the beam is perpendicularly incident to the test mass, the additional path length due to the offset is given by,

$$\begin{aligned} \Delta S_{\text{piston}} &= y_{\text{off}} \cdot \sin\Omega + x_{\text{off}} \cdot (1 - \cos\Omega) \\ &\approx y_{\text{off}}\Omega + \frac{x_{\text{off}}}{2}\Omega^2 \end{aligned} \quad (2.26)$$

where  $y_{\text{off}}$  is the lateral offset,  $x_{\text{off}}$  is the longitudinal offset, and  $\Omega$  is the rotation angle of the test mass.

Figure 2.10: *Depiction of the piston effect. A beam is reflected on the surface of a test mass which is rotating around its centre of mass.  $\Omega$  is the angle of rotation of the test mass, and  $y_{\text{off}}$  and  $x_{\text{off}}$  denote a lateral and longitudinal offset between the beam's reflection point and pivot point of the test mass.*



### 2.3.2 Non-geometric tilt-to-length coupling

TTL coupling caused by the angular misalignment of beams is occasionally misinterpreted by only the above geometric effects because the geometric effects are

straightforward. However, it is involved with not only the geometric effect discussed in Chapter 2.3.1 but also a variety of non-geometric effects. Figure 2.11 shows path length variations in a few different scenarios. The red-curve indicates the lever-arm TTL coupling when the distance between the pivot point and the detector is 100 mm. However, when two Gaussian beams interfere with the same pivot distance, the resulting TTL coupling differs from the simple lever-arm TTL coupling, as shown in Figure 2.11. Also, its results are dependant on conditions, which are discussed in below.

### Beam parameter dependency

The TTL coupling is dependant on beam parameters. Note that two graphs labelled with SIM 1 and SIM 2 in the Figure 2.11 were computed via IfoCAD simulation using Gaussian-Gaussian beam interference. In the simulations, the distance from the pivot to the detector (QPD) is 100 mm, but the beam parameters in SIM 1 and SIM 2 are different as listed in Table 2.1.

First of all, two graphs labelled with SIM 1 and SIM 2 are different from the lever-arm TTL coupling (red curve), which demonstrates that the TTL coupling cannot be explained by only geometric effects. Secondly, the comparison between SIM1 and SIM2 reveals that the TTL coupling depends on the Gaussian beam's parameters.

The TTL coupling's dependance on beam parameters was well demonstrated in [43], by means of an illustration shown in Figure 2.12. Red and blue curves in

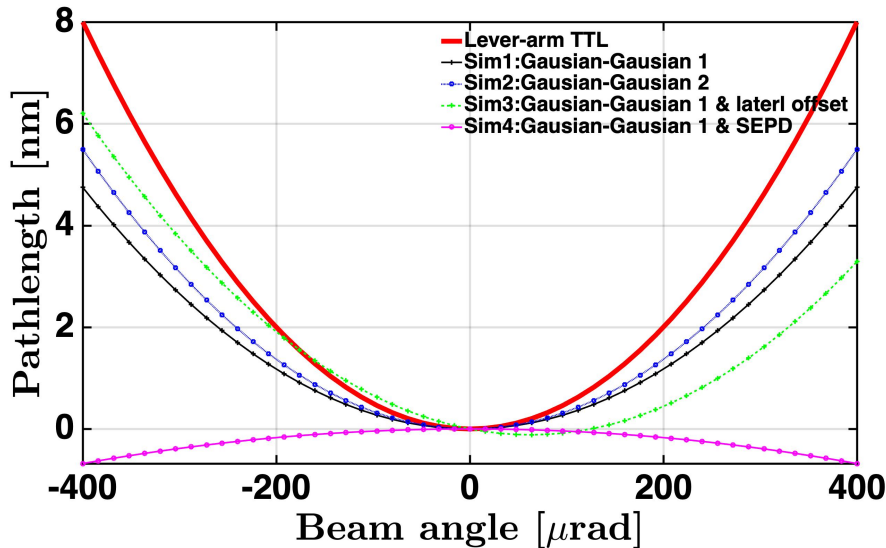


Figure 2.11: *IfoCAD* simulation results for TTL coupling in different scenarios. The red curve shows the lever-arm TTL coupling with 100 mm distance between the pivot point of a beam and a detector. The other four curves are computed by *IfoCAD* as a result of two Gaussian beams interfering. Resulting TTL couplings using Gaussian beams do not obey the lever-arm effect and are dependant on conditions. The parameters for each *IfoCAD* simulation are listed in Table 2.1

Figure 2.12 represent the wavefront for the reference and the measurement beam, respectively. The local phases of the interfering beams are denoted by  $\phi_n$  and depicted by arrows. The total phase, the sum of the local phases of the interfering beams over the surface, is presented on the right-hand side. When the two beams are aligned as depicted on the upper of Figure 2.12, it results in different local phases over the surface and symmetrical phasors on each side of the photodiode around the centre. If one of two beams (or wavefronts) is tilted with respect to the other one, it leads to the change of each local phases and the total phase, as depicted on the lower of Figure 2.12. This variation depends on the curvature of the interfering beams.

### Beam offset effect

Despite attempts to align two beams as precise as possible, small residual misalignments are likely to occur due to uncertainties in alignment procedures or mechanical instabilities. The simulation result labelled SIM 3 in Figure 2.11 represents the TTL coupling under a scenario having lateral misalignment between two beams. The simulation conditions for SIM 3 are identical to SIM 1 except that the measurement beam is laterally shifted with respect to the reference beam by  $30\ \mu\text{m}$ . As a result, the path length readout seems to be laterally shifted on the x-axis. This phenomenon occurs not only in the case of a lateral misalignment between the two beams but also in the case of a lateral misalignment between the beam and the QPD [43].

In general, the path length variation without the lateral misalignment corresponds to the even order of the beam angle if fundamental Gaussian beams interfere.

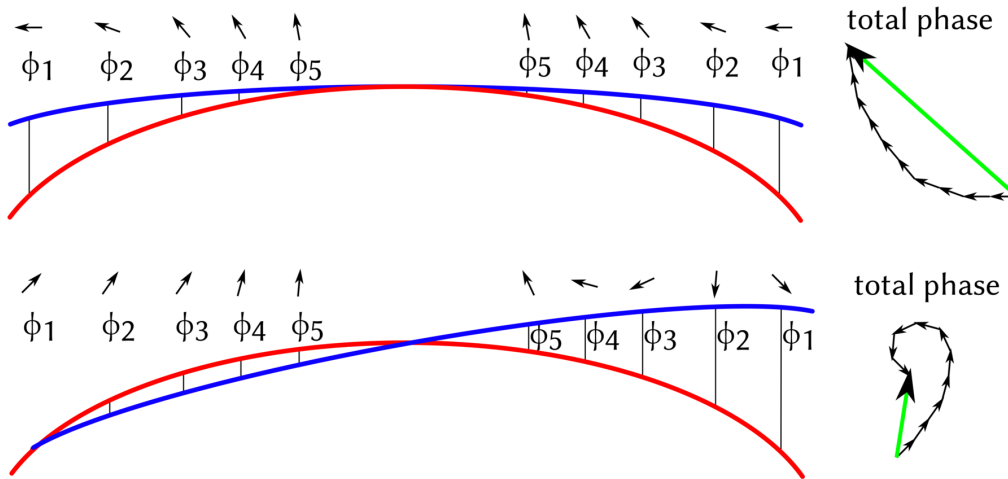


Figure 2.12: Influence of unequal wavefronts on TTL coupling. Red and blue curves represent wavefront curvatures for reference and measurement beams, respectively. The two beams have different wavefront curvatures. The local phases of the interfering beams are denoted by  $\phi_n$  and depicted by arrows (phasor). Tilting beam results in the variation of the total phase (presented on the right-hand side) that is yielded by summing each local phase over the detector's surface. Figure is taken from [43].



Table 2.1: Lists of parameters of the IfoCAD simulations for TTL coupling plotted in Figure 2.11.

Parameters	Sim1	Sim2	Sim3	Sim4
Pivot position [mm]	0	0	0	0
Ref-beam waist radius [mm]	0.4	0.4	0.4	0.4
Mea-beam waist radius [mm]	0.6	0.5	0.6	0.6
Ref-beam waist position [mm]	-100	-100	-100	-100
Mea-beam waist position [mm]	-500	-500	-500	-500
Mea-beam lateral offset [mm]	0	0	0.03	0
Photodiode type	QPD	QPD	QPD	SEPD
Photodiode position [mm]	100	100	100	100
Photodiode diameter [mm]	10	10	10	10
QPD slit full-width [mm]	0.02	0.02	0.02	

On the other hand, the lateral misalignment causes TTL coupling corresponding to odd orders as well as even orders of the rotation angle [43]. The coefficients of each order are dependant on conditions such as beam parameters or the amount of lateral misalignment.

### Detector geometry

TTL coupling is also dependent on the type of photodiode and its geometry. In the simulation labelled SIM 4 in Figure 2.11, a SEPD is used instead of QPD under the same conditions for SIM 1, which yields a different TTL coupling to the result of the SIM 1. The TTL coupling varies depending on the type of photodiode (QPD or SEPD), diameter, and slit-width of the photodiode [56].

### Other effects

Other factors influencing TTL coupling are summarised as follows.

- **Path length signal definition:** Depending on the definitions of the path length (or phase) signal for the QPD, as expressed Equation (2.19) and (2.20), the resulting TTL coupling may vary.
- **Wavefront error:** Unlike the fundamental Gaussian beam applied into the above IfoCAD simulations, beams in real experiments are likely to contain higher-order modes, and its wavefront may be distorted due to imperfect surfaces of optical components. This would lead to different TTL coupling from the result of applying the fundamental Gaussian beam.

## 2.4 Suppression of tilt-to-length coupling

### 2.4.1 Special conditions for reduction of TTL coupling

There are two special cases where the TTL coupling vanishes [45, 56]. The first case is when the pivot point of the beam coincides with the centre of the radius of wavefront curvature. It can be explained by that the wavefront curvature on the detector surface does not change if the Gaussian beam rotates around its centre of the radius of wavefront curvature [56]. The second case is to perfectly match beam parameters between two interfering beams and use a very large SEPD [45]. It was numerically and analytically demonstrated that the lever-arm TTL coupling and non-geometric TTL coupling cancel each other out. However, there are some difficulties in experimentally validating the reduction of TTL coupling based on these two methods. For example, one of the prerequisites is that the two interfering beams should be pure fundamental Gaussian beams, which is very challenging to be accomplished in an experiment. Additionally, it is a nontrivial task to match the centre of the radius of curvature of the wavefront and the pivot point.

### 2.4.2 Imaging systems

In the light of researches concerning the TTL coupling up to now, the imaging system is anticipated to be employed to LISA as the most promising means to reduce the TTL coupling caused by the beam angular misalignment. The imaging system here refers to an optical system composed of optical lenses. Several imaging systems for LISA have been designed, and some of them were tested to verify the reduction of TTL coupling in experiments [23, 43, 56].

One of the optical features of the imaging system is that the reflective surface of the mirror (test mass) and the photodiode's surface become conjugate planes. This optical feature enables suppressing the beam-walk on the photodiode and the variation of optical path length (OPL) of a rotating beam. By considering the variation of the OPL as a branch of the geometrical effects, the imaging system can be regarded as the means to suppress or appropriately adjust the geometrical effects.

At another point, the imaging system is also involved in the non-geometric effect because it alters the beams' parameters. Also, the tilt angle of the beam exiting through the imaging system is magnified. Suppose that the parameters of the interfering beams are not matched and one of the beams rotates. In this case, the imaging system can still suppress the variation of the OPL of the rotating beam, but non-geometric TTL coupling remains.

One approach to reducing the residual non-geometric TTL coupling is matching the beam parameters between two interfering beams. Another approach is slightly modifying the imaging system's design, in order to intentionally introduce the variation of OPL that counteracts the non-geometric TTL coupling.

The imaging systems reported so far can be divided into two types. The first type of imaging system is an afocal system that reduces the beam size and generates a collimated beam. Figure 2.13 shows some examples among the imaging systems designed so far (note that these imaging systems were designed by other; Airbus Defence and Space GmbH, Sönke, Schuster-former member of AEI) [43]. Three imaging systems from the top in Figure 2.13 represent examples of afocal systems aiming to reduce the TTL coupling, and each design consists of a different number of pieces of lenses. It can be seen that this type of imaging systems generates a collimated beam.

The other type of imaging system also suppresses the beam-walk on the photodiode and the OPL's variation by imaging the surface of the test mass onto the photodiode's surface. However, it is not an afocal system, which means that the outgoing beam is not collimated. It is presented at the bottom of Figure 2.13, con-

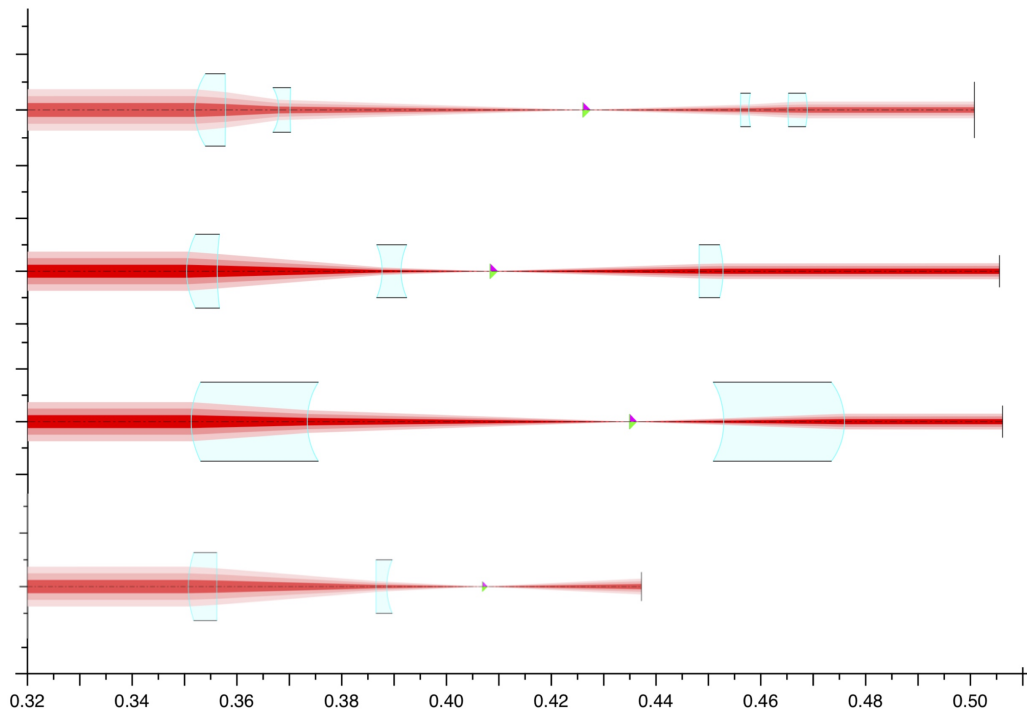


Figure 2.13: *Examples of imaging systems designed for reducing the TTL coupling. The three imaging systems from the top are the afocal system, which demagnifies the beam size and generates a collimated beam. The bottom imaging system consisting of two lenses reduces beam size and images the test mass onto the detector's surface, but does not generate a collimated beam. The scale on the bottom of the figure indicates the distance from the surface of test mass. Credit: Four-lens imaging system on the top was designed by Airbus Defence and Space GmbH, and the other three imaging system designed by Sönke Schuster (former member of AEI) in [43].*

sisting of two lenses (one is a plano-convex lens, and the other is a plano-concave lens). Its optical characteristic is that the exiting beam passing through the imaging system is converged, and its beam waist is located in between the second lens and the photodiode. Then, it reaches the photodiode surface in the form of the diverging beam.

Comparing the two types of the imaging systems, the TTL coupling with the afocal systems tends to be less sensitive in terms of the beam parameters [43]. On the other hand, the advantage of the second type of imaging systems is that the optical system's length is shorter compared to the first type of the imaging system, which is benefit in the aspect of reducing the size of optical benches.

### Design two-lens imaging systems

In this thesis, a two-lens imaging system corresponding to the second branch was designed and built on an optical testbed to verify the reduction of TTL coupling in the experiment (experimental setup and its results is presented in Chapter 5). One of the constraints in designing the imaging system is that lenses should be placed in a limited area near to the photodiode. Because, the optical components of the interferometer occupy the left-hand side near to the test mass, as illustrated in Figure 2.14. Therefore, the lenses can use only the rest of the space on the right-hand side.

The designed imaging system is composed of a Plano-Convex lens and a Plano-Concave lens. Note that the two-lens imaging system in this thesis is based on the previous design of the two-imaging system reported in [22]. Since the Plano-Convex lens of the previous two-lens imaging system design was out of stock, it was not available. Alternatively, the similar lens among off-the-shelf lenses was chosen, and then two lenses' positions were adjusted to suppress the optical path difference between two beams. In Figure 2.15 showing a ray-tracing via OpticStudio (commercial software, also called as Zemax), blue rays represent a reference beam following on the optical axis, and green rays represent a measurement beam that is tilted by the test mass. Two beams exiting through the two lenses become converged, and their beam waists are located in between the second lens and the QPD. The imaging system images the reflective surface of the test mass onto the QPD, resulting in

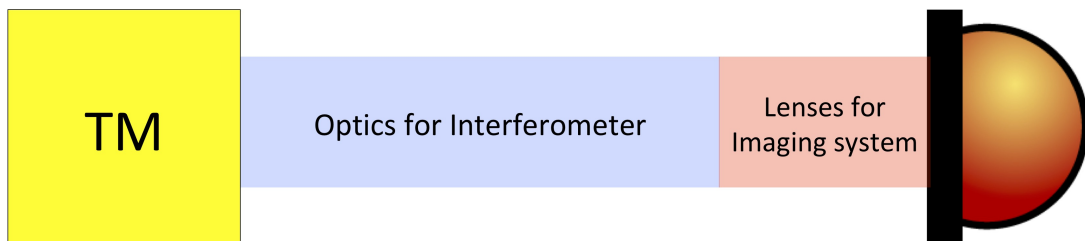


Figure 2.14: *Illustration of spatial constraints in designing imaging systems. Since optical components of interferometers on the optical bench occupy the left side near to the test mass, the lenses of the imaging system are allowed to be placed at near to photodiode.*

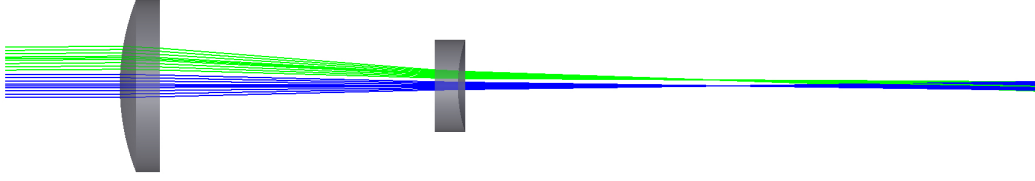


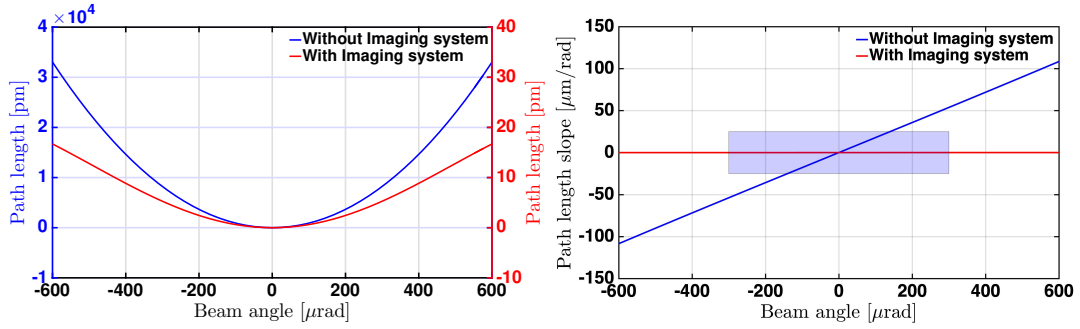
Figure 2.15: *Ray trace for two-lens imaging system via a commercial optical software called Zemax. The blue and green rays represent stationary reference beam and tilting measurement beam, respectively.*

Table 2.2: *Parameters of the two-lens imaging system. The TTL coupling computed via IfoCAD is shown in Figure 2.16.*

Parameters	Unit	Lens 1	Lens 2	QPD
Position	mm	350	377.5	430.077
Radius of curvature for first surface	mm	20.6	$\infty$	
Radius of curvature for second surface	mm	$\infty$	12.7	
Center thickness	mm	3	2	
Diameter of lens	mm	12.7	10	
Material		BK7	Fused-Silica	
Refract index		1.50663	1.44963	
QPD diameter	mm			8
Full width of slit in QPD	mm			0.018

suppression of the beam-walk on the QPD and the invariant OPL for the tilting measurement beam. The angular magnification of the designed imaging system is -2.755, and the beam size at the detector surface is demagnified by a ratio of  $1/2.755$  of the initial beam size. The design parameters for the imaging system are listed in Table 2.2, and the positions for each component are defined by the distance from the surface of the test mass.

On the left-hand side of Figure 2.16, the path length variation with imaging system (red curve) is compared to the case without imaging system (blue curve), computed via IfoCAD simulation. In each simulation, the interfering beams are assumed to have identical beam parameters; beam waist radius of 0.45 mm and beam waist position at the surface of the test mass. In this example, the path length variation with the imaging system is relatively small around 16 pm within the beam tilt angle of  $\pm 600 \mu\text{rad}$ . In contrast, the path length variation without imaging system increases up to 33 nm. On the right-hand side of Figure 2.16, the two path length signals' slopes are compared with the LISA requirement (colour box) that the path length slope should be within  $\pm 25 \mu\text{rad}/\text{rad}$  in the beam tilt angle of  $\pm 300 \mu\text{rad}$ . The path length slope without imaging system violates the LISA requirement, whereas the path length slope with the imaging system is flat within the range of the LISA requirement.



(a) Path length with and without the imaging system

(b) Path length slope without the imaging system

Figure 2.16: Comparison of the path length variation with and without the two-lens imaging system. The left shows path length variation with and without the two-lens imaging system. The graph on the right-hand side represents the path length slopes for the both cases. The parameters of the two-lens imaging system are listed in Table 2.2

Note that the imaging system's performance presented here through simulation is a quite challenging level to be accomplished in an experiment. Firstly, the TTL coupling with the imaging system depends on the beams' parameter. In this simulation, the two beams were assumed to be Fundamental Gaussian beams. In reality, residual high order modes of the interfering beams are likely to be expected in the experiment. Also, the simulation results shown in Figure 2.16 would be changed if the two beams have different parameters. Moreover, the beam wavefront distortion, which is likely appeared in an experiment, was not considered in the above simulations. Secondly, it is essential to investigate the imaging system's tolerance because TTL coupling can be affected by the imaging system's error, such as the lenses' manufacturing error, the lenses' positions, and the surface quality. The two-lens imaging system in this thesis was designed to suppress the OPD by merely adjusting the two lenses' positions without considering the imaging system's tolerance. Besides, other topics, not covered in this thesis, need to be examined for further investigating TTL coupling effects, such as stray light's effect, alignments effects, and the imaging systems' thermal stability.

## 2.5 Summary

This chapter covered the basics for heterodyne readout and introduced TTL coupling effects. On the basis of knowledge from previous researches, a two-lens imaging system was designed to suppress the TTL coupling. Within this thesis, the designed imaging system is prepared to experimentally verify reducing the TTL coupling, which will be discussed in Chapter 5. The following Chapter 3 will demonstrate a novel actuator, which is a crucial device to produce a tilted beam that is needed for

TTL coupling experiments.





## 3 Advanced-Tilt-Actuator

An actuator, one of the critical components to introduce a tilted beam in TTL coupling experiments, should be accurately controllable. A difficulty in TTL coupling experiments employing conventional actuators is a motion error of the actuator. In particular, an actuator's undesired motion error couples into a length readout, interrupting an acquisition of the proper TTL coupling signal in experiments. Aiming to resolve this issue, an optical breadboard that equips an actuator generating a motion in three degrees-of-freedom and measures its motion was developed, named 'Advanced-Tilted-Actuator' (ATA).

This chapter consists of three parts. The first part briefly reviews previous testbeds for TTL coupling investigations and the motivation of the ATA. In the second part explains details of the development of the ATA and its working principle. The third part demonstrates the ATA's alignment procedure which is critical for the ATA's precise readout.

### 3.1 Motivation of Advanced-Tilt-Actuator

#### 3.1.1 Longitudinal displacement error in the ordinary actuator

Experimental investigations on TTL coupling effects are crucial for developing space laser interferometers. However, one of the difficulties in TTL coupling experiments is to equip an actuator that can provide a pure tilted beam without a longitudinal displacement.

Figure 3.1 illustrates an example of a TTL coupling testbed employing an ordinary actuator. The measurement beam (red line), which is s-pol (its electric field is perpendicular to the page), is transformed to the p-pol beam (its electric field is parallel to the paper plane) by a half-wave plate ( $\lambda/2$ ) and passes through a polarisation beam splitter (PBS). Then, the beam changes to a circular polarisation beam by a quarter-wave plate ( $\lambda/4$ ) and is reflected by a conventional actuator. The reflected beam propagating towards the PBS is converted to s-pol beam by  $\lambda/4$ . It is reflected on the PBS and propagates to a beam splitter and interferes with a reference beam (blue lines). The TTL coupling caused by the angular misalignment of the beams is measured at a QPD (labelled with QPD 1 in Figure 3.1), whereas the TTL coupling suppressed via an imaging system is measured at another QPD (labelled with QPD 2 in Figure 3.1)

The conventional actuator serves a tilting beam needed for measuring the TTL couplings, but it is likely to cause an unwanted longitudinal displacement due to its motion error. As the TTL coupling disturbs the longitudinal displacement measurement, the actuator's undesired longitudinal displacement intervenes the path length readout, disturbing to characterise the TTL couplings. As far as known, there is no commercial actuator that satisfies the required accuracy in its motion for TTL

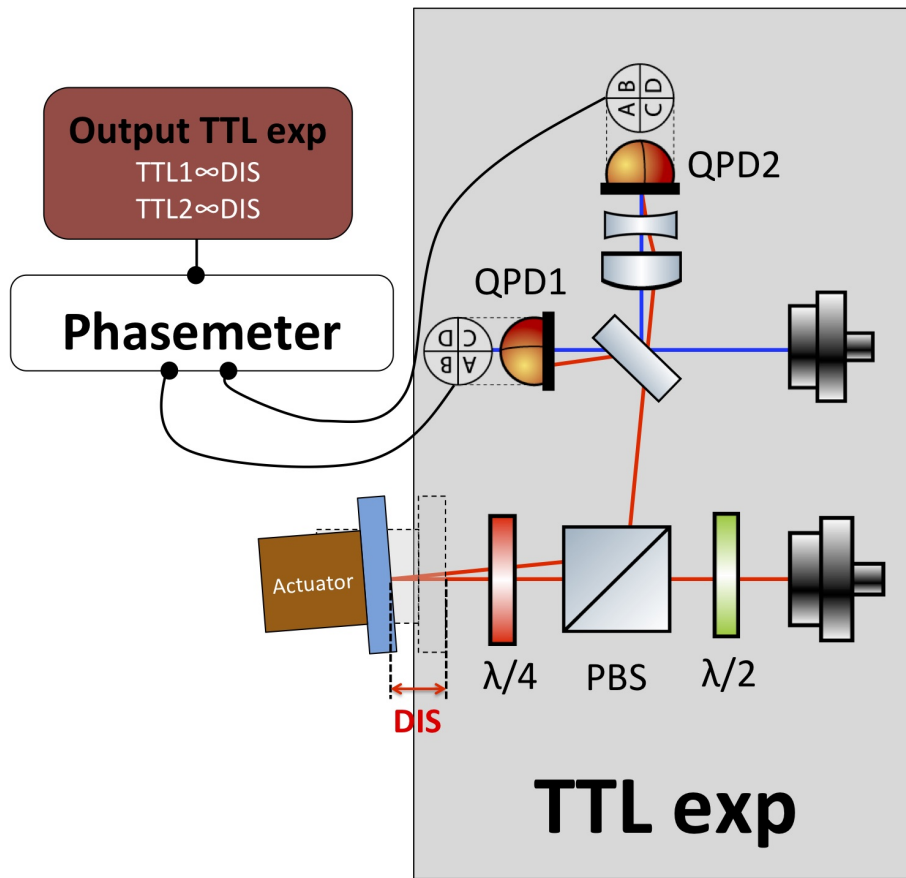


Figure 3.1: *Schematic of a simplified TTL coupling testbed with a conventional actuator. The measurement beam (red line) reaching the actuator through polarisation optics is reflected toward QPD 1 and QPD 2. It interferes with the reference beam (blue line). The TTL coupling caused by the angular misalignment between two beams is measured at QPD 1, and the suppressed TTL coupling via the two-lens imaging system is measured at QPD 2. Ideally, the actuator should provide a pure tilted beam for investigating the TTL coupling effects. But, it produces an unwanted longitudinal displacement because of actuator's error. The longitudinal displacement directly couples into the path length readout, resulting in the disturbance of identifying only TTL coupling effect.*

coupling experiments. Motion error of actuators has been iteratively one of the challenges in previous TTL coupling experiments.

### 3.1.2 previous tilt-to-length coupling experiments

The TTL coupling experiment reported in this thesis is the fourth generation of TTL experiments at the AEI. There have been a few different TTL coupling experiments [44, 53, 54]. The measurement principles of each TTL coupling experiment

are well summarised in [43]. The following section briefly reviews the former TTL coupling experiments and how the actuation errors were dealt with in each experiment.

### First generation AEI TTL experiment

The first generation AEI TTL experiment employed a conventional actuator to introduce a tilted beam, but its longitudinal displacement was inevitably due to the actuator's motions error. For eliminating the length readout error due to the actuator's unintended longitudinal displacement, the first experiment adopted a unique characteristic of the TTL coupling that vanishes under the particular conditions explained in Chapter 2.4; the two interfering beams are fundamental Gaussian beams, two beams are identical, the photodiode is a large SEPD [45, 53]. In this scenario, the SEPD, denoted by 'actuator readout' in Figure 3.2 illustrating the simplified schematic of the first TTL coupling experiment, senses only the actuator's longitudinal displacement. By subtracting the pathlength signal measured at the SEPD from one measured at the QPD (denoted by 'measurement interferometer'), the TTL coupling measured with the imaging system could be characterised. However, the two beams used in the first TTL coupling experiment had different beam parameters because they were generated by different fibre injectors. Thus, the path length readout measured at the SEPD likely contained not only the actuator's longitudinal displacement but also unknown additional TTL coupling effect, meaning the path length signal measured in the measurement interferometer after subtracting the SEPD's path length readout might not fully represent the TTL coupling.

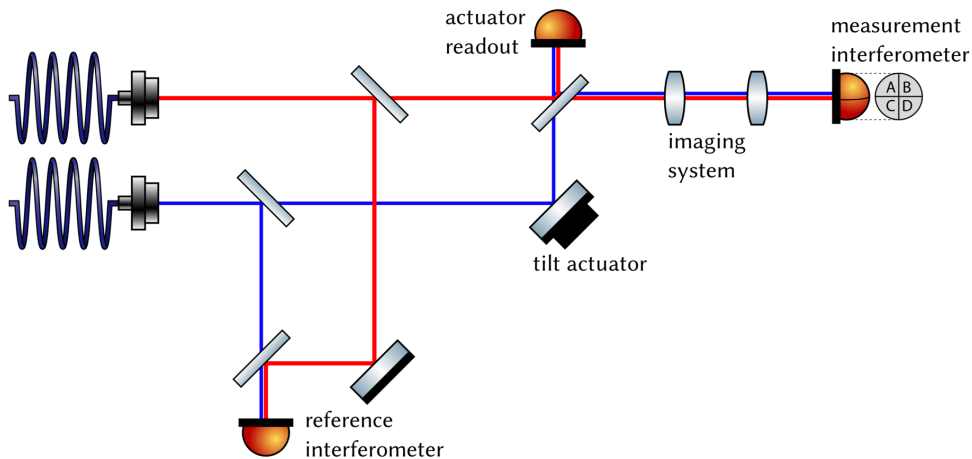


Figure 3.2: Schematic of the first TTL coupling experiment testbed. Under the condition that if using two identical beam (fundamental Gaussian beam) and a large SEPD, the longitudinal displacement of tilt actuator can be measured by the large SEPD (denoted by 'actuator readout'). The readout can be either used for stabilising the longitudinal displacement of the tilt-actuator via a feedback loop or subtracted from the readout of QPD (denoted by 'measurement interferometer'). This figure is taken from [43]

## Second generation AEI TTL coupling experiment

In the second TTL coupling experiment, the beam parameter mismatch between two interfering beams was mitigated. Based on the homodyne interferometry, the two beams were generated by one laser source, intending to make their beam parameters to be analogous. Also, a dedicated mode cleaner(not drawn in Figure 3.3, but it can be found in the full schematic in [44]) in the setup enhanced the beam quality, such that the output beam from the mode cleaner become mostly the fundamental Gaussian beam by suppressing the high order modes of the beam. As done in the first generation AEI TTL coupling experiment, the large SEPDP was used to measure only the actuator's longitudinal displacement in the second TTL coupling experiment. As a result, the second TTL coupling experiment proved that an imaging system could suppress the TTL coupling [44]. However, the homodyne interferometry in this setup is not fully representative for space laser interferometers adopting heterodyne interferometry. Additionally, this experiment was valid for this particular case when two equal Gaussian beams' interference, not unmatched Gaussian-Gaussian beam interference or Gaussian-top-hat beam interference.

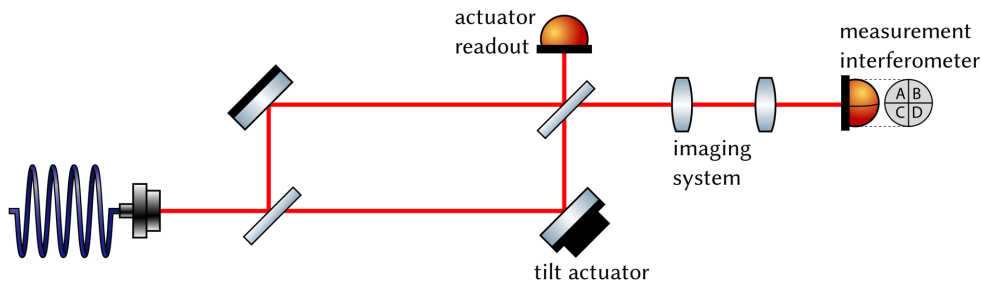


Figure 3.3: *Schematic of the second TTL coupling experiment testbed. Since the second TTL coupling testbed is based on the homodyne interferometry scheme, the interfering beams are identical by being generated from one fibre coupler. It dismisses the issue that the two beams in the first TTL coupling experiment were unequal. This figure is take from [43]*

## Third generation AEI TTL coupling experiment

The third generation AEI TTL coupling experiment [22, 43, 54], called ‘LISA optical bench testbed’, was developed with more elaborate and complicated techniques, compared to the two previous TTL couple experiments. It consists of two main parts; the optical bench and the telescope simulator.

The optical bench in this paragraph refers to a testbed mimicking the future optical bench of LISA and contains multiple interferometers to test the TTL coupling measurement. In its construction, optical components such as mirrors and beam splitters were glued on a baseplate of Zerodur material that has an extremely low coefficient of thermal expansion. In the optical bench testbed, two different imaging systems were tested to prove a suppression of the TTL coupling.

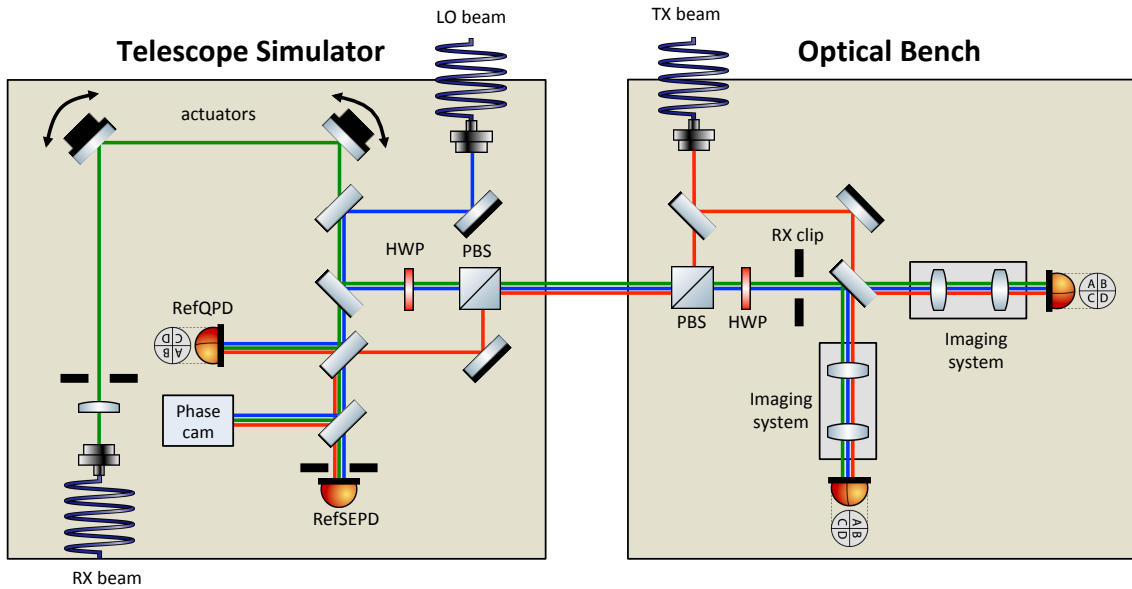


Figure 3.4: *Concept of LISA optical bench testbed. The LISA optical bench testbed consists of two main parts; telescope simulator on the left-hand side of the figure and optical bench on the right-hand side of the figure. The telescope simulator provides a tiled beam through an aperture (called ‘RX clip’), and imaging systems installed on the optical bench are used to reduce the TTL coupling. This figure was reproduced from [33], Credit: Maike Danielle Lieser.*

The telescope simulator was developed to provide a beam tilt and minimise the effect of actuation error to path length readout. In the first and second TTL coupling experiments, the actuators were employed to reflect and tilt a beam like a test-mass in LISA. In contrast, the telescope simulator in the third TTL coupling experiment transmits a beam through a fixed aperture called ‘RX clip’, and rotates the beam around the centre of the RX clip as if a beam is tilted through the large telescope of LISA or a testmass. One notable feature was it could produce not only a simply Gaussian beam but also a tophat beam that enables simulating the long-arm interferometer. As the schematic of the LISA optical bench testbed is shown in Figure 3.4, a QPD (named ‘RefQPD’) and a SEP (RefSEPD) in the telescope simulator are installed at equivalent positions where are optical copies of the RX clip. It means that each RX-beam splitting to the RX-clip on the optical bench, RefQPD, and RefSEPD experiences the same phase variation [23]. The DPS signal measured via the RefQPD is fed to actuators in order to tilt the RX-beam without beam-walk on the RefQPD, which is equivalent to rotating the RX-beam round the RX clip. The phase variation before the RX clip is measured on the RefSEPD, and a feedback loop minimises the phase variation by phase-locking between beams, which is initialising the phase zero at the RX clip [23].

The LISA optical bench testbed experiment had proved that the imaging systems could suppress the TTL coupling, fulfilling the LISA’s requirement that the TTL

coupling should be below  $25 \mu\text{m}/\text{rad}$  in the beam rotation angle of  $300 \mu\text{rad}$  [54].

However, it has a few disadvantages in the aspect of its complexity. Despite high thermal stability by constructing the testbeds in a vacuum chamber, it required much more effort on its construction and alignment. Moreover, the setup cannot be easily modified and adjusted to test for different settings like different distances or beam properties, because most optical components are glued onto the baseplate.

### 3.1.3 Concept of advanced-tilt-actuator

The advanced tilt actuator (ATA)' was developed to resolve the troublesome difficulty regarding the actuation error and the LISA optical bench testbed's lack of flexibility. Its design concept is based on providing a tilted beam to a TTL coupling testbed and simultaneously measuring its motion by dedicated laser interferometers.

As shown in Figure 3.5 illustrating a simplified schematic, it can be divided into two main parts: the actuation platform (AP) and multiple interferometers that measure the AP's motion. The AP, driven by three piezo actuators, produces the motion in three degrees-of-freedom (3-DOF) for yaw, pitch and longitudinal displacement, suppressing the other 3-DOF motion for two lateral displacements and roll. A flat mirror attached on the AP's front surface reflects and tilts the measurement beam (red line) of the TTL coupling testbed. The most prominent feature of the ATA is to measure the AP's motion. Four retroreflectors are installed on the AP's rear, and their vertices are regarded as reference points of the AP. The multiple interferometers in the ATA trace the longitudinal displacement of the vertices, such that the AP's 3-DOF motion can be measured.

For the TTL coupling experiment, the AP's longitudinal displacement measured by the ATA can be either subtracted from the length readouts via two QPDs (labelled with QPD 1 and QPD 2, in Figure 3.5) or stabilised via a feedback loop system. Furthermore, by exploiting the feedback loop control, the ATA can be driven to have any desired motion in 3-DOF.

One advantage of the ATA is that it can be flexibly utilised. Since it was designed and constructed as an independent testbed, it can be utilised not only for one specific TTL coupling experiment but also for other experiments requiring the ATA's 3-DOF motion. Unlike the simplified schematic shown in Figure 3.5, the more details regarding the ATA's development will be demonstrated in the following section.

## 3.2 Development of advanced-tilt-actuator

The ATA was built on an independent optical breadboard, as its design concept that the ATA can be employed for a variety of TTL coupling experiments. A CAD drawings in Figure 3.6 show an overview of the ATA testbed. In the top-down view (upper), the beam paths of the measurement and reference beams are drawn

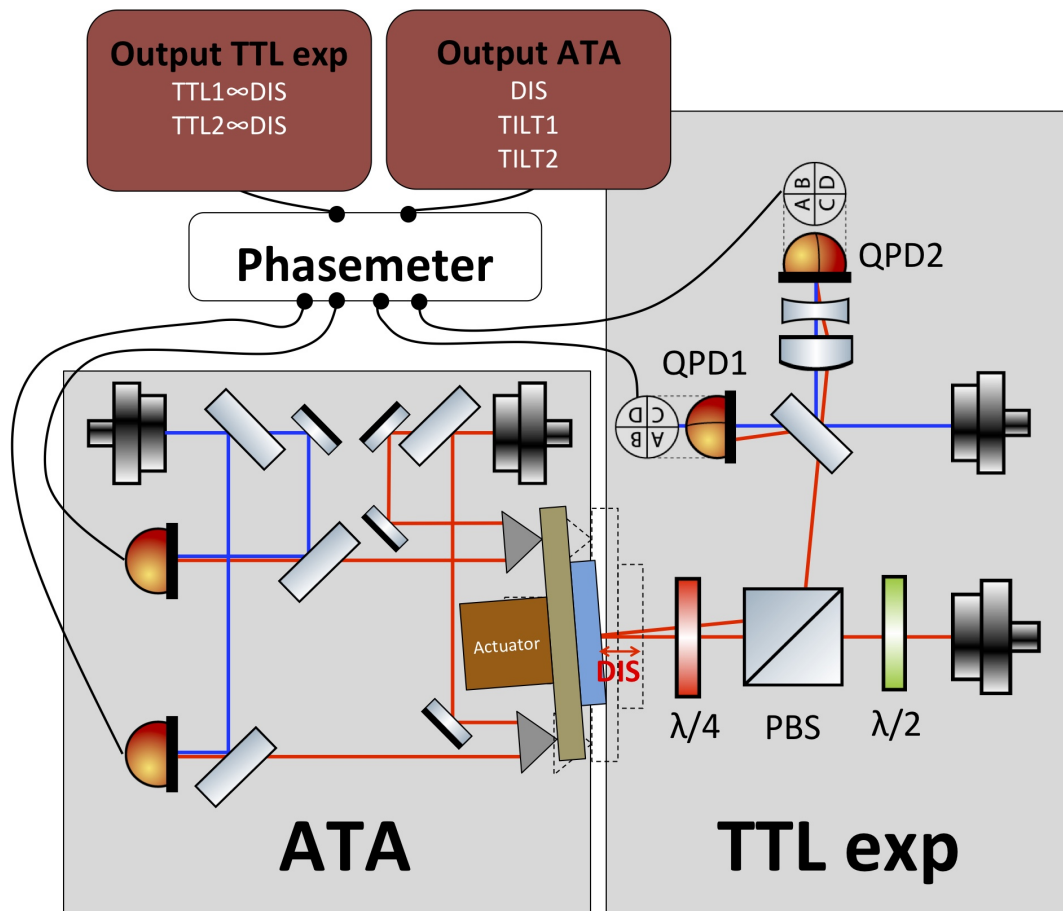


Figure 3.5: Concept of the advanced tilt actuator for the TTL coupling experiment. To resolve the actuation error that couples into the path length readout, the advanced tilt actuator would measure the motion of the actuation. Several retroreflectors are attached on the rear surface of the actuator, and multiple interferometers track the longitudinal displacement of each retroreflector. The ATA measures two tilt angles for yaw and pitch, as well as a longitudinal displacement. The actuator's longitudinal displacement measured by the ATA can be subtracted from the readouts of QPD 1 and QPD 2 or suppressed via a feedback loop control.

by red and blue lines respectively. An orthographic projection in the bottom of Figure 3.6 presents a more detailed view with many components including optical mounts on an optical breadboard, the AP with three piezo actuators and several retroreflectors, and two periscopes used for delivering beams towards the upper retroreflectors in the AP.

The AP placed on the lower-right corner of the optical breadboard is driven by three piezo actuators. It produces 3-DOF motion for two tilts (yaw and pitch) and a longitudinal displacement. A flat mirror is attached on the front of the AP and reflects the measurement beam needed for TTL coupling experiment. The vertices of the four retroreflectors installed on the AP's rear are regarded as reference points for the AP.

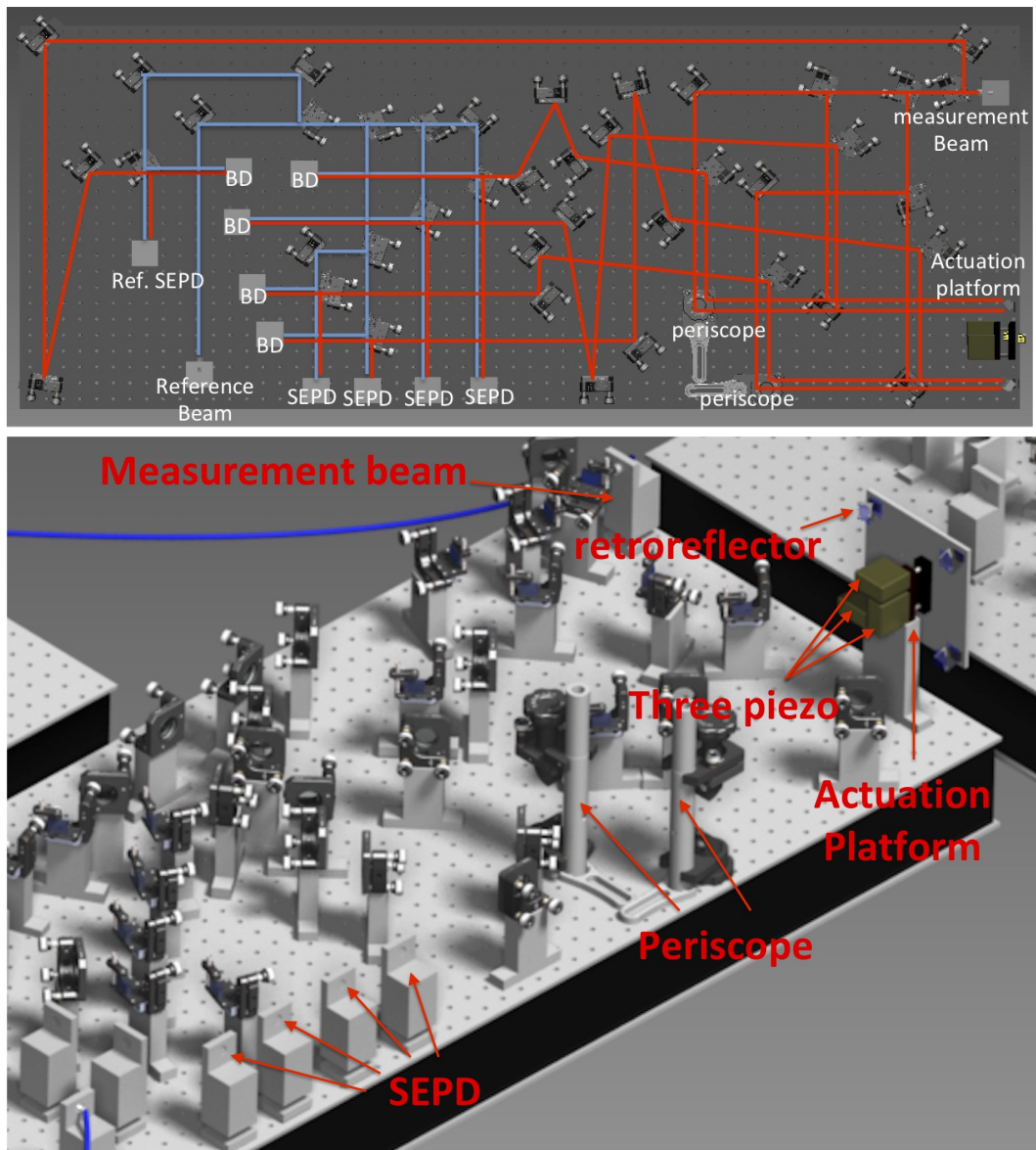


Figure 3.6: *CAD model of the advanced tilt actuator. The upper illustration shows a top-view of the ATA with beam paths of each interferometer. The ATA includes four measurement interferometers and one reference interferometer. The red and blue lines indicate beam paths for the measurement and reference beams, respectively. As shown on the bottom, the ATA constructed on an optical breadboard consists of many components including optical mounts, the actuation platform with three piezo actuators and four retroreflectors, two periscopes used for delivering beams towards two upper retroreflectors of the actuation platform, and several SEPDs sensing beams.*



Among five interferometers on the ATA testbed, four interferometers measure each retroreflector's longitudinal displacement, and the fifth interferometer serves as a reference interferometer. The interfering beams in each of the five interferometers are sensed by SEPDs.

### 3.2.1 Retroreflectors in the ATA

Four retroreflectors attached to the AP are the core optical components in the ATA. One of the retroreflectors' unique features is that the outgoing beam is antiparallel with respect to the incident beam regardless of the incident beam angle (or rotation of the retroreflector). That means that the outgoing beam's direction is stationary while the AP rotates, which cannot be accomplished by an ordinary flat mirror. This feature enables preventing the angular misalignment between two interfering beams, which may cause an additional TTL coupling. The vertices of the four retroreflector represent reference points for the AP, and their longitudinal displacement tracked by the dedicated interferometers are used to measure the AP's motion.

As shown on the bottom of Figure 3.6, the four retroreflectors are attached on a metal plate vertically supported by a kinematic mount. One of the important considerations in choosing retroreflectors to be installed in the ATA is the mass. Because, if the retroreflectors vertically attached are heavy, the stability of the kinematic mount that supports them may deteriorate. Therefore, a lightweight retroreflector is preferable to be installed on the AP. The selected retroreflector (PLX Inc., USHM-10-1) for the ATA, shown in Figure 3.7, weighs 34 grams and has a one-inch clear aperture.

### 3.2.2 Actuation platform

The AP acts as a testmass in the TTL experiment. It is driven by three piezo actuators integrated with a kinematic mount and produces 3-DOF motion for yaw, pitch, and longitudinal displacement.

As shown on the upper left of Figure 3.8, four retroreflectors are attached on the rear of a rectangular aluminium plate, and the distance between two retroreflectors separated horizontally and vertically is approximately 120 mm. The height from the floor to the vertex of the lower retroreflectors is about 100 mm. A flat mirror glued on the other side of the metal plate reflects the measurement beam used in the TTL coupling testbed, as shown on the upper right of Figure 3.8. The height from the floor to the centre of the flat mirror is around 100 mm.

To fully mimic a testmass of space laser interferometers, an actuator system should be capable of 6-DOF motion, but it requires a relatively complex configuration to measure its motion in all degrees of freedom. In the aspect of producing a pure tilting beam for TTL coupling experiment, the horizontal and vertical displacements and roll rotation are not critical or may disturb to characterise TTL coupling.

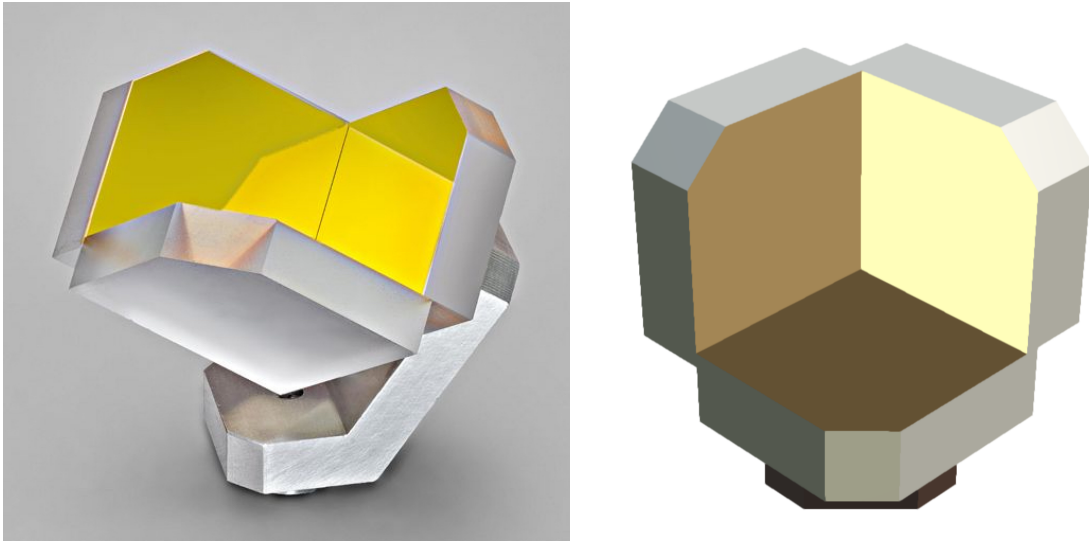


Figure 3.7: *Hollow retroreflector used for the ATA. The retroreflectors used for the ATA should be lightweight. Because, when the retroreflectors are attached to the AP's metal plate that is perpendicular to the optical breadboard, their weight affects the stability of the AP. The selected retroreflector (PLX Inc, USHM-10-1) weighs 34 grams and has a one-inch clear aperture.*

For these reasons, the AP was developed to allow the yaw and pitch rotations and longitudinal displacement, restricting the other 3-DOF motions.

Three piezo actuators (Newport, NPM140), integrated with the kinematic mount, are a type of flexure-guided piezo actuator, which amplifies a stacked piezo's displacement by mechanical flexure. It moves back and forth with the maximum displacement of  $140\ \mu\text{m}$ , which can lead the AP's maximum tilt angle of about 2 mrad. One advantage of using this piezo actuator is that the movement can be controlled not only by actuation of piezo but also by manual screws. As shown on the lower-left of figure 3.8, each piezo actuator hosts a manual screw which can be used to align the kinematic mount manually. Three spherical tips at the end of each piezo actuator are in contact with grooves of the kinematic mount. In particular, the lower-left tip in the upper-left illustration of Figure 3.8 is in contact with a conical hole, and the front part of the kinematic mount including the metal plate with retroreflectors rotates around the centre of the lower-left spherical tip. Since the three tips are confined to have only longitudinal displacement by the actuators, the AP is not allowed to have lateral movement, which means that the other 3-DOF motion (the roll rotation and the horizontal and vertical displacements) are constrained. The three tips' longitudinal movements enable 3-DOF motions for the metal plate.

The applied voltage to the three piezo actuators is in the range from -20 to 140 V. Instead of controlling each piezo actuator via three respective voltage sources, an electronic circuit called 'voltage amplifier' (developed at AEI by Gerhard Heinzl) enable a single input voltage to drives the three actuators for single-DOF motion.

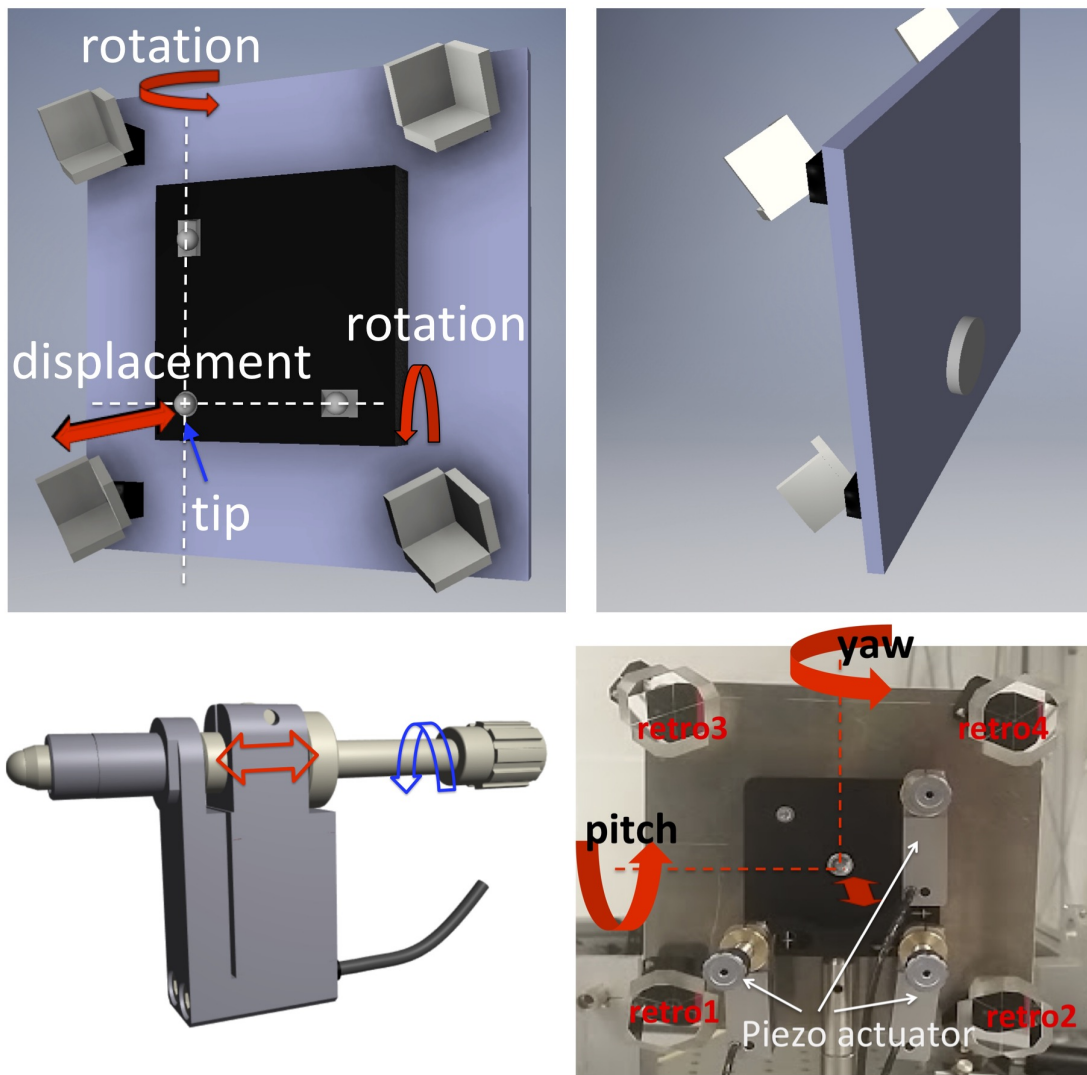


Figure 3.8: Actuation platform of the ATA. As shown on the upper-right, four retroreflectors are installed on a metal plate that is attached to a kinematic mount. Three spherical tips belonging to the kinematic mount are moved back and forth by three piezo actuators. The kinematic mount rotates around the centre of the spherical tip at the bottom left and moves longitudinally. As shown on the upper-right, a flat mirror is attached on the front of the metal plate in order to reflect a beam in the TTL coupling testbed. The lower-left illustration shows the CAD model of the piezo actuator employed for the ATA. Since this actuator is integrated with an adjustment screw, it is driven by applying a voltage but also allows manual displacement by the adjustment screw. A lower-right picture shows the AP integrated by three piezo actuators, the kinematic mount, the metal plate and four retroreflectors, enabling 3-DOF motions; yaw, pitch and longitudinal displacement. Credit: The CAD model of the piezo actuator, which is shown on the lower-left, originates from the company of Newport.

As the simplified schematic of the voltage amplifier shown in Figure 3.9, each of the three input sources corresponds to each motion of the AP for the yaw, pitch and longitudinal displacement. The three input voltages are distributed and mixed on the mixing stage, then the signals after the mixing stage are amplified by a factor of ten on the amplifier stage. The amplified voltages are delivered to the three piezo actuators. The amplitude of the motion of the ATA is mostly linear linearly proportional to the applied voltage. The developed voltage amplifier also allows three input signals simultaneously to execute an arbitrary complex motion of the AP.

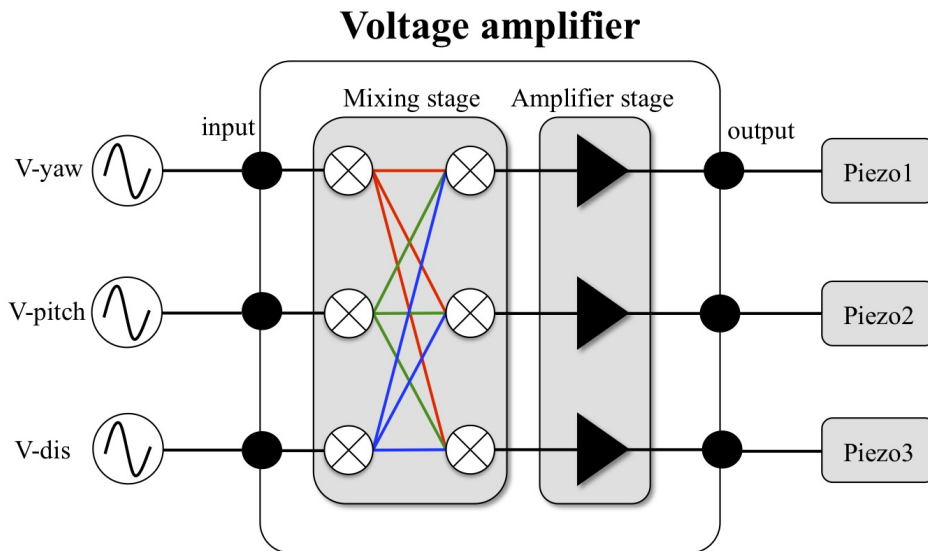


Figure 3.9: Schematic of the voltage amplifier used for the ATA's actuation. The input voltage sources ( $V$ -yaw,  $V$ -pitch,  $V$ -dis) to the voltage amplifier correspond to each degree of freedom motion of the actuation platform. The input voltages are distributed and mixed on 'mixing stage', and 'amplifier stage' amplifies the mixed signals by a factor of ten. Final outputs from the voltage amplifier are delivered to each piezo actuator. The voltage amplifier was designed by Gerhard Heinzl (AEI).

### 3.2.3 Multiple interferometers

The ATA contains a total of five interferometers; four measurement interferometers and a reference interferometer. The measurement interferometers trace the longitudinal displacements of the four retroreflectors that are attached on the rear of the AP, such that the AP's motion in 3-DOF can be measured. The reference interferometer is set to cancel the environmental noise in the readouts of the measurement interferometers.

The ATA testbed was built on an optical breadboard (size 1500 mm  $\times$  600 mm). Two laser beams are delivered from the modulation bench through fibres (details

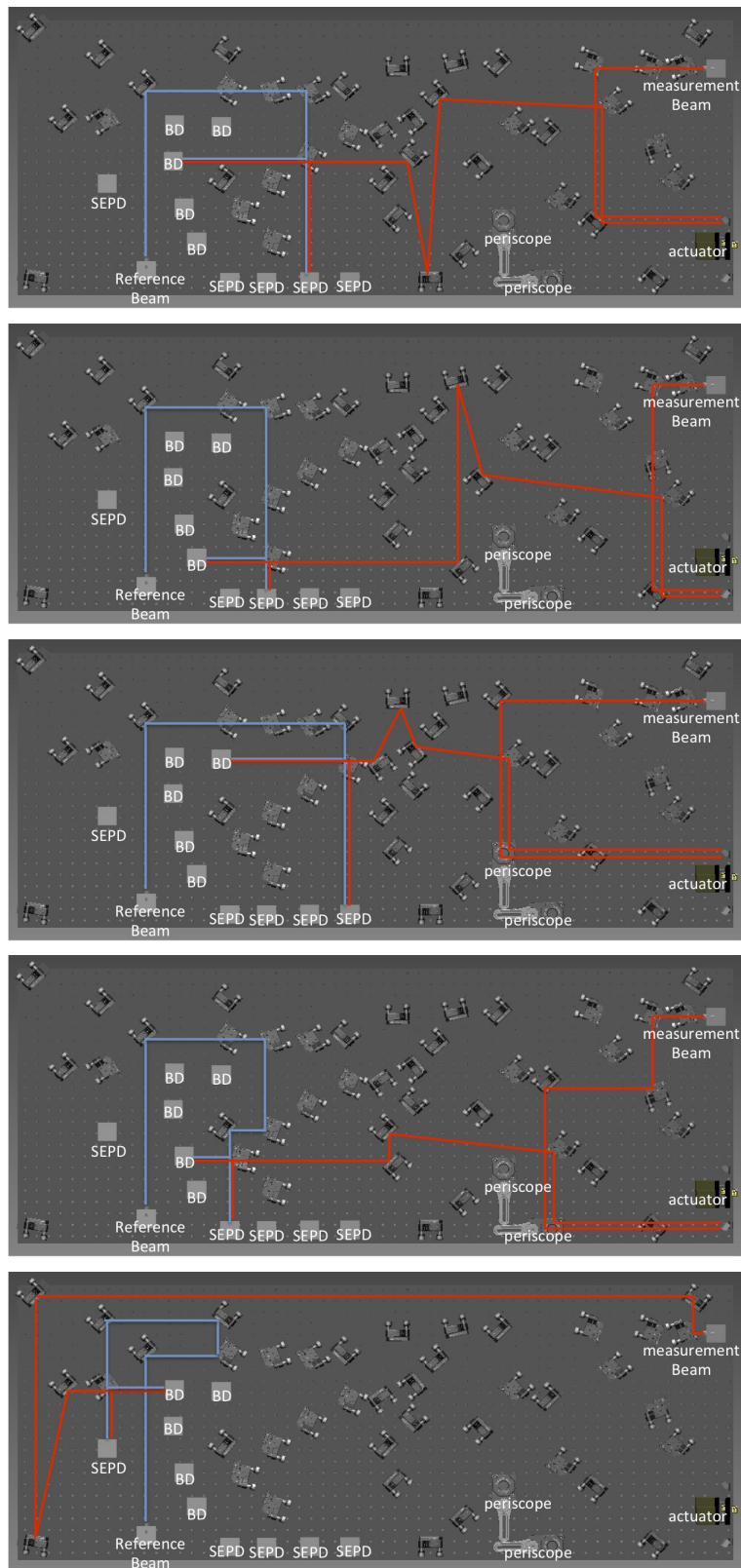


Figure 3.10: *Beam path for respective interferometers in the ATA. Four CAD models from the top show the beam paths for each measurement interferometer, and the bottom one depicts the beam path for the reference interferometer.*

are described in Chapter 5.1.1), and the heterodyne frequency of the two beams is 12.5 kHz. The two beams in the ATA are produced by fibre collimators (Schäfter-Kirchhoff GmbH, 60FC-4-A6.2-03), having the beam diameter of approximately 1 mm. The polarisation for both beams is s-pol (electric field's direction is perpendicular to the optical breadboard's surface). Beam paths for each interferometer in the ATA are shown in the CAD drawings of Figure 3.10. In each CAD drawing, red and blue lines indicate measurement and reference beams, respectively. The first and second drawing in Figure 3.10 represent measurement interferometers that correspond to the two bottom retroreflectors of the AP. The other two measurement interferometers corresponding to the two upper retroreflectors are presented in the third and fourth drawings of Figure 3.10. They contain two periscopes to change the beam's height, such that two beams can be delivered to the two upper retroreflectors. The fifth interferometer drawn on the bottom of Figure 3.10 is a reference interferometer. In the ATA, all interferometers employ SEPDs to sense the interfering beams.

### 3.2.4 Working principle of ATA

To measure the AP's 3-DOF motion, it requires two essential pieces of information. The first information is the longitudinal displacements of each retroreflector, which are traced by the dedicated interferometers. The second information is positions of vertex of the retroreflectors, which are regarded as reference points of the AP (the method to measured the retroreflectors' vertex will be described in Chapter 3.3.1). Based upon a premise that both information is accurate, the working principle to measure the AP's 3-DOF motion is mathematically explained in this section.

As aforementioned, four interferometers tracking the longitudinal displacement of the retroreflectors' vertices (labelled with P1, P2, P3, and P4) are set up in the ATA. In principle, using only three retroreflectors are sufficient to measure the AP's motion in 3-DOF. The fourth retroreflector is redundant but can also be used to confirm the ATA's performance in particular for longitudinal displacement measured via using three retroreflectors, which will be discussed in Chapter 4.3.1. In here, three retroreflectors whose vertices are labelled with 'P1', 'P2', 'P3' determine the ATA-plane, which is drawn as a colour quadrangle in Figure 3.11. The following explanation describes an analytical solution in terms of the 3-DOF motion of the ATA-plane, using the retroreflectors' positions and longitudinal displacement.

Each position of the three vertices is notated by  $P_n(t)$  in the Cartesian coordinate, numbered with  $n=\{1, 2, 3, 4\}$

$$\vec{P}_n(t) = (X_n, Y_n, Z_n(t)), \quad n = 1, 2, 3, 4. \quad (3.1)$$

Lateral movement of each vertex during the AP's rotation is so small that its  $x$  and  $y$  coordinates  $X_n, Y_n$  can be regarded as being static and time independent.  $Z_n(t)$  are the retroreflectors' longitudinal displacements measured by dedicated interferometers. To measure the AP's 3-DOF motion, three vertices ( $\vec{P}_1, \vec{P}_2, \vec{P}_3$ ) are chosen

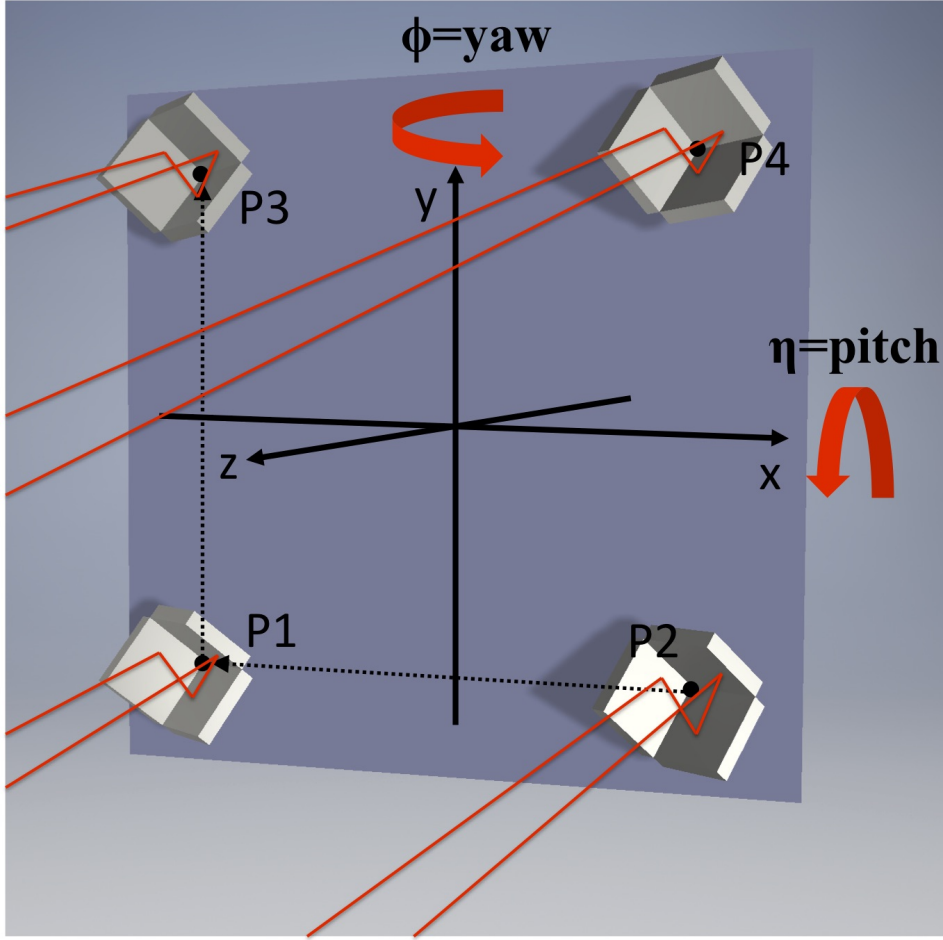


Figure 3.11: Illustration of the ATA-plane determined by the vertices of three retroreflectors. The multiple retroreflectors' vertices (marked with  $P_1$ ,  $P_2$ ,  $P_3$ , and  $P_4$ ) are regarded as reference points for the AP. Among four retroreflectors, three retroreflectors whose vertices are labelled with  $P_1$ ,  $P_2$ , and  $P_3$  determine the ATA-plane drawn by the colour square. Their longitudinal displacement measured by dedicated interferometers are used for measuring the ATA-plane's (or AP's) 3-DOF motion (yaw, pitch, and displacement). The fourth retroreflector is redundant, but its longitudinal displacement can be used for calibrating the ATA's longitudinal displacement measured by using the other three retroreflectors.

to describe the ATA-plane. If we denote a vector from  $\vec{P}_2$  to  $\vec{P}_1$  by  $\overrightarrow{P_2P_1}$  and another vector from  $\vec{P}_1$  to  $\vec{P}_3$  by  $\overrightarrow{P_1P_3}$ , they can be notated by

$$\begin{aligned}\overrightarrow{P_2P_1} &= (X_1 - X_2, Y_1 - Y_2, Z_1(t) - Z_2(t)) \\ \overrightarrow{P_1P_3} &= (X_3 - X_1, Y_3 - Y_1, Z_3(t) - Z_1(t)).\end{aligned}\quad (3.2)$$

The normal vector of the ATA-plane  $\vec{N}$  is derived by the cross product of the two vectors  $\overrightarrow{P_2P_1}$  and  $\overrightarrow{P_1P_3}$  as

$$\vec{N}(t) = [N_x(t), N_y(t), N_z(t)] = \overrightarrow{P_2P_1} \times \overrightarrow{P_1P_3}(t). \quad (3.3)$$

The each component of  $\vec{N}$  is

$$\begin{aligned} N_x(t) &= Z_1(t) \cdot (Y_2 - Y_3) + Z_2(t) \cdot (Y_3 - Y_1) + Z_3(t) \cdot (Y_1 - Y_2) \\ N_y(t) &= Z_1(t) \cdot (X_3 - X_2) + Z_2(t) \cdot (X_1 - X_3) + Z_3(t) \cdot (X_2 - X_1) \\ N_z &= X_1 \cdot (Y_3 - Y_2) + X_2 \cdot (Y_1 - Y_3) + X_3 \cdot (Y_2 - Y_1) = \text{const}. \end{aligned} \quad (3.4)$$

In Equation (3.4),  $N_x(t)$  and  $N_y(t)$  is shown to be a superposition of  $Z_n$  with coefficients determined by the set of  $Y_n$ , and  $N_z$  becomes a constant value.  $N_z$  and each coefficient of  $N_x(t)$  and  $N_y(t)$  are determined by the three retroreflectors' vertex positions  $X_n$  and  $Y_n$ .

The plane equation describing all points  $(x, y, z)$  on the ATA-plane can be expressed by using the normal vector  $\vec{N}$  and one of the vertices (here, we choose  $P_1(t)$ )

$$N_x(t) \cdot (x - X_1) + N_y(t) \cdot (y - Y_1) + N_z \cdot (z - Z_1(t)) = 0. \quad (3.5)$$

Equation (3.5) describes the motion of the ATA-plane in 3-DOF.

An arbitrary 3-DOF motion can be decomposed into the following three independent motions. The yaw, denoted by  $\phi(t)$ , represents the ATA-plane's rotation around the y-axis. And the pitch, denoted by  $\eta(t)$ , is defined by the ATA-plane's rotation around the x-axis. The displacement, denoted by  $D(t)$ , means the ATA-plane's displacement along the z-axis at  $x = 0$  and  $y = 0$ .

The tilt angles for yaw  $\phi(t)$  and pitch  $\eta(t)$  are derived from the ATA-plane's normal vector  $\vec{N}$ , as

$$\phi(t) = \tan^{-1} \left( \frac{N_x(t)}{N_z} \right) \approx \frac{N_x(t)}{N_z} \quad (3.6)$$

$$\eta(t) = -\tan^{-1} \left( \frac{N_y(t)}{N_z} \right) \approx -\frac{N_y(t)}{N_z}. \quad (3.7)$$

The displacement  $D$  is derived by substituting zero for  $x$  and  $y$  in Equation (3.5), like

$$\begin{aligned} N_x(t) \cdot (0 - X_1) + N_y(t) \cdot (0 - Y_1) + N_z \cdot (D(t) - Z_1(t)) &= 0 \\ \implies D(t) &= \frac{N_x(t) \cdot X_1 + N_y(t) \cdot Y_1}{N_z} + Z_1(t). \end{aligned} \quad (3.8)$$

The most important readout from the ATA is the longitudinal displacement for the measurement beam's reflection point in the TTL coupling experiment. If the beam reflection point notated by  $(x, y, z)$  is placed on the ATA-plane, its longitudinal displacement  $z(t)$  can be calculated by using  $\phi(t)$ ,  $\eta(t)$ ,  $D(t)$ , as



$$z(t) = \underbrace{[-x \times \phi(t)]}_{\text{yaw contribution}} + \underbrace{[y \times \eta(t)]}_{\text{pitch contribution}} + \overbrace{D(t)}^{\text{displacement contribution}}, \quad (3.9)$$

or can be derived by solving Equation (3.5) for  $z$ , as

$$z(t) = \frac{-N_x(t) \cdot (x - X_1) - N_y(t) \cdot (y - Y_1)}{N_z} + Z_1(t). \quad (3.10)$$

Note that Equation (3.9) and (3.10) are equivalent. The  $\phi(t)$ ,  $\eta(t)$  and  $z(t)$ , expressed in Equation (3.6), (3.7) and (3.10) are the ATA's main readouts for the 3-DOF motion of the ATA-plane. These three equations can be reorganised by using the vertices' position  $X_n$ ,  $Y_n$  and the longitudinal displacement readouts of  $Z_n$  from each retroreflector, as

$$\phi(t) = \overbrace{\left(\frac{Y_2 - Y_3}{N_z}\right)}^{\text{constant: } g_{11}} \cdot Z_1(t) + \overbrace{\left(\frac{Y_3 - Y_1}{N_z}\right)}^{\text{constant: } g_{12}} \cdot Z_2(t) + \overbrace{\left(\frac{Y_1 - Y_2}{N_z}\right)}^{\text{constant: } g_{13}} \cdot Z_3(t), \quad (3.11)$$

$$\eta(t) = \overbrace{\left(\frac{X_2 - X_3}{N_z}\right)}^{\text{constant: } g_{21}} \cdot Z_1(t) + \overbrace{\left(\frac{X_3 - X_1}{N_z}\right)}^{\text{constant: } g_{22}} \cdot Z_2(t) + \overbrace{\left(\frac{X_1 - X_2}{N_z}\right)}^{\text{constant: } g_{23}} \cdot Z_3(t), \quad (3.12)$$

$$z(t) = \overbrace{\left[\frac{(X_1 - x) \cdot (Y_2 - Y_3) + (Y_1 - y) \cdot (X_3 - X_2)}{N_z} + 1\right]}^{\text{constant: } g_{31}} \cdot Z_1(t) \\ + \overbrace{\left[\frac{(X_1 - x) \cdot (Y_3 - Y_1) + (Y_1 - y) \cdot (X_1 - X_3)}{N_z}\right]}^{\text{constant: } g_{32}} \cdot Z_2(t) \\ + \overbrace{\left[\frac{(X_1 - x) \cdot (Y_1 - Y_2) + (Y_1 - y) \cdot (X_2 - X_1)}{N_z}\right]}^{\text{constant: } g_{33}} \cdot Z_3(t), \quad (3.13)$$

where  $N_z$  is constant as defined in Equation (3.4), and each  $g_{mn}$  is constant coefficient. The three readouts  $\phi(t)$ ,  $\eta(t)$  and  $z(t)$  from Equation from (3.11) to (3.13) can be merged in one equation in a matrix form, as

$$\begin{pmatrix} \phi(t) \\ \eta(t) \\ z(t) \end{pmatrix} = \hat{G} \cdot \begin{pmatrix} Z_1(t) \\ Z_2(t) \\ Z_3(t) \end{pmatrix} = \begin{pmatrix} g_{11} & g_{12} & g_{13} \\ g_{21} & g_{22} & g_{23} \\ g_{31} & g_{32} & g_{33} \end{pmatrix} \cdot \begin{pmatrix} Z_1(t) \\ Z_2(t) \\ Z_3(t) \end{pmatrix}, \quad (3.14)$$

where the matrix  $\hat{G}$  consists of the above constant coefficients  $g_{mn}$ , which are determined by the geometric position of each retroreflector.

In short,  $Z_n(t)$  are the longitudinal displacement readouts of each retroreflector, which can be regarded as input values obtained by dedicated interferometers in the ATA. The  $\hat{G}$  matrix is determined by lateral positions of the retroreflectors. The final outputs  $\phi(t)$ ,  $\eta(t)$  and  $z(t)$  are obtained by applying the operator of  $\hat{G}$  matrix to the input  $Z_n(t)$ .

### 3.3 Alignment campaign

There are two crucial assumptions in the above analytic solution for the ATA's 3-DOF readouts. Firstly, the retroreflectors' vertices positions are perfectly known. Secondly, the longitudinal displacements of the retroreflectors are measured without error. The accuracy of these two parameters directly influences the ATA's performance. In this context, alignments during the construction of the ATA setup are nontrivial tasks. The mentioned alignments involve two kinds of issues; how to measure the positions of the installed retroreflectors' vertices and how to align the incident beams towards the retroreflectors. The following section describes alignment strategies applied to the ATA's construction.

#### 3.3.1 Measurement of vertices for the retroreflectors

As shown in Figure 3.8, the four retroreflectors are installed on a metal surface by screwing them through holes. Initially, the lateral distances between each hole were intended to be 120 mm. However, the holes' positions likely deviate from the initially intended positions in the order of a few millimetres. It may be possible to measure the position of each hole with high accuracy. However, even if possible, the retroreflectors' vertices do not coincide with the holes' centre. For this reason, measuring the centre of the holes does not guarantee the positions of the vertices.

For measuring the vertices, a coordinate-measurement-machine (CMM), possessed by AEI Hannover (DEA Global Advantage, Hexagon Metrology GmbH), was used. As shown in Figure 3.12, the probe that is mounted on the moving frame of the CMM moves in three directions. The spherical tip at the end of the probe makes contact with the object, and the CMM measures the contact point's position.

In the procedure to measure the vertices of the retroreflectors, a few things need to be considered. Firstly, since the probe tip has a specific size, it cannot directly touch the vertex at the corner of the retroreflector. Alternatively, the CMM's probe contacts several points on each mirror of the retroreflector to measure the mirror surfaces. Then, the point where the three mirror surfaces meet can be computed, which is supposed to be the vertex. Secondly, when measuring each mirror surface, the probe's tip touches the edges of each surface. Since physically touching an optical surface may bring about some scratches on the surface, touching the mirror's middle area where a beam may be reflected is not preferable.

Figure 3.13 illustrates points where the probe's tip contacts the retroreflectors' mirror surface and the procedure of measuring the vertices. At first, it starts measuring the vertex of the 'Retro1' at the lower-left. As mentioned above, the probe's tip contacts three points on the edge of a mirror surface and measures a plane determined by the three points. Likewise, the other two surfaces can be measured in the same manner. Subsequently, a point where the three planes meet is computed, which is regarded as the retroreflector's vertex of  $\vec{P}_1$ .

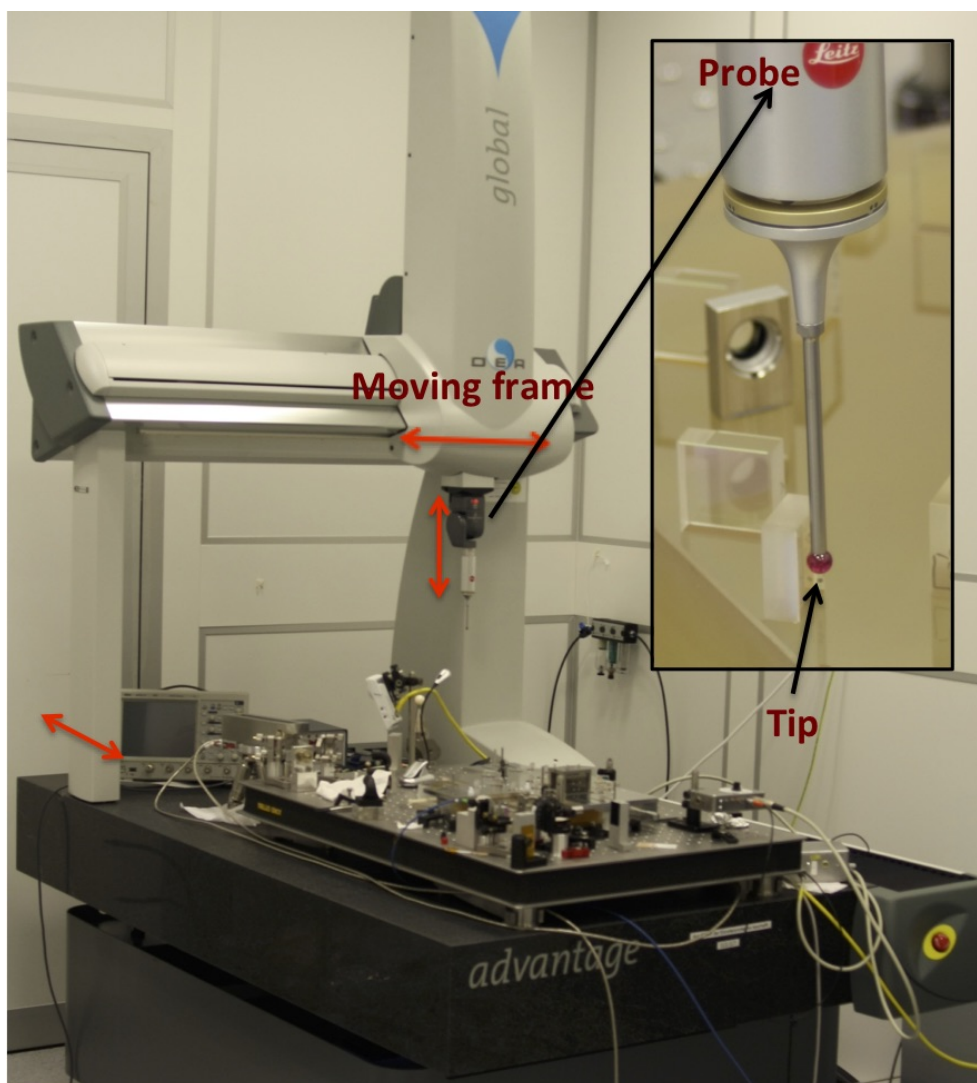


Figure 3.12: *Photograph of a coordinate-measurement-machine (CMM). The CMM machine (DEA Global Advantage, Hexagon Metrology GmbH) was used to measure the vertices of the retroreflectors of the ATA. A probe tip moves along with the ‘moving frame’ and measures its contact positions. These photographs were provided by AEI LISA backlink team.*

In the next step, the probe moves towards the second retroreflector (Retro2) at the lower-right and measures the second vertex position as done in measuring the vertex position of the Retro1. Also, the same procedure is applied to measuring the vertex of the Retro3 at the upper-left. After measuring the three vertices, the ATA’s Cartesian coordinate system can be established through the following three conditions. In the first condition, the measured first vertex point is defined as a reference point at  $(-60 \text{ mm}, -60 \text{ mm}, 0)$ . In the second condition, a plane determined by the measured three vertices, called ‘ATA-plane’, is defined to be on the x-y plane in the ATA’s coordinate system. In the third condition, the line between the first and second vertex is defined to be parallel to the x-axis. After establishing the

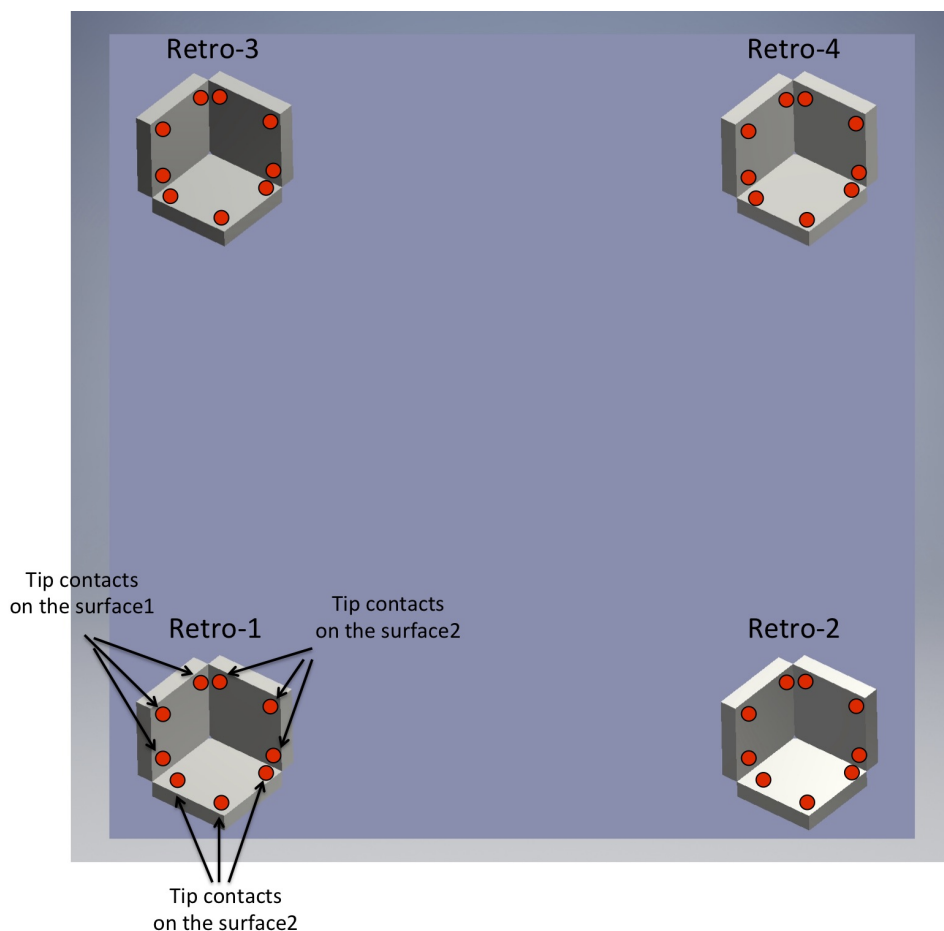


Figure 3.13: *Illustration of the procedure to measure the vertices of the four retroreflectors. The procedure starts with measuring the vertex of the retroreflector on the lower-left ('Retro-1'). The CMM's probe tip (red circle) touches three points on the edge of a mirror surface in order to describe the plane determined by the three points. Likewise, the other two mirror surfaces of 'Retro-1' are measured. Then, the point that the three surfaces meet can be calculated, which is supposed to be the vertex. In the same manner, the vertices for the other retroreflectors can be measured.*

ATA's Cartesian coordinate system, the fourth retroreflector's vertex position  $\vec{P}_4$  can be determined. In Table 3.1, each retroreflector's vertex measured by the CMM are listed.

### 3.3.2 Alignment for four beams

While an interferometer measures the retroreflector's longitudinal displacement, the angular misalignment between the incident beam towards the retroreflector and the direction of the retroreflector's displacement causes the readout error. Figure 3.14

Table 3.1: Measured vertex positions of the four retroreflectors by using the Coordinate Measuring Machine.

Retroreflector	Unit	$x$	$y$	$z$
Retro1	mm	-60	-60	0
Retro2	mm	60.131	-60	0
Retro3	mm	-60.097	60.961	0
Retro4	mm	59.446	60.839	0.114

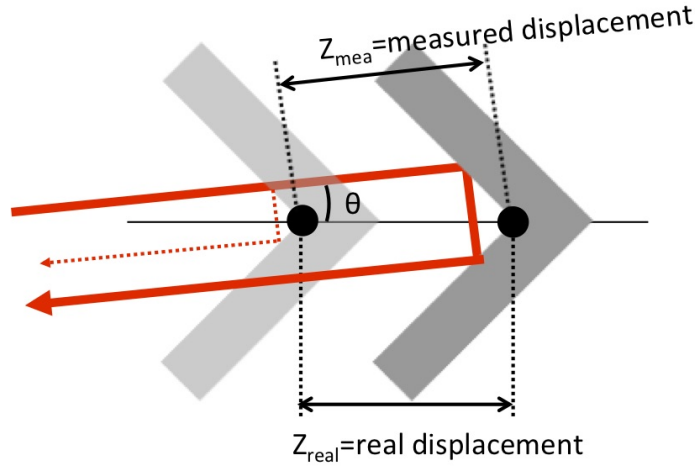


Figure 3.14: Illustration of cosine error of a retroreflector. A retroreflector moves back and forth with a displacement of  $Z_{real}$ , and an incident beam towards the retroreflector has an angle of  $\theta$ . The resulting deviation between the real displacement and the measured displacement from the interferometer, as shown in Equation 3.15, is called ‘cosine error’.

depicts a retroreflector moving back and forth and an incident beam that is tilted with respect to the axis of displacement. In this case, the displacement readout from the interferometer is given by

$$Z_{mea} = Z_{real} \cdot \cos \theta, \quad (3.15)$$

where  $Z_{mea}$  denotes the displacement readout from the interferometer,  $Z_{real}$  is an actual displacement of the retroreflector along its axis, and  $\theta$  is the angle between the beam and the displacement axis. Since the  $Z_{mea}$  is proportional to the cosine of incident angle, this effect is called ‘cosine error’ in laser interferometry [16, 17, 52]. If each of four beams in the ATA has different incident angles to the ATA-plane, the resulting displacement readouts from each retroreflector acquire a different amount of cosine error, leading to error in the ATA’s readouts.

For minimising this angular misalignment in the ATA, the following alignment procedures are carried out in two steps; In the first step, the four beams are co-aligned to be parallel to each other, In second step, the ATA-plane is perpendicularly aligned with respect to one of the beams.

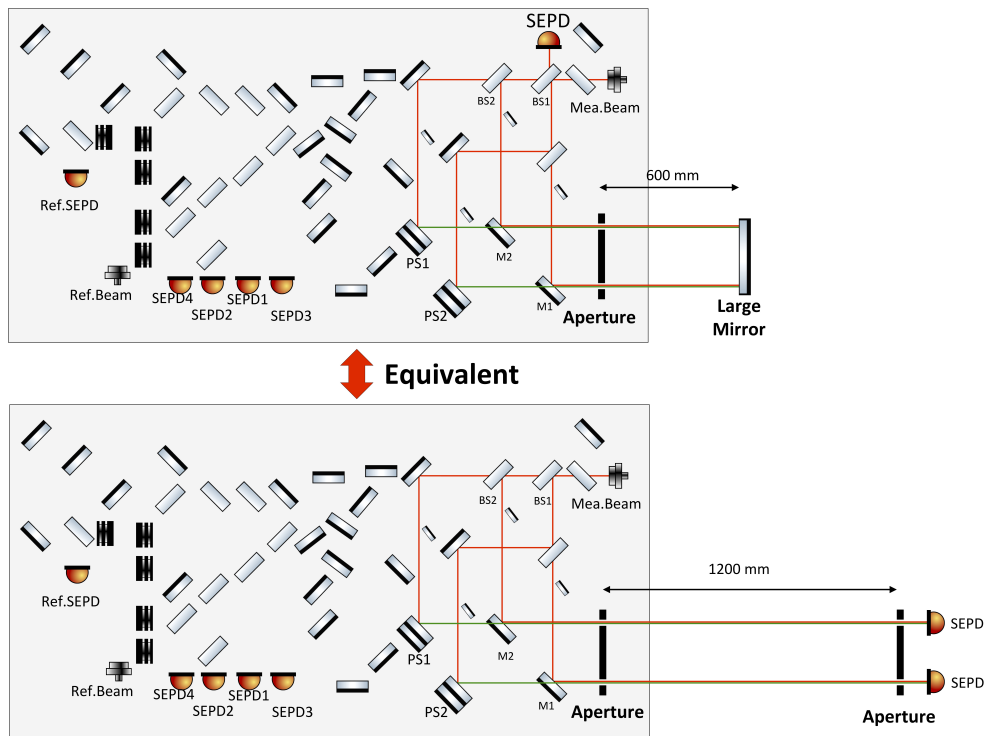


Figure 3.15: *Schematic of a setup for the beam parallel alignment in the ATA. As shown in the upper illustration, an aperture plate was installed at the initial position of the AP, and a large mirror whose size is  $600\text{ mm} \times 600\text{ mm}$  was placed at where is about  $600\text{ mm}$  away from the aperture plate. Several optical components (mirrors and beam splitters) were adjusted to allow four beams to pass through and return to the aperture after reflection from the large mirror. By fine-adjustment of the optical components until the maximal power of each beam sensed by a SEPD, the four beams are aligned to be parallel. This alignment procedure is equivalent to using two separated apertures as shown in the lower illustration.*

### 3.3.2.1 Beams parallel coalignment

To accomplish that the four beams are co-aligned to be parallel to each other, an additional configuration is set up, as shown in the upper drawing of Figure 3.15. Key components in this configuration are a large flat mirror and an aperture plate which are installed on lower-right of the ATA testbed. In Figure 3.15, the two beams towards the upper retroreflectors through two periscopes are drawn by green lines for being distinguishable with the two beams towards the lower retroreflectors. The strategy to align the beams parallel is to adjust folding mirrors (or beam splitters) so that all four beams pass through respective holes of the aperture plate and return through the holes after being reflected on the large mirror.

The first step is to remove the AP and install the aperture plate shown in the left of Figure 3.16. The aperture plate has four holes at each corner, and the lateral

distances between each hole are approximately 120 mm corresponding to the lateral distance of two retroreflectors. As an option, the aperture plate has additional holes with different diameters (2, 1.5, 1, 0.5 mm) at each corner. Using smaller size holes has an advantage in enabling more precise angular alignment, but it reduces the power of the beam passing (or returning) through the holes due to beam clipping. Using larger size holes leads to the opposite effects. In the alignment procedure, the holes with 1 mm diameter were chosen by considering the beam's power and size.

Secondly, a large flat mirror (see the photograph on the right-hand side of Figure 3.16) is installed 600 mm away from the aperture plate. The mirror, whose size is 200 mm by 200 mm, fully covers the four beams. Since fabricating a mirror having a large size with high surface quality typically requires much effort, time, and costs, a commercial mirror for housewares was used. The concerns about the mirror surface's quality (flatness) will be discussed later.

The third step is to align the four beams to pass through the aperture holes and return after reflection on the large mirror. A single element photodiode (SEPD) is installed behind 'BS1', as can be seen on the upper of Figure. 3.15. Then, folding mirrors and beam splitters are adjusted until the beam power detected on the SEPD being maximal.

The procedure to adjust the folding optical components complies with the following steps. Firstly, the 'BS1' and 'M1' are adjusted to align the beam towards the Retro2 (lower-right). Secondly, the 'BS2' and 'M2' are adjusted to align the beam towards the Retro1 (lower-left). Then, two mirrors in the periscope1 ('PS1') are adjusted to align the beam towards the Retro3 (upper-left). Finally, two mirrors in the periscope2 ('PS2') are adjusted to align the beam towards the Retro4 (upper-right).

This procedure is equivalent to use of two identical apertures, as shown in the lower drawing of Figure 3.15. If the method using two apertures is adopted, it is important that both aperture plates should be identical. Also, the two aperture plates should be perfectly aligned in parallel without an angular misalignment. Since it is nontrivial to satisfy these two conditions, the method using two identical apertures for this beam co-alignment was expected to be more challenging. In contrast, the advantage of the first alignment method is more practical and manageable for beams co-alignment, such that the first method with the mirror was chosen in this thesis instead.

### **Test the large mirror's flatness**

However, a precondition for this alignment method is that the employed large mirror should have high flatness over its surface. As aforementioned, a commercial household mirror was used due to considerable costs to fabricate a large mirror with high quality. The likelihood of irregular or curved mirror surface, which may deflect the beams, cannot be ruled out. Therefore, the flatness of the mirror used in this beam alignment needs to be confirmed.

One of the well-known methods to evaluate the optical component's surface quality is using interferograms measured by the phase-shifting Twyman-Green interferometer or the Fizeau interferometer [34]. This method can serve precise and quantitative information regarding the surface's quality. However, it requires additional

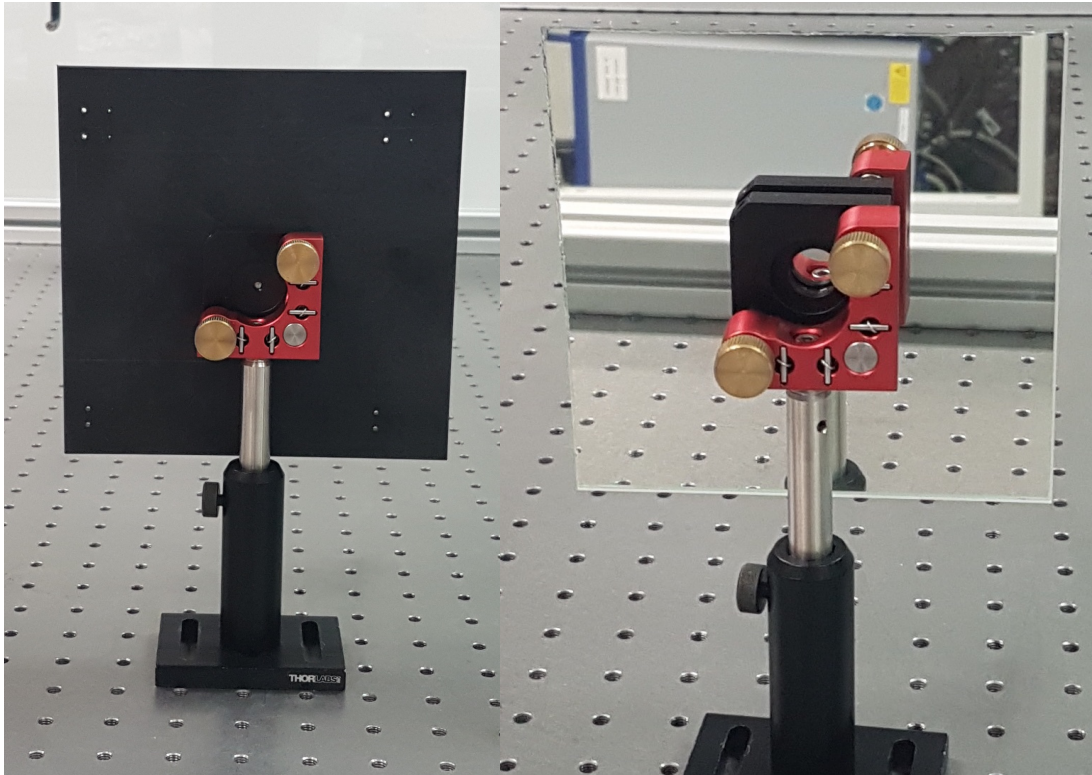


Figure 3.16: *Photograph of the aperture plate and the large mirror used for beam parallel alignment. The aperture plate (left) includes four different sizes of holes (2 mm, 1.5 mm, 1 mm, 0.5 mm diameter) as an option at each corner. The large mirror (right) reflects four beams towards the aperture plate.*

effort in particular when the optical surface is too large like the mirror used in this beams parallel alignment. Because Twyman-Green interferometer or the Fizeau interferometer require a reference mirror that should also be large with high flatness over its surface, which is a non-trivial optical component. In addition, the beam size should be larger than the mirror used for the beam co-alignment, which is also challenging.

Due to the difficulties above, alternative approaches were employed to test the large mirror's flatness. When selecting a large mirror among many, 'Naked Eye Test' method was used to check the mirror's flatness qualitatively [32]. As shown in the Figure 3.17, a grid-shape object is placed far away on the left-hand side, and the test mirror reflects the light of the object with a high oblique angle. Testing the optical surface with the high oblique angle is so sensitive that even the naked eyes might detect a radius curvature up to about ten thousand times of the length of the test mirror [32].

Although the Naked Eyes Test is a simple method to evaluate the used mirror's flatness without cost, it does not provide a quantitative value. Also, the possibility of residual errors that may occur in the Naked Eyes Test cannot be excluded. In order to confirm that the chosen large mirror has a sufficient flatness and the four



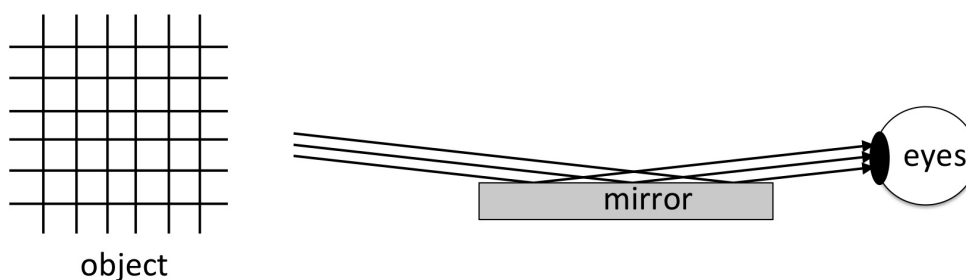


Figure 3.17: *Naked eyes test for the flatness of a mirror surface. The light from a grid-shaped object is reflected on a high inclined mirror, and the naked eye detects the image of the object. If the mirror surface has some spherical form, the eyes can detect a distorted image of the grid object.*

beams are enough parallel to each other, an additional test was performed.

Suppose that the large mirror has an irregular surface. In this case, the beam parallel alignment method does not make all beams to be parallel even though they return through the holes of the aperture plate, as shown on the upper left of Figure 3.18. If rotating the large mirror around the perpendicular axis (or laterally shifting) and aligning the mirror to allow one of the beams passing through the hole of aperture, then the other three beams are deflected so that they cannot pass through the aperture plate, as shown in the lower-left illustration of Figure 3.18.

On the other hand, if the large mirror is sufficiently flat, the four beams would be aligned in parallel, as shown in the upper-right illustration of Figure 3.18. In this case, if rotating the large mirror and realigning the mirror so that one beam passes through the aperture, the other three beams can still pass through the aperture plate, as shown in the lower-right illustration of Figure 3.18. Consequently, the beams transmitted through the aperture can be sensed on the SEPD.

Based on this idea, the large mirror was rotated by 90 degrees around its perpendicular axis and shifted laterally. Then, the powers of the beams returned through the aperture's holes were measured. The procedure followed the steps below:

- 1 Align the four beams in parallel using the aperture plate and the large mirror as shown in the upper illustration of Figure 3.15.
- 2 Measure the powers of the four beams that return through the aperture-plate after reflection on the large mirror. The measurements in this step are regarded as reference measurement.
- 3 Rotate the large mirror around its perpendicular axis by 90 degrees.
- 4 Taking the Beam 1 (lower left), the large mirror is adjusted via the manual screws integrated with the piezo actuators so that the power of Beam 1 returning through the aperture becomes maximal on the SEPD.
- 5 If the mirror surface is flat enough, the other three reflected beams are also transmitted back through the aperture. Then, the SEPD detects the power of each beam.

- 6 After measuring the powers of the four beams, shift the large mirror in the lateral direction and repeat the fourth and fifth step in order for reconfirmation.

Instead of measuring absolute beam power, the voltages proportional to the beam power were measured using a transimpedance-amplifier, and those results are listed in Table 3.2. Concerning the measurements after the rotation and lateral shift of the large mirror, not only each beam's power but also their relative ratios to the references' powers that were measured before the mirror's rotation (or lateral shift) are listed.

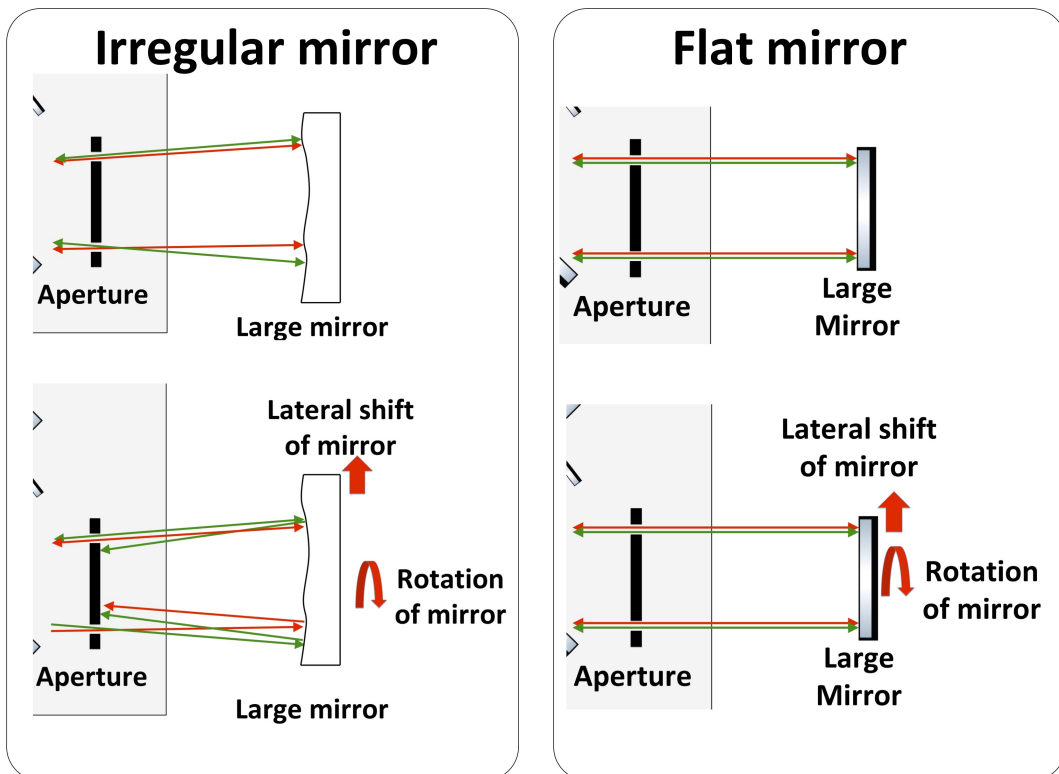


Figure 3.18: *Irregular mirror surface versus flat mirror surface for the parallel beam alignment. Illustrations on the left-hand side depict the situation when the large mirror used for the parallel beam alignment is irregular. If the large mirror used in the beam parallel alignment method as described in Figure 3.15 is irregular, the four beams are not parallel, as shown in the upper-left illustration. In this case, that the four beams are not parallel can be confirmed by using the fact that they cannot pass through the aperture plate when rotating or laterally shifting the mirror as shown in the lower-left illustration. In contrast, if the mirror used for the alignment has a sufficiently flat surface, the beams would be aligned parallel as depicted in the upper-right illustration. In this case, even if the mirror is rotated or laterally shifted, the four beams aligned in parallel will pass through the holes of the aperture plate. Based on this principle, it was checked whether the four beams of the ATA are sufficiently parallel.*

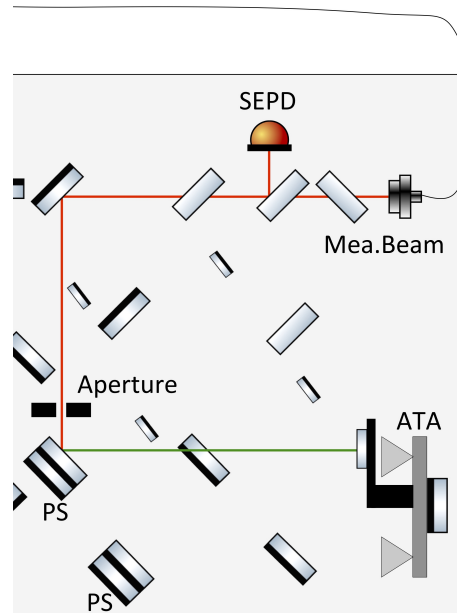
In the measurement listed in Table 3.2, the power of the Beam 1 after the mirror's rotation and shift show approximately 3% deviation from the reference measurement. Ideally, all measured powers for Beam 1 should be equal regardless of the rotating or shifting mirror. Because it was attempted to realign the Beam 1 towards the aperture for maximising its beam power sensed by the SEPD. This could be attributed to the different partial reflectance on the mirror surface, a small error of aligning the large mirror. Another point is that the powers of the other beams (Beam 2, 3, 4) that were measured after the rotation (or lateral shift) of the mirror decrease. When the mirror was laterally shifted, the power of Beam 4 decreases to 63.8% with respect to the reference measurement. This significant decrease of the beam powers is presumed to be caused by mainly the mirror surface's irregularity.

This measurement does not provide an accurate quantitative value regarding how parallel the four beams are in the experimental setup. However, we can roughly estimate the approximated range of the beam parallelism, based on the following description. The distance between the aperture plate and the mirror is 600 mm, which is equivalent to having two apertures that are 1200 mm away from each other as shown in Figure 3.15. Regard the beam clipped by the aperture with 1 mm diameter as a ray with 1 mm diameter. Taking the Beam 1 and Beam 4 as an example, if both beams are parallel to each other, both beams will pass through the aperture plate entirely. In contrast, if the angle between the two beams was more than 0.83 mrad (this value is from  $1 \text{ mm}/1200 \text{ mm} = \text{aperture diameter}/\text{twice distance between the aperture and the flat mirror.}$ ), the Beam 4 would be blocked while the Beam 1 passes through the aperture. From the test result listed in Table 3.2, the most significant reduction of the beam powers was 67%, which could be interpreted as the angular deviation between the four beams might be less than 0.83 mrad. It is important to note that this interpretation is based on rough assumptions such as treating the clipped beam like a ray, and not considering the beams' divergence or diffraction.

Table 3.2: *Measurement of the power of four beams returning through the aperture plate in the beam alignment. The voltage measured via a transimpedance-amplifier is proportional to the beam power. 'Reference' in this table refers to the voltage measured before the rotation of the mirror.*

Beam	Reference	90°rotation/ratio to Ref	Lateral shift/ratio to Ref
Beam1	354 mV	344 mV/97.2%	348 mV/98.3%
Beam2	384 mV	260 mV/67.7%	302 mV/78.6%
Beam3	192 mV	154 mV/80.2%	157 mV/81.7%
Beam4	210 mV	193 mV/91.9%	134 mV/63.8%

Figure 3.19: *Schematic of setup for beam perpendicular alignment. This setup is for aligning the four beams to be perpendicular to the ATA-plane. Beam3 propagating towards the upper-left retroreflector passes through aperture before a periscope. It returns through the aperture after being reflected on a mirror that is attached on the L-shape mount. The actuation platform is adjusted by the manual screws shown in Figure 3.8 until the maximal power is sensed on the SEPD.*



### 3.3.2.2 The ATA-plane alignment

To establish Equation (3.14) describing the ATA's 3-DOF motion, two assumptions are applied. The first assumption is that all incident beams are perpendicular to the ATA-plane. The second assumption is that the retroreflector's lateral movement while the AP rotates is so small as can be negligible.

However, if these two assumptions are not satisfied, the expressed Equation (3.14) is not strictly valid. Even if the incident beams were in parallel through the beam coalignment strategy explained above, an angular misalignment (non-perpendicular angle) between the incident beam and the ATA-plane may increase the retroreflectors' lateral movement during the AP's rotation from the beam point of view, bringing about either invalidation of Equation (3.14) or correcting the equation to a complex form with more variables.

For minimising this effect, the ATA-plane should be perpendicularly aligned to the beams. Figure 3.19 depicts an approach to align the ATA-plane perpendicularly. First of all, the co-alignment for parallel beams, described in Chapter 3.3.2.1, should be preceded. And then, an L-shaped metal mount attaching a flat mirror is installed on the AP's rear surface, such that the attached flat mirror can be parallel with the ATA-plane. Afterwards, the AP is placed in its initial position and coarsely aligned. The flat mirror with L-shaped mount is attached to the AP at the upper-left and reflects the beam towards the Retro3. By adjusting the manual screws integrated into the piezo actuators, as shown in Figure 3.8, the beam reflected on the flat mirror passes through the aperture installed behind the periscope. Fine-tuning of three screws until maximal power sensed on the SEPD leads the ATA-plane to be perpendicularly aligned with respect to the Beam 3.

### 3.3.3 Limitations of alignment campaigns and future works

The above alignment campaigns could be the beneficial and strategic methods not only for the ATA but also for other applications. However, there are still some limitations.

#### Vertex position measurement

A CMM is regarded as a practical and proper choice to measure the vertex positions of the retroreflectors with high accuracy. Despite the well-known fact that a CMM is capable of measuring a position with an accuracy in the order of a micrometre, we cannot exclude the CMM's measurement error due to various reasons such as the table's vibration, environmental temperature variation, probe error, and so on [38]. Also, only the Aluminium plate part, including the four retroreflectors, was set up on the table of CMM during the vertex position measurement. Afterwards, that part was brought back to the laboratory and assembled with a kinematic mount. During the assembly procedure, the positional shift of the retroreflectors on the metal plate might occur.

#### Beam parallel alignment

The large mirror used in the parallel beam co-alignment was not a qualified optical mirror with high quality and flatness. Also, the naked eyes test for checking the mirror's flatness does not provide accurate and quantifiable information. Despite the tests to check the parallel beam alignment and the large mirror's surface flatness as described in Figure 3.18, the test result shown in Table 3.2 implies that there are still residual angles between the four beams.

To reduce the uncertainty related to the mirror's flatness, a high-quality mirror that has the flatness of  $\lambda/4$  with protected silver-coating on a 200 mm diameter substrate is prepared now, as shown in Figure 3.20. By using this high-quality mirror, the beam alignment method explained in Chapter 3.3.2 is foreseen to improve the parallelism of the four beams.

Furthermore, another setup to align the four beams parallel is possible by using the large mirror and a beam profiler. As shown in the left illustration of Figure 3.21, the four beams are reflected on the large mirror and towards the beam profiler. If they are well aligned in parallel, they should be overlapped each other at the beam profiler regardless of the beam profiler's position. Also, this setup is beneficial to measure the angles between the four beams quantitatively. By tracing the four beams' spot positions on the beam profiler moving in the longitudinal direction, each beam's angle and direction can be measured.



Figure 3.20: Picture of a new large mirror for future alignment. The mirror (fabricated by ‘Union Optics’) has the flatness of  $\lambda/4$  and protected-silver coating on a substrate with 200 mm diameter.

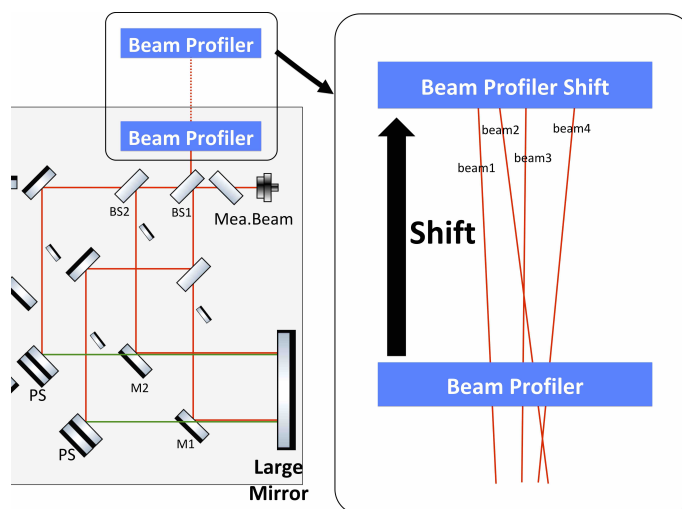


Figure 3.21: A different setup for aligning beams parallel. Four beams reflected on the large mirror (in Figure 3.20) are towards a beam profiler. If the beams are in parallel to each other, they are overlapped at the beam profiler. Also, this configuration allows not only checking the parallelism of the four beams but also measuring the angle and direction of each beam by tracing the spot position of beams at several positions of the beam profiler.

### **ATA-plane perpendicular alignment**

In the ATA-plane alignment procedure, the four beams were aligned perpendicular to the AP's Aluminium metal surface, not with respect to the ATA-plane determined by the retroreflector's vertices. The Aluminium metal's surface may not be perfectly parallel with the ATA-plane. Measuring the residual angle between the two surfaces is not a trivial task. Utilising a sophisticated instrument like a CMM may allow measuring the angles between the two surface. Even if this alignment can be accomplished with high precision, another uncertainty regarding alignment between the ATA-plane and the flat mirror attached on the L-shaped mount may arise.

Further investigations in future, such as developing better alignment strategies that ensure higher precision, analysing margins of alignment tolerances, would be beneficial not only for the ATA but also for other experiments.





## 4 Optical simulations

This chapter concentrates on analysing the ATA's readout error due to various misalignments. Despite attempts to align beams and components as described in Chapter 3.3, residual misalignments couple into ATA's readouts for its 3-DOF motion, degrading the ATA's performance. Understanding the misalignments' influences on the readouts is essential to establish strategies for calibrating the readout errors. Potential misalignments are specified in the following paragraphs, and their influence on the ATA's readout is investigated through numerical and analytical calculations.

**Misalignment of beam reflection point:** The ATA's primary purpose is to produce a pure tilted beam without a longitudinal displacement by rotating the actuator around the beam's reflection point (BRP) or to measure the actuator's longitudinal displacement at the BRP so that the TTL coupling can be distinguished. However, due to the difficulty to precisely identify where the beam reflects on the mirror, the offset between the BRP and the ATA's measurement point (or the rotation point of the actuator) directly couples into the path length readout.

**Lateral misalignment of the retroreflector:** Although the coordinate measurement machine (CMM) is the most suitable instrument for measuring each retroreflector's vertex position in the ATA, its measurement is likely to involve residual error due to the CMM's limited accuracy. The resulting lateral misalignment between the real and measured vertex position causes the ATA's readout errors.

**Beam angular misalignment:** Unlike the ideal scenario that the incident beams towards the retroreflectors are supposed to be perpendicular to the ATA-plane, each beam is likely to have a different amount of residual angle. In general, it is known that the angular mismatch between the beam direction and the retroreflector's displacement axis leads to cosine error on the displacement readout. However, the incident beam angle, especially in the ATA, is also correlated with retroreflectors' lateral movement while the ATA rotates. As explained in Chapter 3.2.4, if the beams are perpendicularly aligned to the ATA's plane, the lateral movement of retroreflectors during the ATA's rotation is so small that its effect on the ATA's readout can be negligible. On the contrary, if the incident beam angle to the ATA-plane increases, it enlarges the retroreflector's lateral movement from the beam point of view. By taking account of this effect into computing the ATA's readouts, the ATA's 3-DOF motion can still be measured, but this is the case only if the residual angular misalignment of all beams of the ATA can be fully identified. Otherwise, the ATA's readout errors are unavoidable.

**Dihedral angle error of the retroreflector:** The direction of the beam reflected from the retroreflector is antiparallel to the incoming beam and insensitive to the retroreflector's rotation. Owing to these properties, the angular misalignment between two interfering beams, which may cause the TTL coupling, can be evitable while the ATA rotates. Another unique property is that the optical path length is insensitive to rotating the retroreflector around its vertex. However, these unique

features are no longer valid if the dihedral angles between the retroreflector's three mirrors deviate from 90 degrees.

This chapter consists of three parts. The first part covers analyses for the influence of each misalignment on the ATA's readouts. In the second part, a realistic scenario, which likely happens in the ATA testbed, is simulated via the IfoCAD software by applying the actuator's 3-DOF motion and several possible misalignments simultaneously. Then, the ATA's readout errors resulted from the simulation are analysed to predict possible scenarios in the real experiment. In the third part, calibration strategies for the ATA's readout errors due to the misalignments are discussed. It is noteworthy that analyses on the effect of the misalignments in this chapter are beneficial for not only the ATA but also other multi-DOF interferometers.

## 4.1 Analysis of misalignment effect in the ATA

This section focuses on analysing the impact of each misalignment introduced at the beginning of this chapter. The effect of each misalignment is analysed through IfoCAD simulation, and their results are compared with analytic solutions.

### 4.1.1 Misalignment of beam reflection point

The beam's reflection point (BRP) refers to the point which the measurement beam for TTL coupling experiment reflects on the flat mirror of the ATA. Due to the mismatch between the actuator's rotation point and the BRP, an actuator's tilt causes an additional longitudinal displacement coupling into the path length signal. More details about this effect will be demonstrated in the following paragraphs.

The ATA aims to provide a pure tilting beam without the actuator's longitudinal displacement to TTL coupling experiments. The primary condition to achieve this is that the ATA should measure the AP's motion precisely. Afterwards, there are two options. The first option is measuring the longitudinal displacement at BRP so that it can be subtracted from the length readout measured in the TTL coupling experiment. The second option is physically suppressing the longitudinal displacement via a feedback control system. Whichever option is chosen, both approaches are effectively equivalent in principle for TTL coupling experiment.

However, one difficulty is that the measurement beam's reflection point cannot be directly pinpointed, but can only be coarsely estimated. The BRP's offsets can be divided into the longitudinal offset and lateral offset. The longitudinal offset originates from that the flat mirror's reflection surface on the right-hand side of the ATA does not match with the ATA-plane. The lateral offset is caused due to the difficulty that there is no means to pinpoint the BRP's position.

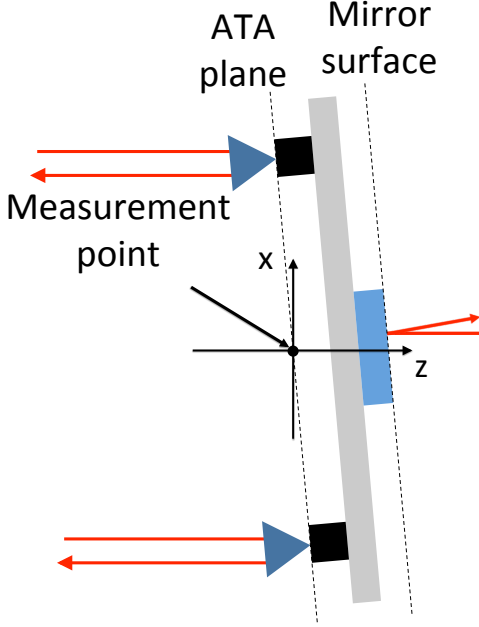


Figure 4.1: *Illustration of beam reflection point (BRP) offset in the ATA setup. The measurement point on the illustration refers to the point that the ATA measures the longitudinal displacement. This point can be regarded as the rotation point of the ATA-plane, since subtracting the longitudinal displacement measured by the ATA is equivalent to rotating around the measurement point. The BRP on the mirror has lateral and longitudinal offsets with respect to the rotation point (or measurement point in figure). This leads to a longitudinal displacement of BRP which couples to path length readout in TTL coupling experiment.*

First of all, we analytically calculate the longitudinal displacement of the BRP while the ATA rotates around a fixed point. Suppose that the ATA-plane is on the x-y plane before its rotation, and the mirror surface is longitudinally shifted from the ATA-plane by  $z_{\text{brp}}$ . Both planes are parallel to each other. And the rotation point of the ATA-plane is set to the origin, as shown in Figure 4.1. In this case, the normal vector of the mirror surface is given by

$$\vec{N}_{\text{msp}} = (0, 0, 1)^T. \quad (4.1)$$

The BRP's position is denoted by

$$\vec{P}_{\text{brp}} = (x_{\text{brp}}, y_{\text{brp}}, z_{\text{brp}})^T, \quad (4.2)$$

where  $x_{\text{brp}}$  and  $y_{\text{brp}}$  are x and y-position of the BRP. To describe the mirror surface's rotation, the rotation matrix for yaw  $\phi$  and pitch  $\eta$  is employed, and it is notated by

$$\hat{R}(\phi, \eta) = \hat{R}_y(\phi)\hat{R}_x(\eta) = \begin{pmatrix} \cos \phi & 0 & \sin \phi \\ 0 & 1 & 0 \\ -\sin \phi & 0 & \cos \phi \end{pmatrix} \begin{pmatrix} 1 & 0 & 0 \\ 0 & \cos \eta & -\sin \eta \\ 0 & \sin \eta & \cos \eta \end{pmatrix}, \quad (4.3)$$

where  $\hat{R}_y(\phi)$  and  $\hat{R}_x(\eta)$  are the rotation matrices for the yaw and pitch, respectively. By applying the rotation matrix to the normal vector of the mirror surface, the normal vector for the rotated mirror surface can be derived, as

$$\hat{N}'_{\text{msp}} = \hat{R}(\phi, \eta)\vec{N}_{\text{msp}} = \begin{pmatrix} \cos \eta \sin \phi \\ -\sin \eta \\ \cos \eta \cos \phi \end{pmatrix}. \quad (4.4)$$

In addition to the tilted mirror's normal vector  $\vec{N}'_{\text{msp}}$ , it also requires an arbitrary point on the mirror surface in order to describe the plane of the rotating mirror. For the sake of simplicity, we choose  $\vec{P}'_{\text{ab}} = (0, 0, z_{\text{brp}})^T$  as the arbitrary point before rotating the mirror surface. Supposing that the mirror rotates around the origin,  $\vec{P}'_{\text{ab}}$ 's new position can be derived as

$$\vec{P}'_{\text{ab}} = \hat{R}(\phi, \eta)\vec{P}_{\text{ab}} = z_{\text{brp}} \begin{pmatrix} \cos \eta \sin \phi \\ -\sin \eta \\ \cos \eta \cos \phi \end{pmatrix}. \quad (4.5)$$

Using the derived normal vector  $N'_{\text{msp}}$  in Equation (4.4) and the point  $P'_{\text{ab}}$  in Equation (4.5), the plane equation for the rotating mirror surface can be expressed as

$$N'_{\text{msp}\cdot x}(x - P'_{\text{ab}\cdot x}) + N'_{\text{msp}\cdot y}(y - P'_{\text{ab}\cdot y}) + N'_{\text{msp}\cdot z}(z - P'_{\text{ab}\cdot z}) = 0. \quad (4.6)$$

To calculate the longitudinal distance of the BRP from Equation (4.6), the BRP's lateral positions  $x_{\text{brp}}$  and  $y_{\text{brp}}$  are substituted into  $x$  and  $y$  of Equation (4.6). And then, transposing all terms excepting  $z$  to the right-hand side of Equation (4.6) yields the BRP's longitudinal displacement, as

$$z'_{\text{brp}} = -\frac{N'_{\text{msp}\cdot x}(x_{\text{brp}} - P'_{\text{ab}\cdot x}) + N'_{\text{msp}\cdot y}(y_{\text{brp}} - P'_{\text{ab}\cdot y})}{N'_{\text{msp}\cdot z}} + P'_{\text{ab}\cdot z}. \quad (4.7)$$

Eventually, the longitudinal distance variation of the BRR can be derived, as

$$\begin{aligned} \Delta z_{\text{brp}} &= z'_{\text{brp}} - z_{\text{brp}} \\ &= z_{\text{brp}}(\cos \eta \cos \phi - 1) \\ &\quad + \frac{\sin \eta(y_{\text{brp}} + z_{\text{brp}} \sin \eta) - \cos \eta \sin \phi(x_{\text{brp}} - z_{\text{brp}} \cos \eta \sin \phi)}{\cos \eta \cos \phi}. \end{aligned} \quad (4.8)$$

By applying Taylor series, Equation (4.8) can be approximated as

$$\Delta z_{\text{brp}} \approx -x_{\text{brp}} \left( \phi + \frac{\phi^3}{3} \right) + y_{\text{brp}} \left( \eta + \frac{\eta^3}{3} \right) + z_{\text{brp}} \left( \frac{\eta^2}{2} + \frac{\phi^2}{2} \right) + y_{\text{brp}} \frac{\eta \phi^2}{2}. \quad (4.9)$$

In Equation (4.9), the first term shows that  $x_{\text{brp}}$  is associated with  $\phi$ , and the second term presents the relationship between  $x_{\text{brp}}$  and  $\eta$ . Third-order terms of  $\phi$  and  $\eta$  in the first and second brackets are small as can be negligible. The third term shows that the BRP's longitudinal offset  $z_{\text{brp}}$  couples with a square of  $\phi$  and  $\eta$ .

It is noteworthy that the  $z_{\text{brp}}$ , which is the longitudinal offset between the ATA-plane and the mirror surface, is measurable value in the experiment, which is about 24 mm. Thus, the third term can be disentangled and removed by post-processing. The last term consists of the product of  $x_{\text{brp}}$ ,  $\eta$ , and  $\phi$  squares. If the two angles are small, the last term could be negligible.

In the end, only the BRP's lateral offset remains as the primary concern. One important topic to discuss is how much the BRP's lateral offset is expected in the

ATA. Without employing any special tools or techniques, it can be simply over a millimetre. Using a CMM may be one possible way to reduce this lateral offset in micrometre level. However, this brings about several difficulties. For instance, not only the ATA but also another testbed for TTL coupling experiment should be transported to the CMM because the ATA was built on an independent optical breadboard. Also, it is not compact.

Figure 4.2 shows analytic results regarding the additional displacement of the ATA due to the BRP offset effect. In this analysis, the ATA rotates around the origin by  $\pm 300 \mu\text{rad}$ , only yaw rotation angle is consider. Without the BRP's longitudinal offset, the BRP is laterally shifted up to 3 mm at 1 mm interval. The additional displacement of the ATA as a result of the this effect increases up to about 900 nm at the yaw angle of  $300 \mu\text{rad}$ .

This effect is regarded as the most significant error source in TTL coupling experiments using the ATA. It seems to be possible to measure the BRP's offset because its contribution to the longitudinal displacement is mostly linear against the rotation angle. That might be true in the ideal case when there is no other linear error of the rotation angle in all the other potential error sources. However, there are other potential error sources that cause a linear error in the path length readout. Apart from error sources discussed in this chapter, the lateral misalignment between a QPD and beams (or between two beams) in TTL coupling experiment is one example, which causes linear path length error [43]. Although it may be possible to cancel out all linear displacement (or path length) errors from all potential error sources by post-processing, it is still challenging to identify the BRP offset's contribution to displacement readout explicitly.

#### 4.1.2 Lateral misalignment of retroreflector

Although the CMM is practically the most suitable and precise instrument to measure the retroreflector's vertex, it accompanies a certain amount of measurement error. As a rule of thumb, its error on the positional measurement is known in the order of a few micrometres, but it can be worse depending on the test condition. In Equation (3.14) for the ATA's 3-DOF readouts, the positional error of the vertex point of the retroreflector due to the CMM's measurement error couples into the matrix of  $\hat{G}$ , which is determined by each vertex's positions. It leads to correction of the matrix  $\hat{G}$ , as

$$\hat{G}' = \begin{pmatrix} g_{11} + \Delta g_{11} & g_{12} + \Delta g_{12} & g_{13} + \Delta g_{13} \\ g_{21} + \Delta g_{21} & g_{22} + \Delta g_{22} & g_{23} + \Delta g_{23} \\ g_{31} + \Delta g_{31} & g_{32} + \Delta g_{32} & g_{33} + \Delta g_{33} \end{pmatrix}, \quad (4.10)$$

where  $g_{mn}$  denotes the geometric coefficients determined by the real vertex positions, and  $\Delta g_{mn}$  signifies the geometric coefficient's error due to the CMM's measurement error. By applying the modified matrix  $\hat{G}'$  to the longitudinal displacement readouts

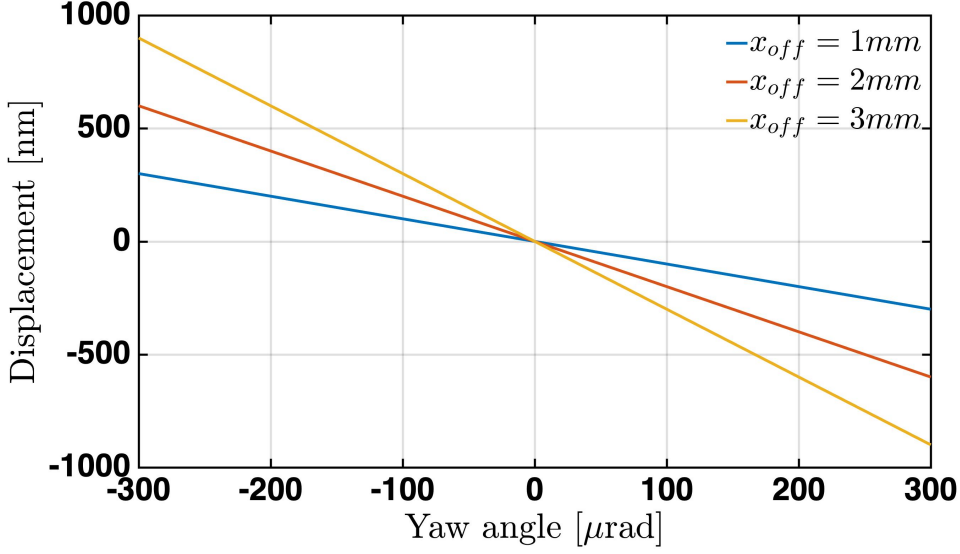


Figure 4.2: Additional displacement of the ATA due to the BRP's lateral offset. Based on the analytic solution in Equation (4.9), the ATA's longitudinal displacement at the BRP is computed. Only the yaw rotation is considered. Also, the beam's longitudinal offset is not taken into account, because it is measurable value (24 mm) so that its contribution to the additional displacement can be removed in post-processing. The beam's lateral offset changes up to 3 mm at 1 mm interval.

of the three retroreflectors  $(Z_1(t), Z_2(t), Z_3(t))^T$ , the ATA's three readouts for its 3-DOF motion are derived, as

$$\begin{aligned}
 \phi_m(t) &= (g_{11} + \Delta g_{11}) \cdot Z_1(t) + (g_{12} + \Delta g_{12}) \cdot Z_2(t) + (g_{13} + \Delta g_{13}) \cdot Z_3(t) \\
 \eta_m(t) &= (g_{21} + \Delta g_{21}) \cdot Z_1(t) + (g_{22} + \Delta g_{22}) \cdot Z_2(t) + (g_{23} + \Delta g_{23}) \cdot Z_3(t) \\
 z_m(t) &= (g_{31} + \Delta g_{31}) \cdot Z_1(t) + (g_{32} + \Delta g_{32}) \cdot Z_2(t) + (g_{33} + \Delta g_{33}) \cdot Z_3(t).
 \end{aligned} \tag{4.11}$$

Denoting the errors of the ATA's three readouts by  $\Delta\phi_{\text{err}}(t)$ ,  $\Delta\eta_{\text{err}}(t)$ , and  $\Delta z_{\text{err}}(t)$ , they can be expressed by

$$\begin{aligned}
 \Delta\phi_{\text{err}}(t) &= \phi_m(t) - \phi_{\text{real}}(t) = \Delta g_{11} \cdot Z_1(t) + \Delta g_{12} \cdot Z_2(t) + \Delta g_{13} \cdot Z_3(t) \\
 \Delta\eta_{\text{err}}(t) &= \eta_m(t) - \eta_{\text{real}}(t) = \Delta g_{21} \cdot Z_1(t) + \Delta g_{22} \cdot Z_2(t) + \Delta g_{23} \cdot Z_3(t) \\
 \Delta z_{\text{err}}(t) &= z_m(t) - z_{\text{real}}(t) = \Delta g_{31} \cdot Z_1(t) + \Delta g_{32} \cdot Z_2(t) + \Delta g_{33} \cdot Z_3(t),
 \end{aligned} \tag{4.12}$$

where  $\phi_{\text{real}}(t)$ ,  $\eta_{\text{real}}(t)$  and  $z_{\text{real}}(t)$  signify the ATA's real motions. As shown in Equation (4.12), those readout errors are expressed by superpositions of the retroreflectors' longitudinal displacement readout  $Z_n$  with the coefficient's error  $\Delta g_{mn}$ . In order to confirm this mathematical analysis, IfoCAD simulations are implemented.

#### 4.1.2.1 IfoCAD simulation-ideal case without vertex's misalignment

As a preliminary step before examining effects due to the vertex's lateral misalignment, the ideal case without lateral misalignment of vertexes is simulated via the IfoCAD software to validate the analytic solutions for the ATA's three readouts presented in Equation (3.14). More specifically, three retroreflectors and corresponding three interferometers measuring the displacement of each retroreflector are built in the simulation. The vertex positions of the three retroreflectors in the simulation follow the lists in Table 3.1, which were measured by the CMM. Regarding the ATA's motion in this simulation, only the yaw rotation without the other motions is applied. For computing the ATA's readout, the geometric matrix  $\hat{G}$  in Equation (3.14), which is determined by the vertex positions listed in Table 3.1, are calculated, then it is multiplied with the  $(Z_1, Z_2, Z_3)^T$ , where  $Z_n$  are each retroreflector's longitudinal displacement readout. Two interfering beams in each interferometer of the ATA are set to be perfectly aligned before the ATA's rotation. The other simulation parameters are listed in Table 4.1

Table 4.1: *IfoCAD simulation parameters for a case without lateral misalignment of retroreflector. 'Mea-beam' and 'Ref-beam' respectively stand for measurement beam and reference beam.*

Parameter	Value	Unit
Photodiode (SEPD) radius	5	mm
Longitudinal distance between SEPD and vertex	2000	mm
Mea-beam waist radius	0.7	mm
Ref-beam waist radius	0.7	mm
Mea-beam propagation distance from waist to detector	2070	mm
Ref-beam propagation distance from waist to detector	1893	mm

The deviations of the ATA's readouts computed from the IfoCAD simulation are plotted in Figure 4.3. The upper left plot signifies the difference between the yaw rotation angle applied to the ATA and the computed ATA's yaw readout. Although this difference for the yaw rotation is small about twenty picoradians, it appears as a deviation, not a numerical error. This deviation originates from the approximation in Equation (3.14) for the ATA's readouts, which does not take into account of each retroreflector's small lateral movement during the ATA's rotation.

There are two main reasons for applying the approximation to the ATA's readouts. Firstly, applying this approximation is beneficial to attain the simplified matrix formulation as presented in the Equation (3.14). Secondly, the retroreflectors' lateral movement is dependent on the angular alignment between the ATA-plane and the incident beams towards the ATA. In principle, extending the analytic equation with considering the vertex point's lateral movement is possible even though it compels Equation(3.14) to be a more complex form, it is can. However, suppose the ATA-plane is not on its nominal position, which means that the ATA-plane is not perpendicular to the beams with unknown angular misalignment. In that case,

the retroreflector's lateral movement from the beam's point of view cannot be determined unless the incident angle of the beams are well defined or known. This effect will be discussed in Chapter 4.1.3. Nevertheless, since the yaw readout error is relatively small compared to the other significant effects which will be detailed in the following sections, we consider this effect as an insignificant contribution.

The upper-right plot in Figure 4.3 shows the ATA's pitch angle readout during the ATA's yaw rotation. Since only the yaw rotation is applied to the ATA's motions, it is reasonable that no pitch rotation readout appears. Likewise, the longitudinal displacement at the origin does not appear as shown in the lower-left plot in Figure 4.3.

The lower-right plot shows deviations of the ATA's longitudinal displacement readouts at three different points laterally separated, where  $x = 0, 30, 60$  mm and  $y = 0$  mm. Note that the longitudinal displacement referred in here depends on the position on the ATA-plane. Ideally, the ATA's longitudinal displacement readout error at any point should be zero. However, due to the residual yaw readout error shown on the upper-left of Figure 4.3, the longitudinal displacement increases as the measurement point being shifted along the lateral direction. In this example, the only yaw rotation is applied to the ATA. If the pitch rotation is applied to the ATA, the longitudinal displacement error would be dependent on the measurement point's vertical position as well. Note that longitudinal displacement readout error revealed from this simulation is just in the order of a few picometres.

In short, the simulation was implemented to confirm the ATA's readouts for the ideal case without any misalignments. Its simulation results revealed small errors of the ATA's readouts. However, they seem to be minor effects that do not significantly degrade the ATA's performance, compared to other effects that will be discussed in the following sections.

#### 4.1.2.2 IfoCAD simulation with vertex's misalignment

For analysing the effect of the lateral misalignment of the vertex positions via the simulation, the vertex positions listed in Table 3.1 are assumed as the CMM's measurement and used to compute the ATA's readouts. However, actual vertex positions in the simulation are deliberately shifted from the positions listed in Table 3.1 in order to mimic a scenario that likely happens in experiments. Thus, random numbers generated within  $\pm 100$   $\mu\text{m}$  range are used for the lateral shifts of each vertex in the simulation, listed in Table 4.2. One can claim that it may be possible to reduce the CMM's measurement error below a few micrometres. However, we consider a broader range of error margins for each vertex's lateral shift because it is possible that the CMM's measurement error may be much larger due to various disturbances. Regarding the ATA's motion in the simulation, only yaw rotation is applied to the ATA. Other parameters of the IfoCAD simulation for beams and photodiodes are listed in Table 4.1

Before implementing IfoCAD simulation, the analytical calculation regarding the



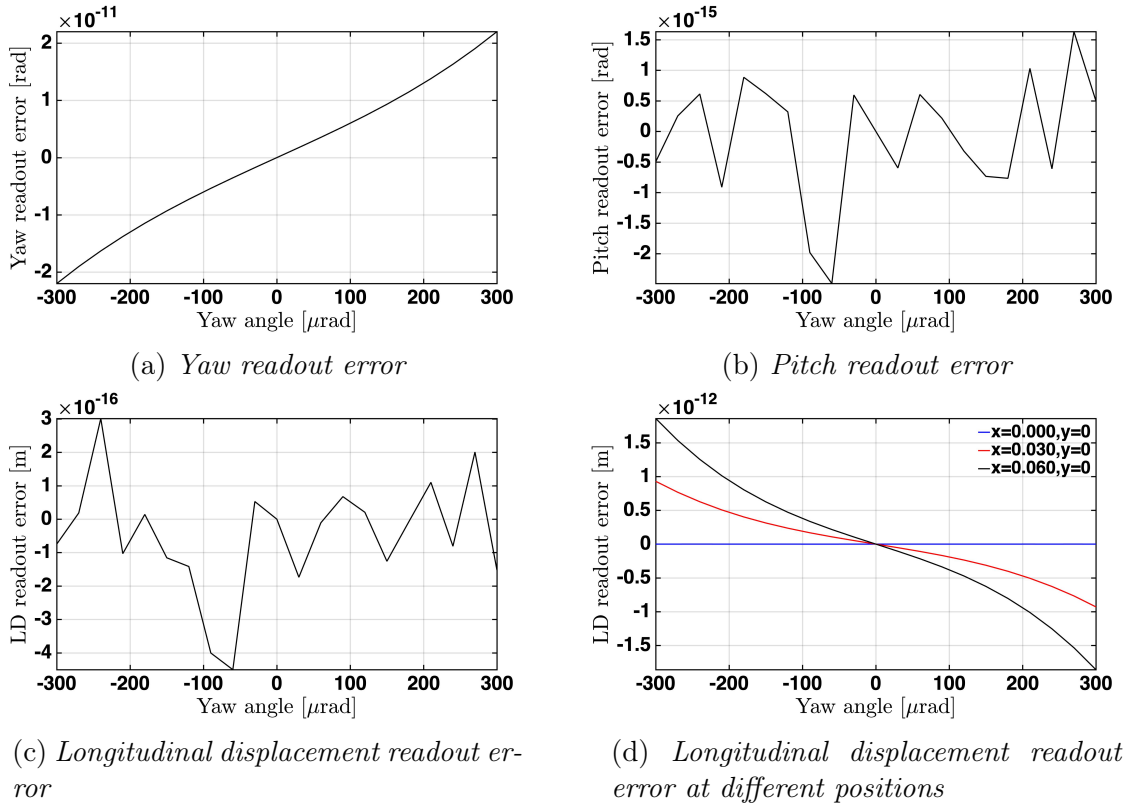


Figure 4.3: *IfoCAD* simulation for the ATA's readout errors without the lateral misalignment of the retroreflectors. In the *IfoCAD* simulation, only yaw rotation is applied to the ATA. The upper left represents the ATA's readout error for yaw rotation. The readout errors for the pitch rotation and longitudinal displacement are presented on the upper-right and lower-left, respectively. The plot on the lower-right shows the readout error of the longitudinal displacement at three different positions laterally separated, where  $x = 0, 30, 60$  mm and  $y = 0$  mm.

ATA's readout errors is implemented using two given data; the first data is vertex positions measured by the CMM and listed in Table 3.1, and the second data is the lateral misalignment between the known vertex positions and the actual vertex positions, listed in Table 4.2. From these data, the geometric coefficients' error  $\Delta g_{mn}$  introduced in Equation 4.12 can be derived. By combining the  $\Delta g_{mn}$  with the retroreflectors' displacement readouts  $Z_n$ , the ATA's three readout errors can be calculated as

$$\begin{aligned}
 \Delta\phi_{\text{err}} &= 9.437 \times 10^{-3} \cdot Z_1 - 9.542 \times 10^{-3} \cdot Z_2 + 1.046 \times 10^{-4} \cdot Z_3 \\
 \Delta\eta_{\text{err}} &= -1.360 \times 10^{-2} \cdot Z_1 + 2.533 \times 10^{-3} \cdot Z_2 + 1.106 \times 10^{-2} \cdot Z_3 \\
 \Delta z_{\text{err}} &= 1.015 \times 10^{-4} \cdot Z_1 - 1.033 \times 10^{-4} \cdot Z_2 + 1.809 \times 10^{-6} \cdot Z_3.
 \end{aligned} \tag{4.13}$$

As shown in Equation 4.13, the ATA's readout errors are dependant on not only the lateral misalignment of the vertex positions but also the the retroreflectors'

Table 4.2: *Lateral shift of each retroreflector in IfoCAD simulation. Considering the CMM's measurement error, each vertex position for three retroreflectors in IfoCAD simulation is intentionally shifted with respect to the measured vertex position shown in table. 3.1.*

	Unit	$\Delta x$	$\Delta y$
Retroreflector1	$\mu\text{m}$	62.94474	81.15839
Retroreflector2	$\mu\text{m}$	-74.60264	82.67517
Retroreflector3	$\mu\text{m}$	26.47185	-80.49192

displacement readout  $Z_n$  determined by the ATA's motion. If there is only yaw rotation in the motion of the ATA, the  $Z_n$  can be notated by a function of yaw angle and the x-position of each retroreflector's vertex, as

$$\begin{aligned}
 Z_1 &= -X_1 \cdot \tan(\phi) \approx -X_1 \cdot \phi = 5.987 \times 10^{-2} \cdot \phi \\
 Z_2 &= -X_2 \cdot \tan(\phi) \approx -X_2 \cdot \phi = 5.998 \times 10^{-2} \cdot \phi \\
 Z_3 &= -X_3 \cdot \tan(\phi) \approx -X_3 \cdot \phi = 6.004 \times 10^{-2} \cdot \phi,
 \end{aligned} \tag{4.14}$$

where  $\phi$  is yaw angle, and a set of  $X_n$  denote the x-positions for each retroreflector's vertex. By substituting outputs of Equation (4.14) for  $Z_n$  of Equation (4.13), each ATA's readout error for 3-DOF motion is derived as a function of yaw angle  $\phi$ , like

$$\begin{aligned}
 \Delta\phi_{\text{err}} &\approx 1.145 \times 10^{-3} \cdot \phi, \\
 \Delta\eta_{\text{err}} &\approx -3.024 \times 10^{-4} \cdot \phi, \\
 \Delta z_{\text{err}} &\approx 1.239 \times 10^{-5} \cdot \phi.
 \end{aligned} \tag{4.15}$$

Note that the linearity of the ATA's readout errors shown in Equation (4.15) is a particular case when the ATA has only 1-DOF motion. For its more complex motion in 3-DOF, the ATA's readout errors would be different and should be calculated by Equation (4.13). One notable point from Equation (4.15) is that non-negligible amount of readout errors for the pitch rotation and longitudinal displacement appear, even though there is only the yaw rotation in the ATA's motion. It means that the vertex position's lateral misalignment leads to cross-couplings between each of the ATA's readouts.

The longitudinal displacement error for an arbitrary point on the ATA-plane is expressed as

$$\begin{aligned}
 \Delta Z_{\text{ref}} &\approx (-X_{\text{ref}} \times \Delta\phi_{\text{err}}) + (Y_{\text{ref}} \times \Delta\eta_{\text{err}}) + \Delta z_{\text{err}} \\
 &= (-1.145 \times 10^{-3} \cdot X_{\text{ref}} - 3.024 \times 10^{-4} \cdot Y_{\text{ref}} + 1.235 \times 10^{-5}) \cdot \phi,
 \end{aligned} \tag{4.16}$$

where  $X_{\text{ref}}$  and  $Y_{\text{ref}}$  denote the x and y position of the arbitrary point on the ATA-plane, respectively.

In order to confirm the analytic calculations above, the ATA's readout errors are computed through an IfoCad simulation, and its results (solid lines) are compared with analytical calculations (dot mark) in Figure 4.4. In the upper-left plot

of Figure 4.4, the x-axis is the yaw rotation angle applied the ATA, and the y-axis indicates the difference between the yaw angle applied to the simulation and the computed yaw readout. The two results from the analytical calculation and IfoCAD simulation match each other, showing the yaw readout error in the order of a few hundred nanoradians within the yaw rotation angle of  $\pm 300 \mu\text{rad}$ . Also, the readout errors for the pitch rotation (upper-right) and longitudinal displacement (lower-left) appear, even though these motions are not applied to the ATA. The lower-right plot shows the longitudinal displacement readout errors at three different positions that are laterally separated, where  $x = 0, 30, 60 \text{ mm}$  and  $y = 0 \text{ mm}$ . Compared to the case without the lateral misalignment shown in Figure 4.3, the ATA's readout errors are much more significant. In lower-right plot of Figure 4.4, the longitudinal displacement increases up to about 17 nm depending on the position of the measurement points.

In Figure 4.4, all analytic results agree with the IfoCAD simulation results, meaning that the above analytic calculations are valid to demonstrate the ATA's readout error due to the vertex position's lateral misalignment. A couple of knowledge is acquired from the above analyses. Firstly, the lateral misalignment of the vertex positions causes cross-couplings between each 3-DOF motion. Even though the only yaw rotation is applied to the ATA as the above simulation, the readouts for the yaw and displacement are produced. Secondly, the ATA's readout errors depend on the actuator's motion. Although the simulation in this section covers only a single motion with a pure yaw rotation, the analytic calculation in Equation (4.12) implies that the three readout errors are dependant on not only the vertex lateral misalignment but also the retroreflectors' longitudinal displacements  $Z_n$  determined by the ATA's rotation.

### 4.1.3 Incident beam angle to retroreflector

Ideally, all incident beams in the ATA should be parallel to each other and perpendicular to the ATA-plane in order to fulfil Equation (3.14) regarding the ATA's 3-DOF readouts. Otherwise, the ATA's readouts accompany undesired errors. Despite the efforts on the beam angular alignment procedure described in Chapter 3.3.2, a small amount of residual misalignments likely exists. This section demonstrates how the angular misalignments affect the longitudinal displacement readout for each retroreflector and the ATA's three readouts.

In many kinds of displacement interferometers adopting retroreflector, one of the main readout errors is induced by an angular misalignment between an incident beam and the retroreflector's displacement direction, named 'cosine error' described in Chapter 3.3.2. However, there is another effect in the ATA. When the ATA rotates, an increase in the incident beam angle toward the ATA-plane leads to an effect that enlarges the lateral movements of retroreflectors during the ATA's rotation from the beam's point of view. As a result, a displacement readout error appears in a more complex form than the simple 'cosine error'.

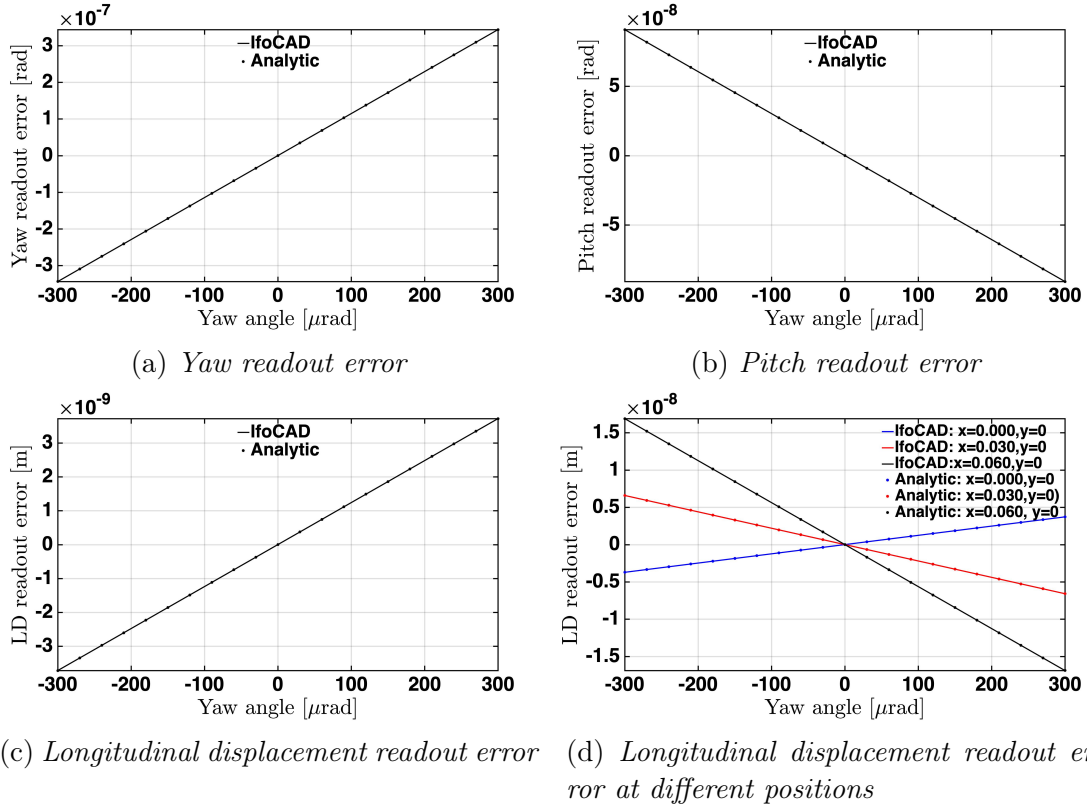


Figure 4.4: The ATA's readout errors due to the lateral misalignment of the vertex positions. The results from the IfoCAD simulation are plotted with solid lines, and analytic results are indicated by dot marks. Only yaw rotation without other motions is applied to the ATA. The upper-left plot shows the yaw angle readout error in the range of  $\pm 0.35 \mu\text{rad}$  within the yaw rotation angle of  $\pm 300 \mu\text{rad}$ , which is significant compared to the results in Figure 4.3. Although the ATA has only pure yaw rotation without other motions, the vertex lateral misalignments lead to the readouts for the pitch rotation (upper-right) and longitudinal displacement (lower-left). The lower-right plot indicates the readout errors of the longitudinal displacement at three different positions laterally separated, where  $x = 0, 30, 60 \text{ mm}$ , and  $y = 0 \text{ mm}$ . The positional dependency of the longitudinal displacement error is due to the error contributions from the pitch and yaw readouts.

The discussion on this effect begins with defining the three different lengths occurred when the ATA rotates, as illustrated in Figure 4.5:

- $Z_{\text{long}}$  is the distance between the initial vertex position and the rotated ATA-plane. The line is perpendicular to the initial ATA plane before rotation.
- $L_{\text{ver}}$  denotes the distance between the initial vertex position and its new position after rotation.
- $Z_{\text{mea}}$  stands for the interferometric readout for the longitudinal displacement

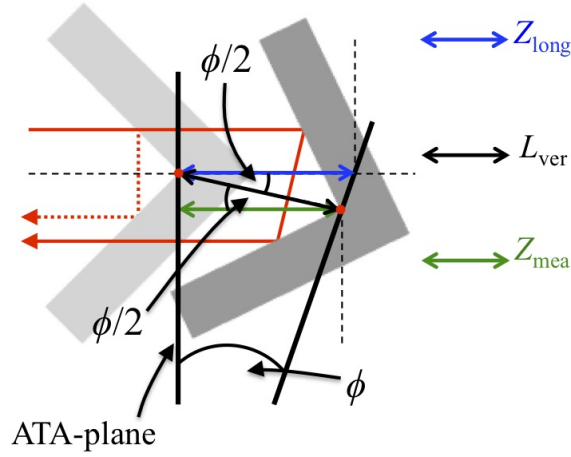


Figure 4.5: Three different distances while the ATA-plane tilts: ‘ $Z_{\text{long}}$ ’ is the distance of a straight line between the initial vertex position and the rotated ATA-plane as well as perpendicular to the initial ATA-plane. ‘ $L_{\text{ver}}$ ’ is distance between the initial vertex position and its new position after rotation.  $Z_{\text{mea}}$  denotes displacement readout from an interferometer. Here, only one degree of rotation angle  $\phi$  is considered and shown for simplification.

of the retroreflector.

### Perpendicular alignment of beam to the ATA-plane

For deriving the ATA’s readouts of Equation (3.14), using  $Z_{\text{long}}$  instead of  $Z_{\text{mea}}$  makes more sense and yields a better precision. Or, the geometrical matrix  $\hat{G}$  of Equation (3.14) needs to be modified by taking into account the lateral movement of each retroreflector while the ATA rotates, but this work leads  $\hat{G}$  to be much more complex. Nevertheless, using  $Z_{\text{mea}}$ , which is the longitudinal displacement readout from each retroreflector, is valid for the computation of the ATA’s readouts, assuming that the beam is perpendicular to the ATA-plane.

Suppose that a retroreflector is rotating around a fixed point which is laterally shifted from the vertex, as illustrated in Figure 4.5. Its rotation axis is perpendicular to the plane of the figure. In this case, the relationship between the three distances are given by

$$Z_{\text{long}} = L_{\text{ver}} \frac{\cos(\phi/2)}{\cos(\phi)} = \frac{Z_{\text{mea}}}{\cos(\phi)}, \quad (4.17)$$

where  $\phi$  is the ATA-plane’s tilt angle. The length difference between  $Z_{\text{long}}$  and  $Z_{\text{mea}}$ , regarded as the displacement readout error, is expressed as

$$\Delta Z_{\text{err}} = Z_{\text{long}} - Z_{\text{mea}} = Z_{\text{long}} \cdot (1 - \cos(\phi)) \approx \frac{Z_{\text{long}}}{2} \phi^2. \quad (4.18)$$

If the lateral distance from the rotation point to the retroreflector's vertex is  $d$ , then the distance of  $Z_{\text{long}}$  becomes

$$Z_{\text{long}} = d \times \tan(\phi). \quad (4.19)$$

By substituting  $Z_{\text{long}}$  of Equation (4.19) into Equation (4.18), the  $\Delta Z_{\text{err}}$  can be notated by a function of  $d$  and  $\phi$ , as

$$\Delta Z_{\text{err}} = \frac{d}{2} \phi^3 \quad (4.20)$$

For instance, suppose the ATA's rotation angle is 300  $\mu\text{rad}$  and the vertex is laterally shifted by 60 mm from the rotation point. In this case, the displacement error  $\Delta Z_{\text{err}}$  is around 0.8 pm. Since this effect is insignificant, using the  $Z_{\text{long}}$  to describe the ATA's motion is valid and enables establishing a simplified expression as Equation (3.14) for the ATA's readouts.

Note that the above analysis is for a simple rotation of the ATA. For the 3-DOF motion of the ATA, the above equations need to be extended. Nevertheless,  $\Delta Z_{\text{err}}$  for the ATA's 3-DOF motion would be insignificant in the case without the beam angular misalignments.

This effect causing a subtle error on the ATA's readouts can be eliminated by revising Equation (3.14). However, this is possible only if the beams are perfectly perpendicular to the ATA-plane or each beam angle is perfectly known. Because the  $\Delta Z_{\text{err}}$  is dependant on the beam angle, which will be explained in the following paragraphs.

### Non-perpendicular angle of beam to the ATA-plane

Suppose that the beam is not perpendicular to the ATA-plane, as illustrated in Figure 4.6. Then, the relationships between the three different lengths are given by

$$Z_{\text{long}} = L_{\text{ver}} \cdot \frac{\cos(\phi/2)}{\cos(\phi)} = Z_{\text{mea}} \cdot \frac{\cos(\phi/2)}{\cos(\phi)\cos(\beta)}, \quad (4.21)$$

where  $\phi$  is the rotation angle,  $\beta$  is the angle between the direction of  $L_{\text{ver}}$  and the incident beam. In this simple rotation case,  $\beta = \alpha + \phi/2$ , where  $\alpha$  is the incident beam angle. By substituting  $\beta$  into Equation (4.21), the displacement readout error  $Z_{\text{err}}$  can be derived, as

$$\Delta Z_{\text{err}} = Z_{\text{long}} - Z_{\text{mea}} = Z_{\text{long}} \left[ 1 - \frac{\cos(\phi) \cdot \cos(\alpha + \phi/2)}{\cos(\phi/2)} \right]. \quad (4.22)$$

Substituting  $Z_{\text{long}}$  of Equation (4.19) into Equation (4.22), the displacement readout error  $\Delta Z_{\text{err}}$  can be approximated by a Taylor series, as

$$\Delta Z_{\text{err}} \approx \frac{d}{2} \phi^3 + \left( \frac{d \cdot \alpha^2}{2} \phi + \frac{d \cdot \alpha}{2} \phi^2 - \frac{d \cdot \alpha^2}{12} \phi^3 \right) \quad (4.23)$$

The first term in Equation (4.23) is equal to Equation (4.18) when the beam is perpendicularly aligned, and the rest of terms are generated due to the incident beam angle  $\alpha$ . Note that Equation (4.23) is valid for only this simple rotation. For the ATA's other rotation with additional degrees of freedom, the equation should be extended.

In order to confirm the above analysis, the displacement readout error  $\Delta Z_{\text{err}}$  is computed via IfoCAD simulation, and its results are compared with analytical results. As illustrated in Figure 4.6, the retroreflector in the IfoCAD simulation rotates around a fixed point where is laterally 60 mm away from the vertex, and its rotation axis penetrates the plane of the figure. The incident beam starts at a point where is shifted by 20 mm in the longitudinal direction and 5 mm in the lateral direction from the vertex. Also, its incident angle towards the retroreflector varies up to 5 mrad. The beam reflected from the retroreflector interferes with a reference beam, and both beams in each simulation are perfectly aligned before the retroreflector's rotation. An SEPD for sensing the beams is placed at 1000 mm away from the vertex. The simulation parameters are listed in Table 4.3.

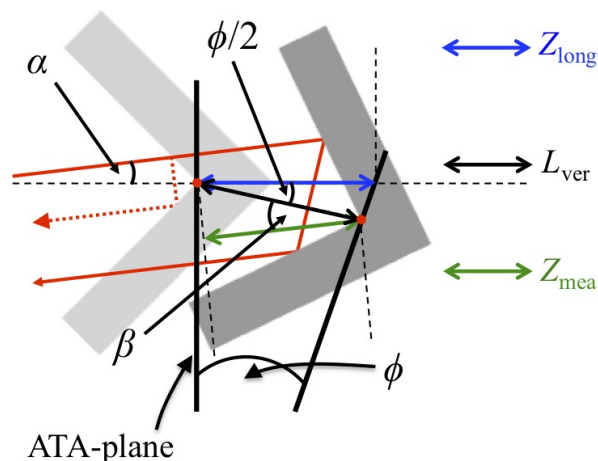


Figure 4.6: Three different distances with oblique incident beam angle towards retroreflector. As shown in Fig. 4.5, three different distance are drawn in the case of oblique incident beam.  $\beta$  is the angle between the  $L_{\text{ver}}$ 's direction and incident beam direction.

Table 4.3: IfoCAD simulation parameters for incident beam angle effect.

Parameter	Value	Unit
Photodiode (SEPD) radius	7	mm
Longitudinal distance between SEPD and vertex	1000	mm
Mea-beam waist radius	0.6	mm
Ref-beam waist radius	0.6	mm
Mea-beam propagation distance from waist to detector	1080	mm
Ref-beam propagation distance from waist to detector	893	mm
Lateral distance between the vertex and rotation point	60	mm

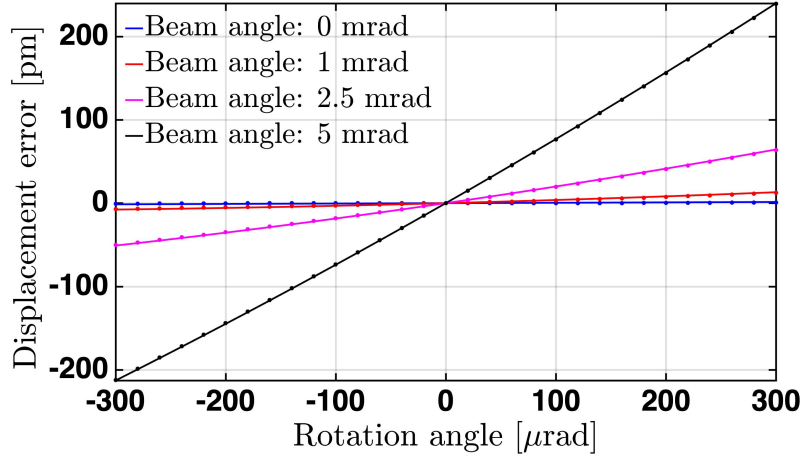


Figure 4.7: *Displacement readout error for a single retroreflector under the rotation of the ATA, depending on incident beam angle. IfoCAD simulation (solid lines) and analytic results (dot mark) agree well with each other. Higher incident beam angle leads to an increase in displacement readout error.*

The displacement readout errors depending on the incident beam angle are plotted in Figure 4.7, indicating IfoCAD simulation results by solid lines and analytical results by dots. As can be seen, both results agree well to each other, which supports the above analytic solution. Also, the displacement readout error becomes more significant as the incident beam angle is higher. The displacement readout error in this example is dominantly linear against the ATA’s rotation angle. If the incident angle increases more, the second-order terms of the rotation angle would be more significant, as explained in Equation 4.23.

It is important to remind that the above analysis is examined under the simplified condition as a single example. Also, the beam in the analysis above is confined to be parallel with the plane of Figure 4.6. In principle, not only the absolute angle of the incident beam but also its direction can affect the displacement readout error  $\Delta Z_{\text{err}}$  in a strict sense. The analytical expression that considers the beam’s direction and the ATA’s complex motion would be more complicated with more parameters.

In the ATA testbed, the incident beams towards each retroreflector are likely to have different angles. As a result, the longitudinal displacement readouts from each retroreflector would contain different amounts of errors, like

$$\begin{aligned}
 Z_1(t) &= Z_{1\text{real}}(t) + \Delta Z_{1\text{err}}(t) \\
 Z_2(t) &= Z_{2\text{real}}(t) + \Delta Z_{2\text{err}}(t) \\
 Z_3(t) &= Z_{3\text{real}}(t) + \Delta Z_{3\text{err}}(t).
 \end{aligned}
 \tag{4.24}$$

In the end, the ATA’s readout errors can be expressed by a superposition of the



singular contributions

$$\begin{aligned}
\Delta\phi_{\text{err}}(t) &= g_{11} \cdot \Delta Z_{1\text{err}}(t) + g_{12} \cdot \Delta Z_{2\text{err}}(t) + g_{13} \cdot \Delta Z_{3\text{err}}(t) \\
\Delta\eta_{\text{err}}(t) &= g_{21} \cdot \Delta Z_{1\text{err}}(t) + g_{22} \cdot \Delta Z_{2\text{err}}(t) + g_{23} \cdot \Delta Z_{3\text{err}}(t) \\
\Delta z_{\text{err}}(t) &= g_{31} \cdot \Delta Z_{1\text{err}}(t) + g_{32} \cdot \Delta Z_{2\text{err}}(t) + g_{33} \cdot \Delta Z_{3\text{err}}(t).
\end{aligned} \tag{4.25}$$

#### 4.1.4 Dihedral angle error of retroreflector

Owing to the retroreflector's unique properties, each interferometer of the ATA senses the longitudinal displacement of the retroreflector without the TTL coupling caused by the angular misalignment of two beams. However, suppose that dihedral angles between three mirror surfaces of the retroreflector are not exactly 90 degrees. In that case, the retroreflector's optical features are not valid anymore and need to be revised as below.

- The outgoing beam is not antiparallel any longer and has a certain angle with respect to the incident beam, depending on the dihedral angle errors.
- The direction of the outgoing beam is not stationary and varies, depending on the rotation angle of the retroreflector, the retroreflector's posture and the dihedral angles between each mirror.
- When an imperfect retroreflector rotates around its vertex, the optical path length changes, depending on the rotation angle of the retroreflector, the retroreflector's posture and the dihedral angles between each mirror.

These revised properties regarding the imperfect retroreflector may bring about two kinds of TTL couplings. Firstly, if the beam reflected from the retroreflector varies as the revised second property, it leads to an angular misalignment between two interfering beams, which may result in the TTL coupling. Secondly, unlike the ideal case that optical path length should correspond to the twice longitudinal displacement of the vertex point regardless of the retroreflector's rotation, an additional optical path length as the revised third property mentioned above is treated as another TTL coupling.

These possible TTL couplings are undesirable in the ATA. In this context, the variation of the outgoing beam direction and optical path length in the imperfect retroreflector having dihedral angle errors are examined through analytic ray-tracing based on literature from [36]. Furthermore, to confirm that variation of the path length readout is influenced by whether the geometrical effect or non-geometrical effect, the optical path length's variation calculated via the ray-tracing is compared to the path length signal computed from the IfoCAD simulation using slightly different two beams.

The analytic ray-tracing follows procedures listed below:

- 1 The first step is to define each mirror surface by the normal vectors and vertex.

- 2 An initial beam described as a ray can be defined in the form of a vector using a unit vector for beam direction, a point where the beam starts, and its propagation length.
- 3 The intersection point between the initial beam and the first mirror surface is derived, and then the beam's propagation distance can be calculated.
- 4 In order to continue the ray-tracing, the reflected beam's direction is derived by rotating the initial beam's vector around the first mirror's normal vector. By using the derived reflecting beam's direction together with the intersection point (computed in the third step), the reflected beam can be described.
- 5 By iterating above procedure, reflected beams on the second and third mirror can be described.
- 6 Eventually, the beam's propagation distance, reflection point, and propagation direction can be computed.

The analytical details regarding the ray-tracing procedure above are described in Appendix A.

As shown in Figure 4.8, each mirror surface are labelled with  $m_1$ ,  $m_2$  and  $m_3$ . The yaw and pitch are defined as the rotation around the y-axis and x-axis, respectively. The vertex where the three surfaces meet is placed on the origin of the Cartesian coordinate system. Regarding the posture of the retroreflector, its geometry is symmetry around the y-axis, and the  $m_3$  mirror surface is inclined at 45 degrees to the x-y plane. In this case, each normal vector of three mirrors,  $\vec{N}_1$ ,  $\vec{N}_2$  and  $\vec{N}_3$ , are respectively given, as

$$\vec{N}_1 = \begin{pmatrix} \frac{1}{\sqrt{2}} \\ -\frac{1}{2} \\ \frac{1}{2} \end{pmatrix} \quad \vec{N}_2 = \begin{pmatrix} 0 \\ \frac{1}{\sqrt{2}} \\ \frac{1}{\sqrt{2}} \end{pmatrix} \quad \vec{N}_3 = \begin{pmatrix} -\frac{1}{\sqrt{2}} \\ -\frac{1}{2} \\ \frac{1}{2} \end{pmatrix}. \quad (4.26)$$

Regarding the imperfect retroreflector, there are many possible geometries. The normal vector of a mirror surface has three-DOF, and the sum of all-DOF for the three mirrors ends up with nine-DOF to describe the imperfect retroreflector. Due to many variables in terms of all the nine-DOF, a straightforward equation to calculate the path length error cannot be derived. For this reason, this subsection deals with only two dihedral angle errors  $\delta_{12}$ ,  $\delta_{13}$

$$\delta_{12} = \angle m_{12} - 90^\circ, \quad \delta_{13} = \angle m_{13} - 90^\circ, \quad (4.27)$$

where  $\angle m_{12}$  is the angle between the  $m_1$  and  $m_2$ ,  $\angle m_{13}$  is the angle between the  $m_1$  and  $m_3$ . To be more precise, the  $m_2$  is rotated around the line of intersection between the  $m_1$  and  $m_2$  by an angle of  $\delta_{12}$ , and the  $m_3$  is rotated around the line of intersection between the  $m_1$  and  $m_3$  by an angle of  $\delta_{13}$ . For the sake of convenience,

the vertex is located at the origin of the coordinates in this analysis. The initial beam starts at  $b_{po} = (-0.005, 0, 1)^T$  in meters, where is longitudinally one metre away from the vertex, and its direction is  $b_{in} = (0, 0, -1)^T$  towards the mirror  $m_1$  of the retroreflector. The centre of a detector is placed at  $d_{po} = (0.005, 0, 1)^T$ . From the ray tracing analysis, the outgoing beam's direction while the imperfect-retroreflector rotates is derived, as

$$\begin{aligned} \vec{b}_{out} \approx & \begin{pmatrix} 0 \\ 0 \\ 1 \end{pmatrix} + \frac{1}{2} \begin{pmatrix} 2\delta_{12} + 2\sqrt{2}\delta_{13} + 4\delta_{12}\delta_{13} - \sqrt{2}\delta_{12}^2 \\ -2\sqrt{2}\delta_{12} + 2\sqrt{2}\delta_{12}\delta_{13} - \delta_{12}^2 + 2\delta_{13}^2 \\ 3\delta_{12}^2 - 2\sqrt{2}\delta_{12}\delta_{13} - 2\delta_{13}^2 \end{pmatrix} \\ & + \begin{pmatrix} \delta_{12} + \sqrt{2}\delta_{13} \\ \delta_{12} - \sqrt{2}\delta_{13} \\ 0 \end{pmatrix} \cdot \begin{pmatrix} \eta \\ \phi \\ 0 \end{pmatrix} \end{aligned} \quad (4.28)$$

where  $\eta$  denotes the pitch angle, and  $\phi$  is the yaw angle. Since the roll rotation does not appear in the ATA, its effect is ruled out in here. Since the full equation contains many high order terms in a complex form, second-degree polynomials of the full equation is presented in Equation (4.28). The first term in Equation (4.28) implies that the outgoing beam from the retroreflector is antiparallel if there is no dihedral angle error between each mirror. The second term implicates that the dihedral angles error alter the outgoing beam direction. The third term demonstrates that the outgoing beam direction is not stationary anymore when the imperfect-retroreflector rotates.

Consequently, the retroreflector's dihedral angle error could causes an angular misalignment between two interfering beams, which may result in a TTL coupling. However, the dihedral angle's deviation for the installed retroreflector in the ATA is presumed to be in the order of a few micro radians. Also, the ATA's rotation angle is below one milliradian. Based on these facts, the outgoing beam's angle variation is anticipated to be in the order of a few nano-radians, implying that the TTL coupling effect due to the beam angular misalignment is presumed to be insignificant.

Apart from the angle variation of the outgoing beam, the dihedral angle deviation also causes an additional optical path length when the retroreflector rotates around its vertex. In the ray-tracing analysis, the accumulated optical path length depends on many parameters such as the beam starting point, detector position, dihedral angle errors, and retroreflector's rotation angles. In the simulation condition given as described above, the optical path length's variation when the retroreflector rotates around its vertex is calculated by the ray-tracing, as

$$\begin{aligned}
 \Delta p \approx & \left[ \frac{-\delta_{12} + \sqrt{2}\delta_{13}}{200} \right] \eta + \underbrace{\left[ \left( 1 + \frac{\sqrt{2}}{400} \right) \delta_{12}^2 + \frac{\delta_{12}\delta_{13}}{100} - 2\delta_{13}^2 \right]}_{\text{small}} \eta \\
 & + \underbrace{\left[ \frac{\delta_{12} - \sqrt{2}\delta_{13}}{400} \right]}_{\text{small}} \eta^2 + \underbrace{\left[ \left( \frac{1}{400} - \sqrt{2} \right) \delta_{12}^2 + \left( 2 + \frac{\sqrt{2}}{200} \right) \delta_{12}\delta_{13} + \frac{1}{200} \delta_{13}^2 \right]}_{\text{small}} \phi \\
 & + \underbrace{\left[ \frac{\sqrt{2}}{200} \delta_{12} \right]}_{\text{small}} \eta \phi. \quad (4.29)
 \end{aligned}$$

Note that Equation (4.29) is a third-degree polynomial that approximates the full equation containing many high order terms. In Equation. (4.29), the first and second brackets shows the linear coupling by the pitch rotation of  $\eta$ . However, the second bracket involves second-degree polynomials of the dihedral angle error, which implies that its contribution to the optical path length's variation is insignificant if the dihedral angle deviations are small. The third bracket indicates the variation of the optical path length corresponding to second-degree polynomials of the pitch angle. Similar to the second bracket, its effect can be negligible for the small pitch angle and dihedral angle errors. The fourth bracket exhibits a linear coupling by the yaw rotation of  $\phi$ . Since second-degree polynomials of the dihedral angle deviation are small, the fourth bracket does not significantly influence on the optical path length's variation. Likewise, the fifth bracket's contribution is likely inconsiderable.

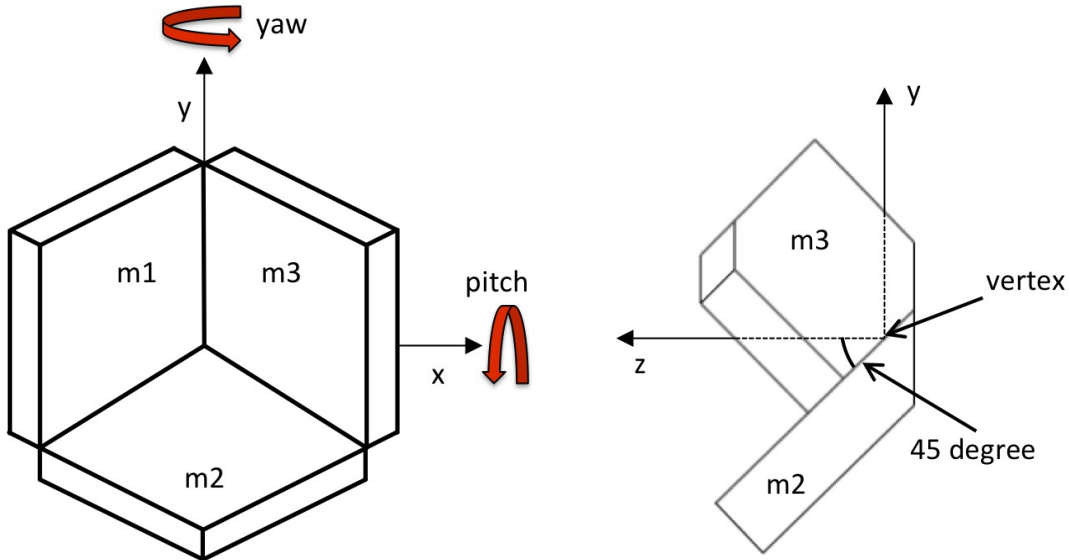


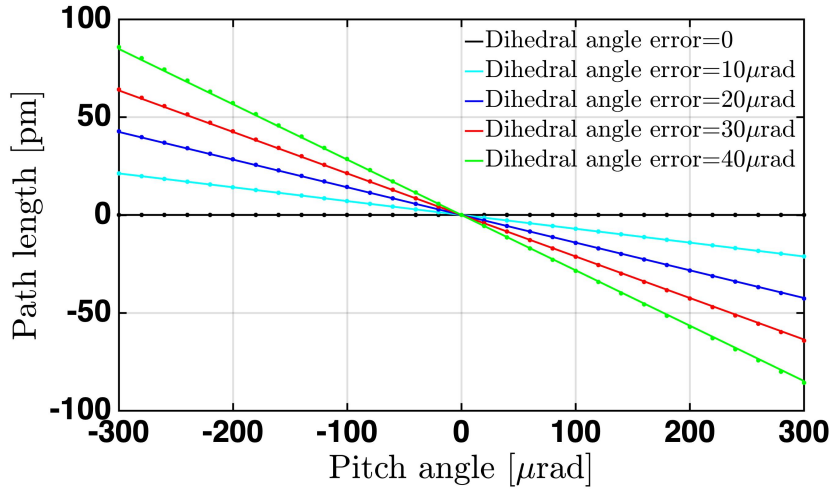
Figure 4.8: *Geometry of a retroreflector. The vertex is placed at the origin of Cartesian coordinate system. Its geometry is bilateral symmetry, and the angle between  $m_2$  and  $z$ -axis is 45 degrees. The yaw and pitch are respectively defined by rotation around the  $y$ -axis and the  $x$ -axis.*

The optical path length variation shown in Equation (4.29) is entirely based on the analytic ray-tracing, not taking into account any effects such as the influence of the beam parameter and the possible TTL coupling due to the beam angle's variation. However, the outgoing beam's angle variation during the retroreflector rotation is expected to be in the order of a few nanoradians, as discussed above through Equation (4.28), which means the resulting TTL coupling effect is anticipated to be insignificant. For more accurate analysis, the path length readout in the case that an imperfect-retroreflector rotates around its vertex is analysed via IfoCAD simulation and compared with analytical result. In this analysis, we set the dihedral angle error of  $\delta_{12}$  is zero and consider only the dihedral angle deviation of  $\delta_{13}$ . Although this simple condition is just one case among many possible geometries for an imperfect-retroreflector, the comparison between the IfoCAD simulation and the analytical result is worthy of checking whether the beam parameter's effect and the TTL coupling due to interfering beams' angular misalignment are significant or not. The measurement beam in the simulation starts at the position where is longitudinally 30 mm away from the vertex with the lateral offset of 5 mm. Each mirror of the retroreflector has enough large width with area of  $20 \times 20 \text{ mm}^2$  to cover the measurement beam without clipping. Also, different beam parameters are intentionally applied into the IfoCAD simulation for checking the effect of the beam parameter. Relevant simulation parameters are listed in Table 4.4.

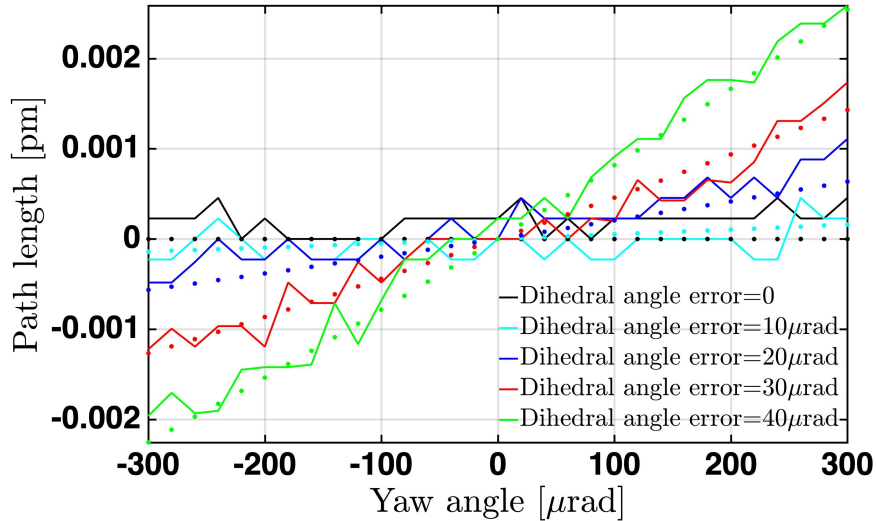
Table 4.4: *Simulation parameters for the rotation of the imperfect retroreflector. 'Mea-beam' and 'Ref-beam' refer to the measurement beam and reference beam, respectively.*

Parameter	Value	Unit
Retroreflector vertex position	(0, 0, 0)	mm
Dihedral angle error $\delta_{12}$	0	$\mu\text{rad}$
Dihedral angle error $\delta_{13}$	0~40	$\mu\text{rad}$
Photodiode (SEPD) radius	7	mm
Photodiode position	(0, 0, 1000)	mm
Mea-beam starting position	(-5, 0, 30)	mm
Mea-beam direction	(0, 0, -1)	
Mea-beam waist radius	0.5	mm
Ref-beam waist radius	0.7	mm
Mea-beam propagation distance from waist to detector	1030	mm
Ref-beam propagation distance from waist to detector	893	mm

In the IfoCAD simulation, the dihedral angle deviation of  $\delta_{13}$  is varied from zero to  $40 \mu\text{rad}$  in  $10 \mu\text{rad}$  increments, and the retroreflector rotates around its vertex by  $\pm 300 \mu\text{rad}$ . The path length variations for the pitch rotation are plotted in on the upper of Figure 4.9. The IfoCAD simulation results are plotted by solid lines, and the analytic results via the ray-tracing are marked dots. As expected, the larger deviation of the dihedral angle leads to more path length variation, and the linear coupling between the pitch rotation and the path length variation is dominated. For



(a) Path length error for the pitch rotation



(b) Path length error for the yaw rotation

Figure 4.9: Dihedral angle deviation's influence to path length error for ATA's rotation. While an imperfect-retroreflector with dihedral angle for  $\delta_{13}$  rotates around its vertex point, path length variations are plotted for pitch (upper) and yaw (lower) rotations. The IfoCAD simulations' results are plotted with solid lines, the analytical results are marked with dots. Both results match each other.

the yaw rotation, both analyses plotted on the bottom of Figure 4.9 reveal much lower path length variation compared to the case for pitch rotation.

The small path length variation for the yaw rotation can be demonstrated from analytical solution of Equation (4.29). All terms excepting the fourth bracket are cancelled out because there is no pitch rotation in this example. The remaining fourth bracket demonstrates the linear path length variation by the yaw rotation angle. However, it yields a small amount of path length variation due to the square

of the dihedral angle deviation.

Please note that the analysis above demonstrates a single case with a simple condition. For other geometries of the retroreflector, the path length variation would differ from Equation (4.29). In addition, the result could also be different for other conditions such as different postures, larger dihedral angle deviations, or significant differences between two beam's parameters, which may cause a more significant TTL coupling effect. Although more in-depth analyses are required, the above explanation can be a preliminary analysis for further investigation.

The dihedral angle deviation of a retroreflector should be lower as possible. In general, commercial retroreflectors have manufacture error of the dihedral angle in the range from one to several tenth arcseconds (one arcsecond is approximately equivalent to  $4.84 \mu\text{rad}$ ). According to the manufacturer (PLX) specification, the beam deviation for the chosen retroreflectors (USHM-10-1, PLX) of the ATA, meaning the angle between the incoming and outgoing beams, is below one arcsecond. In this case, the dihedral angles are expected to be below an arcsecond.

#### 4.1.5 Relevance of the various misalignments

Although this chapter does not cover all other possible error sources, the error sources discussed above are presumed as primary disturbances that degrade the ATA's performance and TTL coupling experiment.

Due to limited knowledge about how much each of the various misalignments discussed above appears in the ATA testbed, their impact on the ATA's readout cannot be quantified. Instead, we can presume each misalignment's impact by discussing the difficulties encountered in setting up the ATA testbed and conducting the experiment.

First of all, the BRP offset is presumed to be the most significant among the above error sources for the TTL coupling experiments with using ATA. As already discussed, it is challenging to pinpoint the BRP's position with respect to the vertices of the retroreflectors. It allows only a rough estimation of the BRP's position on the ATA's coordinates, which may be up to even a few millimetres, particularly for the BRP lateral offset. Consequently, a large longitudinal displacement likely couples into the path length readout measured in the TTL coupling testbed. The BRP's longitudinal offset is measurable in the experimental setup, so only the BRP's lateral offset is the primary concern. Since the occurring longitudinal displacement due to the BRP's lateral offset is mostly linear against the ATA's rotation angle, as shown in Equation (4.9), it may be deemed to be readily calibrated. However, if other possible error sources generate the linear longitudinal displacement error against the rotation angle as the BRP's lateral offset causes, they cannot be distinguishable. For instance, the slight residual lateral misalignment between two interfering beams in a TTL coupling experiment also causes the linear path length against the rotation angle. Generally, this misalignment is undesirable, but one may be interested in experimentally investigating this effect. In this case, it is difficult to identify the

origin of linear error of longitudinal displacement error.

The lateral misalignment of the vertices of the retroreflectors is a non-trivial error source in the ATA. This error is caused by several possible reasons such as the CMM's measurement precision, installation error, and mechanical stability in the long term. Although the CMM is known as being capable of measuring a position with micrometre-level accuracy, its measurement precision may deteriorate due to many error sources like environmental condition, measurement speed, probe related error [38]. Regarding the installation error, when measuring the vertex positions by means of the CMM, the metal plate part with four retroreflectors was detached from the ATA because the entire ATA testbed cannot be transported to the CMM. After the vertex position measurement, the metal plate had to be brought back and re-assembled to the ATA. The possibility that the retroreflectors might be shifted in the process of the re-assembly cannot be excluded. Concerning mechanical stability, it is difficult to affirm that all retroreflectors maintain their positions for the long term because all retroreflectors are vertically installed on the metal plate.

Concerning the beam angular alignment, the parallelisation of each beam and the ATA-plane's angle with respect to the beams are involved with the ATA's readout error. The angular deviation between each beam is assumed to be in the order of a milliradian, based on the beam parallel alignment procedure described in Chapter 3.3.2.1 and the test result listed in Table 3.2. Its impact on the readout error can be roughly estimated through a simple calculation. Suppose that the lateral distances between the ATA's rotation axis and the vertexes of retroreflectors are 60 mm, and the ATA's rotation angle is 300  $\mu\text{rad}$  (this is sufficient rotation angle to carry out the TTL coupling experiment even though the ATA is capable of rotating over 1 mrad.). A retroreflector's longitudinal displacement  $Z_{\text{real}}$  is obtained through the product of the retroreflector's lateral offset and the ATA rotation angle, as  $60 \text{ mm} \times 300 \mu\text{rad} = 18 \mu\text{m}$ . In the case that the beam angular error is 1 mrad, by substituting 18  $\mu\text{m}$  for  $Z_{\text{real}}$  and 0.001 (from the beam angular error of 1 mrad) for  $\theta$  in Equation (3.15), the readout error for the longitudinal displacement,  $\Delta Z_{\text{err}} = Z_{\text{real}} - Z_{\text{mea}}$ , becomes about 9 pm. This error seems to be trivial, but we did not consider the ATA-plane's angle with respect to the beam yet. Despite the attempt to align the ATA-plane perpendicular to the beams as described in Chapter 3.3.2.2, The ATA-plane's residual angle is likely to appear due to geometric errors of the components used in the alignment. For instance, the L-shaped mount's angle (see Figure 3.19) might be deviated from 90 degrees, or the angle between the flat mirror attached to the L-shaped mount and the ATA-plane might not be fully parallel. The angular error is expected to be more significant than the angular deviation between each beam. Assume that the angle between the ATA-plane and a beam is one degree ( $\approx 0.0175 \text{ rad}$ ), the retroreflector's lateral offset from the ATA's rotation point is 60 mm, and the ATA's rotation angle is 300  $\mu\text{rad}$ . In this case, the longitudinal displacement error calculated from Equation (4.23) is about 2.75 nm, which is not trivial for the TTL coupling experiment.

According to the retroreflector's specification provided by its manufacturer, the retroreflector's dihedral angle error is below one arcsecond ( $\approx 4.8 \mu\text{rad}$ ). In this case, based on analyses in Chapter 4.1.4, it is expected that the dihedral angle error of the



retroreflector does not cause a significant effect on the interferometer's readout for the retroreflector's longitudinal displacement. However, since any test to measure dihedral angles of the retroreflectors used in the ATA was not conducted in this thesis, it cannot be assured that the dihedral angle error fulfils its specification.

## 4.2 Simulation for more realistic scenario

Though the above analyses are valuable to understand each potential error source's characteristics, they provide limited knowledge in some aspects. Firstly, each error source was investigated under simple conditions, such as applying only the yaw rotation in the analysis. Secondly, each misalignment was individually analysed. In reality, it would never happen that only a single misalignment appears in the ATA. All misalignments discussed above would simultaneously appear and influence the performance of the ATA and TTL coupling's readout, resulting in difficulty identifying the extent to which each misalignment contributes to the ATA's readout error.

Beyond the analyses in the previous section, IfoCAD simulations considering more realistic conditions need to be performed to predict the ATA's readout error that may occur in actual experiments. Furthermore, its ultimate purpose is to provide a foothold to establish calibration strategies for the ATA's readout errors.

### 4.2.1 Simulation conditions

All simulations implemented from now on take into account the following three conditions. Firstly, the ATA's realistic motion in 3-DOF is applied in the simulation. Secondly, the two-lens imaging system for reducing the TTL coupling is set on the opposite side of the ATA. Thirdly, the multiple misalignments discussed in Chapter 4.1 are simultaneously applied in the simulation. The details of these settings are described in the following.

#### 4.2.1.1 Realistic ATA motion

Unlike the simple rotation of the ATA presented in Chapter 4.1, the ATA in an actual experiment would instead move in 3-DOF, having a motion error like hysteresis. One can conceive that the ATA's single motion, for instance, a pure yaw, could be feasible through feedback loop control. However, as discussed above, the various misalignments cause the ATA's readout error, resulting in the ATA's undesired motion even if the feedback loop control is employed. Regardless of whether employing the feedback loop to the experiment or not, applying a realistic model of the ATA's motion into the IfoCAD simulation is beneficial to predict the ATA's motion error.

For this reason, the ATA was driven in open-loop control mode in the corresponding experiment, and its 3-DOF motion was measured. Then, the measured data was regarded as a representative realistic model for the ATA's motion and consequently imported into the IfoCAD simulation.

During driving the ATA in yaw by  $\pm 200 \mu\text{rad}$ , the unintended pitch and longitudinal displacement of the ATA were measured as shown in Figure 4.10. The yaw rotation, which is the dominant motion of the ATA, starts from zero to a maximum angle of about  $200 \mu\text{rad}$ , and the ATA tilts to the other direction by the minimum angle of approximately  $-200 \mu\text{rad}$ , then again it returns to zero. Due to the open-loop control, the residual pitch rotation and displacement that appeared in the ATA's motion show hysteresis property. Note that the left y-axis in the plot of Figure 4.10 represents the residual pitch during the yaw rotation, and the y-axis on the right-hand side indicates the residual displacement at the origin in the ATA's coordinate. This motion measured in the experiment may contain an amount of error due to many misalignments. However, since the following simulations' purpose is to focus on mimicking a realistic condition, this ATA's motion can be deemed as a reasonable model in the simulation regardless of whether the small readout errors are included or not.

#### 4.2.1.2 Setting up an imaging system

The ATA was developed for TTL coupling investigations, such as verifying that imaging systems can reduce TTL coupling. In order to analyse how the ATA's readout error due to the misalignments discussed above may affect the TTL coupling experiment, the two-lens imaging system on the opposite side of the ATA is configured in the IfoCAD simulation.

Its design parameters are listed in Table 2.2. In the simulations, the ATA's flat mirror reflecting the measurement beam of the TTL coupling experiment is placed at  $(x, y) = (0, -60 \text{ mm})$  where it is located in the middle between the lower two retroreflectors of the ATA. Note that the longitudinal offset of the flat mirror attached on the AP's front (see Figure 4.1) was not taken into account in the simulations. This longitudinal offset, which is about 24 mm in the experimental setup, produces an additional second-order optical path length, as shown in Equation (4.9). Since the expected error for the longitudinal offset would result in negligible optical path length variation, the second-order effect could be precisely subtracted in post-processing. For this reason, the mirror's longitudinal offset was not considered in the simulations.

On the imaging system side, two identical beams are set in the simulations, which have a waist radius of 0.45mm located on the flat mirror's centre. Note these beam parameters are just an example and does not represent the actual beams' parameters.

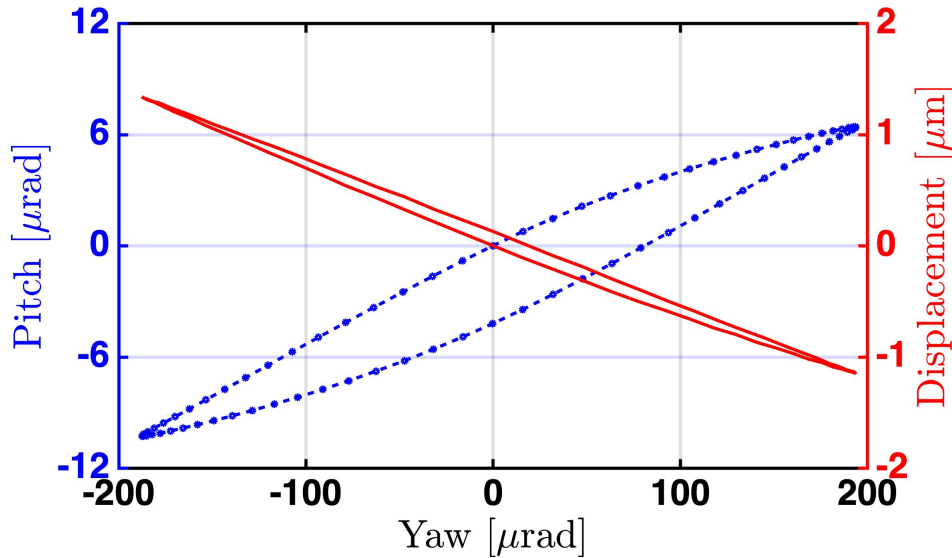


Figure 4.10: The ATA's 3-DOF motion measured in an experiment was applied to the IfoCAD simulations in Chapter 4.2 and 4.3. In the experiment, the yaw is the main rotation. Since the ATA was driven in open-loop control, there are residual pitch rotation and displacement at the origin in the ATA's coordinate frame. The blue curve represents the residual pitch angle during the yaw rotation and follows the y-axis on the left. The red curve indicates the longitudinal displacement at the origin during the yaw rotation and follows the y-axis on the right-hand side. The hysteresis property shown in this plot is due to the open-loop control. This measurement was imported in the IfoCAD simulations that will be demonstrated in the following. In the simulations, the ATA rotates around the origin for the yaw and pitch motion. At the same time, the entire ATA moves longitudinally for the displacement motion.

#### 4.2.1.3 Applying multiple misalignments

In the actual experimental setup, the various misalignments appear at the same time. To predict the ATA's readout errors that are likely to occur, the various misalignments discussed in Chapter 4.1 are simultaneously applied to the simulation. The details are explained in the following paragraphs.

#### Lateral misalignment of retroreflectors

Lateral misalignments for each retroreflector, applied in the IfoCAD simulation, are listed in Table 4.5. In the table,  $x$  and  $y$  signifies the CMM's measurement for the retroreflectors' vertices and are used in computing the ATA's readouts. With taking into account the CMM's measurement uncertainty, the actual vertex positions in the simulation are intentionally shifted by  $\Delta x$  and  $\Delta y$  in the lateral direction from

$x$  and  $y$ .  $\Delta x$  and  $\Delta y$  were determined by a random number generator within  $500 \mu\text{m}$  range. Since the first retroreflector's vertex position (RR1) is regarded as reference, only lateral shifts for the second and third retroreflector are applied.

Table 4.5: *Vertex positions for three retroreflectors and their lateral shifts in simulations. The sets of the  $x$  and  $y$  in the table stand for each retroreflector's known vertex positions, which are measured by the CMM. These values are taken for the computation of the ATA's readouts. Considering the CMM's measurement error, the retroreflectors' vertex position in the simulation are laterally shifted by  $\Delta x$  and  $\Delta y$  on purpose, which are regarded as the retroreflectors' lateral offsets.*

Retroreflector	Unit	$x$	$y$	$\Delta x$	$\Delta y$
RR1	mm	-60	-60	0	0
RR2	mm	60.131	-60	0.23036	0.49081
RR3	mm	-60.097	60.961	0.07820	0.42776

### Incident beam angle towards each retroreflector

In an ideal case, all incident beams towards the retroreflectors should be parallel to each other and perpendicular to the ATA plane, which means that each beam's direction is  $(0, 0, 1)$ . Due to the uncertainties in the beam alignment procedure demonstrated in Chapter 3.3.2, each beam's incident angle are considered in the simulation, as listed in Table 4.6. The ATA-plane is set on the x-y plane, and each incident beam has a slight angular deviation within 5 mrad in an arbitrary direction.

Table 4.6: *Simulation parameters for the incident beams' angle and direction in the ATA. In the ideal case, the measurement beams towards the retroreflectors in the ATA should be parallel to each other and perpendicular to the ATA-plane, and its direction is notated by  $(0, 0, 1)$ . By considering uncertainties in the beam alignment procedures explained in Chapter 3.3.2, the incident beams' directions are set to arbitrary directions within 5 mrad angle in the IfoCAD simulation. The beam directions in the table are denoted by unit vectors.*

Incident beam	Beam direction	Angle
Beam1 (lower-left)	(0.00296053, 0.00394697, 0.99998783)	4.93392 mrad
Beam2 (lower-right)	(-0.00081435, -0.00053429, 0.99999953)	0.97397 mrad
Beam3 (upper-left)	(-0.00397723, 0.00140321, 0.99999111)	4.21752 mrad

### Dihedral angle error for retroreflector

The dihedral angle error of the retroreflector, as discussed in Chapter 4.1.4, is taken into account as well. In the first step, each retroreflector is configured without

Table 4.7: *Parameter for modelling imperfect retroreflectors with dihedral angles in the simulation. Before imposing dihedral angles, three retroreflectors without dihedral angles were configured as illustrated in Figure 4.8. Then, each segment (mirror) of the retroreflectors is rotated around each vertex. The rotation angles are randomly generated within  $20\mu\text{rad}$ . The axis of rotation for rotating each mirror surface was determined in an arbitrary direction in three-dimension and is expressed as a unit vector.*

Segment	Direction of rotation axis	Rotation angle
RR1-M1	(-0.54879191, 0.43017250, 0.71678383)	11.69 $\mu\text{rad}$
RR1-M2	(0.57433643, -0.55330259, -0.60331907)	15.79 $\mu\text{rad}$
RR1-M3	(-0.78433603, 0.32526432, 0.52822355)	7.35 $\mu\text{rad}$
RR2-M1	(-0.38378338, -0.67141169, -0.63396897)	4.12 $\mu\text{rad}$
RR2-M2	(-0.31832249, -0.38724482, -0.86528160)	1.73 $\mu\text{rad}$
RR2-M3	(-0.81850018, 0.27329963, 0.50533629)	15.44 $\mu\text{rad}$
RR3-M1	(0.61964222, 0.54903616, 0.56089465)	4.11 $\mu\text{rad}$
RR3-M2	(-0.50530498, -0.56980238, 0.64806800)	7.77 $\mu\text{rad}$
RR3-M3	(0.49729023, 0.70345574, -0.50779173)	11.04 $\mu\text{rad}$

the dihedral angle error, as drawn in Figure 4.8. The vertex positions are listed in Table 4.5. Then, three mirrors of each retroreflector are rotated around the vertex. The rotation angles are determined by random numbers within  $20\mu\text{rad}$ , and arbitrary directions in three dimensions are chosen for the rotation axes. The rotations applied to each mirror of the retroreflectors are listed in Table 4.7. The incident beam is reflected on the M1 (in Figure 4.8) at first and towards the M2 and M3 in sequence.

### Beam reflection point's lateral offset

The two-lens imaging system in the IfoCAD simulations is built on the other side of the ATA. The two interfering beams follow the imaging system's optical axis that is perpendicular to the ATA-plane.

The TTL coupling with the imaging system is characterised by the following steps. In the first step, the path length signal is taken as it is. In the second step, the ATA measures the longitudinal displacement at the point where the beam is supposed to be reflected. Finally, the ATA's longitudinal displacement is subtracted from the path length signal that is acquired in the first step.

The point where the ATA measures the longitudinal displacement, which is mentioned in the second step, is called the measurement point and used for the ATA's longitudinal displacement readout. Since it is difficult to pinpoint the BRP on the flat mirror of the ATA, the measurement point is in the vicinity of the BRP. In the simulation, the BRP was placed at  $(-0.072, -59.041)$  mm in the ATA coordinate frame. The measurement point was set to  $(0, 60)$  mm, it was therefore displaced from the BRP by an offset of  $(-0.072, 0.059)$  mm (see Table 4.8).

Table 4.8: *Beam reflection point's lateral offset in the IfoCAD simulation. The measurement point refers to the point where the ATA measures the longitudinal displacement that is subtracted from the path length signal with the imaging system. The beam reflection point is the point at which the beam is actually reflected on the mirror in the simulation. The BRP offset signifies the offset between the two points, which affects residual TTL coupling expected in the simulation.*

	Unit	x	y
Measurement point	[mm]	0	-60.000
Beam reflection point	[mm]	-0.072	-59.041
BRP offset	[mm]	-0.072	0.059

Table 4.9: *IfoCAD simulation Parameters for beams and photodiodes in the ATA.*

Parameter	Value
Mea-beam waist radius	0.7 mm
Ref-beam waist radius	0.7 mm
Mea-beam propagation distance from waist to detector	1015 mm
Ref-beam propagation distance from waist to detector	900 mm
Longitudinal distance between SEPD and vertex	1000 mm
SEPD radius	7 mm

#### 4.2.1.4 Beam parameter in the ATA

In the simulation, the beam waist radii for the measurement and reference beam in the ATA are set to 0.7 mm. The distance from the measurement beam's waist to the SEPD is 1015 mm. For the reference beam, the distance from its waist to the SEPD is 900 mm. The beam parameters for the ATA in the simulation are listed in Table 4.9. Note that these values are just an example and does not represent the actual beams of the ATA testbed.

#### 4.2.2 Simulation result

The simulation results for two cases are given in the following sections. The first section, demonstrating simulation results for the case without the misalignments, aims to validate the ATA's performance even under the complex 3-DOF motion. In the second section, the ATA's readout error and TTL coupling readout error that would be likely to occur in the actual experiment are analysed via the simulation that considers the ATA's 3-DOF motion as well as the multiple misalignments.

### 4.2.2.1 Perfect alignment case

Prior to performing the IfoCAD simulation with the multiple misalignments, an ideal case without the misalignments is simulated as a sanity test. This simulation's primary purpose is to confirm the ATA's performance even under the ATA's 3-DOF motion shown in Figure 4.10.

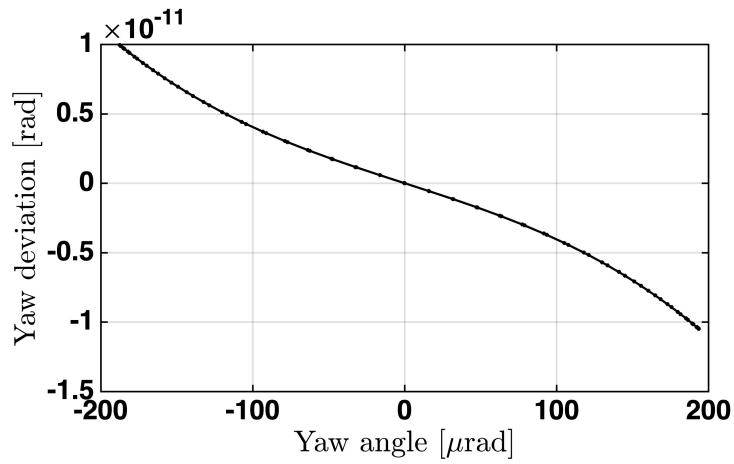
#### The performance for the ATA's readouts

The ATA's readout errors computed via the IfoCAD simulation are presented in Figure 4.11. In the top plot of Figure 4.11, the x-axis is the yaw rotation angle applied to the ATA, and the y-axis is the difference between the applied yaw angle and the ATA's yaw angle readout. The resulting yaw readout error in this simulation shows a curved-deviation in the order of  $\pm 1 \cdot 10^{-11}$  rad within the yaw rotation angle of  $\pm 200$   $\mu$ rad. This error is similar to the simulation result shown in the upper-left plot of Figure 4.3, which is caused due to the approximation that does not consider the retroreflectors' slight lateral shift during the rotation, as discussed in Chapter 4.1.2. Unlike the yaw readout error, the pitch readout error shown in the middle of Figure 4.11 is linear against the pitch rotation angle. That is because the range of the pitch rotation angle is narrow compared to the yaw rotation angle. If increasing the pitch rotation angle as much as the yaw angle, the pitch readout error would be a curve's shape. The bottom graph of Figure 4.11 represents the error for the longitudinal displacement readout at the point where  $x = 0$  and  $y = 0$  in the ATA's coordinate, showing the error in the order of  $10^{-14}$  m while the ATA moves about  $\pm 1.3$   $\mu$ m along the longitudinal direction. Note that the middle and bottom graphs in Figure 4.11 are not symmetric to the x-axis or y-axis. Because the ATA's pitch angle and displacement in its motion are not symmetric, as shown in Figure 4.10.

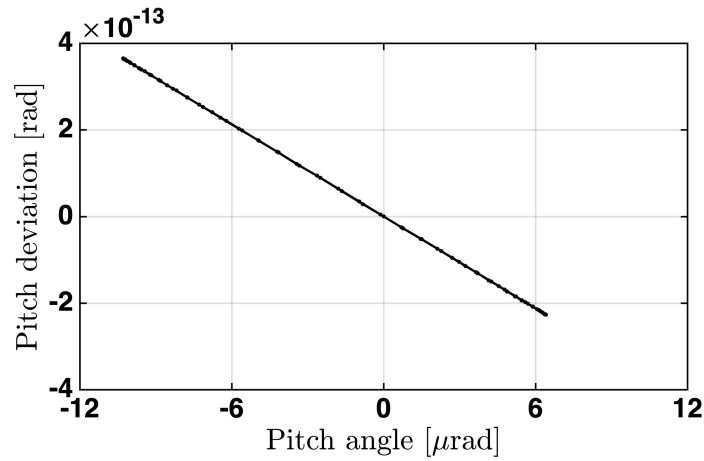
From the simulation results shown in Figure 4.11, the ATA readouts are anticipated to describe the ATA's motion accurately with only marginal readout errors if perfect alignment case. Since the readout errors are small, their influence on the TTL coupling measured on the opposite side of the ATA is expected to be insignificant. In order to confirm this interpretation, further analyses on the TTL coupling with the imaging system are carried out in the following paragraphs.

#### The performance for the TTL coupling

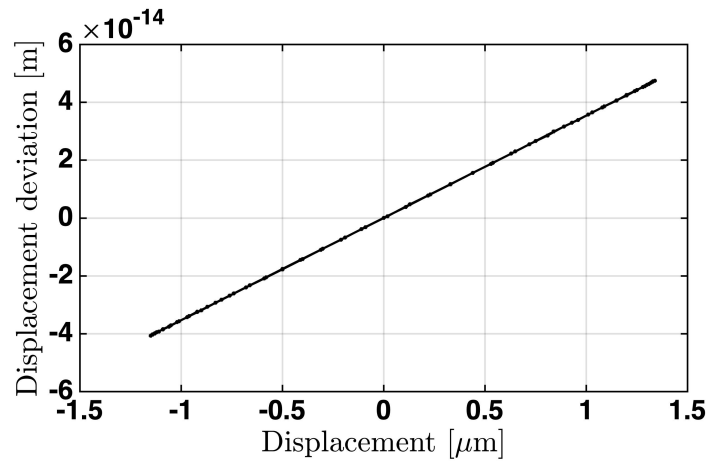
Ideally, the ATA rotates around the BRP so that the TTL coupling due to the pure tilted beam can be characterised. However, this is considerably challenging to accomplish in an experimental setup. In this simulation, the ATA's motion in 3-DOF, which is shown in Figure 4.10, does not have a fixed rotation point. As a result, the longitudinal displacement that the beam experiences couples into the length readout. As an alternative way to the ideal case, the ATA measures the longitudinal displacement at the BRP and subtracts it from the path length signal in order to characterise the TTL coupling performed on the opposite side of the



(a) *Yaw readout error*



(b) *Pitch readout error*



(c) *Longitudinal displacement readout error*

Figure 4.11: *ATA's 3-DOF readout errors under the perfect alignment. Under the 3-DOF motion given in Figure 4.10, the ATA's readout errors are analysed. The yaw error, which is the difference between the yaw rotation angle applied to the simulation and the ATA's yaw readout, is shown on an upper plot. The pitch readout error is plotted in the middle, and the displacement readout error is shown on the bottom.*



ATA. The simulation in the following paragraphs aims to compare the two TTL couplings acquired through the two methods mentioned above and analyse the two's differences.

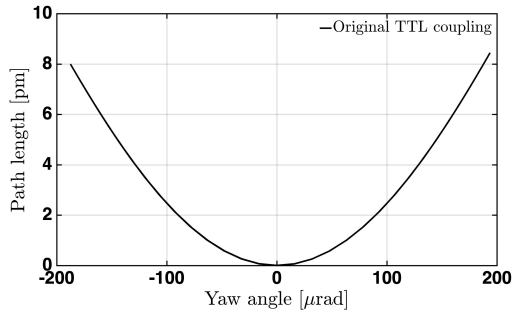
The plot on the upper-left of Figure 4.12 shows the TTL coupling with the imaging system when the ATA's rotation point coincides with the BRP, called 'original TTL coupling'. It represents the ideal case that is desired to be performed in the experiment. Rotating the ATA around the BRP enables characterising the TTL coupling without the ATA's longitudinal displacement on the path length signal. Thus, the original TTL coupling here is regarded as a reference. The yaw rotation is the main motion in the simulation, but also the residual pitch rotation, which is the blue curve shown in Figure 4.10, is applied. Note that the ATA rotates around the BRP without no longitudinal displacement in the simulation for the original TTL coupling. The two-lens imaging system's parameters are listed in Table 2.2.

Unlike the case of the original TTL coupling, the ATA does not rotate around the BRP, moving in 3-DOF as shown in Figure 4.10. In this condition, the path length with the imaging system is plotted by the blue curve on the upper-right of Figure 4.12 and follows the y-axis on the left-hand side. It contains a significant path length with a strong hysteresis and hardly provides pertinent information about TTL coupling. The main cause of this originates from the ATA's additional longitudinal displacement at the BRP, which should be measured and subtracted from the path length signal. The red dots in the same plot represents the ATA's longitudinal displacement readout measured at the BRP and follows the y-axis on the right-hand side. This result matches the blue line's path length readout in the micrometre scale, which seems to make it possible to characterise TTL coupling. Note that the y-axis on the right for the ATA's longitudinal displacement is half of the left y-axis representing the path length signal with the imaging system, since the ATA's displacement is equivalent to half of the path length.

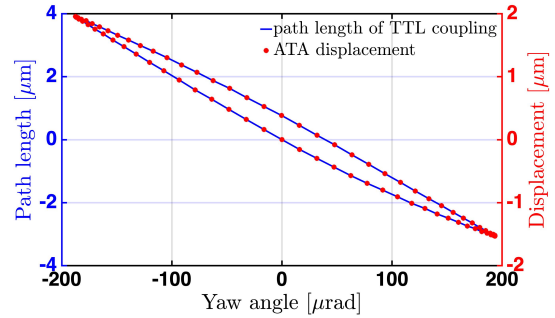
For characterising TTL coupling, twice the ATA's longitudinal displacement is subtracted from the path length signal. Then, its result, plotted by the red curve in the lower-left plot of Figure 4.12, is directly compared to the original TTL coupling drawn by the black curve. This comparison implies the TTL coupling acquired through the subtraction process is almost identical to the original TTL coupling obtained when the ATA was rotated around the BRP.

Nevertheless, a subtle difference between the two results, observed in the lower-left plot, is regarded as TTL coupling error. It is enlarged in the lower-right plot of Figure 4.12 by the blue curve and show an error of about  $\pm 0.5$  pm. One possible cause contributing to this error may be the ATA's longitudinal displacement readout error, which means the difference between the ATA's real and measured longitudinal displacement. Its result is plotted by the red curve on the lower-right graph of Figure 4.12, showing the error in the range of  $\pm 0.1$  pm. This shows that the TTL readout error cannot be fully explained by the residual error of the ATA longitudinal displacement readout. That means that there might be additional effects that contribute to the TTL readout error, which is not fully demonstrated in this thesis yet.

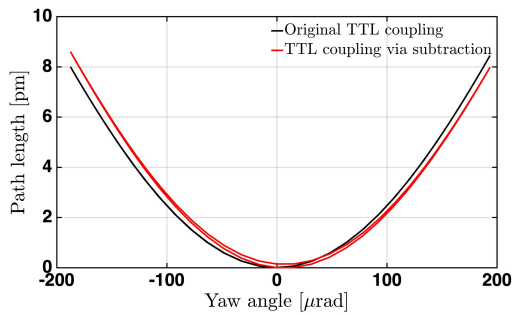
Reviewing the differences in each procedure of obtaining the two TTL couplings



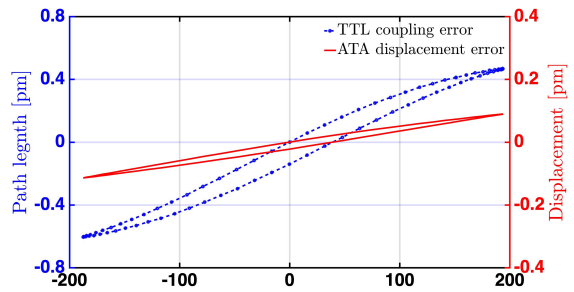
(a) Original TTL coupling



(b) Initial path length with the imaging system (blue) and the ATA's longitudinal displacement readout (red dots)



(c) Original TTL coupling (black) and Calibrated TTL coupling (red)



(d) Calibrated TTL coupling's error (blue) and the ATA's longitudinal displacement readout error (red)

Figure 4.12: Characterising the TTL coupling with the ATA. Upper-left: TTL coupling obtained if the ATA rotates around the BRP. Upper-right: ATA displacement and path length readout, when the realistic motion is applied. Lower-left: difference of the blue line and red dots of the upper left graph results in the effective TTL estimate (red line), which is compared to the original TTL coupling from the upper left graph. Lower-right: The blue curve is TTL coupling error that is the difference between the black and red curve of the lower left graph, and the red curve is the ATA longitudinal displacement readout error. The original TTL coupling on the upper-left is regarded as a reference to evaluate the TTL coupling obtained by the subtraction process. In the upper-right plot, the path length signal with the imaging system (blue curve), following the y-axis on the left, is compared to the ATA's longitudinal displacement (red curve) following the y-axis on the right-hand side. The hysteresis is due to the residual pitch and displacement of the ATA motion shown in Figure 4.10, which couples into the path length. In the lower-left graph, the TTL coupling (red curve) via subtraction method effectively agrees with the original TTL coupling. In the lower-right graph, the two curves' mismatch signifies that the TTL coupling error is not fully demonstrated by the ATA's longitudinal displacement readout error.

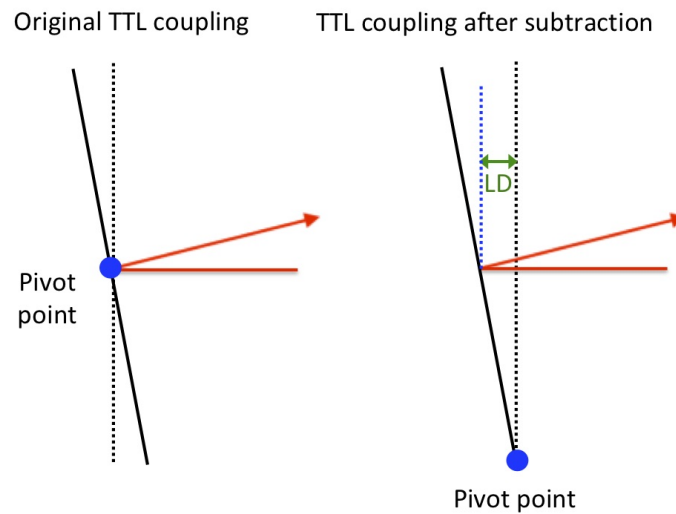


Figure 4.13: Illustrations of the ATA's difference rotations corresponding to the two TTL couplings. The left drawing depicts the case when the ATA's pivot point coincides with the BRP, corresponding to the original TTL coupling. The drawing on the right-hand side illustrates the ATA's pivot point is laterally offset. Then, the ATA's longitudinal displacement at the BRP is subtracted from the path length signal to characterise the TTL coupling. In the latter case, two possible causes may affect the TTL coupling error shown in the lower-right graph of Figure 4.12; the tilted beam's lateral shift at the initial mirror plane (dashed black line), the difference between the BRP's longitudinal displacement (labelled by  $LD$ ) and the optical path length from the BRP to the intersection point between the tilted beam and the initial mirror plane

can be an approach to qualitatively understanding the TTL coupling error. The left of Figure 4.13 depicts when the ATA's rotation point matches with the BRP, corresponding to the original TTL coupling. The drawing on the right-hand side illustrates the case that the TTL coupling is acquired by subtracting the ATA's longitudinal displacement. In the latter case, the tilting beam reflected on the rotating mirror (solid black line) has a slight lateral offset at the plane of the initial mirror surface (black dash line). The tilting beam's tiny lateral offset may be a cause that attributes to the TTL coupling error. Another effect might be due to slightly longer optical path length, which means that the length from the tilting beam's reflection point to the intersection point between the tilting beam and the initial mirror surface (drawn by the black dash line) is slightly longer than the longitudinal displacement (labelled by  $LD$  in Figure 4.13). Since the imaging system is not considered in this discussion yet, many other effects may be attributed to the TTL coupling error, which needs further investigations in the future.

### Summary

The above analyses demonstrated that the ATA could perform well under the ideal condition without the misalignments, even if the ATA had a realistic motion

in 3-DOF. Firstly, the ATA's readout errors for its 3-DOF motion, revealed in the simulation, are assumed to be negligible as their magnitude is hardly measurable experimentally. Secondly, the simulation exhibited that the TTL coupling could be characterised via the subtraction process, even if the ATA does not rotate around the BRP. The ATA's longitudinal displacement readout was subtracted from the path length signal with the imaging system to characterise the TTL coupling. As long as the ATA's measurement point for the longitudinal displacement readout coincides with the BRP, the TTL coupling can be recovered with only marginal error.

#### 4.2.2.2 Under multiple misalignments

##### IfoCAD simulation result for the ATA's readout errors

In this section, the IfoCAD simulation for a realistic scenario is implemented with the various misalignments mentioned in Chapter 4.2.1. The ATA's three readout errors resulted from the simulation are presented in the Figure 4.14. The yaw readout error plotted in the top graph of Figure 4.14 is in the range of  $\pm 0.4 \mu\text{rad}$  within the yaw rotation angle of  $\pm 200 \mu\text{rad}$ . The ATA's readout error for the pitch rotation shown in the middle of Figure 4.14 is about  $\pm 0.15 \mu\text{rad}$ . For the longitudinal displacement at the origin, the ATA's readout error shown in the bottom plot of Figure 4.14 is about  $\pm 35 \text{ nm}$ .

Compared to the simulation results without misalignments in Figure 4.11, the ATA's readout errors due to the various misalignments are much more significant. Another notable point is that the ATA's readout errors are not merely linear but contain the hysteresis.

##### Analytical understanding of the ATA readout errors

In order to understand the behaviour of the errors shown in the simulation, we analytically examine the equation for the ATA's readout, taking the yaw as an example. From Equation (3.14), the yaw readout without the misalignments is given by

$$\phi_{\text{real}}(t) = g_{11} \cdot Z_1(t) + g_{12} \cdot Z_2(t) + g_{13} \cdot Z_3(t), \quad (4.30)$$

where the set of  $g_{mn}$  are coefficients determined by the position of each retroreflector, and the set of  $Z_n(t)$  are the longitudinal displacements of the retroreflectors. The ATA's yaw readout in the case with the various misalignment can be expressed by

$$\begin{aligned} \phi_{\text{mea}}(t) = & (g_{11} + \Delta g_{11}) \cdot (Z_1(t) + \Delta Z_1(t)) + (g_{12} + \Delta g_{12}) \cdot (Z_2(t) + \Delta Z_2(t)) \\ & + (g_{13} + \Delta g_{13}) \cdot (Z_3(t) + \Delta Z_3(t)), \end{aligned} \quad (4.31)$$

where the set of  $\Delta g_{mn}$  are the errors of the coefficient  $g_{mn}$  due to the lateral misalignment of each retroreflector, and the set of  $\Delta Z_n(t)$  are the error of the longitudinal

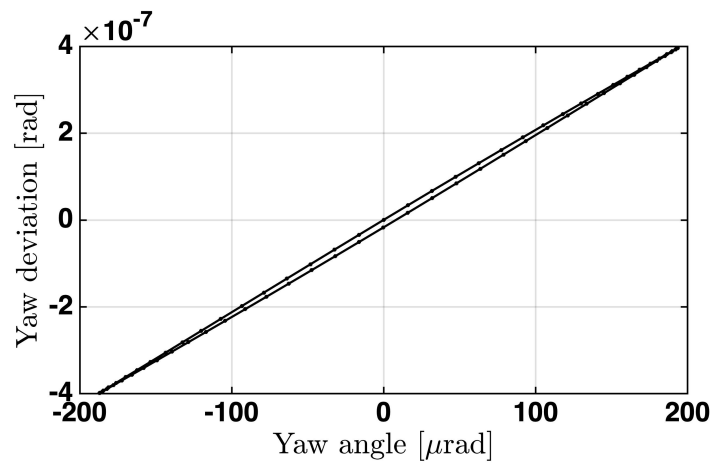
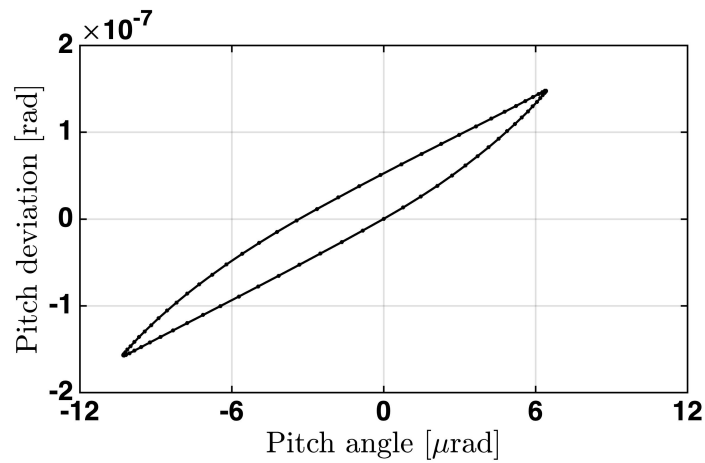
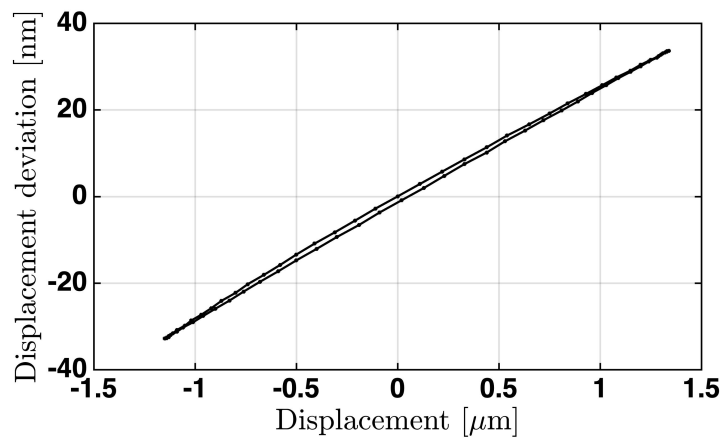
(a) *Yaw readout error*(b) *Pitch readout error*(c) *Longitudinal displacement readout error*

Figure 4.14: The ATA's 3-DOF readout deviations due to the misalignments. Like Figure 4.11, the ATA's readout errors for its 3-DOF motion are computed via the IfoCAD simulation, but taking into account the various misalignments described Chapter 4.2.1. Compared to the ideal case shown in Figure 4.11, the readout errors due to the misalignment are much more significant, involving hysteresis error.

displacement of each retroreflector due to the beam angle and dihedral angle error. The difference between  $\phi_{\text{real}}(t)$  of Equation (4.30) and  $\phi_{\text{mea}}(t)$  of Equation (4.31), meaning the ATA's yaw readout error, becomes

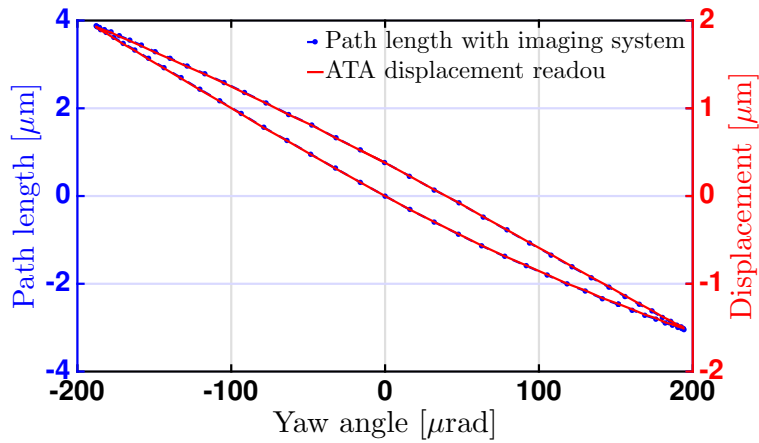
$$\begin{aligned} \Delta\phi(t) = & [(g_{11} + \Delta g_{11}) \cdot \Delta Z_1(t) + (g_{12} + \Delta g_{12}) \cdot \Delta Z_2(t) + (g_{13} + \Delta g_{13}) \cdot \Delta Z_3(t)] \\ & + [\Delta g_{11} \cdot Z_1(t) + \Delta g_{12} \cdot Z_2(t) + \Delta g_{13} \cdot Z_3(t)]. \end{aligned} \quad (4.32)$$

In Equation (4.32), the yaw readout error depends on  $\Delta g_{nm}$  and  $\Delta Z_n$ , which are affected by the various misalignments. In addition, the terms of the second bracket in Equation (4.32) imply that the yaw readout error varies depending on the ATA's motion that determines the set of  $Z_n(t)$ . This fact that the ATA's error depends on its motions will be discussed more in Chapter 4.3 with regard to calibration methods for the ATA's readout.

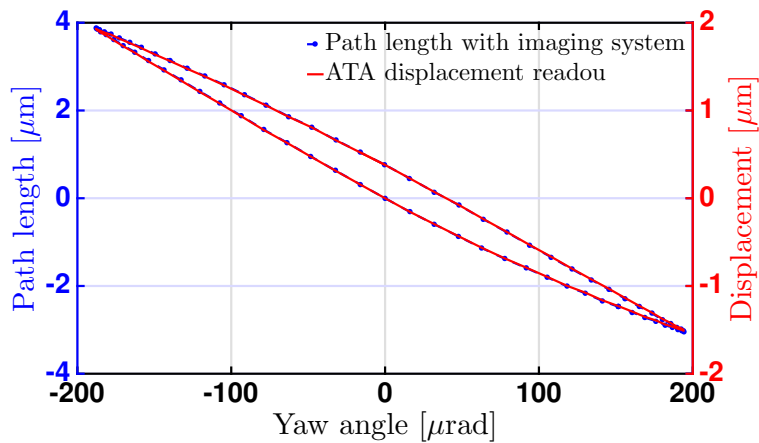
The observed hysteresis of the ATA's readout error in Figure 4.14 can be demonstrated from Equation (4.32). Assume a scenario that there is no hysteresis in the ATA's motion. In this case, when the ATA's yaw angle returns to zero (the ATA's initial position), all  $Z_n(t)$  and  $\Delta Z_n(t)$  are zero, meaning  $\Delta\phi(t)$  in Equation (4.32) is zero as well. Now, suppose another case that the ATA's motion contains residual pitch and displacement with hysteresis, as shown in Figure 4.10. When the ATA's yaw angle returns to zero, there is residual pitch rotation and displacement, meaning that each retroreflector's longitudinal displacement is not zero. In this case, the set of  $Z_n(t)$  and  $\Delta Z_n(t)$  in Equation (4.32) do not vanish, leading to residual yaw readout error  $\Delta\phi(t)$  even though the yaw rotation angle is zero. Although only yaw rotation is taken as an example so far, this demonstration is valid to the ATA's pitch rotation and displacement case, as well.

### **IfoCAD simulation result for the TTL coupling signal**

In the top graph of Figure 4.15, the path length signal with the imaging system is indicated by blue dots, and the ATA's longitudinal displacement readout is plotted by the red line in the same graph. Both signals seem to correspond to each other in the range of a few micrometres. In order to check the difference between the two results, twice the ATA's longitudinal displacement readout is subtracted from the path length, and its result is presented by blue dots in the lower graph of Figure 4.15. Compared to the simulation results under perfect alignment conditions in Figure 4.12, the path length signal with the imaging system accompanies a significant error with hysteresis due to the various misalignments. That means the TTL coupling of interest cannot be recovered due to the ATA's longitudinal displacement readout error (red curve in the bottom plot of Figure 4.15). Since the ATA readout errors would be unknown in a corresponding experiment, it would not be possible to subtract the ATA displacement error from the TTL readout. It is therefore essential to calibrate the system in order to recover the actual TTL coupling given in the upper-left graph of Figure 4.12.



(a) Initial path length signal with the imaging system (blue dot) and the ATA's longitudinal displacement readout (red)



(b) TTL coupling error (blue dot) and the ATA's longitudinal displacement readout error (red)

Figure 4.15: Path length readout with the imaging system and the ATA's displacement readout under multiple misalignments. On the upper plot, the path length readout with the imaging system (blue-dot curve) seems to match with the ATA's displacement readout (red curve) on large scale. However, as shown the path length readout after subtraction of the ATA's readout on the bottom plot, the TTL coupling shown in the upper-left graph of Figure 4.12 could not be recovered. Instead, the observed TTL readout matches the ATA displacement error, which is about 3 orders of magnitude higher than the TTL coupling of interest.

### 4.3 Calibration strategy for the ATA readout

The above simulation results revealed that the ATA's readout error due to the misalignments prevents recovering the TTL coupling performed on the opposite

side experiment. This leads to a necessity of calibrating the ATA's readout. In the following paragraphs, three potential strategies in regard to calibrating the ATA's readouts are discussed.

- 1 Identify all misalignments and remove them as much as possible.
- 2 Measure the ATA's 3-DOF motions together with other instruments and compare both measurements to calibrate that ATA's readout.
- 3 Induce more error that counteracts the longitudinal displacement readout error affecting the TTL coupling readout.

### **Approach one: reducing misalignments**

The first approach is to eliminate existing misalignments in the ATA as much as possible. However, it is considerably challenging to be accomplished in reality. Because the many misalignments can be identified by means of some tools, techniques, or instruments, but they have limited accuracy. Another point is there are so many misalignments in the ATA so that hunting down all of them is nearly impossible. Despite these difficulties, this idea does not have to be ruled out. Of course, all misalignments cannot be hunted down at once. However, even if only a few misalignments can be hunted down, it can contribute to reducing the ATA's readout error. For example, driving the ATA for a pure longitudinal motion (assuming it is possible) is useful to acquire the beams' angular misalignment. Either, generating a pure rotation of the ATA (assuming it is possible) can be useful to know each retroreflector's lateral position. In this context, developing methods to trace or reduce the misalignments are worthy and needed for the ATA as well as other multi-DOF interferometers.

### **Approach two: calibrating the ATA using another experiment**

The second approach is a comparative calibration by means of other instruments or techniques. There are a few other methods or instruments that are capable of measuring the actuator's motions. For instance, an autocollimator or the differential wavefront sensing (DWS) technique can be exploited to compare the ATA's rotation angle.

However, this approach is fundamentally limited by the measurement accuracy of the instruments (or techniques). As an example for the ATA's angular motion, the IfoCAD simulation in Chapter 4.2.2.2 exhibits that the ATA's angular readout error could be in the order of a few  $10^{-7}$  radians in the rotation angle of  $\pm 200$   $\mu$ rad. In general, commercial autocollimators' measurement error for angular motion is known to be in the order of a few micro radians. Perhaps some sophisticated instruments may perform better with a measurement error below a micro radian. Even if it is possible, this approach entirely relies on the instrument's measurement accuracy.



The DWS technique, regarded as another method for measuring angular motion, requires a calibration, which means that the DWS signal accuracy is also dependent on the other comparative instrument.

Even if assuming that the instrument employed to calibrate the ATA's motion was performing perfectly without measurement error, another critical issue would be that this calibration strategy might be valid for only a specific motion of the ATA. It is associated with the fact that the ATA's readout error depends on its motion, as analytically demonstrated in Equation (4.31) in Chapter 4.2.2.2. As an example, suppose a situation that attempts to calibrate the ATA's yaw readout by a reliable instrument. Imagine someone operates the ATA for yaw rotation and compares the ATA's yaw readout with the other instrument's result. By taking the yaw measurement from the reliable instrument as a reference, one can conceive that the ATA's yaw angle can be calibrated through the comparison. However, if the ATA has another motion in 3-DOF, the ATA's yaw angle readout would be different from the reliable instrument's yaw measurement.

This phenomenon is demonstrated via IfoCAD simulations in the following paragraphs. The core of this simulation focuses on comparing two yaw readout errors under two different motions of the ATA. Note that the various misalignment explained in Chapter 4.2.1.3 are taken into account in the simulations. Among four plots in Figure 4.16, the two plots on the left-hand side represent two different motions of the ATA in 3-DOF. The motion on the upper-left is the same that is already shown in Figure 4.10. The only difference between the upper-left and lower-left plot, the pitch angle in the lower-left plot is ten times larger than the motion on the upper-left. In Figure 4.16, two plots on the right-hand side stand for the yaw readout errors corresponding to the motions on the left-hand side. As discussed above, the yaw readout errors in the two plots on the right-hand side differ from each other, demonstrating its dependency on the ATA's motion. In the yaw rotation angle of about  $\pm 200 \mu\text{rad}$ , the yaw readout error on the upper-right plot is in the range of  $\pm 0.4 \mu\text{rad}$ , whereas one on the lower-right plot is about  $\pm 0.7 \mu\text{rad}$ . Another notable point is that the lower-right plot's yaw error contains much more substantial hysteresis than the upper-right plot.

These numerical results demonstrate that even if a perfect instrument was used for the calibration of the ATA with a specific motion, this calibration would not guarantee precise readout for a different motion. Although the above simulation represents only the yaw rotation, this phenomenon appears in the pitch and displacement readouts as well.

### **Approach three: Counteracting the longitudinal displacement readout error**

The third approach is suppressing the residual longitudinal displacement error in the path length signal by counterbalancing the ATA's three readout errors. It is noteworthy that this strategy focused on calibrating only the ATA's longitudinal displacement at a specific point on the ATA-plane rather than correcting each of the ATA readout errors.

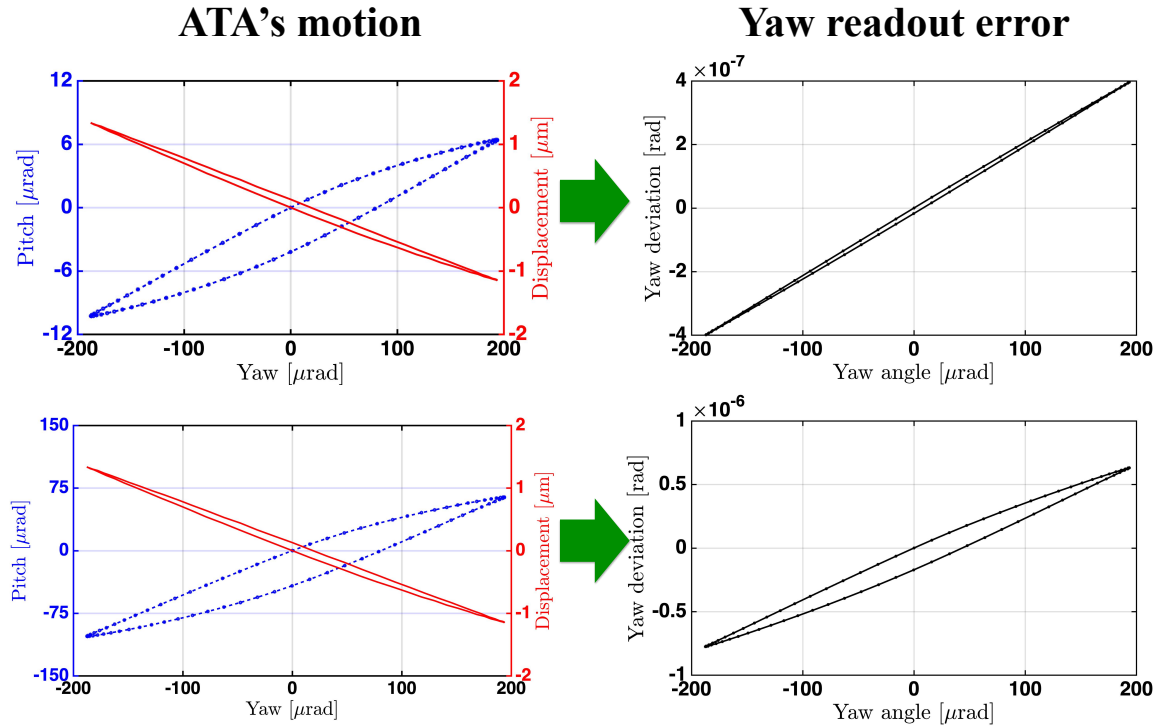


Figure 4.16: Variation of yaw readout error under the different ATA's motion. Two graphs on the upper-left and lower-left represent two different ATA's 3-DOF motions applied into the IfoCAD simulation. Yaw rotation and displacement are the same between both ATA's motion, but pitch rotation in the lower-left graph is ten times larger than one in the upper left graph. Two graphs on the upper-right and lower-right stand for the yaw rotation readout error resulted from IfoCAD simulation under multiple misalignments described Chapter 4.2.2.2. In the same range of yaw rotation angle, the upper-right graph shows  $0.4 \mu\text{rad}$  whereas the lower-right shows  $0.7 \mu\text{rad}$ . In the lower-right graph, relatively stronger hysteresis appears.

In the bottom plot of Figure 4.15, the path length signal of the two-lens imaging system, subtracted the ATA's longitudinal displacement, does not exhibit a proper characteristic of TTL coupling and even includes a hysteresis curve. It originates from the ATA's longitudinal displacement readout error due to the various misalignments.

The ideal way is to prevent or identify the ATA's three readout errors contributing to the longitudinal displacement readout error. Unfortunately, as discussed in the first and second approach, this is not easy to achieve. An alternative method is to cancel out the longitudinal displacement error by balancing the ATA's three readout errors because the longitudinal displacement error results from the ATA's three readout errors.

The fundamental question is how to validate whether the longitudinal displacement error in the path length signal is suppressed. There are two possible ways.

- 1 Employ the fourth retroreflector with its corresponding interferometer as a reference and compare its readout with the longitudinal displacement measured by using the other three retroreflectors.
- 2 Suppress the observed hysteresis and linear error in the path length readout of TTL coupling.

At the beginning of the description of the ATA in Chapter 3.2, it is mentioned that the ATA has four retroreflectors. So far, only three retroreflectors have been utilised for the ATA's readouts. The fourth retroreflector is redundant but also can be used as a reference to calibrate the longitudinal displacement readout. The longitudinal displacement readout from the fourth retroreflector can be compared with the other longitudinal displacement readout measured by using the other three retroreflectors.

Although the path length signal shown in the bottom plot of Figure 4.15 does not recover the expected TTL coupling performance, the existence of the longitudinal displacement error in the path length signal is observable. Assuming that the two beams in the TTL coupling testbed are fundamental Gaussian beams and all alignments are perfect, the resulting path length signal for the TTL coupling is anticipated to be symmetric in both directions of the rotation angle of the ATA. Hence, the hysteresis and linear error observed in the path length signal are regarded as being caused by the ATA's longitudinal displacement error. By balancing the ATA's three readout errors until the hysteresis and linear errors in the TTL coupling signal disappear in post-processing, the ATA's longitudinal displacement error can be cancelled out. As a result, the path length signal representing the characteristics of TTL coupling could potentially be recovered.

Details to demonstrate this calibration method are given in the following sections.

### 4.3.1 Calibration based on counteracting

In this section, the analytical description of the calibration concept, based on counteracting the longitudinal displacement readout error by inducing more error, is begun. Then, as a purpose of validating this calibration method, two IfoCAD simulations will be implemented. In the first simulation, the longitudinal displacement readout acquired by using three retroreflectors will be calibrated, taking the fourth retroreflector's readout as reference. The second simulation will demonstrate that the calibration method enables suppressing the path length error measured with the imaging system on the opposite of the ATA, such that the TTL coupling could be recovered.

When the ATA moves in 3-DOF, the longitudinal displacement at a specific point (called reference point) can be expressed by

$$z_{\text{real}} \approx -x_{\text{ref}} \cdot \phi_{\text{real}} + y_{\text{ref}} \cdot \eta_{\text{real}} + D_{\text{real}}, \quad (4.33)$$

where  $x_{\text{ref}}$  and  $y_{\text{ref}}$  denote the reference point's x and y positions in the ATA's coordinate,  $\phi_{\text{real}}$  and  $\eta_{\text{real}}$  are the ATA's real rotation angles for the yaw and pitch, and  $D_{\text{real}}$  signifies the real displacement at the origin. Note that the reference point is any arbitrary point that we are interested, such as the BRP or the four retroreflector's vertex.

On the other hand, the ATA's three readouts, taking into account the multiple misalignments, can be notated as

$$\begin{aligned}\phi_{\text{mea}} &= \phi_{\text{real}} + \Delta\phi_{\text{err}} \\ \eta_{\text{mea}} &= \eta_{\text{real}} + \Delta\eta_{\text{err}} \\ D_{\text{mea}} &= D_{\text{real}} + \Delta D_{\text{err}},\end{aligned}\tag{4.34}$$

where  $\Delta\phi_{\text{err}}$ ,  $\Delta\eta_{\text{err}}$  and  $\Delta D_{\text{err}}$  stand for the ATA's three readout errors caused by the misalignments. Similar to Equation (4.33), the ATA's longitudinal displacement readout can be derived as

$$z_{\text{mea}} \approx -x_{\text{mea}} \cdot \phi_{\text{mea}} + y_{\text{mea}} \cdot \eta_{\text{mea}} + D_{\text{mea}},\tag{4.35}$$

where  $x_{\text{mea}}$  and  $y_{\text{mea}}$  denote the point that the ATA measures the longitudinal displacement, called measurement point. Note that the reference point  $x_{\text{ref}}$  and  $y_{\text{ref}}$  in Equation (4.33) differs from the measurement point  $x_{\text{mea}}$  and  $y_{\text{mea}}$  in Equation (4.35). Imagine the situation that the ATA measures the longitudinal displacement at the BRP for characterising the TTL coupling. Assuming that the flat mirror is on the ATA-plane, the BRP's position can be regarded as the reference point. However, since it is difficult to pinpoint the BRP's position in the experiment, we can only estimate its position. In this case, the estimated position in the vicinity of the BRP is deemed as the measurement point and expected to contain a positional error with respect to the BRP as

$$\begin{aligned}x_{\text{mea}} &= x_{\text{ref}} + \Delta x \\ y_{\text{mea}} &= y_{\text{ref}} + \Delta y,\end{aligned}\tag{4.36}$$

where  $\Delta x$  and  $\Delta y$  stands for the measurement point's lateral offset with respect to the reference point. Substituting the results of Equation (4.34) and Equation (4.36) into Equation (4.35), the ATA's longitudinal displacement readout is rewritten as

$$\begin{aligned}z_{\text{mea}} &= -(x_{\text{ref}} + \Delta x)(\phi_{\text{real}} + \Delta\phi) + (y_{\text{ref}} + \Delta y)(\eta_{\text{real}} + \Delta\eta) + (D_{\text{real}} + \Delta D) \\ &= \underbrace{[-x_{\text{ref}} \cdot \phi_{\text{real}} + y_{\text{ref}} \cdot \eta_{\text{real}} + D_{\text{real}}]}_{\text{real LD shown in Equation 4.33}} + \\ &\quad \underbrace{[-x_{\text{ref}} \cdot \Delta\phi + y_{\text{ref}} \cdot \Delta\eta + \Delta D - \Delta x(\phi_{\text{real}} + \Delta\phi) + \Delta y(\eta_{\text{real}} + \Delta\eta)]}_{\text{LD readout error}}.\end{aligned}\tag{4.37}$$

In Equation (4.37), the first bracket equals to the real longitudinal displacement shown in Equation (4.33), and the second bracket means the error of the longitudinal displacement readout.

A way to calibrate the ATA's longitudinal displacement readout is to intentionally introduce an offset that counteracts the second bracket labelled with 'LD readout error' in Equation (4.37). To do that, it needs to modify Equation (4.36) regarding the measurement point, as

$$\begin{aligned}x_{\text{mea}} &= x_{\text{ref}} + \Delta x + x_{\text{off}} \\y_{\text{mea}} &= y_{\text{ref}} + \Delta y + y_{\text{off}},\end{aligned}\tag{4.38}$$

where  $x_{\text{off}}$  and  $y_{\text{off}}$  are new terms that would be used to produce additional error that counteract the longitudinal displacement readout error. Substituting the new measure point of Equation (4.38) and the ATA's three readouts of Equation (4.34) into Equation (4.35), the new longitudinal displacement is written, as

$$\begin{aligned}z_{\text{cal}} &= - (x_{\text{ref}} + \Delta x + x_{\text{off}})(\phi_{\text{real}} + \Delta\phi) + (y_{\text{ref}} + \Delta y + y_{\text{off}})(\eta_{\text{real}} + \Delta\eta) + (D_{\text{real}} + \Delta D) \\&= \underbrace{[-x_{\text{ref}} \cdot \phi_{\text{real}} + y_{\text{ref}} \cdot \eta_{\text{real}} + D_{\text{real}}]}_{\text{real LD shown in Equation 4.33}} + \\&\quad \underbrace{[-x_{\text{ref}} \cdot \Delta\phi + y_{\text{ref}} \cdot \Delta\eta + \Delta D - \Delta x(\phi_{\text{real}} + \Delta\phi) + \Delta y(\eta_{\text{real}} + \Delta\eta)]}_{\text{LD readout error}} + \\&\quad \underbrace{[-\overbrace{x_{\text{off}}}^{\text{tuning value}}(\phi_{\text{real}} + \Delta\phi) + \overbrace{y_{\text{off}}}^{\text{tuning value}}(\eta_{\text{real}} + \Delta\eta)]}_{\text{counteracting against LD readout error}}.\end{aligned}\tag{4.39}$$

Compared to Equation (4.37), the new longitudinal displacement  $z_{\text{cal}}$  in Equation (4.39) contains the third bracket part that is produced by adding  $x_{\text{off}}$  and  $y_{\text{off}}$  into the measure point as shown in Equation (4.38). The role of the third bracket part is to cancel out the LD readout error in the second bracket. To accomplish it, the  $x_{\text{off}}$  and  $y_{\text{off}}$ , labelled with 'tuning value' in Equation (4.39), should be properly tuned so that the third bracket counteracts against the second bracket.

#### 4.3.1.1 Calibration with using the fourth retroreflector

The ATA uses three retroreflectors for measuring the longitudinal displacement, but also has one more retroreflector, which could provide the most knowledgeable displacement readout. Of course, the ATA's longitudinal displacement readout for the TTL coupling investigation should correspond to the BRP. Although the fourth retroreflector is not located at the BPR, its displacement readout could be advantageous to test the calibration method explained in the previous section alternatively.

Hence, we take the longitudinal displacement readout from the fourth retroreflector as the reference and calibrate the longitudinal displacement measured by using the other three retroreflectors. For confirming this calibration method and its precision, the IfoCAD simulation's condition described in Chapter 4.2.2.2 is extended by setting up the fourth retroreflector with two interfering beams.

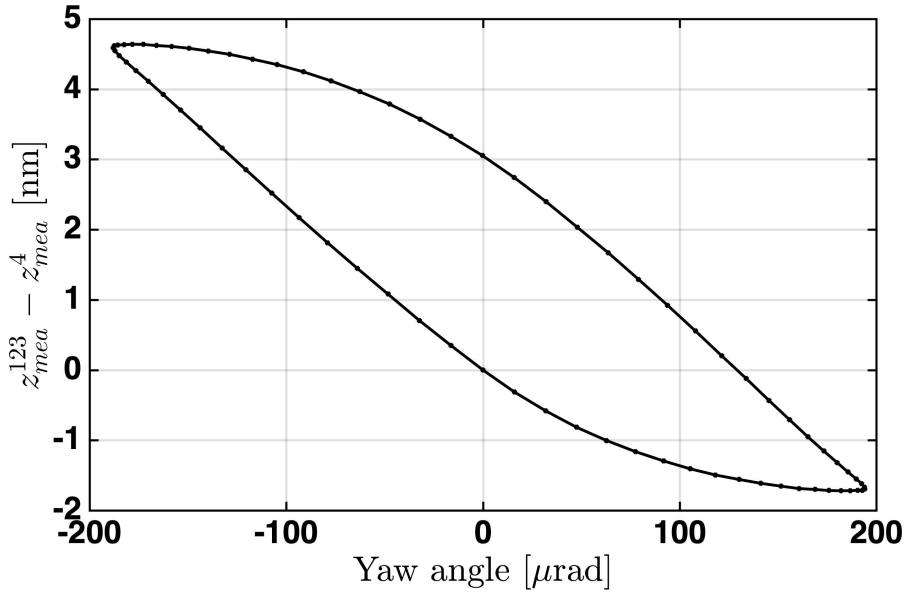


Figure 4.17: *Difference between two longitudinal displacement readout for the fourth retroreflector's vertex. The longitudinal displacement readout from the fourth retroreflector is denoted by  $z_{mea}^4$ , whereas the other one measured by using the other three retroreflectors is notated by  $z_{mea}^{123}$ . The plot shows the difference between these two readouts, which contains the hysteresis and linear error due to misalignments in the ATA.*

The fourth retroreflector's vertex is placed at the point corresponding to the 'RR4' in Table 3.1 containing the CMM's measurements for the retroreflectors' vertex. Note that its position has the longitudinal offset of 0.114 mm with respect to the ATA-plane. The rest of the simulation parameters are the same as explained in Chapter 4.2.1. Regarding beams and photodiode for the fourth interferometer, same parameters as shown in Table 4.9 are applied. The measurement beam toward the fourth retroreflector is perpendicular to the ATA-plane. The ATA's 3-DOF motion shown in Figure 4.10 is applied to the simulation.

The longitudinal displacement readout at the fourth vertex  $x_{mea} = 59.449$  mm and  $y_{mea} = 60.839$  mm, obtained using three retroreflectors, is notated by  $z_{mea}^{123}$ . And, the longitudinal displacement readout from the fourth retroreflector is notated by  $z_{mea}^4$ . The difference between the two readouts is shown in Figure 4.17. Unlike the ideal case that the difference should be minimal regardless of the ATA's rotation angle and motion, the simulation result reveals a substantial hysteresis error. By taking  $z_{mea}^4$  as reference, we regard this discrepancy as the readout error of  $z_{mea}^{123}$ , which should be calibrated.

To counteract the observed error of  $z_{mea}^{123}$ , the measurement point  $x_{mea}$  and  $y_{mea}$  containing the tuning values  $x_{off}$  and  $y_{off}$ , explained in Equation (4.38) and (4.39), are tuned. Firstly, the  $y_{mea}$  is tuned with monitoring the variation of the error of  $z_{mea}^{123}$ , as shown in the upper plot of Figure 4.18. As a result, the hysteresis in the error of  $z_{mea}^{123}$  is gradually suppressed by tuning the value of the  $y_{mea}$ . When the  $y_{mea}$

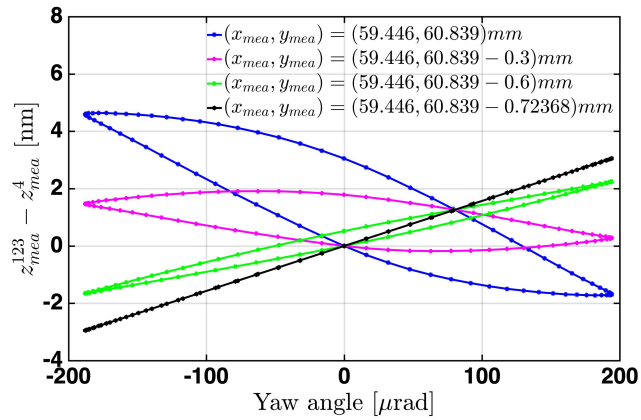
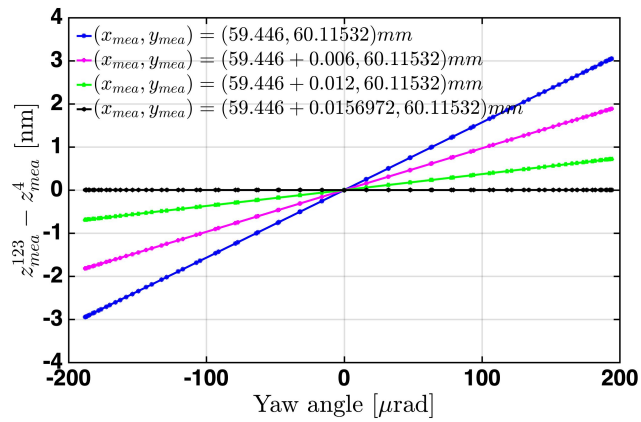
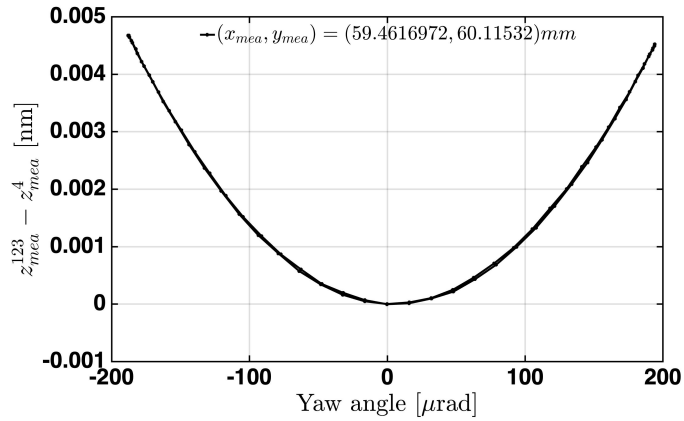
(a) *Suppression of hysteresis error*(b) *Suppression of linear error*(c) *Residual error of the ATA's LD readout after calibration*

Figure 4.18: Reducing the error of  $z_{mea}^{123}$  by tuning the measurement point  $x_{mea}$  and  $y_{mea}$ . By taking the four retroreflector's longitudinal displacement  $z_{mea}^4$  as reference, the difference of  $z_{mea}^{123}$  from  $z_{mea}^4$  is regarded as the error of  $z_{mea}^{123}$ . The plots above explain the error of  $z_{mea}^{123}$  can be reduced by tuning the measurement point. The upper plot shows the suppression of the hysteresis by tuning the  $y_{mea}$  of the measurement point. When the  $y_{mea}$  of the measurement point is tuned to 60.11532 mm, the hysteresis error disappears. In the middle plot, residual linear error gradually vanishes along with tuning the  $x_{mea}$ . When the  $x_{mea}$  equals to 59.4616972 mm, the residual error is minimal. The bottom plot enlarged the middle plot's black line, showing the residual error in the order of a few picometres.

is tuned from 60.839 mm to 60.11532 mm, the hysteresis error effectively disappears. It can be demonstrated by that the pitch angle's hysteresis counteracts the hysteresis error of  $z_{\text{mea}}^{123}$ .

To reduce the remaining linear error, the  $x_{\text{mea}}$  is tuned, keeping  $y_{\text{mea}}=60.11532$  mm. From the simulation result shown in the middle plot of Figure 4.18, the residual linear error gradually diminishes by tuning the  $x_{\text{mea}}$ . When  $x_{\text{mea}}$  is tuned to 59.4616972 mm (black line in the middle plot of Figure 4.18), the error of  $z_{\text{mea}}^{123}$  seems to be notably suppressed in the nanometre scale view. For checking the residual error of  $z_{\text{mea}}^{123}$ , its result is enlarged in the bottom plot of Figure 4.18. As can be seen, there is a residual error in the order of few picometres showing second-order of yaw angle. This residual error could be attributed to a few potential sources such as small lateral movement during the ATA's rotation, incident beam angle, fourth vertex's longitudinal offset to the ATA-plane. Nonetheless, the observed error of a few picometres would not impact the TTL coupling experiment.

There are a few limitations in this calibration method. Firstly, this calibration method is valid for a specific motion of the ATA, which means that it requires another tuning value of  $x_{\text{mea}}$  and  $y_{\text{mea}}$  for the ATA's different motion. As aforementioned, the ATA's three readout errors can be altered depending on the ATA's motion. Since this calibration is based on counterbalancing the ATA's three readout errors for minimising the longitudinal displacement readout error, the  $x_{\text{mea}}$  and  $y_{\text{mea}}$  need to be tuned with different values when the ATA's another motion causes different readout error. Secondly, the BRP in the TTL coupling testbed side does not coincide with the fourth vertex. The ultimate purpose of this calibration method for the TTL coupling experiment is to remove the parasitic longitudinal displacement readout error in the TTL coupling signal. To utilise the ATA to TTL coupling experiments, we need to calibrate a longitudinal displacement readout at the BRP point instead of the fourth vertex.

#### 4.3.1.2 Suppress hysteresis and linear error for TTL coupling

The path length after subtracting the ATA's longitudinal displacement readout, shown in the lower plot of Figure 4.15, contains significant linear and hysteresis error, such that the TTL coupling cannot be characterised. However, assuming the TTL coupling signal should be symmetric on both sides of the ATA rotation angle if the whole setup of the imaging system is well aligned, it can be deduced that a hysteresis and linear path length in the lower plot of Figure 4.15 originate from the ATA's longitudinal displacement readout error. In the same manner as the calibration method demonstrated in Chapter 4.3.1.1, we counteract the occurred longitudinal displacement error by tuning the measurement point  $x_{\text{mea}}$  and  $y_{\text{mea}}$  until the hysteresis and linear error disappear in the path readout.

To verify that this calibration method is valid for the TTL coupling investigation, the IfoCAD simulation performed in Chapter 4.2.2.2 is further continued. Note that the explained multiple misalignments, such as dihedral angle error, lateral offsets



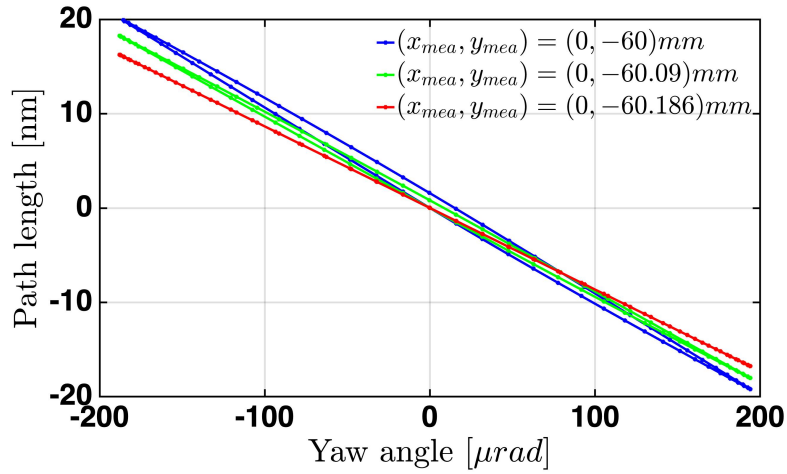
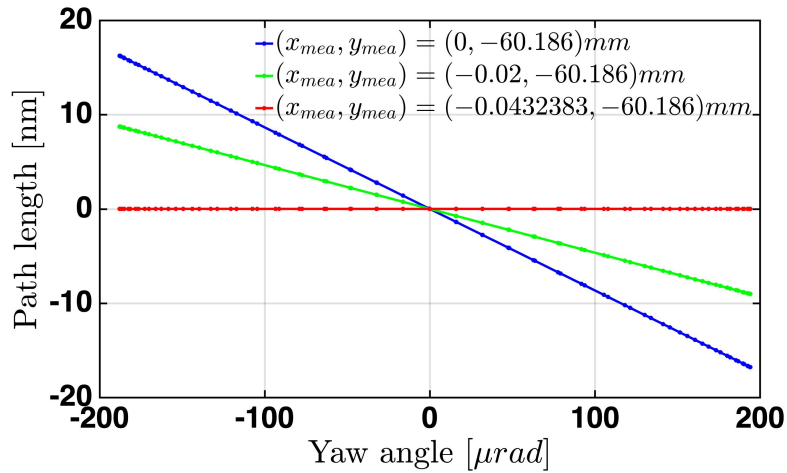
(a) *Suppression of hysteresis of path length*(b) *Suppression of linear path length*

Figure 4.19: *Cancelling out the linear and hysteresis error in path length readout. As a result of the IfoCAD simulation, the occurring linear and hysteresis error, originated from the ATA's longitudinal displacement readout error due to the various misalignments, can be mitigated by tuning the measurement point. The upper plot shows that the hysteresis error is suppressed by turning the  $y_{mea}$ . The lower plot represents the residual linear error on the path length signal vanishes by tuning the  $x_{mea}$  of the measurement point.*

for retroreflectors, incident beam angle and BRP offset, are maintained.

The upper plot in Figure 4.19 shows the path length variation by tuning the  $y_{mea}$ . The blue curve indicates the initial path length readout prior to the calibration. This initial path length readout is acquired after subtracting the ATA's longitudinal displacement computed with using the measurement point of  $x_{mea} = 0$  mm and  $y_{mea} = -60$  mm. By tuning the  $y_{mea}$  to  $-60.186$  mm, most of hysteresis disap-

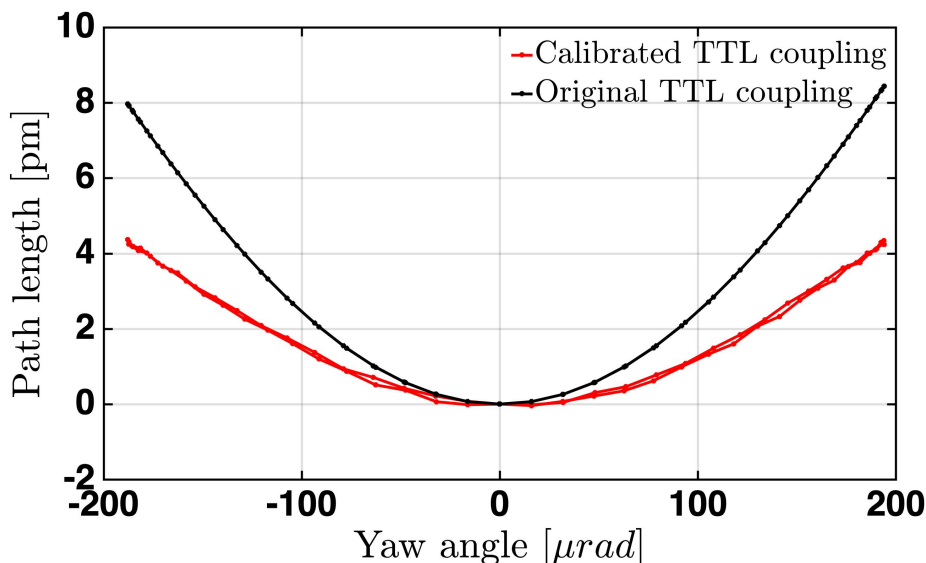


Figure 4.20: Comparison between the original TTL coupling and the TTL coupling via the calibration. The red curve indicates the path length signal with the imaging system after cancelling out the hysteresis and linear path length through the calibration, which is shown on the bottom of Figure 4.19. The black curve represents the original TTL coupling with the imaging system when the ATA's rotation point coincides with the BRP. By comparing both results, path length difference around 4 pm is observed in the ATA's yaw rotation angle of 200  $\mu\text{rad}$ , which signifies residual error of the calibration.

pears (the red curve in the upper plot of Figure 4.19).

Following that, the  $x_{\text{mea}}$  is tuned for reducing the residual linear error of the path length signal, keeping  $y_{\text{mea}}$  equals to -60.186 mm. As shown in the lower plot of Figure 4.19, when the  $x_{\text{mea}}$  is tuned to -0.0432383 mm, the linear slope in the path length readout vanishes (red line).

In Figure 4.20, the path length signal through this calibration method (red line) is compared with the original TTL coupling signal (black line) in order to check the precision of this calibration. The original TTL coupling signal in here refers to path length readout when the rotation point of the ATA matches with the BRP. The comparison of the two results explains that the ATA readout error could be effectively suppressed from the path length readout, but the TTL curve could not be fully recovered, showing the difference of 4 pm at the edge of the rotation angle. This TTL coupling error stands for the limitation of the ATA's performance and the calibration method.

It is worthy to note that the original TTL coupling signal with the imaging system, drawn by the black line in Figure 4.20, represent a high suppression of the TTL coupling below a few picometres. It means that its performance is a highly stringent level to be achieved in a real experiment. From this aspect, the TTL

coupling error of 4 pm from this calibration method could be evaluated that this calibration method could effectively perform.

#### 4.3.1.3 Further analyses for counteracting each misalignment

The above analyses via the numerical simulations demonstrate that the calibration method effectively cancels out the ATA's longitudinal displacement readout error. However, the TTL coupling error, which is the difference between the two plots shown in Figure 4.20, is not entirely negligible. It is presumed to be due to the residual error after calibrating ATA's longitudinal displacement error, but not clear yet which effect mainly contributes to it.

The IfoCAD simulation in Chapter 4.3.1.2 took into account several misalignments; the lateral offset of each retroreflector, the BRP offset, the beams' oblique incident angles, the dihedral angle errors of the retroreflectors. In order to understand the cause of the residual TTL coupling, the calibration method is reimplemented in simulations that independently consider each misalignment instead of simultaneously applying all the misalignments. Then, by analysing each residual TTL coupling obtained through the calibration method, the degree to which each misalignment contributes to the final residual TTL coupling shown in Figure 4.20 is examined.

Figure 4.21 contains a total of twelve plots arrayed in three columns and four rows, which are the results through the calibration method in each simulation that respectively applies the misalignments. The three plots in each row are paired with each other, resulting from a simulation for each misalignment. In the first column plots, the TTL couplings obtained when each misalignment is applied are compared to the original TTL coupling. The second column plots show comparisons between the TTL coupling through the calibration method and the original TTL coupling. The third column plots represent residual TTL coupling errors, which mean the difference between the two curves shown in the second column plots. More details regarding the simulation results will be explained in the following paragraphs.

First of all, the explanation of Figure 4.21 begins with the three plots in the first row. The BRP offset listed in Table 1 was applied to an IfoCAD simulation. The ATA's initial measurement point was set to  $x_{\text{mea}} = 0$  and  $y_{\text{mea}} = -60$  mm. The imaging system and the two interfering beams were laterally shifted as much as the BRP offset listed in Table 4.8, which means that the BRP is  $x_{\text{brp}} = -0.072$  mm and  $y_{\text{brp}} = -59.041$  mm in the ATA's coordinate. In the first column's left plot, the red curve represents the path length signal with the imaging system, subtracted the ATA's longitudinal displacement readout at the initial measurement point. Compared to the black curve of the original TTL coupling, the red curve increases to about 30 nm. Afterward, as described in Chapter 4.3.1, the TTL coupling was calibrated by tuning the measurement point until the linear path length and hysteresis disappeared. This result is compared with the original TTL coupling in the middle plot. Two curves are highly overlapped, meaning the calibration method enables

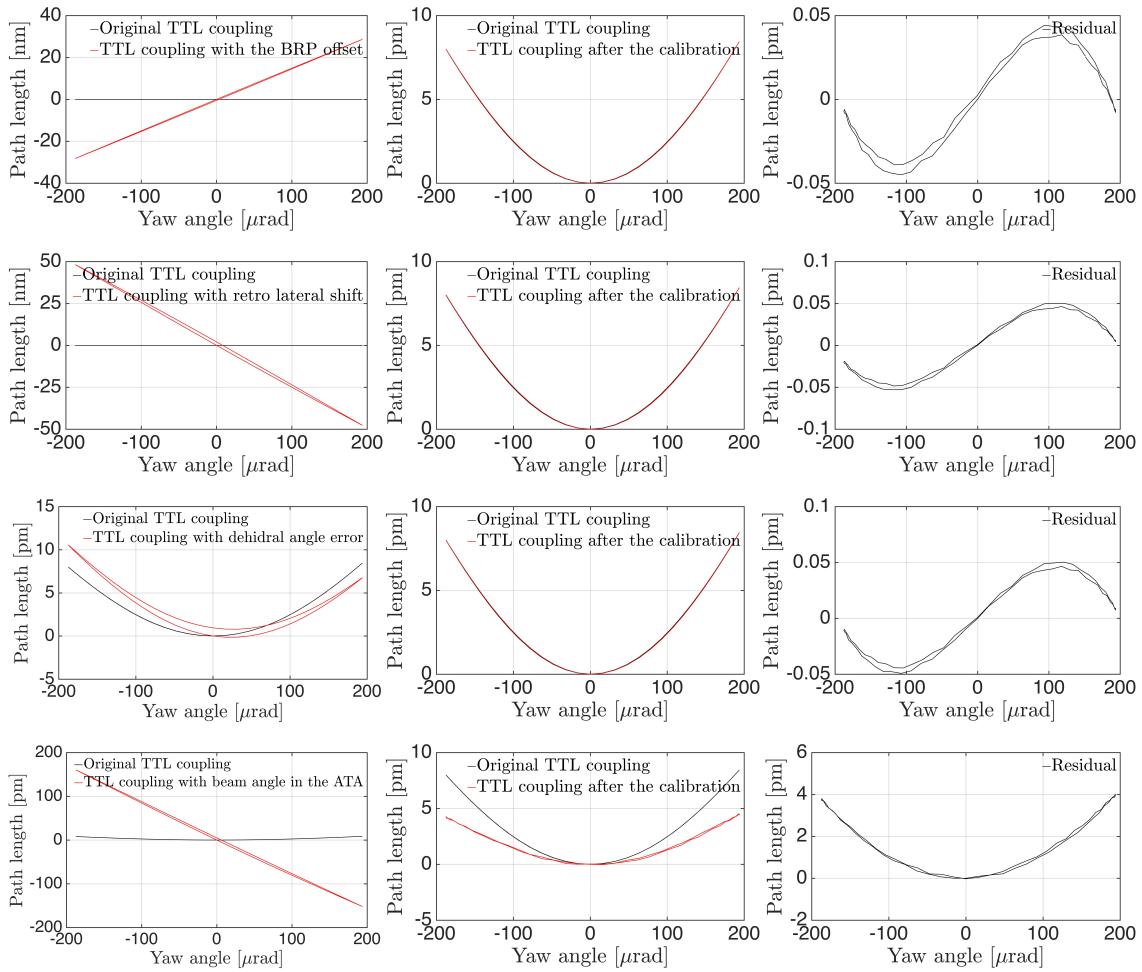


Figure 4.21: *Residual TTL couplings via the calibration method for each misalignment. As an extension of the simulation performed in Chapter 4.3.1.2, additional IfoCAD simulations were performed to understand the cause of the difference between the two TTL couplings shown in Figure 4.20. Unlike the simulation in Chapter 4.3.1.2, which considers the four misalignments explained in Chapter 4.2.1.3 simultaneously, each misalignment is independently applied to the ATA in this simulation. The three plots in each row are paired and show the results of simulations applying each misalignment (BRP offset, retroreflectors' lateral offset, dihedral angle error of the retroreflectors, and incident angle of the beams in the order from the top row). In the plots in the right column, the red curves represent TTL couplings before the calibration, whereas the black curve represents the original TTL coupling. In the middle column's plots, the red curves, which are the TTL couplings obtained through the calibration based on tuning the ATA's measurement point, are compared with the original TTL coupling (black curve). The plots in the left column exhibit the difference between the two plots shown in the middle plots. The first column's plots demonstrate that the BRP offset and the retroreflectors' lateral offset among the four misalignments cause most significantly TTL coupling's error. The plots in the third column support the fact that the incident beam angle is the primary cause of the difference between the TTL couplings shown in Figure 4.20.*

recovering to the original TTL coupling. The plot on the right-hand side, showing the difference between the two plots in the order of a few  $10^{-14}$  pm, confirm that the BRP offset's effect can be effectively calibrated by the calibration method.

Next, the second-row plots exhibit the simulation results, applying the lateral offset for the retroreflectors. In the simulation, the sets of  $x$  and  $y$  listed in Table 4.5 are regarded as the CMM's measurements for the vertices of the three retroreflectors, which are needed to calculate the ATA's readout. However, their actual vertex positions are laterally shifted as much as  $\Delta x$  and  $\Delta y$  in Table 4.5. The ATA measures the longitudinal displacement at the BRP which  $x_{\text{mea}} = 0$  and  $y_{\text{mea}} = -60$  mm. Note that the BPR offset is not considered in this simulation, and we only apply the lateral offsets for the retroreflectors. In the second row's left plot, the red curve, representing the path length signal subtracting the ATA's longitudinal displacement readout, rises up to about 50 nm. Then, it was suppressed by means of the calibration method tuning the measurement point. As shown in the middle plot, the red curve representing the TTL coupling that is resulted from the calibration agrees with the original TTL coupling, showing the difference between two plots less than 0.05 pm in the right plot.

The three plots in the third row correspond to the simulation results when applying the dihedral angles errors to the three retroreflectors according to Table 4.7. As shown in the left plot, the simulation result reveals that the dihedral angle error leads to a smaller deviation of the TTL coupling than the above two cases. In the same manner as done in the previous case, the path length signal consistent with the original TTL coupling was obtained by tuning the ATA's measurement point, as shown in the middle plot. The right plot, showing that the difference between the two TTL couplings is less than 0.05 pm, explains that the calibration was well performed.

Finally, the simulation results that take into account the beam angle are presented in the three plots in the fourth row. According to Table 4.6, the incident angles of the beams towards the retroreflectors were introduced in the simulation. The resulting path length signal indicated by the red curve in the left plot change up to about 170 pm. Then, its linear slope and small hysteresis are suppressed by tuning the ATA's measurement point. The resulting TTL coupling via the calibration is compared with the original TTL coupling in the middle plot. When the yaw rotation is the maximum (or minimum), the difference between the two TTL coupling is about 4 pm, showing a quadratic curve in the right plot. This result is very similar to the plot in Figure 4.20, which is interpreted that the effect of the incident beam angle towards the retroreflectors is the main contributor in the residual TTL coupling shown in Figure 4.20.

The above simulation results demonstrate that the BRP offset and the retroreflectors' lateral offset primarily affect the TTL coupling error before the calibration. The effect of the dihedral angle errors of the retroreflectors is less influential than the other misalignments. On the other hand, the results in Figure 4.21 reveal that the incident beams angle towards the retroreflectors are the main cause for the residual TTL coupling error that appeared after the calibration. The above analysis results suggest that it is crucial to minimise the BRP offset and the lateral offset of the

retroreflector as much as possible in experiments to reduce the ATA's longitudinal displacement readout error before the calibration. Also, the residual TTL coupling after the calibration, which is caused by the angle of the incident beams on the ATA, intimates that the angular alignment of the beams is not trivial in order to achieve high precision in TTL coupling experiments.

#### 4.3.1.4 Limitation

This calibration method entails several limitations.

Firstly, instead of correcting all three readouts errors for the ATA's 3-DOF motion, it focuses on only counteracting the longitudinal displacement readout error by tuning the measurement point. Due to the difficulties in the other calibration methods discussed at the beginning of Chapter 4.3, we adopted the counteraction method as an alternative. In order to use the ATA for many other experiments beyond examining this TTL coupling effect, it is necessary to investigate further for calibration of the two tilt motions as well.

Secondly, since the ATA's three readout errors are dependant on the ATA's motion, as demonstrated in Figure 4.16, the ATA's other motion results in a different amount of the ATA three readout errors. That means that it requires a re-calibration again if the ATA is driven to a different motion. Consequently, this calibration is valid for the specific motion of the ATA.

Thirdly, this calibration may cancel out some part of the actual TTL coupling because it suppresses all linear path lengths. In the above simulation, all beams and components on the TTL coupling experiment were optimally well aligned. However, there could be many kinds of misalignment in the actual experimental setup, such as residual lateral misalignment of two beams, lateral offsets of the QPDs, the imaging system's misalignments. In this case, the resulting TTL coupling could include linear or higher-order terms in the path length signal [43]. Since this calibration method removes residual linear path length, the effects of these misalignments cannot be identified.

## 4.4 Summary of optical simulation

Despite attempts to minimise misalignments as much as possible in the ATA, residual misalignments coupling into the ATA's readouts degrade the ATA's performance. Thus, calibrating the ATA's readouts is indispensable for proper TTL coupling investigations.

As a preliminary step, how each misalignment influences the ATA's readouts were individually examined through the IfoCAD simulation and analytical calculation. However, since many misalignments are involved together in the ATA, it is challenging to identify each of those contributions to the ATA's readout error. The

ideal scenario is to hunt down all misalignments and correct them, but this is not realistic to achieve. As another option, we discussed the comparative calibration method, based on comparing the ATA's readouts with other instrument's measurement. However, this calibration method is fundamentally limited by the accuracy of the other instruments used to compare with the ATA's readout.

The alternative method is to counteract the longitudinal displacement readout error by intentionally introducing another error via tuning the ATA's measurement point. Applying realistic conditions with various misalignments to the IfoCAD simulation, the ATA's readout errors were analysed. For confirming the validity of the calibration method, we implemented two simulations. In the first simulation, the fourth retroreflector's longitudinal displacement readout is regarded as a reference. Then, the longitudinal displacement readout acquired by using the other three retroreflectors was calibrated such that its linear and hysteresis error could be suppressed to below a few picometres. In the second simulation, the imaging system was built on the opposite of the ATA. Compared to the original TTL coupling when the ATA's pivot point coincides with the beam's reflection point on the mirror, the resulting TTL coupling error could be reduced in a few picometres through the calibration method. Further investigation on the residual TTL coupling error demonstrated that the calibration method effectively mitigates the linear part of the TTL coupling error caused by each misalignment. We also learned that the beams' incident angles towards the retroreflectors remain a second-order effect after the calibration.





## 5 Measurement campaign

Apart from the ATA, two additional optical breadboards were built in this thesis. One of them, named TTL coupling experiment, was constructed for investigating TTL coupling effects. The other optical breadboard, called Modulation Bench, produces heterodyne beams with the frequency difference of about 12.5 kHz and delivers them to the other optical breadboard. This chapter reports three experiments and their results. In the first experiment, the calibration method for the ATA's longitudinal displacement readout, discussed in Chapter 4.3, was carried out. In the second experiment, we measured two TTL couplings with and without a two-lens imaging system and experimentally demonstrated the suppression of the TTL coupling via the two-lens imaging system. In the third experiment, the ATA's angular readout was compared with the DWS signal measured in the TTL coupling experiment.

### 5.1 Experimental setup

For performing experimental campaigns, the whole setup consists of the Modulation Bench (MB), the ATA and the TTL coupling experiment, as a schematic shown in Figure 5.1. The MB provides two beams having a slightly different frequency for heterodyne detection to the two other testbeds. The ATA provides the rotating mirror and measures its motions. The TTL coupling experiment is constructed to experimentally examine the TTL coupling's characteristics and verify the reduction of the TTL coupling via the two-lens imaging system. As shown in Figure 5.2, each of the three subsystems was independently constructed on an optical breadboard. Since all subsystems are movable on a big optical table, the ATA can be flexibly utilised not only to one specific experiment but also to other experiments. The three optical breadboards are placed on a big optical table and shielded by acrylic glasses to reduce the influence of external environments such as air turbulence or temperature variation.

#### 5.1.1 Modulation Bench

The key role of the MB is to provide two heterodyne beams to the ATA as well as the TTL coupling experiment. The modulation bench shown on the top in Figure 5.1 was built on an optical breadboard with  $60 \times 60 \text{ cm}^2$  size. In the MB, Nd:YAG lasers (Coherent, Mephisto-500) with 1064 nm wavelength is used as the light source.

Then, the beam passes through two wave-plates; a half-wave and a quarter-wave plate. There are two purposes of using the two wave-plates. Firstly, they are employed to transform the polarisation of the laser source into the optimal linear polarisation. The Mephisto-500, laser used in the MB, emit a beam with elliptical polarisation. The intensity ratio of p-pol and s-pol (p-pol is when the electric field

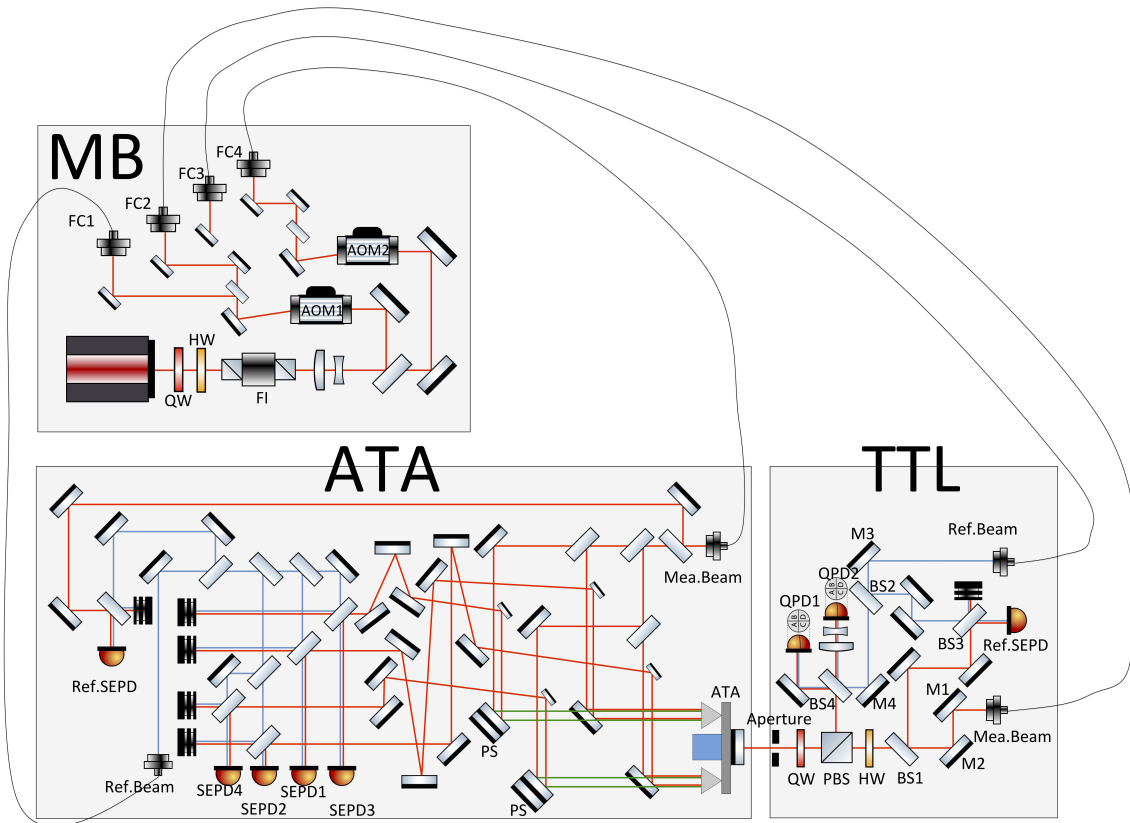


Figure 5.1: *Schematic of the experimental setup. The setup consists of three testbeds; Modulation Bench, ATA and TTL coupling experiment. The role of the modulation bench is to generate frequency-shifted beams for heterodyne detection and serve them to the ATA and TTL coupling experiment. The ATA provides a rotating beam for TTL coupling experiment and measures its motion itself to decouple the longitudinal displacement. In the TTL coupling experiment, two path length readouts with and without the two-lens imaging system are compared to verify the suppression of TTL coupling via the imaging system.*

direction of the beam is parallel to the optical table, and s-pol is when the electric field direction of the beam is perpendicular to the optical table) is approximately  $I_{p-pol}/I_{s-pol}=0.2$ . However, the beam's polarisation desired at the input polariser of the Faraday Isolator (FI) is the linear polarisation rotated by 45 degrees from p-pol. Hence, the laser source's elliptical polarisation can be transformed into the linear polarisation rotated 45 degrees by adequately adjusting the fast axes of the two wave-plates.

Secondly, the two wave-plates allow controlling the power of the output beams delivered from the modulation bench to the other two subsystems. The simplest way of controlling the laser beam power is tuning the current of the laser power controller, but it is sometimes hard to fine-tune the power. Another approach is intentionally mismatching the polarisation of the beam passing through the two wave-plates with respect to the axis of the FI's input polariser so that the mismatched polarisation

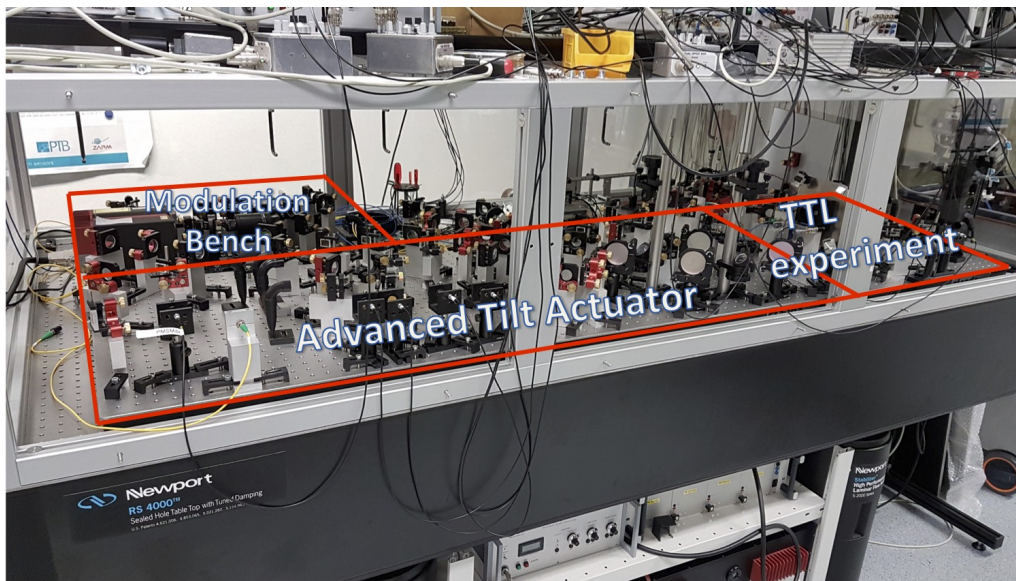


Figure 5.2: *Picture of the experimental setup on an optical table. By constructing each of three testbeds on own optical breadboards, the ATA can be employed not only for this TTL coupling setup but also for other experiments. Several pieces of windows shield the optical table in order to reduce the influence of external disturbances.*

beams can be pointed into a different direction. The two wave-plates together with the input polariser of the FI can be utilised for fine adjustment. However, this method is suitable for controlling a small amount of power. If this method is applied to reduce a large amount of beam power, unwanted polarisation may be leaked from the FI's output port, degrading linear polarisation.

The beam linearly polarised at 45-degree angle by the wave-plates reaches the FI consisting of a faraday rotator and two linear polarisers. The FI transforms the input beam from a 45-degree linear polarisation to s-pol by the faraday rotator. The role of the FI is to prevent back-reflected light from the optical system to reach the laser source, which could cause power fluctuations, noise of the laser source or even damage.

After that, the output beam from the FI reaches an optical beam expander that consists of a convex lens with a focal length of 50 mm and a concave lens with a focal length of -30 mm. The optical beam expander reduces the input beam by a factor of  $3/5$  in order to increase coupling-efficiency into the fibre couplers.

The beam after the beam expander is split by a beam splitter with 50:50 split ratio, and then the split two beams are respectively towards two AOMs that are driven by a phase-lock loop (PLL) circuit and two drivers that deliver 2 watts RF power at 80 MHz. The first-order diffracted beams by the two AOMs are chosen, and the frequency difference between the two first-order diffracted beams is about 12.5 kHz, which is tuned by the PLL. In order to deliver the two heterodyne beams to the ATA and the TTL coupling experiment, each beam is split by a beam splitter, and a total of four split beams couple into each fibre coupler (FC). The beams coupled

to FC1 and FC4 are delivered to the ATA, and the beams coupled to FC2 and FC3 are delivered to the TTL coupling experiment through fibres.

### 5.1.2 The ATA testbed

The ATA consists of an actuation platform (AP) that provides a rotating beam to the TTL coupling experiment and several interferometers that measure the AP's motion in 3-DOF. Among five interferometers in the ATA, four of them measure the longitudinal displacement of the four retroreflectors attached to the AP, and the fifth interferometer serves as reference interferometer. The green lines in Figure 5.1 indicate two beams toward two upper retroreflectors installed in the ATA through two periscope (PS). More details regarding the ATA setup are described in Chapter 3 and Chapter 4.

### 5.1.3 TTL coupling experiment

The primary purpose of the TTL coupling experiment shown on the right corner of Figure 5.1 is to investigate characteristics of TTL couplings and verify the suppression of the TTL coupling via an imaging system. The TTL coupling experiment consists of two measurement interferometers and a reference interferometer. In the first measurement interferometer, the TTL coupling caused by an angular misalignment between two beams is measured. On the other hand, the second measurement interferometer contains a two-lens imaging system for verifying the suppression of the TTL coupling by comparing its result with one from the other measurement interferometer. The reference interferometer is for rejecting the common-mode noise.

The TTL coupling experiment receives two beams with a frequency difference of 12.5 kHz from the MB through single-mode fibres. Two fibre couplers in the TTL coupling experiment produce beams with a diameter of about 1 mm, and the polarisation of the beams is s-pol. In the schematic of the TTL coupling experiment of Figure 5.1, red lines represent the beam path for the measurement beam, and blue lines indicate the beam path for the reference beam. Two folding mirrors M1 and M2 are exploited to align the measurement beam towards the ATA. The beam reflected from the folding mirrors reaches a beam splitter (BS1). The reflected beam at the BS1 is used for the reference interferometer, and the transmitted beam propagates towards the ATA.

The measurement beam propagating towards the flat mirror attached to the AP of the ATA is preferable to be perpendicular to the flat mirror because the ATA measures the longitudinal displacement of the beam's reflection point. Otherwise, the beam's incident angle should be taken into account in the translation between the ATA's longitudinal displacement and the beam's OPD, which brings about one more experimental task to measure or define the beam angle accurately.

For this configuration, a few polarising optical components and an aperture are used. The s-pol beam transmitted through the BS1 is transformed into a p-pol beam by a half-wave plate (HW). Then, the p-pol beam passes through a polarising beam splitter (PBS), and its polarisation is converted to circular polarisation by a quarter-wave plate (QW). The beam that is perpendicular to the flat mirror of the ATA is reflected and returns through the QW. The beam's polarisation after the QW is s-pol, and it is reflected by the PBS and reaches a beam splitter (BS4).

For the perpendicular alignment of the measurement beam to the ATA's mirror, an aperture is installed between the ATA's flat mirror and the QW, and two folding mirrors M1 and M2 are adjusted until the power of the beam returning through the aperture becomes maximal at the photodiode. Note that the aperture allowing for varying its hole size was fully opened without beam-clipping after the alignment.

Meanwhile, the reference beam is reflected by a folding mirror M3 and split by a beam splitter (BS2). A beam reflected by the BS2 passes through two folding mirrors and reaches another beam splitter (BS3). At the BS3, the reference and measurement beam interferes and forms the reference interferometer. A transmitted beam through the BS2 is reflected on a folding mirror M4 and propagates to the BS4 for the measurement interferometers.

At the beam splitter BS4, the measurement beam and the reference beams are split into two beams toward QPD1 and QPD2. A TTL coupling caused by an angular misalignment between two beams is measured at QPD1, and another TTL coupling via the two-lens imaging system is measured at QPD2. In particular, the primary purpose of the TTL coupling experiment is to experimentally verify that the imaging system can suppress the TTL coupling, which is implemented here by the two different paths (with and without the imaging system) to QPD1 and QPD2.

### **Alignment procedure for the imaging system**

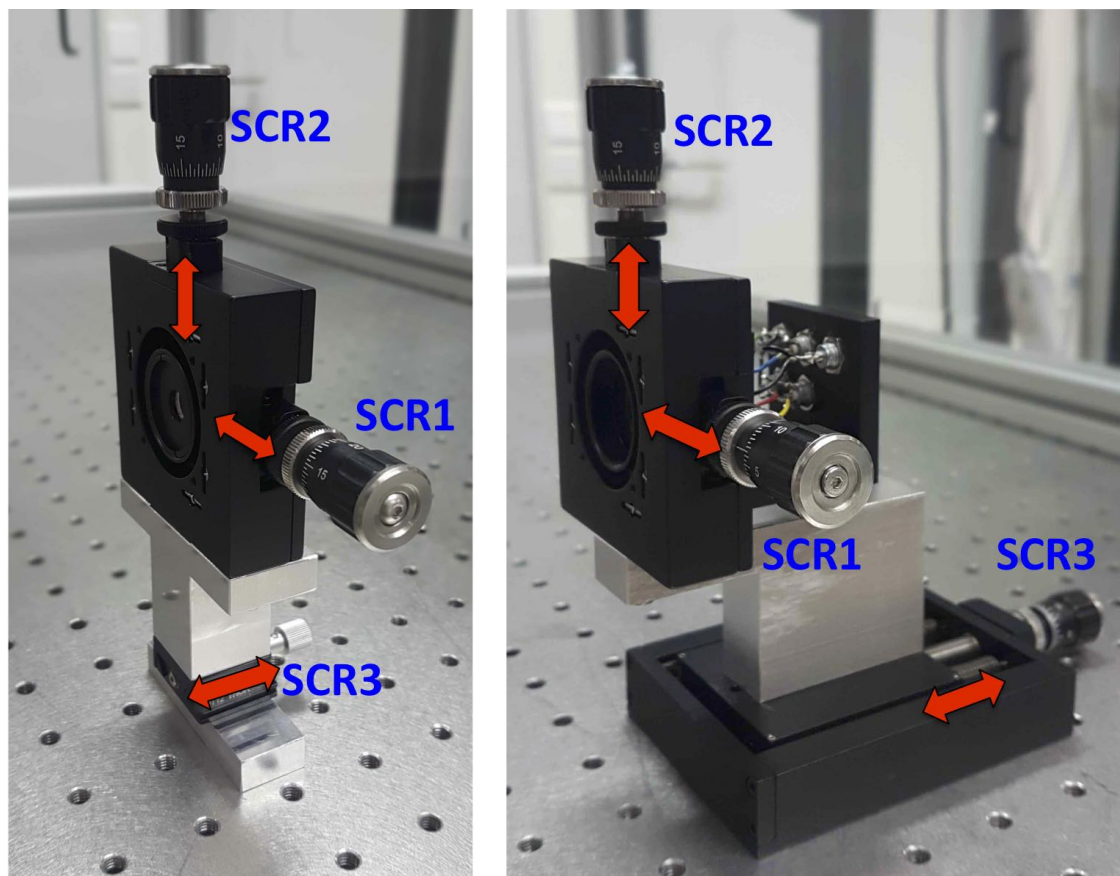
In principle, alignment for the imaging system involves 5-DOF for each lens (the lenses are circular symmetric): three displacements and two rotations for yaw and pitch. However, the angular alignment of each lens with high precision is not a simple task. The main reason is because of the difficulty in diagnosing whether the lens is tilted or not. As one way, a reflected beam from the lens could be used to check its angular alignment of the lens. However, the reflected beam power is too weak particularly because of the anti-reflection coating on the lens surfaces. Another reason is due to the spatial constrain of the imaging system. Specifically, the space between the first and second lens is small about 25 mm such that it is difficult to manufacture a compact mount enabling control in 5-DOF with high precision. Due to these difficulties, only three displacements were considered in the alignment procedure for each lens of the imaging system.

The left picture in Figure 5.3 shows a mounting module for the imaging system's lenses. It consists of a longitudinal translation stage (Thorlab, DT12) that can shift a position along the longitudinal direction and a lens mount (Thorlab, ST1XY-D) being capable of horizontal and vertical alignment. Two manual screws integrated with the lens mount, labelled with SCR1 and SCR2 in Figure 5.3, allow fine control

with  $0.5\ \mu\text{m}$  in the lateral direction. The third screw SCR3 in the longitudinal translation stage installed at the bottom allows the longitudinal shift of  $0.35\ \text{mm}$  per revolution, and its maximum travel length of  $12.7\ \text{mm}$ .

Similar to the lens mount, the mounting module for the QPDs, shown in the right picture of Figure 5.3, allows aligning its position in 3-DOF. The QPD is inserted into the same lateral translation mount used for the lenses, and LEMO connectors linked with the QPD's pins are installed on the mount's rear. The longitudinal position of the QPD can be adjusted by using a linear translation stage (Thorlabs, PT1A-1) installed at the bottom.

The alignment campaign for the two beams and the two-lens imaging system on the TTL coupling experiment was carried out in three steps, as illustrated in



(a) Lens mounting module

(b) QPD mounting module

Figure 5.3: Mounting modules for the imaging system. The left picture shows a mounting module for a lens, consisting of a lateral translation lens mount (Thorlab, ST1XY-D) and a linear translation stage (Thorlab, DT12). Likewise, a mounting module for the QPDs shown on the right-hand side consists of the same lateral translation mount and a linear translation stage (Thorlabs, PT1A-1), which allow alignment in 3-DOF. Two screws, labelled with SCR1 and SCR2 are used for lateral alignment, and SCR3s are used to control longitudinal position for each component.

Figure 5.4. In the first step, the reference and measurement beam was aligned using a pair of QPDs with different arm-lengths (see the upper illustration in Figure 5.4). Using only the measurement beam at first, QPD2 was placed at the nominal position following the imaging system's design, whereas QPD1 was situated where its path-length was about 1 m longer than for QPD2. Then, the manual screws SCR1 and SCR2 for each QPD were adjusted until the DPS signals became minimal so that two measurement beams were aligned at the centre of the two QPDs. Afterwards, the reference beam was aligned by adjusting the two folding mirrors M3 and M4 until the DPS signals on each QPD became minimal.

In the second step, the imaging system's first lens was inserted and aligned in the lateral direction. Since the lateral offset between a beam and the lens's axis causes a deflection of the exiting beam, the SCR1 and SCR2 screws on the lens mount were used for lateral alignment of the first lens until the DPS signal at QPD2 became minimal. QPD1 was then placed from the far-field position to the nominal position in order to make QPD1's arm-length equivalent with QPD2's arm-length. This action was intended to compare two TTL coupling measured via QPD1 and QPD2 under the same arm-length.

In the third step, the second lens was laterally aligned by adjusting the lens mount's two screws SCR1 and SCR2 until the DPS signal measured via QPD2 became minimal. One importance in this step was aligning the second lens in the longitudinal direction. In this work, the lens mount's dimensions, which are relevant to determine the distance between the two lenses, were measured. Then, for positioning the second lens, a metal piece, whose longitudinal length was measured in advanced, was placed between the first and second lens mounts. There might be a deviation in the second lens's longitudinal position during this process due to dimension measurement's errors, which results in the beam walk of the measurement beam on QPD2. For this reason, the second lens's longitudinal position was fine-tuned by using the screw SCR3 of the longitudinal translation stage until minimal beam-walk on QPD2. Simultaneously, the second lens's lateral offset occurred during its longitudinal positioning was adjusted by the screw SCR1 and SCR2.

#### 5.1.4 Electronics

The three testbeds are operated with several electronic devices, as shown in Figure 5.5 that depicts the overall configuration of the experiment.

The phasemeter, developed by Nils Christopher Brause (a former member of AEI) and Thomas Schwarze (AEI), processes the experimental data. It mainly consists of an Analogue to Digital Converter (ADC), a Digital to Analog Converter (DAC) and a Field Programmable Gate Array (FPGA). The ADC converts analogue signals to digital signals and transmits the digital signals to the FPGA. The FPGA is used to process the received digital signals and deliver the data to a computer or the DAC. The DAC converts the received digital signals into analogue signals that can be used as the signal source for driving the ATA.

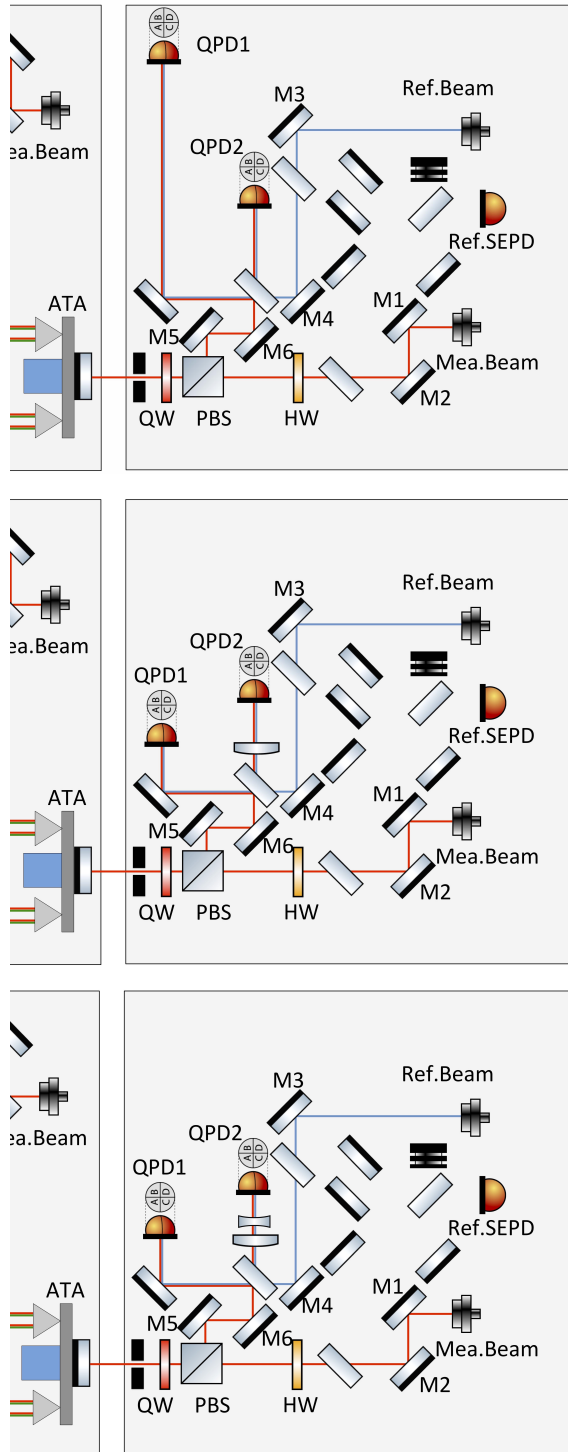


Figure 5.4: *Alignment procedure for the two-lens imaging system. Note that the illustrations of the ATA on the left hand side, not relevant to this alignment, were intentionally clipped on purpose. The alignment for the two-lens imaging system proceeds through three steps. In the first step illustrated on the top, two-beams are aligned by a pair of QPDs having different arm length to each other. In the second step, the first lens is placed at its longitudinal position and laterally aligned until the minimum DPS signal, as shown in the middle. In the third step depicted on the bottom, the second lens is laterally aligned in the same way as the second step, and its longitudinal position is adjusted until the DPS signal becomes minimal.*



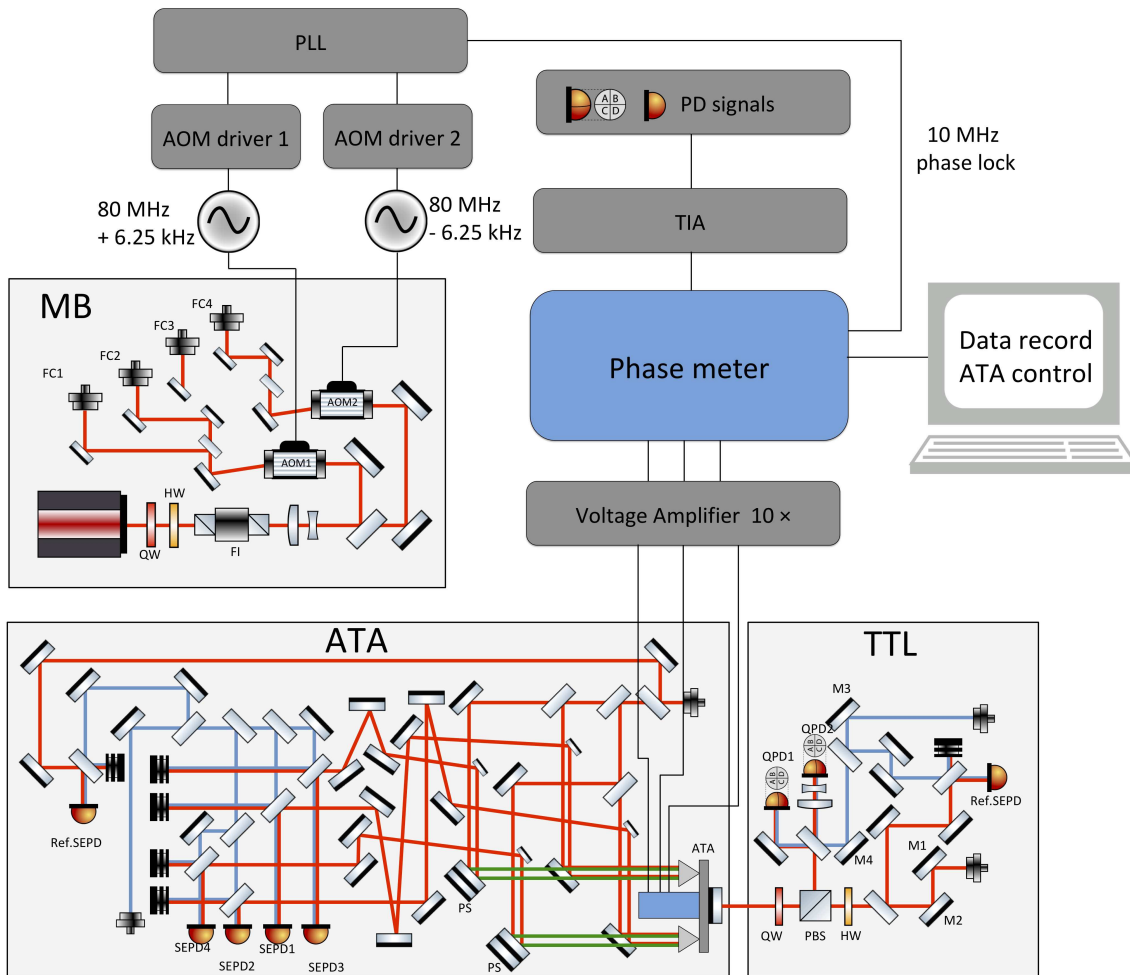


Figure 5.5: Schematic of the three testbeds with electronic devices. Several photodiodes (SEPDs and QPDs), which sense interfering beams, deliver electric currents to a trans-impedance-amplifier (TIA). The TIA converts the received currents to the voltages that are transmitted to a phasemeter. The phasemeter processes the data, interconnecting with a computer that records data and controls the ATA's motion. The voltage signals generated from DAC in the phasemeter are amplified by a factor of ten through a Voltage-Amplifier in order to drive the actuator of the ATA. Two AOM drivers supply RF power to two AOMs, and a phase-locked-loop (PLL) controls the output frequency difference between RF outputs of two AOM drivers.

The process of delivering signals begins with sensing the beams. Several photodiodes (SEPD and QPD), installed in the ATA and TTL coupling experiment, generate electric currents which are proportion to the sensed beams' power. The electric currents are delivered to a Trans-impedance-amplifier (TIA), developed by Germán Fernández Barranco (AEI). The TIA converts the received current into a voltage and transmits it to the phasemeter. Among the available sixteen input channels in the phasemeter, a total of fifteen input channels are used for the whole experiment; eight channels for two QPDs in the TTL coupling experiment, six channels for six SEPDs (five SEPDs in the ATA and a reference SEPD in the TTL coupling experiment), and one channel for the reference signal from the PLL. The phasemeter processes the data and transmits its results to a computer that records phase, DWS, and DPS signals.

The computer records the results from the phasemeter and transmits the digital signals to the phasemeter for operating the ATA. Then, the phasemeter outputs voltages through the DAC that converts the digital signals into analogue signals. Then, the voltage amplifier described in Figure 3.9 amplifies the output voltages from the DAC by a factor of ten. The amplified voltages are distributed to three piezo actuators of the ATA for yaw, pitch and displacement.

Three electronic devices are used in MB for generating the heterodyne beams. Two AOM drivers supply RF signals of approximately 80MHz with 2W of power to each AOM. The PLL interconnected with two AOM drivers locks the RF signal frequency of two AOM drivers via feedback loop control. It introduces the RF signal with the frequency of  $f_1 = 80 \text{ MHz} + 6.25 \text{ kHz}$  for one AOM driver and  $f_1 = 80 \text{ MHz} - 6.25 \text{ kHz}$  for the other AOM driver, resulting in the heterodyne frequency of  $f_{\text{het}} = 12.5 \text{ kHz}$ . The PLL and the phasemeter are interlocked via 10 MHz reference to match the frequency between two devices. Beside, the PLL also delivers a reference signal with 12.5 kHz frequency to the phasemeter.

## 5.2 Preliminary test

Before implementing the TTL coupling experiment, two preliminary tests were carried out. Firstly, to check the beam alignment's stability, a beam-walk on a QPD's surface was measured while the temperature varied. Secondly, the beam parameters, which influence the TTL coupling signals, were characterised. These experiments are described within this section.

### 5.2.1 Beam walk on QPD by temperature effect

Alignment is a critical factor that affects or degrades an interferometer's performance. For instance, lateral offsets between two beams (or between beams and a QPD) introduce an additional path length variation corresponding to first and po-

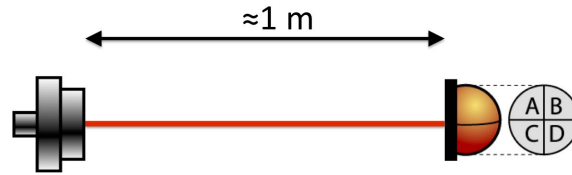


Figure 5.6: *Test setup to measure beam walk on a QPD due to the air temperature variation. The setup consists of a QPD and a fibre coupler, which are used in the TTL coupling experiment. The distance between two components is approximately 1 m, and the beam walk on the QPD is measured by using the DPS signal after its calibration, while the air temperature is recorded.*

tentially also higher-order odd degrees of the beam rotation angle [43], which is not desirable in the TTL coupling experiment. To avoid this effect, the beams or QPDs need to be precisely aligned in the setup, but also they should be stable and less influenced by external conditions.

In an attempt to reduce the influence from the external conditions, several acrylic windows were used to shield the optical table hosting the MB, ATA and TTL coupling experiment. Despite shielding the optical table, the DPS signal's drift was observed after aligning the two beams in the TTL coupling experiment, which implied that the beams' alignment was unstable. It was presumed that optical mounts in the TTL coupling experiment might be influenced by temperature variation. For examining its influence on beam alignment stability, a beam-walk on a QPD is monitored while the air temperature varied.

As shown in Figure 5.6, the experimental setup for testing the beam-walk consists of the fibre collimator and a QPD. The fibre collimator (60FC-4-A6.2S-03, Schäfter + Kirchoff GmbH), taken from the TTL coupling experiment, generates a Gaussian-beam with a diameter of approximately 1.2 mm. The QPD that is shown on the right of Figure 5.3 was placed one metre away from the fibre collimator and measures the DPS signal. This test was set up on the optical table where the experiments are performed. By removing the acrylic windows that shield the optical table, the test setup was intentionally more exposed to the outer air, expecting an increased variation of air temperature.

Note that this test was performed with only a single beam to measure the DPS. To measure the beam-walk on the QPD, the DPS signal needs to be calibrated. Hence, the QPD was laterally shifted in several steps by means of the lateral translation mount's two screws SCR1 and SCR2 shown in Figure 5.3, and the DPS signals were measured in each step. Then, the measured DPS signals were linearly fitted with the lateral the QPD's lateral shifts.

## Test result

Since the lab's air temperature did not rapidly vary in a short period, the measurement was conducted for a total of 4000 minutes. In Figure 5.7, the red curve indicates the recorded temperature variation with the resolution of 0.1 degrees, and

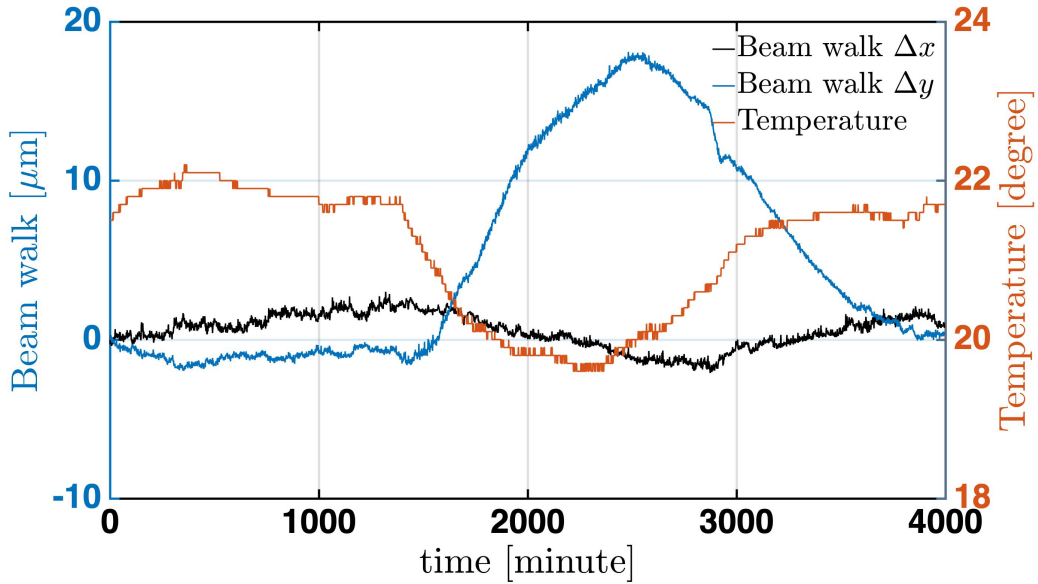


Figure 5.7: Test result for correlation between beam walk and air temperature variation. A red line on the plot shows temperature variation, and blue and black lines indicate beam walk along a horizontal and vertical direction, respectively. While air temperature had been fluctuating between 20 and 22 degrees, beam walk on the QPD was observed, which was significantly stronger in vertical direction than in horizontal direction.

the black and blue curve represents the beam-walk on the QPD along the horizontal and vertical direction, respectively. While the air temperature decreased by approximately two degrees in between 1300 and 3000 minutes, the beam-walk of about  $20\ \mu\text{m}$  in the vertical direction was observed. In the meantime, the beam-walk in the horizontal direction was relatively small about  $4\ \mu\text{m}$ .

The test result shows the correlation between the beam-walk and the air temperature, meaning that the air temperature variation might cause the misalignment of the interferometer setup. However, it provides limited information accompanied by many uncertainties. Firstly, the origin of the observed beam-walk is unknown. It is indistinguishable whether the observed beam-walk in this test was due to the QPD's movement or the beam's movement. Also, it is unknown whether the beam-walk was caused by the mechanical mounts' thermal expansion or thermal deformation due to temperature variation. Additionally, the beam walk might also be caused by the lateral shift of the lens of the fibre collimator due to its mechanical instability, which deflects the exiting beam. Secondly, it is unclear whether the measured beam-walk was due to a beam's lateral shift or tilt. To distinguish a cause between the beam's lateral shift and tilt, it would require installing an additional QPD with a different arm length, either measuring the DPS signal and the DWS signal together by employing interfering beams.

## Countermeasure against the misalignment due to temperature variation

The test result reveals that the temperature fluctuation leads to the misalignment of the beams. However, the observed beam-walk does not change rapidly, but changes rather slowly. In the actual TTL coupling experiment, data recording is performed for just a few minutes, so it is expected that the beam drift during the measurement would not be significant. However, from a long-term perspective, this causes an inconvenience that two interfering beams have to be regularly realigned. The alignment method described in Figure 5.4 is inadequate to be adopted for the regular realignment because it forces to disassemble the imaging system. Instead, the two interfering beams were regularly realigned by using the DPS and DWS signals. While allowing only the reference beam, the lateral positions of the two QPDs were adjusted until the DPS signals became minimal so that the reference beam could be placed on the centre of the QPDs. Afterwards, for aligning the measurement beam, the two folding mirrors M5 and M6, shown in Figure 5.4, were adjusted until the DPS and DWS signal became minimal again.

### 5.2.2 Beam parameter measurement

Beam parameters for both interfering beams influence TTL coupling. In particular, the reduction of TTL coupling through the imaging system depends not only on the imaging system's design parameter but also on the two beams' parameters. Being able to generate beams with the desired beam parameters can bring significant advantages in performing various TTL coupling experiments.

However, producing the desired beam is challenging in reality. Each fibre coupler installed in the TTL coupling experiment contains an aspherical lens that can be shifted in only the longitudinal direction. Shifting the aspherical lens can modify the beam parameter in some degree, but it is not sufficient to acquire the fully desired beam. Another approach is employing an optical lens system in front of the fibre couplers, which alters the beams' properties such as the waist size and its location. However, it involves some difficulties, such as mechanical stability or alignment for multiple lenses.

For these reasons, instead of an attempt to modify the beam's parameters, we accepted the two beams generated by the fibre couplers used in the TTL coupling experiment and measured their beam parameters. By applying the measured beam parameters into the IfoCAD simulations, path length signals with and without the two-lens imaging system were computed, and their results were compared with experimental results, which will be discussed in Chapter 5.3.2.3

The principle of measuring beam parameters is based on scanning a beam's intensity profile at multiple positions along the beam's propagation direction. By applying Gaussian fitting to the measured beam size at the multiple positions, the measuring beam's waist size and waist position can be calculated. A beam profiler (DataRay, DAT-WinCamD-LCM) based on a CMOS sensor was used in this

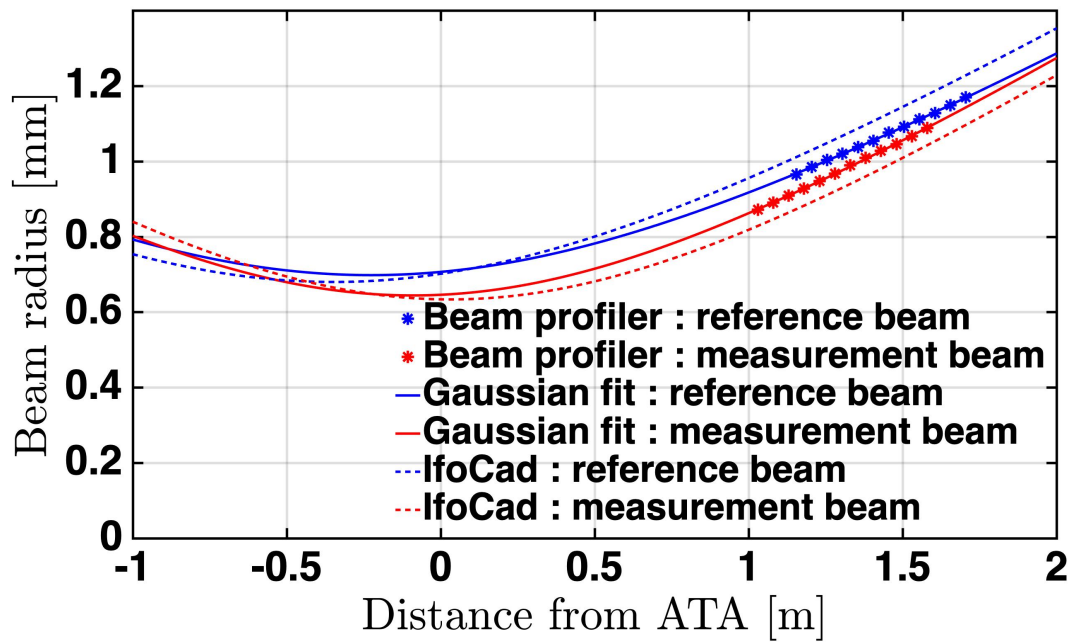
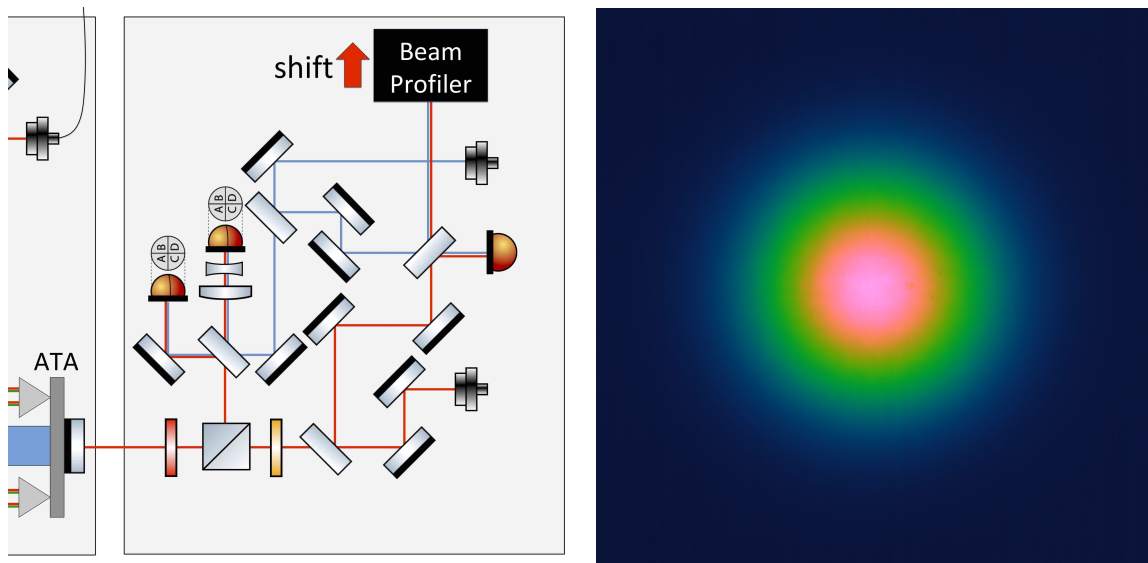


Figure 5.8: *Beam parameter measurement for the TTL coupling experiment. As illustrated on the upper left (the ATA's left part, not relevant to this beam measurement, was intentionally clipped), a beam profiler scans the intensity profiles of the two beams at multiple positions in the TTL coupling experiment. The upper right picture shows a Gaussian beam profile that is measure by the beam profiler. The bottom plot presents beam radii on the distance from the ATA's mirror. Blue and red lines respectively represent the reference and measurement beams. Measured beams by the beam profiler are marked with asterisk symbols, and those Gaussian fitting are plotted with solid lines. Besides, dashed lines indicate two beams applied into the IfoCAD simulation to compare the experimental result of TTL coupling with simulation, which will be explained in Chapter 5.3.2.3.*

measurement. Scanning the beam’s intensity profile was carried out at the reference interferometer’s redundant port as shown on the upper-left of Figure 5.8. The upper-right picture in Figure 5.8 is an intensity profile of the beam measured by the beam profiler, which shows a typical Gaussian beam distribution.

The bottom plot in Figure 5.8 shows the beams’ half-profile along its propagation direction. The x-axis stands for the measurement position of the beams from the ATA’s flat mirror, taking into account each beam’s optical path length. The beam’s profiles were scanned at 5 cm intervals. The y-axis is the beam radius at which the optical intensity drops to  $1/e^2$  ( $\approx 13.5\%$ ) of the value on the centre. The red and blue curves represent the measurement and reference beam, respectively. The beams measured by the beam profile are indicated by asterisk marks, and their Gaussian fitted results are plotted with solid lines.

The dashed lines in Figure 5.8 represent two beams used in IfoCAD simulations whose results were compared with the TTL coupling measured in the experiment. These simulations were conducted for the purpose of supporting the experimental results. In the actual experimental setup, the radius curvatures of the lenses of the imaging system, the position of the lenses and the QPDs, and the beam parameters are factors that influence the TTL coupling result, and their values may contain a certain amount of errors with respect to the values that we know. Considering the margins for these variables, the simulation results matching with the experimental results were computed through optimisation. Details regarding this comparison are given in Chapter 5.3.2.3.

The beams’ waist radius and waist position depicted on the bottom of Figure 5.8 are listed in Table 5.1, where ‘Gaussian fit’ denotes beam parameters resulted from the Gaussian fitting, and ‘IfoCAD’ signifies the beam parameters applied into the IfoCAD simulation.

Table 5.1: *Beam parameters for the TTL coupling experiment. ‘Gaussian fit’ for the measurement and reference beams in this table refer the result of beams’ waist position and radius from applying the Gaussian fit to the measured beam size at multiple positions. ‘IfoCAD’ in this table means the beam’s parameters used in IfoCAD simulation for comparing its TTL coupling computation with the measured TTL coupling in experiment, which will be discussed in Chapter 5.3.2.3.*

	Unit	Beam waist position	Beam waist radius
Mea-beam(Gaussian fit)	mm	-90.356	0.644150
Ref-beam(Gaussian fit)	mm	-226.454	0.697996
Mea-beam(IfoCAD)	mm	31.1563	0.633602
Ref-beam(IfoCAD)	mm	-347.603	0.679895

## 5.3 Experimental result

This section covers three kinds of experiments and their experimental results. In the first experiment, the longitudinal displacement measured by using three retroreflectors is compared with the fourth retroreflector's longitudinal displacement readout, applying the calibration method demonstrated in Chapter 4.3.1. In the second experiment, two path length readouts measured with and without the two-lens imaging system in the TTL coupling experiment are compared to verify the TTL coupling suppression via the imaging system. In the third experiment, the ATA's angular readouts are compared with the DWS signals measured in the TTL coupling experiment. The first and second experiment are interrelated. The third experiment is independent of them and shows the possibility of applying the ATA to future experiments for angular measurements.

### 5.3.1 Longitudinal displacement calibration

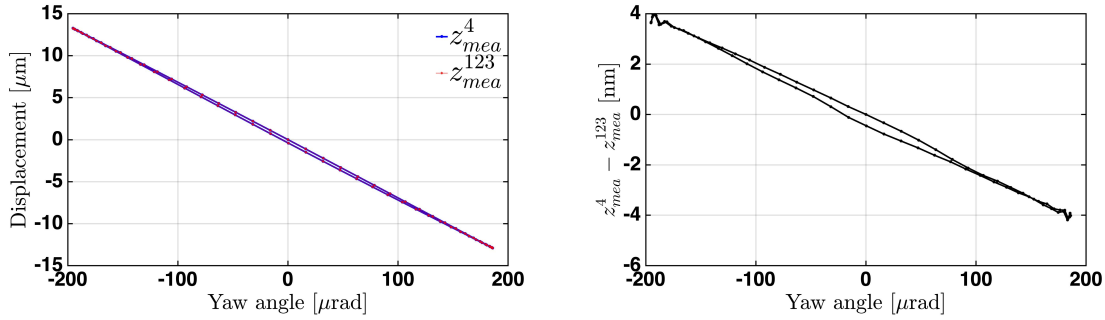
The ATA's most crucial role is to decouple a parasitic longitudinal displacement of the actuator from the measured path length signal. As discussed in Chapter 4.3, the core of the calibration strategy is to intentionally introduce the error that counteracts the ATA's longitudinal displacement readout error through tuning the measurement point. One way to confirm this strategy is to take the longitudinal displacement readout from the fourth interferometer as a reference (denoted by ' $z_{\text{mea}}^4$ ') and compare its result with the other longitudinal displacement measured by using other three retroreflectors (denoted by ' $z_{\text{mea}}^{123}$ '). This section presents the experimental result that compares the two longitudinal displacement readouts, following the calibration strategy discussed in Chapter 4.3.

In the experiment, the ATA was driven in open-loop control, and the yaw was the main rotation. For the computation of the longitudinal displacement, the vertex positions of the retroreflectors listed in Table 3.1, which were measured by the CMM, were used. To eliminate the noise in the displacement readout of each interferometer due to external disturbances, the coherent-filtering technique applies to the data containing multiple periods of rotation of the ATA [44, 53].

As the first step,  $z_{\text{mea}}^{123}$  and  $z_{\text{mea}}^4$  against the ATA's yaw rotation angle are compared on the left-hand side of Figure 5.9, before calibration. The two graphs seem to be almost overlapped in the plot, which means that the two readouts agree well with each other on the micrometres scale. While the ATA rotates by  $\pm 200$   $\mu\text{rad}$ , the fourth retroreflector's vertex longitudinally moves from  $-13$  to  $13$   $\mu\text{m}$ .

For checking how much both results match, the difference between the two readouts is plotted on the right-hand side of Figure 5.9. As a result, the  $\pm 4$  nm difference between the two longitudinal displacement readouts were observed. Similar to the simulation result shown in Figure 4.17, the experimental result reveals the linear slope as well as hysteresis in the longitudinal displacement readout error, which is attributed to the several misalignments discussed in Chapter 4.





(a) Comparison between two LD readouts from fourth retroreflector and using the three retroreflectors

(b) Difference between two LD readouts from fourth retroreflector and using the three retroreflectors

Figure 5.9: The ATA's two longitudinal displacements measured in the experiment. On the left-hand side, a red curve represents  $z_{\text{mea}}^{123}$  signal measured by using the three retroreflectors, and a blue curve indicates  $z_{\text{mea}}^4$  signal measured by the fourth retroreflector. Both curves are overlapping, which means that the two readouts match in the micrometre scale. A plot on the right-hand side shows the difference between the two readouts while the ATA rotates around  $\pm 200 \mu\text{rad}$ .

Taking the measured  $z_{\text{mea}}^4$  as a reference, the error of  $z_{\text{mea}}^{123}$ , shown in the right plot of Figure 5.9, was calibrated through tuning the measurement point as the calibration method discussed in Chapter 4.3.1, which is based on introducing error that counteracts the ATA's longitudinal displacement error. The initial measurement point for  $z_{\text{mea}}^{123}$  was set to  $x_{\text{mea}} = 59.446 \text{ mm}$  and  $y_{\text{mea}} = 60.893 \text{ mm}$ . Then, the  $y_{\text{mea}}$  of the measurement point was tuned. Figure 5.10 shows variations of  $z_{\text{mea}}^{123}$ 's error with tuning the  $y_{\text{mea}}$  at  $40 \mu\text{m}$  intervals. The green curve represents  $z_{\text{mea}}^{123}$ 's error at the initial measurement point. When the  $y_{\text{mea}}$  was tuned to  $60.919 \text{ mm}$ , the hysteresis error of  $z_{\text{mea}}^{123}$  could be suppressed (red curve in Figure 5.10).

The next step is tuning the  $x_{\text{mea}}$  to mitigate the residual linear error. The  $x_{\text{mea}}$  begins with  $59.446 \text{ mm}$  as nominal value and is gradually tuned until the linear error disappears. The variations of  $z_{\text{mea}}^{123}$  error along with tuning x-values is plotted in Figure 5.11, which shows a green curve for  $x_{\text{mea}} = 59.446 \text{ mm}$ , a blue curve for  $x_{\text{mea}} = 59.454 \text{ mm}$  and a red curve for  $x_{\text{mea}} = 59.4633 \text{ mm}$ . As can be seen, the slope of the linear error gradually decreases as shifting the measurement point's x-value. When the  $x_{\text{mea}}$  is tuned to  $59.4633 \text{ mm}$ , the slope of  $z_{\text{mea}}^{123}$  error could be mitigated, which implies that  $z_{\text{mea}}^{123}$  gets closer to  $z_{\text{mea}}^4$ .

The best result plotted by the red curve is enlarged in Figure 5.12. As the result of the calibration,  $z_{\text{mea}}^{123}$ 's residual error could be reduced to the range between  $-200 \text{ pm}$  and  $100 \text{ pm}$  while the ATA rotates around  $\pm 200 \mu\text{rad}$ . This residual error seems to be noise rather than a simple hysteresis or linear error, and its origin has not been identified yet. This residual error can be interpreted as the accuracy limitation of the current ATA for longitudinal displacement measurement.

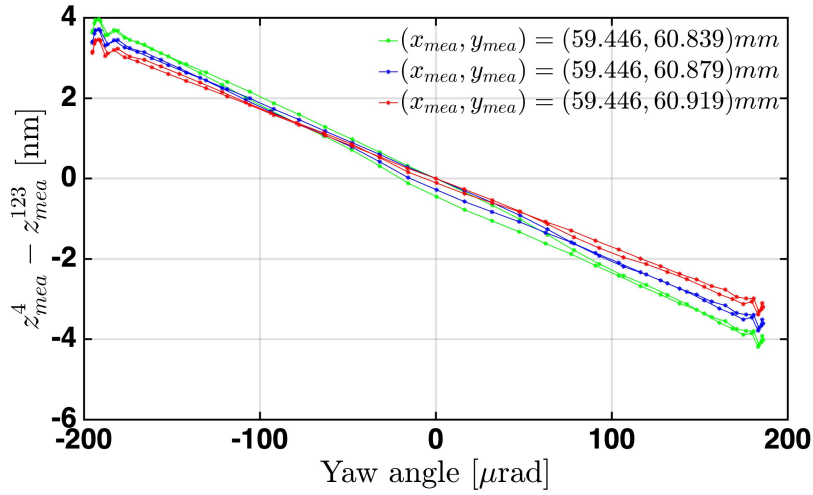


Figure 5.10: *Mitigating hysteresis of  $z_{mea}^{123}$  by tuning the measurement point's  $y$ -value.  $x_{mea}$  and  $y_{mea}$  stand for  $x$  and  $y$ -value of the measurement point of the ATA. The  $y$ -value is tuned from its nominal position of 60.839 mm at 40-micrometre intervals. When the  $x_{mea}$  equals to 60.919 mm as plotted with a red curve, the hysteresis of  $z_{mea}^{123}$  error is mitigated.*

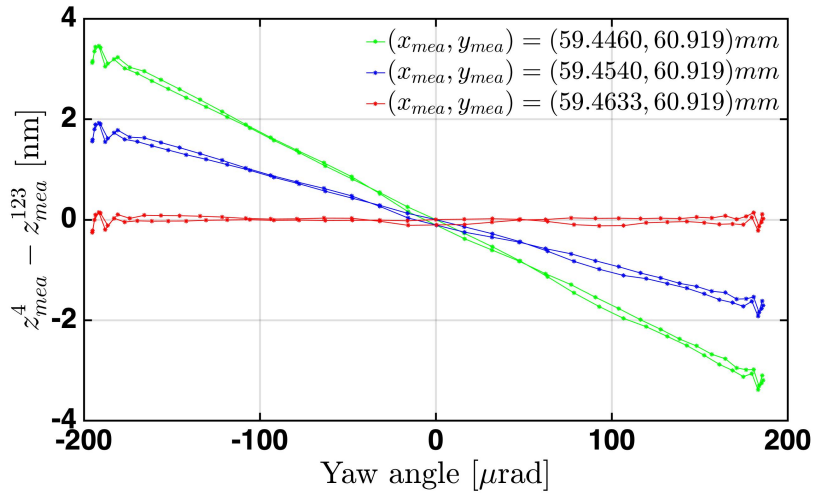


Figure 5.11: *Reduction of residual linear error of  $z_{mea}^{123}$ . Tuning  $x$ -value of the measurement point leads to a decrease in the slope of the linear error of  $z_{mea}^{123}$ , showing a green curve for  $x_{mea} = 59.446$  mm, a blue curve for  $x_{mea} = 59.454$  mm and red for  $x_{mea} = 59.4633$  mm. When  $x_{mea}$  equals to 59.4633 mm, the slope of linear error becomes flat, meaning  $z_{mea}^{123}$  is close to  $z_{mea}^4$  that is a reference.*

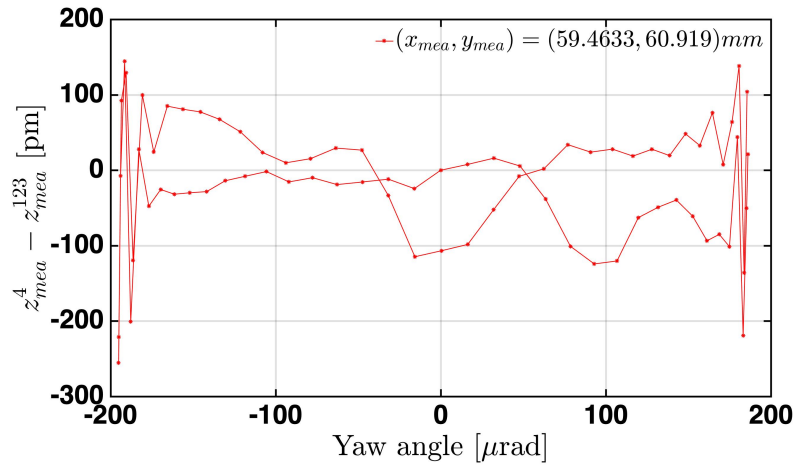


Figure 5.12: Final  $z_{mea}^{123}$  error after calibration.  $z_{mea}^{123}$  error after the calibration based on tuning the measurement point for the ATA could be reduced in the range from  $-200$  pm to  $100$  pm under the ATA rotation angle of around  $\pm 200$   $\mu$ rad. Residual error of  $z_{mea}^{123}$  signal implies the accuracy limitation of the ATA for the TTL coupling experiment.

## Summary

In this experiment, we applied the calibration strategy to the ATA's longitudinal displacement readout, as discussed in Chapter 4.3.1. Regarding the fourth retroreflector's displacement readout as reference, the longitudinal displacement measured by using the other three retroreflectors was calibrated by tuning the measurement point, which induces error that counteracts the longitudinal displacement readout error. The final experimental result exhibits that the ATA's longitudinal displacement readout error after the calibration could be reduced in the range of  $-200$  pm to  $100$  pm. In order to reduce the residual error in the ATA's longitudinal displacement readout, a more detailed investigation and in-depth analysis are required.

### 5.3.2 TTL coupling and its reduction with imaging system

From the two measurement interferometers in the TTL coupling experiment, one includes a two-lens imaging system, but the other does not. This allows a direct test how much the imaging system suppresses the TTL coupling. This section reports experimental results that show reducing of the TTL coupling via the two-lens imaging system, comparing the two path length readouts from both measurement interferometers. Besides, a method for further reduction of residual TTL coupling measured with the two-lens imaging system will be explained.

The ATA's primary purpose for TTL coupling investigations is to disentangle the actuator's parasitic longitudinal displacement that disturbs characterising the

TTL coupling signal. To achieve this, the ATA should measure the longitudinal displacement as precisely as possible. The experimental result shown in Chapter 5.3.1 proved to measure the longitudinal displacement with the measurement error below  $\pm 100$   $\mu\text{m}$ .

However, this measurement corresponds to the fourth retroreflector, not the BRP on the mirror surface. Unfortunately, there is no additional retroreflector whose vertex coincides with the measurement beam's reflection point, implying that a direct measurement of the longitudinal displacement at the BRP is not possible. Not only the BRP offset but also the other misalignments cause the ATA's readout errors, which couples into the path length readout and disturb characterising TTL couplings, as the IfoCAD simulation result shown in Figure 4.15 in Chapter 4.2.2.2.

As an approach to resolve this difficulty, the calibration method based on tuning the measurement point was demonstrated via the IfoCAD simulation in Chapter 4.3.1.2. Firstly, the ATA measures the longitudinal displacement measured at the measurement point that is supposed to be in the vicinity of the BRP. Then, twice the longitudinal displacement is subtracted from the path length signal measured on the other side of the ATA. Expecting that the TTL couplings should be symmetric around the zero of the rotation angle, we tune the ATA's measurement point to counteract the observed linear and hysteresis in the path length.

The path length signals measured at the QPDs in this experiment is defined by an average of phases at four segments and dividing by the wavenumber  $k$ , as presented in Equation (2.19). In addition to the path length signal, the DPS and DWS signals sensed at the two QPDs are recorded. Of the two measurement interferometers, the signals measured without the two-lens imaging system are labelled with '1', and the signals measured with the two-lens imaging system are labelled with '2'.

### 5.3.2.1 Nominal performance

The nominal performance in this section refers to experimental results when QPD2's longitudinal position is located at the two-lens imaging system's conjugate plane, minimising the beam-walk and the optical path length variation for the tilting measurement beam at QPD2.

In this TTL coupling experiment, the ATA was operated in open-loop control. The ATA's three readouts for its motion are plotted in Figure 5.13. The x-axis indicates the yaw angle, and the left-axis represents the pitch angle, and the right-axis stands for the displacement at the origin in the ATA's coordinates. The yaw is the ATA's main rotation in this TTL coupling experiment, and its rotation angle is about  $\pm 200$   $\mu\text{rad}$ . Due to the open-loop control, the residual pitch rotation with a hysteresis (black curve) occurs in the range from  $-10$   $\mu\text{rad}$  to  $6$   $\mu\text{rad}$  during the yaw rotation. Also, the residual displacement (blue curve) simultaneously appears about  $\pm 1.2$   $\mu\text{m}$ .

Relevant to the two beams' alignment, the DWS and DPS signals at both QPDs should be minimal before operating the ATA. For the imaging system's nominal

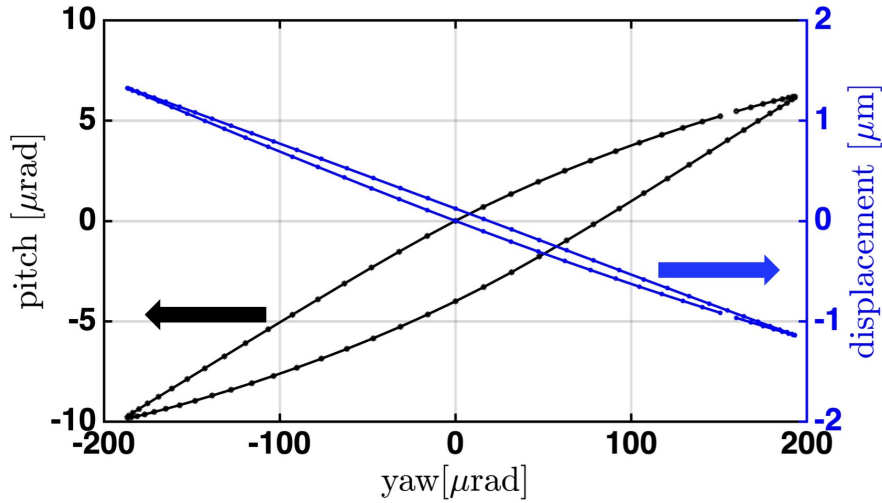
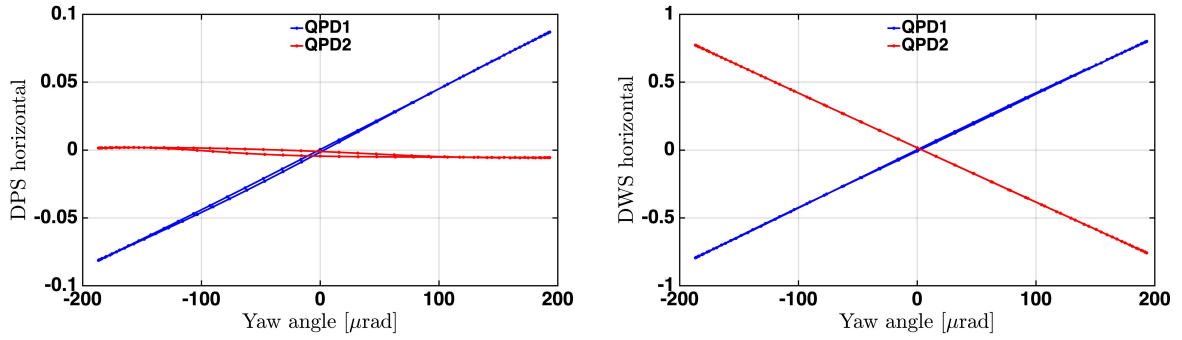


Figure 5.13: *The ATA's motion in 3-DOF for this TTL coupling experiment. Since the ATA is driven in the open-loop control, not only the yaw rotation as the main motion of the ATA but also a residual pitch rotation and displacement appear. The x-axis is the measured yaw rotation angle, the left axis is the pitch rotation angle, and the right axis is the displacement at the origin of the ATA's coordinates. The black curve represents the relation between the yaw and pitch rotation, and the blue curve indicates the relation between the yaw rotation and the displacement.*

performance, the beam walk on QPD2 should be stationary while the ATA rotates, meaning the minimal value of DPS2. The left graph in Figure 5.14 shows the horizontal DPS signals measured from both QPDs during the yaw rotation of about  $\pm 200 \mu\text{rad}$ . DPS1 signal plotted by the blue curve is linear against the ATA's rotation angle. In contrast, DPS2 signal measured with the imaging system is relatively stationary, which means the beam positions on QPD2's surface is kept by the imaging system. The rotation angle's orientation was defined when DWS1 was minimal while the ATA rotated. As shown in the right plot of Figure 5.14, DWS1 and DWS2 signal is minimal at the yaw angle's orientation, which implies that the two beams in each measurement interferometers were angularly well aligned. And they exhibit linear property against the ATA's yaw angle. The two DWS signals' slope against the yaw rotation is opposite direction because two split beams by the beam splitter BS4 (see Figure 5.1) rotate in opposite directions at their QPDs.

The following paragraphs explain the procedure to characterise TTL coupling. First of all, the two path length signals measured at QPD1 and QPD2 were compared with  $2 \times z_{\text{mea}}^{123}$  at a point nearby the BRP on the ATA's mirror. On the top of Figure 5.15, the red and blue curve represents the path length readouts from QPD1 and QPD2 respectively. The black curve indicates twice the ATA's longitudinal displacement  $z_{\text{mea}}^{123}$  at  $x_{\text{mea}} = -3 \text{ mm}$  and  $y_{\text{mea}} = -64 \text{ mm}$ .

There are a few notable features to discuss in the upper graph. Firstly, a strong



(a) Two DPS signals against the yaw angle      (b) Two QPD signals against the yaw angle

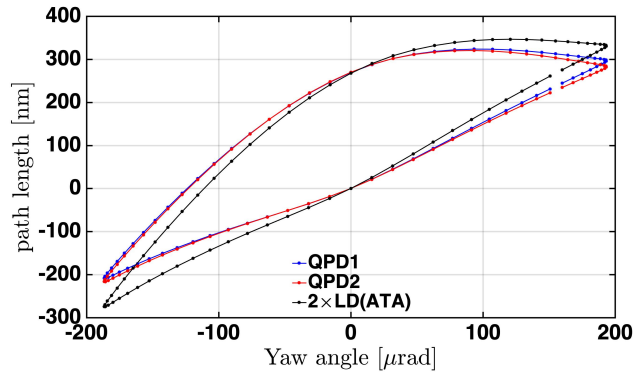
Figure 5.14: *The measured DPS and DWS signals at QPD1 and QPD2. The blue curves represent signals measured at QPD1, and the red curves indicate signals via QPD2. DPS1 shows a linear slope against the ATA’s yaw rotation angle, where DPS2 is stationary. The two DWS signals are linear to the rotation angle. The opposite direction of the two DWS signals is due to the counter direction of two tilting beams split at ‘BS4’ beamsplitter shown in Figure 5.1.*

hysteresis in both path length signal is observed in the order of a few hundred nanometres. The cause of this hysteresis could be demonstrated by the ATA’s pitch rotation and displacement in its motion. The flat mirror attached to the ATA is vertically about 60 mm away from the origin of the ATA coordinates. As plotted in Figure 5.13, the pitch rotation in the ATA’s motion shows the hysteresis with respect to the yaw rotation. Hence, the residual pitch angle when the yaw angle is zero causes the hysteresis of the path length signals. Likewise, the ATA’s displacement also exhibits a hysteresis characteristic with respect to the yaw rotation (see Figure 5.13). So, the displacement motion’s hysteresis also contributes to the hysteresis observed in the top plot of Figure 5.15.

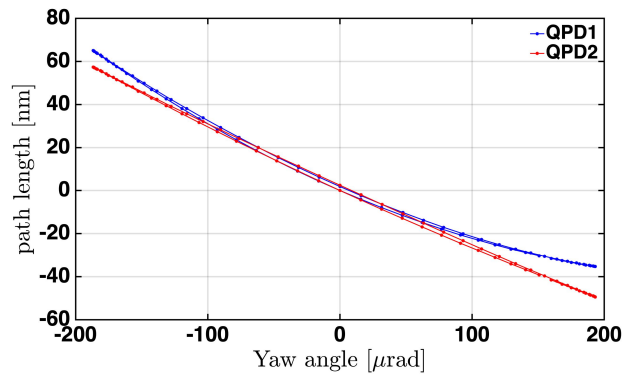
Secondly, another prominent feature in the top graph of Figure 5.15 is that the two path length signals are almost the same on a large scale. It can be interpreted that the ATA’s longitudinal displacement at the BRP equally contributes to the two path length readouts. From these path length signals themselves, it is not simple to characterise TTL coupling, meaning that the longitudinal displacement should be decoupled from the path length signals.

Thirdly, the ATA’s longitudinal displacement’s black curve is similar to the path length signals measured in the TTL coupling experiment. It demonstrates that the significant path length variation with the hysteresis was mainly due to the ATA’s longitudinal displacement. However, it is slightly inclined and does not fully match the two path length readouts. This discrepancy implies that the ATA’s longitudinal displacement readout contains an error due to the various misalignment. In particular, the lateral offset between the BRP and the measurement point is presumed to be the main cause of the discrepancy.

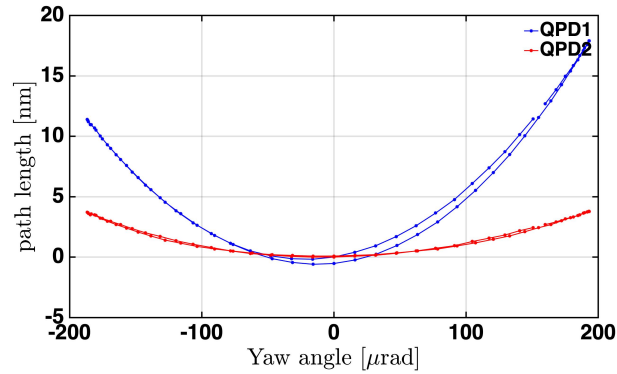
From the above analysis, we can deduce that the significant path length variation



(a) Raw path length signals



(b) Residual path length after subtraction of ATA's LD readout



(c) Path length after calibration

Figure 5.15: Measured path length signals before and after subtracting the ATA's longitudinal displacement. The upper plot shows the initial path length signals measured with and without the imaging system in the TTL coupling experiment, as well as the measured longitudinal displacement of the ATA at  $x_{mea} = -3$  mm and  $y_{mea} = -64$  mm. The graph in the middle shows the same pathlength signals, but after subtracting  $2 \times z_{mea}^{123}$ . The residual TTL signal is almost free of hysteresis but shows an apparent linear coupling. Finally, the bottom graph is identical to the middle one, except that the ATA's measurement point was shifted to  $x_{mea} = -3.1282$  mm and  $y_{mea} = -64.295$  mm. As a result, the path length readout without imaging system (blue curve) increases up to around 18 nm, whereas the path length readout with the imaging system (red curve) is below 4 nm.

is due to the actuator's longitudinal displacement at the BRP. Hence, the ATA's longitudinal displacement (more specifically,  $2 \times z_{\text{mea}}^{123}$  indicated by the black curve in the upper plot) was subtracted from the two path length signals (blue and red curve). After the subtraction, the hysteresis in both path length readouts is significantly mitigated, as shown in the middle of Figure 5.15. However, there are still small residual hysteresis and linear path length readout. As discussed above, this residual path length is caused by the ATA's longitudinal displacement readout error due to the various misalignments. It is presumed that the lateral offset between the BRP and the measurement point or the retroreflectors' lateral offset may be the main cause of the longitudinal displacement error, as analysed via the simulations in Chapter 4.3.1.3.

The simulations in Chapter 4.3.1.2 demonstrated the calibration method on how to suppress the residual TTL coupling. The principle of the calibration is based on intentionally introducing more path length that cancels out the residual TTL coupling through tuning the measurement point. This calibration method was already applied to the experiment in Chapter 5.3.1, which compared the two longitudinal displacement readout in the ATA.

Likewise, the ATA's measurement point was optimally tuned to reduce the residual path length shown in the middle plot of Figure 5.15. In this procedure, we took the path length readout measured with the imaging system, and its residual slope and hysteresis were minimised via tuning  $x_{\text{mea}}$  and  $y_{\text{mea}}$ . When the measurement point for  $z_{\text{mea}}^{123}$  was tuned to  $x_{\text{mea}} = -3.1282$  mm and  $y_{\text{mea}} = -64.295$  mm, the linear slope and hysteresis error in the path length signal from QPD2 is significantly reduced as shown in the bottom plot of Figure 5.15. Denoting the final path length readouts by  $S_{\text{LPS1}}$  and  $S_{\text{LPS2}}$ , the  $S_{\text{LPS1}}$  (blue curve) varies up to 18 nm. On the other hand, the  $S_{\text{LPS2}}$  (red curve) measured with the imaging system is below 4 nm in the yaw rotation angle of  $\pm 200$   $\mu\text{rad}$ .

As a way to evaluate the experimental results, the slopes of the path length signals  $S_{\text{LPS1}}$  and  $S_{\text{LPS2}}$  were plotted in Figure 5.16, comparing with the LISA requirement (colour box area) that the path length slope should be less than 25  $\mu\text{m}/\text{rad}$  in the beam rotation angle of 300  $\mu\text{rad}$ . The path length slopes were computed via the robust local regression of eleven neighbouring data points on each data point. Note that the x-axis in Figure 5.16 was altered to the beam rotation angles for the sake of the norm that the LISA requirement uses a rotating beam angle, thus we multiplied the ATA's rotation angle by a factor of two. The path length slope without the imaging system, plotted with a blue curve, exceeds the LISA requirement. On the other hand, the path length slope with the imaging system, plotted with a red curve, fulfils the LISA requirement, showing approximately 17  $\mu\text{m}/\text{rad}$  at 300  $\mu\text{rad}$  beam angle.

### Limitations of the calibration and discussion

As discussed in Chapter 4.3.1.4, instead of correcting the ATA's three readout errors, the calibration method applied in this experiment counteracts the residual TTL coupling by inducing additional path length or longitudinal displacement. The



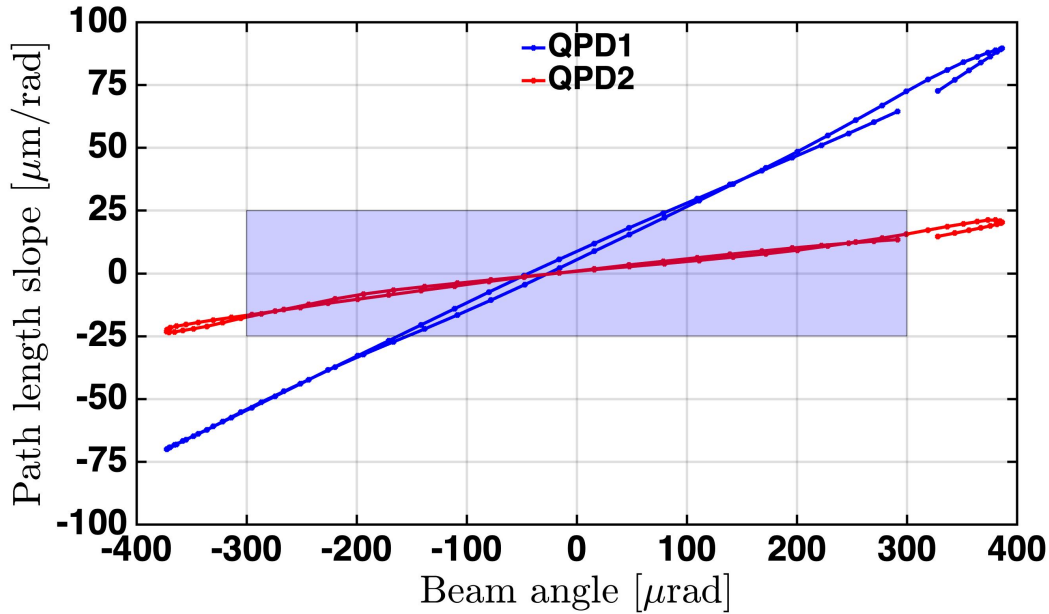


Figure 5.16: *The measured path length slopes in comparison with the LISA requirement. The slopes of the path lengths  $S_{LPS1}$  and  $S_{LPS2}$ , shown in the bottom plot of Figure 5.15, are indicated by the blue and red curve, respectively. The two curves, which are the derivative of  $S_{LPS1}$  and  $S_{LPS2}$ , were computed via the robust local regression of eleven neighbouring data points on each data point. The x-axis was converted from the ATA's rotation angle to the beam rotation angle. The colour box that represents the LISA requirement is drawn in order to compare with the slopes of  $S_{LPS1}$  and  $S_{LPS2}$ . The path length slope without imaging system deviates from the LISA requirement. In contrast, the path length slope with the imaging system meets the LISA requirement, showing less than  $17\mu\text{m}/\text{rad}$  within  $300\mu\text{rad}$  of the beam rotation angles.*

ATA's readout error, which affects the residual path length measured in the TTL coupling experiment, depends on the actuator's motion. As a result, when the ATA has different movements, the occurring readout error needed to be cancelled out recalibration with a different value of the measurement point.

Second, this calibration method cancels out some part of the TTL coupling. Compared to the TTL coupling under the ideal conditions (two beams are fundamental Gaussian beam, the ATA rotates around the BPR, optimal alignment of beams, lenses, QPD), the experimental results are supposed to contain some addition TTL couplings due to various effects such non-fundamental Gaussian beams, BRP offset, lateral misalignments between the two beams or the QPD, and others. These effects in the experimental setup need to be suppressed as much as possible, but it is challenging to put them under perfect control.

Despite the limitations described in the above paragraphs, the calibration method employed in this experiment is a realistic and effective strategy that copes with many

difficulties encountered in performing TTL coupling experiments. In the above experiment, the measurement results demonstrated that the TTL coupling could be reduced through the imaging system. The slope of the reduced path length readout measured with the imaging system satisfied the LISA requirement. Nevertheless, there are residual path length readouts that have not been completely suppressed by the imaging system. In the following chapter, we will discuss the further reduction of the TTL coupling.

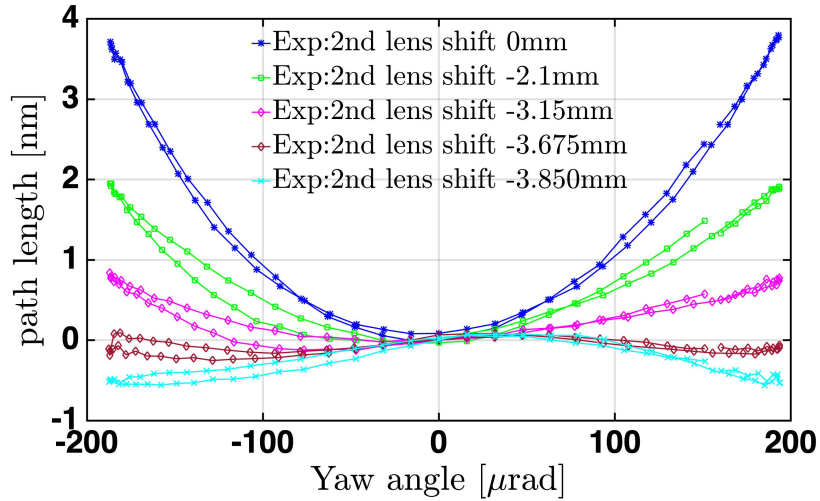
### 5.3.2.2 Further reduction of TTL coupling

The imaging system in the previous section preserves the beam-walk on the centre of QPD2 as well as a variation of optical path length by imaging the beam reflection point on QPD2's surface. Although its performance in the experiment satisfies the LISA requirement, a residual path length remains. This residual is mainly attributed to non-geometrical effects of the TTL coupling. In previous studies, the residual path length could be diminished by adjusting a QPD's position along the lateral and longitudinal direction [23, 43, 54]. An intuitive explanation for this approach is based on cancelling out the residual path length by intentionally inducing an additional TTL coupling. Lateral shift of the QPD introduces a linear TTL coupling, and the QPD's longitudinal shift causes a quadratic TTL coupling. The residual path length signal measured with the imaging system, which is plotted on the bottom of Figure 5.15, shows a quadratic TTL coupling. Therefore, it can be mitigated by the longitudinal shift of QPD2 as done in the previous experiment.

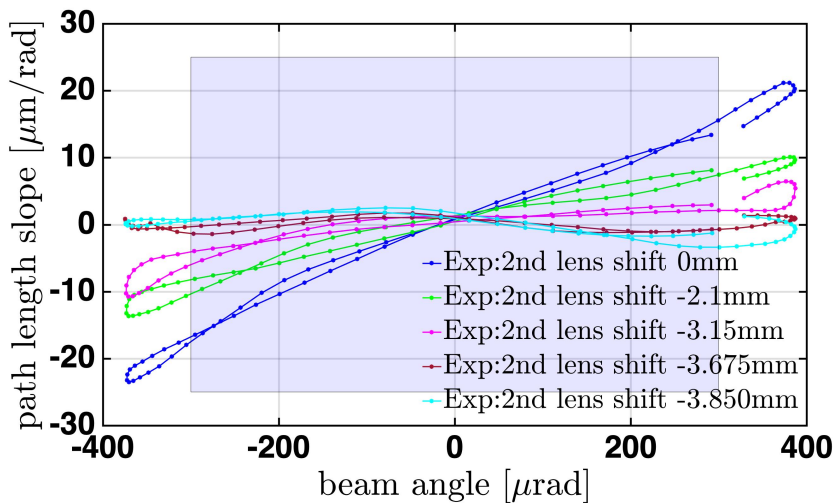
However, instead of longitudinally shifting QPD2, the second lens was longitudinally shifted to further reduce the residual TTL coupling in this thesis. This attempt was initiated due to an inconvenience to shift QPD2 by sufficient distance longitudinally. In an early TTL coupling experiment using the ATA [40], there was an issue that shifting the QPD was interrupted due to a spatial constraint of the QPD's mechanical mount. Although it was possible to resolve the issue by modifying its mechanical design, we attempted to figure out alternative solutions for avoiding the imaging system's realignment and keeping the setup as much as possible. Then, it was found that the second lens's longitudinal shift can bring an equivalent effect as longitudinally shifting the QPD.

To demonstrate this phenomenon, first of all, we discuss the effects of longitudinally shifting the QPD's. This action means the QPD's position deviates from the imaging system's conjugated plane, causing many effects such as increasing (or decreasing) the optical path length of the tilting beam, more beam walk on the QPD, and different beam parameters at the QPD. It is difficult to quantitatively demonstrate each effect's contributions to the TTL coupling's variation. However, it is known that shifting the QPD from the imaging system's conjugated plane induces a quadratic TTL coupling [43, 54]. Likewise, shifting the second lens of the imaging system also leads to deviating the QPD's position from the conjugated plane, which brings about a similar effect of shifting the QPD.

Based on this approach, the imaging system's second lens was gradually shifted along the longitudinal direction towards the first lens to mitigate the residual second order of the path length signal. While longitudinally shifting the second lens



(a) Further reduction of path length by shifting the second lens



(b) Path length slopes with shifting the second lens

Figure 5.17: Further reduction of TTL coupling through longitudinally shifting the second lens of the imaging system. The residual TTL coupling measured in the nominal performance (blue curve) is mitigated by shifting the second lens along with the longitudinal direction. The upper plot shows measured path length readouts with a gradual longitudinal shift of the second lens. The best result (minimum path length readout) appears when the second lens is shifted with 3.675 mm. The bottom plot shows the computed slopes of the path length signals, compared to the LISA requirement of  $25 \mu\text{m}/\text{rad}$  in  $300 \mu\text{rad}$  of beam angles (purple box).

position, a small amount of second lens's lateral shift with respect to the beam was inevitable, deflecting the beams and changing the beam position on QPD2. Hence, the second lens had to be laterally realigned after its longitudinal shift. In the procedure for the longitudinal shift and lateral realignment of the second lens, the only reference beam was used at first, blocking the measurement beam. Before shifting the second lens longitudinally, DPS2 signal was checked whether the reference beam was on the centre of QPD2, then QPD2 was laterally realigned until DPS2 signal was minimal. Then, the second lens was longitudinally shifted by means of the linear translation stage installed on the bottom of the lens mount, as shown on the left of Figure 5.3. After the longitudinal shift, the second lens was laterally realigned by adjusting the two screws 'SCR1' and 'SCR2' shown in the left photograph of Figure 5.3 until DPS2 signal became zero.

Figure 5.17 shows the path length signal measured with gradual shifts of the second lens in the longitudinal direction. The blue curve represents the nominal performance before shifting the second lens. When the second lens was longitudinally shifted by 3.675 mm, the path length signal decreases to a few hundred picometres. By shifting the second lens further, the path length signal varies to a negative value. As shown in the bottom of Figure 5.17, the nominal performance already fulfilled the LISA requirement, but the path length slope could be more significantly mitigated in the order of a few  $\mu\text{m}/\text{rad}$  by longitudinally shifting the lens.

### 5.3.2.3 Comparison between measurement and IfoCAD simulation

In order to support the above experimental results showing that the imaging system reduces the TTL coupling and the residual TTL coupling can be mitigated by longitudinally shifting the second lens, the experimental results need to be compared via IfoCAD simulations. However, there is an important point that has to be considered in implementing comparative simulation. All known parameters relevant to the imaging system are likely to contain a certain degree of deviation despite attempts to construct the imaging system as its design parameters listed in Table 2.2. The deviation may occur due to several reasons such as longitudinal misalignment of each component of the imaging system, manufacturing error of lenses constituting the imaging system, and beam parameters in the experiment.

One way of implementing comparative simulations to the experimental results is to allow all simulation parameters to vary within a certain range around its known values, such that the simulation can yield most consistent results with respect to the experimental results. The purpose of this comparative simulation is not to confirm that each variable obtained through the simulation match with real parameters in the experimental setup, but rather to theoretically demonstrate the measured TTL couplings and its reduction by shifting the second lens.

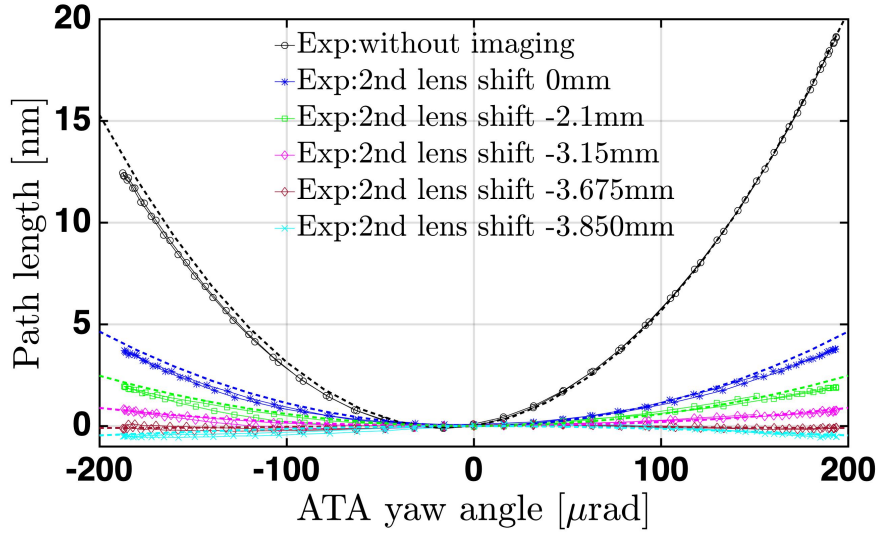
As the preliminary step, we defined variable needed in the simulation. For variables of the imaging system, the radius of curvature for each lens surface, longitudinal positions of the lenses, and QPD2's longitudinal position were considered in the

simulation. Concerning the variables for the two beams, beam waist positions and beam waist radii were taken into account. Based on the initial design parameter for the imaging system listed in Table 2.2 and beam parameter measurement listed in Table 5.1, all variables in the simulation were allowed to vary within some margins. Then, a particle swarm optimisation routine was used to find the best combination of variables which yields corresponding simulation results to the measured TTL coupling.

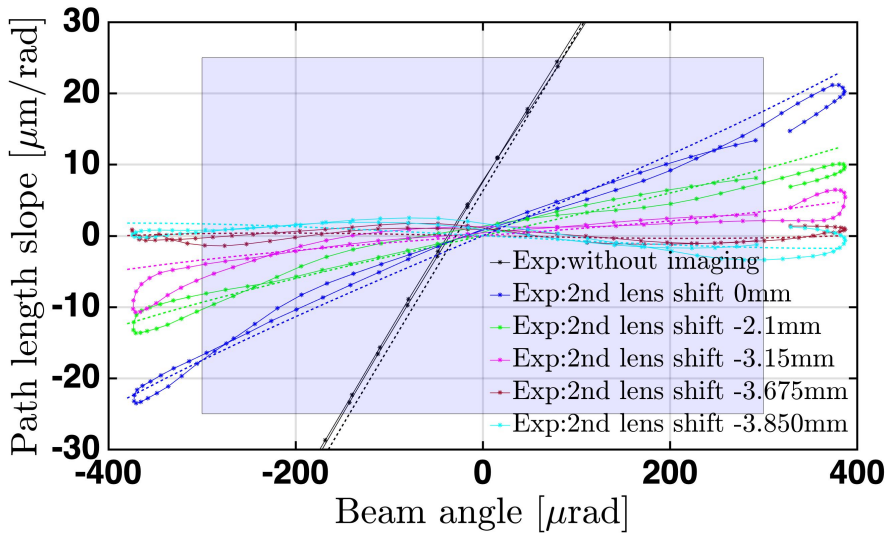
As a result, all parameters obtained through the optimisation process are listed in Table 5.2. Positions for each component are defined as a distance from the ATA's flat mirror. Assuming the two beams in the simulation as fundamental Gaussian beams, the beam parameters resulted from the optimisation are listed in Table 5.1. Also, those beam propagation profiles are plotted in Figure 5.8 to compare with the measured beams' profile and those Gaussian fit. The discrepancy between the simulation's beams and the measured beams' Gaussian fit could be attributed to uncertainty in the beam parameter measurement or the usage of the simple fundamental Gaussian beam in the simulation. Nonetheless, the beams applied into the simulation seem to be reasonable when compared with the measured beams.

Table 5.2: *Applied parameters in IfoCAD simulation for comparison with measured TTL couplings. Parameters found by the described optimisation process, which yield consistent results with respect to the measured TTL coupling as shown in Figure 5.18.*

Parameters	No imaging	With Imaging
Ref-beam waist radius [mm]	0.679895	same
Mea-beam waist radius [mm]	0.633602	same
Ref-beam waist position [mm]	-347.604	same
Mea-beam waist position [mm]	31.1563	same
Radius of curvature front - Lens1 [mm]		20.3851
Radius of curvature rear - Lens1 [mm]		$\infty$
Radius of curvature front - Lens2 [mm]		$\infty$
Radius of curvature rear - Lens2 [mm]		12.9613
Refractive index - Lens1		1.50663
Refractive index - Lens2		1.44963
Thickness - Lens1 [mm]		3
Thickness - Lens2 [mm]		2
Diameter - Lens1 [mm]		12.7
Diameter - Lens2 [mm]		10.0
Position - Lens1 [mm]		343.411
Position - Lens2 [mm]		373.233
Shift Lens2 from initial position [mm]	0, -2.1, -3.15, -3.675, -3.85	
Position - QPD [mm]	435.561	same
QPD diameter [mm]	8	same
QPD slit full-width [mm]	0.018	same
QPD slit lateral shift [mm]	0.011	same



(a) Comparison of path length between measurements and simulation results



(b) Comparison of path length slope between measurements and simulation results

Figure 5.18: TTL coupling comparison between experimental results and IfoCAD simulation. An upper plot shows the path length change depending on the second lens shift. Path length slopes are plotted on the bottom. The dots connected by solid lines indicate experimental data, and the dashed lines represent the IfoCAD simulation results. The purple box in the lower plot stands for the LISA requirement. The simulation results agree with the experimental results for path length readout and its slope.

In Figure 5.18, the results from the IfoCAD simulations (dash curves) are compared with the measured TTL coupling (dots-solid lines). Note that the measured TTL couplings in the graph are identical to the results shown in Figure 5.17. The

TTL coupling without the imaging system was taken from the experimental data performed when the second lens was longitudinally shifted by  $-3.675$  mm. The upper plot in Figure 5.18 shows path length changes depending on the amount of shifting the second lens, and the lower plot represents the slope of path lengths. In the upper plot, path lengths from the simulations match well with the experimental results and demonstrate the suppression of TTL coupling via shifting the second lens as shown as experimental results.

In the absence of the imaging system, the path length signal (black curve) seems to be laterally shifted to the left on the x-axis. It can be interpreted that a linear path length is remaining, which might be caused by a lateral misalignment between beams and the QPD (or between two beams). Based on the assumption that two beams are perfectly overlapped, lateral misalignment of  $11 \mu\text{m}$  between the QPD and the beams was applied into the simulation. Consequently, both results from the simulation and measurement regarding the TTL coupling without the imaging system match well to each other.

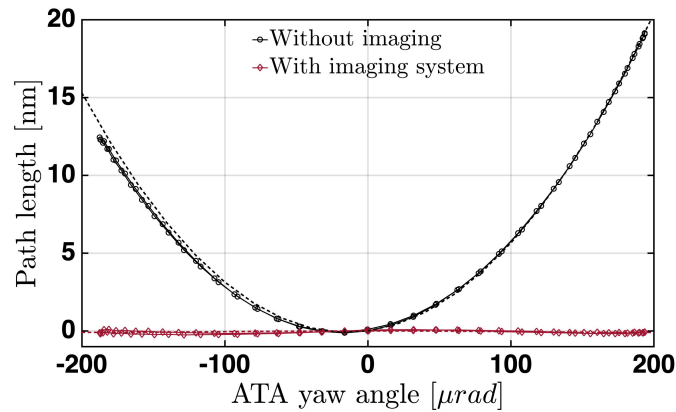
In the lower plot of Figure 5.18, path length slopes from both result are compared. The TTL coupling without the imaging system does not fulfill the LISA requirement. In contrast, all experimental measurements with the imaging system satisfy the LISA requirement, showing less TTL coupling than  $25 \mu\text{m}/\text{rad}$  within the beam tilt range of  $\pm 300 \mu\text{rad}$ . Also, the path length slopes from the simulation are matching to the experimental results for path length slope.

#### 5.3.2.4 Best result

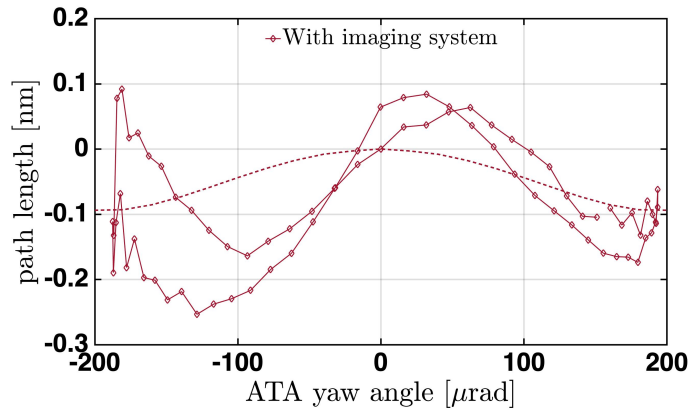
The best result in here refers to the minimum TTL coupling when the second lens was shifted by  $3.675$  mm along the longitudinal direction. In Figure 5.19, the dots-solid lines and the dashed lines indicate experimental results and IfoCAD simulation results respectively. The path length signal in the absence of the imaging system increases up to about  $19 \text{ nm}$  in the ATA's rotation angle of around  $200 \mu\text{rad}$ . The path length signal with the imaging system is flat in the plot.

The reduced TTL coupling is enlarged in the middle plot of Figure 5.19. As can be seen, the imaging system reduces the TTL coupling within  $-250 \text{ pm}$  to  $100 \text{ pm}$  while the ATA rotates by nearly  $200 \mu\text{rad}$ . Unlike quadratic path length in other measurements, the residual TTL coupling in the best performance appears to be fourth order, but is strongly distorted by the residual hysteresis and noisy behaviour at the maximal angles. Its origin has not been identified yet, but it is presumably due to the ATA's limitation regarding its measurement accuracy for the longitudinal displacement, as shown in Figure 5.12.

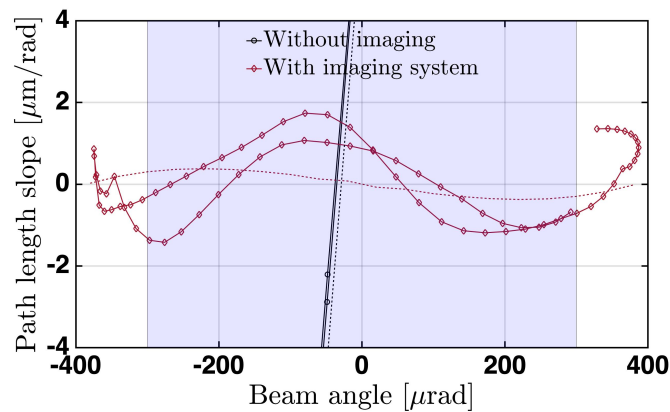
On the bottom of Figure 5.19, the path length slopes in the experiment (solid curves) are compared with simulation results (dashed curve). The TTL coupling measured with the imaging system fully satisfies the LISA requirement by showing its result below  $2 \mu\text{m}/\text{rad}$ , whereas the TTL coupling in the absence of the imaging system is out of range of the LISA requirement.



(a) Path length signals with and without the imaging system



(b) Path length signal with the imaging system



(c) Path length slopes with and without the imaging system

Figure 5.19: Best result in the TTL coupling experiment. The best result refers to the minimum TTL coupling when the second lens is shifted by  $-3.675$  mm. The dots connected by solid lines and the dashed curve respectively indicate the experimental results and the IfoCAD simulation results. The upper plot shows the path length signal with and without imaging system. In the middle, the reduced path length signal via the imaging system is enlarged. On the bottom, the slopes of the path length signal against the beam's tilt angle are plotted. The measured path length slope without the imaging system in the experiment is below  $2 \mu\text{m}/\text{rad}$ .



### 5.3.3 Comparison between the ATA's angular readout and the DWS signal

We compared the ATA's angular readout with the DWS signal measured at QPD1 on the TTL coupling breadboard. This experimental result is helpful to estimate the performance of the ATA's angular readout or understand the DWS signal's property. Simultaneously, this first co-measurement could also be beneficial as a preliminary test for other experiments that compare the ATA's angle with other instruments. The following paragraphs describe the meaning of the co-measurement and its measurement procedures.

Beyond the TTL coupling investigation shown in the previous chapter, the ATA can be used for other experiments that require accurate rotation angle measurements. For instance, characterising the DWS signal that is often used to measure the angle of two interfering beams could be one of the applications of the ATA. Besides, the ATA could also be beneficial for other experiments such as calibration of DPS signal or an auto-collimator

To use the ATA to other applications, one of the critical conditions is that the ATA needs to be calibrated by an instrument capable of measuring the absolute tilt angle. In practice, there are no perfect instruments providing absolute tilt angle without error because every instrument measuring a tilt angle needs calibration due to its measurement error. As an alternative way, if several instruments measure one rotating target at the same time and their results match each other in some degrees, the instruments' performance becomes more reliable. On the other hand, if the residual disagreement between each of the measurements appears, it may lead to amplifying ambiguity. Nevertheless, by understanding each measurement's potential error sources, the disagreement between the measurement results may be diminished in the permissible level.

In this context, another experiment using the ATA is planned in the near future, which is a comparison of the ATA and the 'L-shaped interferometer' (LINT). The LINT is a 6-DOF interferometer platform capable of measuring three displacements and three rotations. It was developed to test TTL coupling of the LRI of GRACE-FO, which is caused by the mismatch between the TMA's vertex and the rotation point of a hexapod [46]. In the ongoing plan for the co-measurement, two actuation platforms from the ATA and LINT will be integrated so that one integrated-platform, including a total of 10 retroreflectors, emerges. Then, each readout from the ATA and LINT for the integrated-platform's motion would be compared.

Prior to the planned measurement campaign between ATA and LINT, this chapter presents the experimental results comparing the ATA's angular readout and the DWS signal. This comparative experiment is helpful in two respects. Firstly, it can be beneficial for calibration or performance evaluation. Here, the calibration and performance evaluation refers to the case of calibrating the ATA readouts through the DWS signal or vice versa. However, the comparative calibration method's fundamental limitation is that the calibration depends on the accuracy of the two measurements. If there is some deviation between the two measurements, it may

be not easy to ascertain which measurement is more accurate. In this case, additional measurement or instrument may be needed to compare to each other. This problematic issue is not trivial at all. Nonetheless, this comparative measurement is obviously beneficial to estimate the precision of the ATA (or DWS signal).

Secondly, this comparative experiment could be a preliminary step for the planned measurement campaign between the ATA and LINT. As mentioned earlier, it is possible to obtain richer results by comparing two or more measurements. In other words, if this measurement campaign considers not only the ATA and LINT but also the DWS signal, this can be a way to enhance the reliability of the measurement result.

In the experiment, QPD1, which does not include the imaging system in the TTL coupling experiment, was used to measure the DWS signal. Driving the ATA for yaw rotation in open-loop control, the ATA's rotation angle's zero is defined at where the DWS signal is minimal.

The upper-left graph in Figure 5.20 shows the ATA's angular readout, where the x-axis is the yaw angle readout, and the y-axis is the pitch angle. The yaw rotation is dominant in the ATA's rotations, and its angle is in the range of about  $\pm 200 \mu\text{rad}$ . Besides, a residual pitch rotation was occurred due to the open-loop operation, showing its rotation angle is in the range from  $-6$  to  $10 \mu\text{rad}$ . The DWS signal measured in the TTL coupling experiment is shown in the upper-right plot of Figure 5.20, where the x-axis represents the horizontal DWS signal denoted by  $\text{DWS}_h$ , and the y-axis represents the vertical DWS signal denoted by  $\text{DWS}_v$ .

As can be seen, the DWS signals have a different scale to the ATA's angular readouts. For comparing both readouts, the ATA's yaw readout was taken as reference, then the  $\text{DWS}_h$  was rescaled to match its value to the yaw readout. The lower-left plot of Figure 5.20 shows the rescaled  $\text{DWS}_h$  (black line) against the yaw readout and its linear fit (red line). The slope of the linear fit is almost one, which signifies the rescaled  $\text{DWS}_h$  corresponds to the yaw readout. In this scaling, the raw data of the DWS signal was divided by 4295.5.

In the lower-right graph of Figure 5.20, the rescaled DWS signal indicated by the red curve is compared with the ATA's readouts plotted by the blue curve. Both curves seem to have a similar shape, but the DWS signal is inclined with respect to the ATA's angular readout. One possible cause of this incline might be the misalignment between the ATA's axis and the QPD's slit lines, as illustrated in Figure 5.21, which might be occurred during the installation of the QPD.

Based on this assumption, the measured DWS signal was calibrated by applying a rotation matrix in order to correct the angle between the ATA's axis and QPD's slit, as

$$\begin{pmatrix} \cos \Omega & -\sin \Omega \\ \sin \Omega & \cos \Omega \end{pmatrix} \begin{pmatrix} \text{DWS}_h \\ \text{DWS}_v \end{pmatrix} = \begin{pmatrix} \text{DWS}_h' \\ \text{DWS}_v' \end{pmatrix}, \quad (5.1)$$

where  $\Omega$  is a rotation angle,  $\text{DWS}_h'$  and  $\text{DWS}_v'$  denote the horizontal and vertical DWS signal after calibration, respectively. Then,  $\Omega$  is optimally tuned until to match the angular readouts between the ATA and  $\text{DWS}'$ .

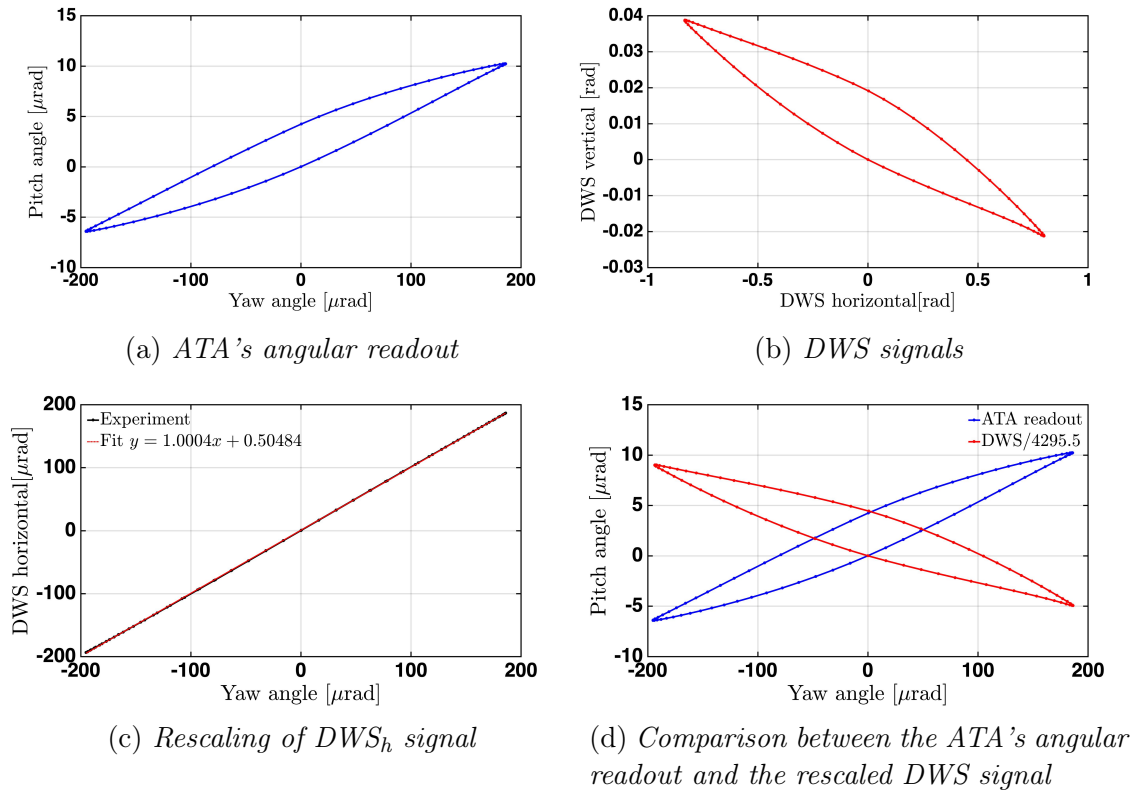


Figure 5.20: *The ATA's angular readouts and DWS signals. While the ATA was driven in open-loop control, the DWS was measured at QPD1 in the TTL coupling experiment. The upper-left graph shows the ATA's angular readout, where the x-axis is the yaw angle, and the y-axis is the pitch angle. The upper-right graph depicts the measured DWS signals, where the x-axis is the horizontal DWS signal, and the y-axis represents the vertical DWS signal. In order to match the scales between the ATA's readouts and DWS signals, the ATA's yaw readout was taken as reference. Then, the DWS signals were rescaled (scale factor=1/4295.5) until the horizontal DWS was linearly fit to the yaw readout, as shown in the lower-left graph. In the lower-right graph, the rescaled DWS signal (red curve) and the ATA's angular readouts (blue curve) were compared.*

As a result, the optimal angle was found to be  $\Omega = 4.6^\circ$ , and the resulting matched readouts are depicted in Figure 5.22. The blue curve shows the ATA's angular readouts, and the red curve represents the calibrated DWS signal.

### The two angular readouts' discrepancy and IfoCAD simulation

In Figure 5.22 showing the ATA's readouts and the calibrated DWS signals, both readouts seem to agree on a large scale, but a subtle discrepancy can be observed. In the following paragraphs, this comparison will be discussed in more detailed.

The left plot of Figure 5.23 shows the linear characteristics of the DWS measured in the experiment, where the x-axis is the ATA's yaw readout, and the y-axis

Figure 5.21: *Illustration of mismatch between the QPD's slit lines and the ATA's orthogonal two axes. This illustration depicts a possible mismatch between the QPD's slit lines and the ATA's axes in the experiment, which might lead to the inclined DWS signal with respect to the ATA's angular readout shown in Figure 5.20*

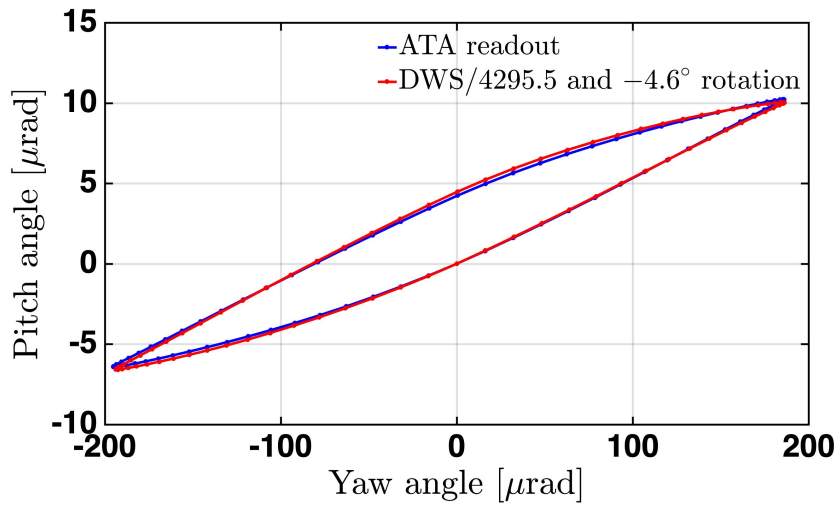
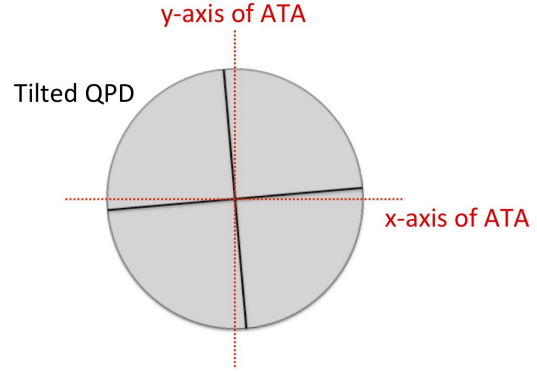


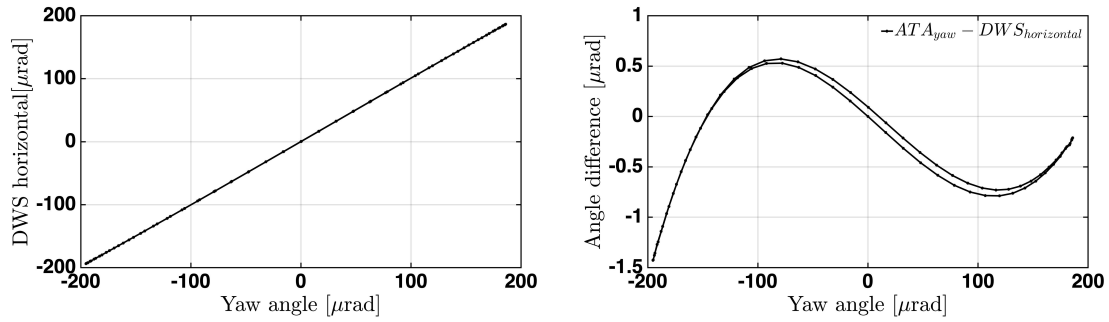
Figure 5.22: *Comparison between the ATA's angular readout and the calibrated DWS signal. The calibrated DWS signal was obtained by dividing the measured DWS signals by 4299.5 and rotating by  $-4.6$  degrees.*

represents the horizontal DWS signal. The observed linearity of the DWS signal is the typical characteristic of the DWS signal, implying a convenience to use DWS signal for measuring the rotation angle of the beam or testmass.

The graph on the right-hand side of Figure 5.23 represents the difference between the ATA's yaw readout and the calibrated  $\text{DWS}_h$ . The resulting difference reveals a cubic polynomial curve in about  $\pm 1\mu\text{rad}$ , which looks like a typical non-linear characteristics of the DWS signal [26].

However, it cannot be asserted that the observed difference between the two readouts was due to the nonlinear characteristics of the DWS signal because there are also other factors. As shown in the simulation in Chapter 4.2.2.2, one of them might be the ATA's readout error due to a number of potential misalignments in ATA. In addition, the DWS signal error due to distortion of the wavefront of the beams cannot be excluded.

As mentioned at the beginning of this section, the limitation of a comparative measurement, which is challenging to accurately analyse errors due to the absence



(a) The calibrated  $DWS_h$  signal against the yaw angle (b) Difference between the  $DWS_h$  signal and the yaw angle

Figure 5.23: The measured difference between the ATA's yaw readout and horizontal DWS signal. In the left graph, the x-axis indicates the measured ATA's angular readout for yaw rotation, and the y-axis represents the calibrated horizontal DWS signal, showing a line correlation between two readouts. The plot on the right-hand side shows the difference between the ATA's angular readout and the calibrated DWS signal.

of the absolute reference, is encountered. One way to reduce the uncertainty of the analysis is to check whether the error between the two readouts shown in the experiment can be reproduced in the simulation.

For this reason, a DWS signal computed in an IfoCAD simulation was compared with the experimental result. In the simulation, a flat mirror regarded as the ATA was rotated around a fixed point, and  $DWS_{AP}$  averaging phases of the left and right, as shown in Equation 2.23, was computed. All relevant simulation parameters are listed in Table 5.3.

The left plot in Figure 5.24 shows the DWS signal computed in the simulation. In the simulation, the ATA had only yaw rotation, and the computed DWS signal was divided by 6006 to be rescaled for being matched with the ATA's rotation angle. The ATA's rotation angle (red line) and the calibrated horizontal DWS (blue line) overlap each other in the form of a linear line. The graph on the right-hand side of Figure 5.24 indicates the difference between the calibrated DWS and the ATA's rotation angle, which demonstrates the nonlinear property of the DWS signal. This result seems quite similar to the experimental result shown in the graph on the right-hand side of Figure 5.23.

These two results were compared in Figure 5.25, where the blue curve is the simulation result, and the black curve indicates the experimental result. From this comparison, the discrepancy between the ATA's readout and the measured DWS signal seems to be demonstrated by the DWS's nonlinear property. However, the aforementioned other causes, such as the ATA's readout error, the beam's distortion, cannot be excluded.

Despite the limited analysis of the experimental result regarding the difference between the two readouts, the experimental and simulation results could be interpreted that the ATA's angular readout error is expected to be less than one mi-

Table 5.3: *IfoCAD simulation parameters for angular readout comparison.*

	Unit	
Mea-beam waist radius	mm	0.633602
Ref-beam waist radius	mm	0.679895
Mea-beam waist position	mm	31.1563
Ref-beam waist position	mm	-347.603
QPD diameter	mm	8
QPD slit width	mm	0.018
QPD longitudinal position	mm	440

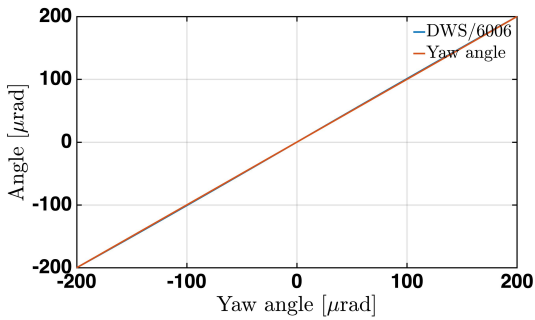
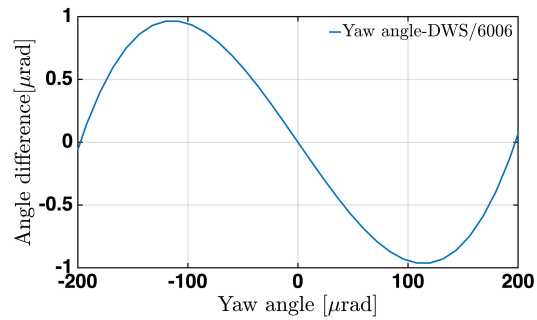

 (a) *The calibrated  $DWS_h$  signal and the yaw angle in the simulation*

 (b) *Difference between the calibrated  $DWS_h$  signal and the yaw angle in the simulation*

Figure 5.24: *IfoCAD simulation result for the angular readout comparison. On the left plot, the red curve represents the rotation angle of the ATA, and the blue curve signifies the calibrate DWS signal. The right plot shows the difference of angular readout between the ATA and DWS.*

roradian. In order to demonstrate the experimental results more precisely, further investigations need to be carried out.

## 5.4 Summary

Using the developed ATA, three experiments were performed. In the first experiment, the calibration method for the ATA's longitudinal displacement readout, discussed in Chapter 4.3.1, was performed with using the fourth retroreflector. Taking the longitudinal displacement readout from the fourth retroreflector as a reference, the longitudinal displacement measured by using the other three retroreflectors was calibrated within the precision of about  $\pm 100$  pm. The second experiment confirmed the suppression of the TTL coupling via the imaging system. In the TTL coupling experiment, the two-lens imaging system designed in Chapter 2.4.2 was set up. The nominal performance of the imaging system showed the TTL coupling satisfied the LISA requirement. In addition, the residual TTL coupling could be further reduced

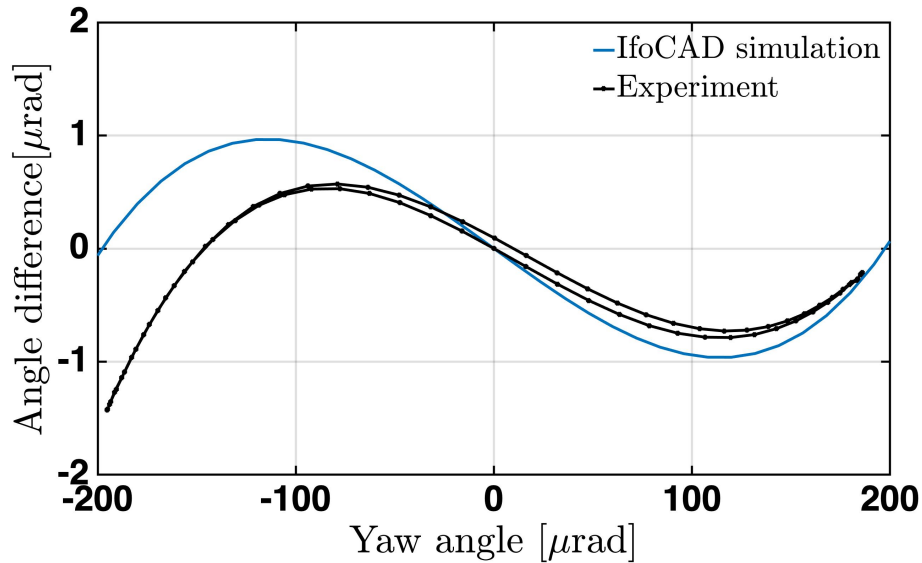


Figure 5.25: *The differences between the ATA’s angular readout and the DWS signal in the experiment and the IfoCAD simulation. The blue curve indicates the simulation result shown in the graphs on the right-hand side of Figure 5.24, and the black curve represents the experimental result shown in the graph on the right-hand side of Figure 5.23.*

by shifting the second lens along the longitudinal direction, and these experimental results were demonstrated by the simulations. The best TTL coupling measured with the imaging system was below about  $\pm 2 \mu\text{m}/\text{rad}$ , satisfying the LISA requirement. In the third experiment, the ATA’s angular readout was compared with the DWS signal measured in the TTL coupling experiment. As a result, the two readouts revealed a discrepancy of around  $1 \mu\text{rad}$  with a curved shape. This result was similar to the DWS’s nonlinear property computed via the simulation, but the ATA’s angular readout error cannot be ruled out, requiring further investigation.





## 6 Summary and discussion

### 6.1 Summary

Investigations on characteristics of the tilt-to-length (TTL) coupling that is one of the significant noises in space laser interferometers, and its suppression are crucial for the development of LISA and the future space laser interferometers. An iterative difficulty in TTL coupling experiments was the motion error of the actuator serving a tilted beam, which produces an unintended longitudinal displacement that disturbs proper TTL coupling measurements. In this thesis, an optical testbed capable of measuring the actuator's motion, named Advanced Tilt Actuator (ATA), was developed to resolve the actuator's motion error. The ATA consists of the Actuation Platform (AP) that produces a motion in three degrees-of-freedom (3-DOF) for two rotations and a longitudinal displacement and several interferometers. The vertices of the four retroreflectors hosted in the AP are regarded as reference points of the AP, and their longitudinal displacements are tracked by the dedicated interferometers, such that the AP's 3-DOF motion can be measured.

To accomplish the ATA's accurate measurement for the 3-DOF motion, two conditions should be satisfied. Firstly, the retroreflectors' vertex positions representing the AP's reference points must be known precisely. To this end, using the Coordinate Measurement Machine (CMM), the coordinates of the vertices of the retroreflectors were measured by following the procedure described in Chapter 3.3.1. Secondly, the beams towards the retroreflectors should be parallel to each other as well as perpendicular to the ATA-plane. The alignment techniques devised to satisfy the second condition, as described in Chapter 3.3.2, were applied for the beam alignment during the construction of the ATA.

There are likely various undesired misalignment errors in the ATA, such as the CMM's measurement error for the retroreflectors' vertex positions, residual angular misalignment of the beams, lateral offset of the beam reflection point, dihedral angle error of the retroreflectors. In Chapter 4.1, the influences of each misalignment error sources on the ATA's readouts were examined analytically and numerically. Furthermore, to predict a possible scenario that may occur in the actual experiment beyond the individual analyses on each misalignment effect, the ATA's readout errors were computed via an IfoCAD simulation simultaneously applying various misalignment. On the basis of the analyses on the effects of the misalignments, three possible strategies to calibrate the ATA's readouts were discussed in Chapter 4.3. In particular, this thesis focused on the third calibration method based on inducing more error via tuning the measurement point to counteract the ATA's longitudinal displacement error. This method's accuracy and effectiveness were demonstrated through IfoCAD simulations in Chapter 4.3.1.3.

In this thesis, three experiments were carried out with the experimental setup consisting of the three breadboard; the ATA, Modulation Bench, and TTL coupling experiment. In the first experiment described in Chapter 5.3.1, the calibration method discussed in Chapter 4.3.1 was applied to the ATA's longitudinal dis-

placement readout. Taking the longitudinal displacement readout of the fourth retroreflector as the reference, the linear and hysteresis error in the longitudinal displacement measured by using the other three retroreflectors could be suppressed to around  $\pm 100$   $\mu\text{m}$ . In the second experiment described in Chapter 5.3.2, two TTL couplings with and without the two-lens imaging system were measured on the TTL coupling breadboard to prove mitigating the TTL coupling via the imaging system experimentally. In this experiment, the linear and hysteresis in the TTL coupling signal were counteracted by tuning the measurement point. Also, the TTL coupling's residual second-order could be further reduced by longitudinally shifting the imaging system's second lens. As a result, the best TTL coupling measured with the imaging system was about  $2 \mu\text{m}/\text{rad}$ , fully satisfying the LISA requirement that the TTL coupling should be less than  $25 \mu\text{m}/\text{rad}$  in the beam rotation angle of  $\pm 300 \mu\text{rad}$ . In the third experiment, the ATA's angular readout was compared with the DWS signal measured on the TTL coupling breadboard. The experimental results demonstrated the linear correlation between the ATA's angular readout and DWS signal. The residual difference between the two readouts, resulted from the comparison, was about  $1 \mu\text{rad}$  and similar to the nonlinear property of the DWS computed via the IfoCAD simulation. However, due to the other uncertainties that might affect the discrepancy, further investigations need to be performed rather than affirming that the measured discrepancy can be demonstrated by the DWS's nonlinearity.

## 6.2 Discussion

Misalignment is a common issue in many interferometric systems. Especially for the ATA, the misalignment discussed in Chapter 4.1 directly couple into the readouts, degrading measurement performance. The alignment techniques demonstrated in Chapter 3.3 was developed for reducing the misalignment of the ATA but could be beneficial for other multi-DOF interferometers having a similar configuration. Nonetheless, in the context of enhancing the ATA's measurement accuracy, it still requires improving the alignment techniques with better precision for reducing the misalignments as much as possible.

The ATA's readout errors caused by the residual misalignments lead to the necessity of calibrating the ATA readouts. Among the three calibration strategies discussed in Chapter 4.3, we adopted the method, which is inducing more error that counteract the linear and hysteresis in the longitudinal displacement (or path length of the TTL coupling).

The main critical drawback of this method is that it also suppresses some part of TTL coupling that might be interested. For instance, it is known that some misalignments such as lateral misalignments of two beams or a QPD cause additional TTL couplings [43]. These effects were also suppressed together with the ATA's longitudinal displacement error by applying the counteraction method. However, they could be dealt with as a critical research topic for TTL coupling investigations.

This might be treated as one of the main limitations in this research. Another important disadvantage entailed in this method is that it is valid for a particular motion of the ATA. For other motions, this method requires recalibration because each ATA's readout errors depend on the ATA's motion.

In order to fundamentally overcome these limitations, further investigations on calibrating the ATA are required. In this context, contemplating the other two methods, briefly introduced at the beginning of Chapter 4.3, could be helpful. For instance, the first method was identifying the misalignments in the experimental setup of the ATA so that Equation 3.14 for the ATA's three readouts can be reconstructed. This calibration method is ideal if it is feasible, but it is practically the most challenging to be adopted because of a large number of misalignments and limited accuracy of measuring instruments. Although it may be impossible to hunt all the misalignments down, if some of them can be identified, this contributes to reducing the ATA's readout errors. Thus, developing more techniques to identify the misalignments with high accuracy will be valuable to the ATA and other multi-DOF interferometers.

The second method, based on comparing the ATA's readouts with other instrument devices, also needs to be examined in-depth. As discussed, this calibration method involves some limitations. For instance, the calibration's performance depends on the accuracy of the other devices. Also, the calibration might be valid for a specific motion, as shown in Figure 4.16. However, it is the most practically adopted method. From comprehensive knowledge regarding potential measurement errors of the devices (or techniques), the uncertainties on calibrating the ATA could be diminished by adopting a suitable instrument. Also, employing more than one instrument for calibrating the ATA's readouts may be beneficial in the aspect of increasing reliability and accuracy. In this regard, a co-measurement between the ATA and another Multi-DOF interferometer named L-shape Interferometer (LINT) is planned. The LINT was initially developed to measure the motion error of a hexapod needed for investigating the TTL coupling effect of the LRI of GRACE-FO. It is based on 6-DOF interferometric readouts, which is capable of measuring three displacements and three rotations. In this experiment's current plan, the LINT's hexapod would host the ATA's retroreflectors, and the comparative measurement between the ATA and the LINT will be performed. Furthermore, similar to the comparative measurement between the ATA's angular readout and the DWS signal, demonstrated in Chapter 5.3.3, introducing the DWS or DPS signals to the co-measurement between the ATA and LINT may be an advantage for the purpose of showing consistency between the three measurements.

Apart from the two-lens imaging system investigated in this thesis, designing other imaging systems have been underway by other researchers. Further experimental investigations on the TTL coupling with various imaging systems should be ongoing for future space laser interferometers. Also, other analyses not covered in this thesis, such as the aberration effects of the imaging system, ghost beam effect, and wavefront of the distorted beam, need to be examined theoretically and experimentally.



## A Ray tracing analysis for the retroreflector

Chapter 4.1.4 covers the dihedral angle deviation of a retroreflector. In particular, its influences on the outgoing beam's angle and the error of longitudinal displacement readout are analysed. This section describes the ray-tracing method that is applied to the above analyses. The procedure of the analytic ray-tracing is summarised as below.

- 1 The first step is to establish each mirror surface of the retroreflector having dihedral angle error.
- 2 The initial beam described as a ray is defined by using vector notation.
- 3 The intersection point between the initial ray and the first mirror surface is derived, and then the beam's propagation distance can be calculated.
- 4 In order to continue the ray-tracing, the reflected beam's direction is derived by rotating the initial beam's vector around the first mirror's normal vector. By using the derived reflecting beam's direction together with the intersection point (computed in the third step), the reflected beam can be described.
- 5 By iterating above procedure, the ray-tracing for second and third mirror can be continued.

### Step 1: Establishing three mirrors with dihedral angle

Figure 4.8 shows the geometry of the retroreflector used in ATA. However, suppose that the mirror surface of the actual retroreflector slightly deviates from Figure 4.8. Since the normal vector of each mirror has three degrees of freedom, a total of nine degrees of freedom are required to model an imperfect retroreflector. Since considering all degrees of freedom regarding the angular deviation of the three mirrors of the retroreflector leads to complex analytic results, only two dihedral angle deviations were taken into account in the analyses in Chapter 4.1.4. Following paragraphs describe the mathematical procedure to set the retroreflector up.

The first of all, the retroreflector consisting of three mirrors, denoted by M1, M2, and M3, needs to be established. Before applying the dihedral angle deviation, suppose that the angles between the three mirror surfaces are 90 degrees. M1, M2 and M3 are placed on the x-y plane, x-z plane and y-z plane, respectively. Then, the normal vectors of the three mirror surfaces are given by

$$\vec{N}_1 = \begin{pmatrix} 0 \\ 0 \\ 1 \end{pmatrix}, \quad \vec{N}_2 = \begin{pmatrix} 0 \\ 1 \\ 0 \end{pmatrix}, \quad \vec{N}_3 = \begin{pmatrix} -1 \\ 0 \\ 0 \end{pmatrix}. \quad (\text{A.1})$$

Now, consider the deviation of the dihedral angle between the three mirrors. Note that only two dihedral angles are taken into account in this section, as discussed in

Chapter 4.1.4. Other possible geometries for the retroreflector can be modelled by extending below calculation procedure. Denote the dihedral angle deviation between M1 and M2 by  $\delta_{12}$  and the dihedral angle deviation between M1 and M3 by  $\delta_{13}$ . For describing the rotated M2 due to the  $\delta_{12}$ , the normal vector  $\vec{N}_2$  is rotated about the x-axis by  $\delta_{12}$ , as

$$\hat{R}_x(\delta_{12})\vec{N}_2 = \begin{pmatrix} 1 & 0 & 0 \\ 0 & \cos \delta_{12} & -\sin \delta_{12} \\ 0 & \sin \delta_{12} & \cos \delta_{12} \end{pmatrix} \begin{pmatrix} 0 \\ 1 \\ 0 \end{pmatrix} = \begin{pmatrix} 0 \\ \cos \delta_{12} \\ \sin \delta_{12} \end{pmatrix}, \quad (\text{A.2})$$

where  $\hat{R}_x$  is the rotation matrix about the x-axis. For the dihedral angle deviation  $\delta_{13}$ , the normal vector  $\vec{N}_3$  is rotated  $\delta_{13}$  about the y-axis in the same manner, as

$$\hat{R}_y(\delta_{13})\vec{N}_3 = \begin{pmatrix} \cos \delta_{13} & 0 & \sin \delta_{13} \\ 0 & 1 & 0 \\ -\sin \delta_{13} & 0 & \cos \delta_{13} \end{pmatrix} \begin{pmatrix} -1 \\ 0 \\ 0 \end{pmatrix} = \begin{pmatrix} -\cos \delta_{13} \\ 0 \\ \sin \delta_{13} \end{pmatrix}, \quad (\text{A.3})$$

where  $\hat{R}_y$  is the rotation matrix about the y-axis. After applying the dihedral angles error, the redefined normal vector are given by

$$\vec{N}'_1 = \begin{pmatrix} 0 \\ 0 \\ 1 \end{pmatrix}, \quad \vec{N}'_2 = \begin{pmatrix} 0 \\ \cos \delta_{12} \\ \sin \delta_{12} \end{pmatrix}, \quad \vec{N}'_3 = \begin{pmatrix} -\cos \delta_{13} \\ 0 \\ \sin \delta_{13} \end{pmatrix}. \quad (\text{A.4})$$

The next step is rotating the three mirrors to be formed as Figure 4.8. For this, rotate each normal vector around the y-axis by 45 degrees, then rotate them around the x-axis by 45 degrees, as

$$\hat{R}_x(45^\circ)\hat{R}_y(45^\circ)\vec{N}'_{1,2,3} = \begin{pmatrix} 1 & 0 & 0 \\ 0 & \cos 45^\circ & -\sin 45^\circ \\ 0 & \sin 45^\circ & \cos 45^\circ \end{pmatrix} \begin{pmatrix} \cos 45^\circ & 0 & \sin 45^\circ \\ 0 & 1 & 0 \\ -\sin 45^\circ & 0 & \cos 45^\circ \end{pmatrix} \vec{N}'_{1,2,3}, \quad (\text{A.5})$$

where  $\vec{N}'_{1,2,3}$  denotes each normal vector before being rotated. From this rotations, the new normal vectors becomes

$$\begin{aligned}
 \vec{N}_1'' &= \begin{pmatrix} \frac{1}{\sqrt{2}} \\ -\frac{1}{2} \\ \frac{1}{2} \end{pmatrix}, & \vec{N}_2'' &= \begin{pmatrix} \frac{\sqrt{2} \cdot \sin \delta_{12}}{2} \\ \frac{\sqrt{2} \cdot \cos \delta_{12} - \sin \delta_{12}}{2} \\ \frac{\sqrt{2} \cdot \cos \delta_{12} + \sin \delta_{12}}{2} \end{pmatrix}, \\
 \vec{N}_3'' &= \begin{pmatrix} \frac{\sin \delta_{13} - \cos \delta_{13}}{\sqrt{2}} \\ \frac{-\sin \delta_{13} - \cos \delta_{13}}{2} \\ \frac{\sin \delta_{13} + \cos \delta_{13}}{2} \end{pmatrix}.
 \end{aligned} \tag{A.6}$$

In general, the equation of plane can be expressed by using the normal vector and an arbitrary point on the plane, as

$$(\vec{p} - \vec{p}_0) \cdot \vec{N} = \begin{pmatrix} x - x_0 \\ y - y_0 \\ z - z_0 \end{pmatrix} \cdot \begin{pmatrix} N_x \\ N_y \\ N_z \end{pmatrix} = 0, \tag{A.7}$$

where  $\vec{p} = (x, y, z)^T$  is the set of points that satisfies a plane,  $\vec{p}_0 = (x, y, z)^T$  is an arbitrary point on the plane, and  $\vec{N} = (N_x, N_y, N_z)$  is the normal vector of plane. Assume that the vertex, where the three mirrors of the retroreflector meet, is located at the origin. In this case, the arbitrary point  $\vec{p}_0 = (0, 0, 0)$ , and the plane equations for the three mirrors are given by

$$\vec{p} \cdot \vec{N}_1'' = 0, \quad \vec{p} \cdot \vec{N}_2'' = 0, \quad \vec{p} \cdot \vec{N}_3'' = 0 \tag{A.8}$$

## Step 2: Defining the initial ray

After establishing the three mirrors with dihedral angles for a retroreflector, the next step is to define a beam. In here, the beam is regarded as a ray and initialised by using a vector notation, as

$$\vec{b}_1 = d_1 \vec{l}_1 + \vec{s}, \tag{A.9}$$

where  $d_1$  denotes the propagation distance of the ray as a scalar,  $\vec{l}_1 = (l_{1x}, l_{1y}, l_{1z})^T$  is an unit vector for the propagation direction of the ray, and  $\vec{s} = (s_x, s_y, s_z)^T$  stands for the initial ray's starting point.

## Step 3: Calculating the ray's propagation distance and point on the mirror

To calculate the intersection point between this ray and the plane of the mirror M1, substitute the vector  $\hat{p}$  of Equation (A.8) by the vector  $\hat{b}_1$  of Equation (A.9), as

$$\vec{b}_1 \cdot \vec{N}_1'' = (d_1 \vec{l}_1 + \vec{s}) \cdot \vec{N}_1'' = d_1 \vec{l}_1 \cdot \vec{N}_1'' + \vec{s} \cdot \vec{N}_1'' = 0 \quad (\text{A.10})$$

By solving Equation (A.10) with respect to  $d_1$ , the initial ray's propagation distance to the mirror M1 can be derived as

$$d_1 = \frac{-\vec{s} \cdot \vec{N}_1''}{\vec{l}_1 \cdot \vec{N}_1''}. \quad (\text{A.11})$$

Also, the intersection point between the initial ray and the mirror M1 can be calculated by substituting  $d$  of Equation (A.11) into Equation (A.9), as

$$\vec{p}_1 = \left( \frac{-\vec{s} \cdot \vec{N}_1''}{\vec{l}_1 \cdot \vec{N}_1''} \right) \vec{l}_1 + \vec{s}. \quad (\text{A.12})$$

#### Step 4: Describing the reflected beam from the mirror

So far, we derived the propagation distance of the initial ray and the intersection point between the ray and the first mirror M1. In order to continue the ray-trace, the reflected ray from the mirror M1 need to be described. To do that, the propagation direction of the beam reflected from the mirror needs to be calculated. And then, using the beam's propagation direction and reflection point derived in Equation A.12, the reflected beam can be described.

For calculating the reflected beam's propagation direction, the initial beam's direction  $\hat{l}$  given in Equation (A.9) is rotated 180 degrees around the first mirror's normal vector  $\vec{N}_1''$ , and then multiply -1 to the rotated vector. In this calculation, the rotation matrix for rotating a vector around an arbitrary axis is exploited, given by

$$\hat{R}(\vec{u}, \phi) = \begin{pmatrix} \cos \phi + u_x^2 (1 - \cos \phi) & u_x u_y (1 - \cos \phi) - u_z \sin \phi & u_x u_z (1 - \cos \phi) + u_y \sin \phi \\ u_y u_x (1 - \cos \phi) + u_z \sin \phi & \cos \phi + u_y^2 (1 - \cos \phi) & u_y u_z (1 - \cos \phi) - u_x \sin \phi \\ u_z u_x (1 - \cos \phi) - u_y \sin \phi & u_z u_y (1 - \cos \phi) + u_x \sin \phi & \cos \phi + u_z^2 (1 - \cos \phi) \end{pmatrix}, \quad (\text{A.13})$$

where  $\vec{u} = (u_x, u_y, u_z)$  is the unit vector of rotation axis and  $\phi$  is the rotation angle. For rotating a vector around the M1's normal vector  $\vec{N}_1''$  by 180 degrees, the rotation matrix is notated by  $\hat{R}(\vec{N}_1'', 180^\circ)$ . Using this rotation matrix, the reflected beam's direction can be derived by

$$\begin{aligned} \vec{l}_2 &= -1 \cdot \hat{R}(\vec{N}_1'', 180^\circ) \vec{l}_1 \\ &= - \begin{pmatrix} -1 + 2N_x^2 & 2N_x N_y & 2N_x N_z \\ 2N_y N_x & -1 + 2N_y^2 & 2N_y N_z \\ 2N_z N_x & 2N_z N_y & -1 + 2N_z^2 \end{pmatrix} \begin{pmatrix} l_{1x} \\ l_{1y} \\ l_{1z} \end{pmatrix}. \end{aligned} \quad (\text{A.14})$$



Now,  $\vec{p}_1$  in Equation (A.12), which is the intersection point between the initial ray and the mirror M1, is regarded as the reflected ray's starting point. By substituting  $\vec{p}_1$  and  $\vec{l}_2$  for  $s$  and  $\vec{l}_1$  in Equation (A.9), the reflected ray can be described as

$$\vec{p}_2 = d_2 \vec{l}_2 + \vec{p}_1, \quad (\text{A.15})$$

where  $d_2$  is the propagation distance of the reflected ray.

### **Step 5: Continuing ray tracing**

The reflected ray in the fourth step is regarded as a new ray. By iterating the procedures from the second to fourth step, the ray-tracing can be continued to compute the beam's intersection points, propagation distance, and reflection angle.

In Chapter 4.1.4, the analyses on the angle variation of the outgoing beam direction and the longitudinal displacement readout's error due to the angular deviation of the mirrors of the retroreflector are carried out under the specific conditions. Based on the above ray-tracing method, these analyses for the retroreflector's other geometries can be implemented.



---

## References

- [1] B. P. Abbott et al. “Gravitational waves and gamma-rays from a binary neutron star merger: GW170817 and GRB 170817A”. In: *The Astrophysical Journal Letters* Vol. 848, No. 2 (2017), p. L13 (cit. on pp. 2, 3).
- [2] B. P. Abbott et al. “GW170814: a three-detector observation of gravitational waves from a binary black hole coalescence”. In: *Physical review letters* Vol. 119, No. 14 (2017), p. 141101 (cit. on p. 2).
- [3] B. P. Abbott et al. “GW170817: observation of gravitational waves from a binary neutron star inspiral”. In: *Physical Review Letters* Vol. 119, No. 16 (2017), p. 161101 (cit. on p. 2).
- [4] B. P. Abbott et al. “Multi-messenger observations of a binary neutron star merger”. In: (2017) (cit. on p. 2).
- [5] B. P. Abbott et al. “Observation of gravitational waves from a binary black hole merger”. In: *Physical review letters* Vol. 116, No. 6 (2016), p. 061102 (cit. on p. 2).
- [6] B. Abbott et al. “LIGO: the laser interferometer gravitational-wave observatory”. In: *Reports on Progress in Physics* Vol. 72, No. 7 (2009), p. 076901 (cit. on p. 2).
- [7] R. Abbott et al. “GWTC-2: Compact Binary Coalescences Observed by LIGO and Virgo During the First Half of the Third Observing Run”. In: *Report from The LIGO Scientific Collaboration and the Virgo Collaboration* (2020) (cit. on p. 3).
- [8] K. Abich et al. “In-orbit performance of the GRACE follow-on laser ranging interferometer”. In: *Physical review letters* Vol. 123, No. 3 (2019), p. 031101 (cit. on pp. 1, 6, 21, 22).
- [9] A. Abramovici et al. “LIGO: The laser interferometer gravitational-wave observatory”. In: *science* Vol. 256, No. 5055 (1992), pp. 325–333 (cit. on p. 2).
- [10] T. Akutsu et al. “First cryogenic test operation of underground km-scale gravitational-wave observatory KAGRA”. In: *Classical and Quantum Gravity* Vol. 36, No. 16 (2019), p. 165008 (cit. on p. 3).
- [11] E. Albert, W. Perrett, and G. Jeffery. “The foundation of the general theory of relativity”. In: *Annalen der Physik* Vol. 49, No. 7 (1916), pp. 769–822 (cit. on p. 1).
- [12] M. Armano et al. “Beyond the required LISA free-fall performance: new LISA Pathfinder results down to  $20 \mu\text{ Hz}$ ”. In: *Physical review letters* Vol. 120, No. 6 (2018), p. 061101 (cit. on p. 5).
- [13] M. Armano et al. “Sub-femto-g free fall for space-based gravitational wave observatories: LISA pathfinder results”. In: *Physical review letters* Vol. 116, No. 23 (2016), p. 231101 (cit. on p. 5).
- [14] P. Astone et al. “Long-term operation of the Rome" Explorer" cryogenic gravitational wave detector”. In: *Physical Review D* Vol. 47, No. 2 (1993), p. 362 (cit. on p. 2).
- [15] P. Astone et al. “The gravitational wave detector NAUTILUS operating at  $T=0.1\text{ K}$ ”. In: *Astroparticle Physics* Vol. 7, No. 3 (1997), pp. 231–243 (cit. on p. 2).

- [16] N. Bobroff. “Recent advances in displacement measuring interferometry”. In: *Measurement Science and Technology* Vol. 4, No. 9 (Sept. 1993), pp. 907–926. DOI: 10.1088/0957-0233/4/9/001. URL: <https://doi.org/10.1088/0957-0233/4/9/001> (cit. on p. 55).
- [17] N. Bobroff. “Critical alignments in plane mirror interferometry”. In: *Precision Engineering* Vol. 15, No. 1 (Jan. 1993), pp. 33–38. DOI: 10.1016/0141-6359(93)90276-g. URL: [https://doi.org/10.1016/0141-6359\(93\)90276-g](https://doi.org/10.1016/0141-6359(93)90276-g) (cit. on p. 55).
- [18] N. C. Brause. “Auxiliary function development for the LISA metrology system”. en. PhD thesis. 2018. DOI: 10.15488/3511. URL: <http://www.repo.uni-hannover.de/handle/123456789/3541> (cit. on pp. 13, 14).
- [19] M. Cerdonio et al. “The ultracryogenic gravitational-wave detector AURIGA”. In: *Classical and Quantum Gravity* Vol. 14, No. 6 (1997), p. 1491 (cit. on p. 2).
- [20] J. L. Chen et al. “Seasonal global mean sea level change from satellite altimeter, GRACE, and geophysical models”. In: *Journal of Geodesy* Vol. 79, No. 9 (Nov. 2005), pp. 532–539. DOI: 10.1007/s00190-005-0005-9. URL: <https://doi.org/10.1007/s00190-005-0005-9> (cit. on p. 6).
- [21] M. Chwalla et al. “Design and construction of an optical test bed for LISA imaging systems and tilt-to-length coupling”. In: *Classical and Quantum Gravity* Vol. 33, No. 24 (2016), p. 245015 (cit. on p. 1).
- [22] M. Chwalla et al. “Design and construction of an optical test bed for LISA imaging systems and tilt-to-length coupling”. In: *Classical and Quantum Gravity* Vol. 33, No. 24 (Nov. 2016), p. 245015. DOI: 10.1088/0264-9381/33/24/245015. URL: <https://doi.org/10.1088/0264-9381/33/24/245015> (cit. on pp. 7, 30, 38).
- [23] M. Chwalla et al. “Optical Suppression of Tilt-to-Length Coupling in the LISA Long-Arm Interferometer”. In: *Physical Review Applied* Vol. 14, No. 1 (July 2020). DOI: 10.1103/physrevapplied.14.014030. URL: <https://doi.org/10.1103/physrevapplied.14.014030> (cit. on pp. 7, 28, 39, 148).
- [24] K. Danzmann. “LISA mission overview”. In: *Advances in Space Research* Vol. 25, No. 6 (2000), pp. 1129–1136 (cit. on pp. 1, 3, 4).
- [25] K. Danzmann et al. *Laser interferometer space antenna*. 2017. eprint: 1702.00786 (cit. on pp. 1, 4, 18, 19).
- [26] H.-Z. Duan, Y.-R. Liang, and H.-C. Yeh. “Analysis of non-linearity in differential wavefront sensing technique”. In: *Optics Letters* Vol. 41, No. 5 (Feb. 2016), p. 914. DOI: 10.1364/ol.41.000914. URL: <https://doi.org/10.1364/ol.41.000914> (cit. on p. 158).
- [27] A. Einstein and N. Rosen. “On gravitational waves”. In: *Journal of the Franklin Institute* Vol. 223, No. 1 (1937), pp. 43–54 (cit. on p. 1).
- [28] A. Goldstein et al. “An ordinary short gamma-ray burst with extraordinary implications: Fermi-GBM detection of GRB 170817A”. In: *The Astrophysical Journal Letters* Vol. 848, No. 2 (2017), p. L14 (cit. on p. 2).
- [29] R. Haagsmans et al. “ESA’s next-generation gravity mission concepts”. In: *Rendiconti Lincei. Scienze Fisiche e Naturali* Vol. 31, No. S1 (Jan. 2020), pp. 15–25. DOI: 10.1007/s12210-020-00875-0. URL: <https://doi.org/10.1007/s12210-020-00875-0> (cit. on p. 6).

- 
- [30] G. M. Harry, L. S. Collaboration, et al. “Advanced LIGO: the next generation of gravitational wave detectors”. In: *Classical and Quantum Gravity* Vol. 27, No. 8 (2010), p. 084006 (cit. on p. 4).
- [31] G. Heinzl et al. “Laser Ranging Interferometer for GRACE follow-on”. In: *International Conference on Space Optics-ICSO 2012*. Vol. 10564. International Society for Optics and Photonics. 2017, p. 1056420 (cit. on pp. 1, 6, 22).
- [32] B. K. Johnson. *Optics and optical instruments*. Tech. rep. Dover, 1960 (cit. on p. 58).
- [33] M. D. Lieser. “LISA optical bench development : experimental investigation of tilt-to-length coupling for a spaceborne gravitational wave detector”. en. PhD thesis. 2017. DOI: 10.15488/9016. URL: <https://www.repo.uni-hannover.de/handle/123456789/9069> (cit. on pp. 16, 39).
- [34] D. Malacara. In: *Optical Shop Testing*. John Wiley & Sons, Inc. (cit. on p. 57).
- [35] E. Mauceli et al. “The Allegro gravitational wave detector: Data acquisition and analysis”. In: *Physical Review D* Vol. 54, No. 2 (1996), p. 1264 (cit. on p. 2).
- [36] V. Müller. “Design considerations for future geodesy missions and for space laser interferometry”. PhD thesis. Hannover: Gottfried Wilhelm Leibniz Universität Hannover, 2017 (cit. on p. 83).
- [37] K. Nicklaus et al. “Laser metrology concept consolidation for NGGM”. In: *CEAS Space Journal* Vol. 12, No. 3 (June 2020), pp. 313–330. DOI: 10.1007/s12567-020-00324-6. URL: <https://doi.org/10.1007/s12567-020-00324-6> (cit. on p. 6).
- [38] S. D. Phillips, B. Borchardt, and G. Caskey. “Measurement uncertainty considerations for coordinate measuring machines”. In: *NASA STI/Recon Technical Report N* Vol. 93 (1993), p. 31196 (cit. on pp. 63, 90).
- [39] T. Prince et al. *LISA: Unveiling a hidden universe: Assessment study report*. Tech. rep. 2011 (cit. on p. 4).
- [40] C. SaiSandesh. “Investigation of Tilt-to-Length coupling using Advanced-Tilt Actuator”. Hannover: Gottfried Wilhelm Leibniz Universität Hannover, 2018 (cit. on p. 148).
- [41] I. E. Sanz, A. Heske, and J. C. Livas. “A telescope for LISA – the Laser Interferometer Space Antenna”. In: *Advanced Optical Technologies* Vol. 7, No. 6 (Dec. 2018), pp. 395–400. DOI: 10.1515/aot-2018-0044. URL: <https://doi.org/10.1515/aot-2018-0044> (cit. on p. 19).
- [42] P. R. Saulson. *Fundamentals of interferometric gravitational wave detectors*. World Scientific, 1994 (cit. on p. 2).
- [43] S. Schuster. “Tilt-to-length coupling and diffraction aspects in satellite interferometry”. en. PhD thesis. 2017. DOI: 10.15488/9064. URL: <https://www.repo.uni-hannover.de/handle/123456789/9117> (cit. on pp. 7, 11, 13, 14, 20, 23, 25–30, 37, 38, 71, 120, 133, 148, 164).
- [44] S. Schuster et al. “Experimental demonstration of reduced tilt-to-length coupling by a two-lens imaging system”. In: *Optics Express* Vol. 24, No. 10 (May 2016), p. 10466. DOI: 10.1364/oe.24.010466. URL: <https://doi.org/10.1364/oe.24.010466> (cit. on pp. 7, 36, 38, 138).

- [45] S. Schuster et al. “Vanishing tilt-to-length coupling for a singular case in two-beam laser interferometers with Gaussian beams”. In: *Applied Optics* Vol. 54, No. 5 (Feb. 2015), p. 1010. DOI: 10.1364/ao.54.001010. URL: <https://doi.org/10.1364/ao.54.001010> (cit. on pp. 23, 28, 37).
- [46] D. Schütze. “Intersatellite laser interferometry: test environments for GRACE follow-on”. en. PhD thesis. 2015. DOI: 10.15488/8576. URL: <https://www.repo.uni-hannover.de/handle/123456789/8629> (cit. on pp. 22, 23, 155).
- [47] T. S. Schwarze. “Phase extraction for laser interferometry in space : phase readout schemes and optical testing”. en. PhD thesis. 2018. DOI: 10.15488/4233. URL: <https://www.repo.uni-hannover.de/handle/123456789/4267> (cit. on pp. 13, 14).
- [48] B. Sheard et al. “Intersatellite laser ranging instrument for the GRACE follow-on mission”. In: *Journal of Geodesy* Vol. 86, No. 12 (2012), pp. 1083–1095 (cit. on pp. 1, 6, 21).
- [49] B. D. Tapley. “GRACE Measurements of Mass Variability in the Earth System”. In: *Science* Vol. 305, No. 5683 (July 2004), pp. 503–505. DOI: 10.1126/science.1099192. URL: <https://doi.org/10.1126/science.1099192> (cit. on p. 6).
- [50] B. Tapley and C. Reigber. “The GRACE mission: status and future plans”. In: *AGU Fall Meeting Abstracts*. Vol. 2001. 2001, G41C–02 (cit. on p. 1).
- [51] B. D. Tapley et al. “The gravity recovery and climate experiment: Mission overview and early results”. In: *Geophysical Research Letters* Vol. 31, No. 9 (2004) (cit. on pp. 1, 5).
- [52] P. L. Teoh et al. “The measurement uncertainties in the laser interferometry-based sensing and tracking technique”. In: *Measurement* Vol. 32, No. 2 (Sept. 2002), pp. 135–150. DOI: 10.1016/s0263-2241(02)00006-4. URL: [https://doi.org/10.1016/s0263-2241\(02\)00006-4](https://doi.org/10.1016/s0263-2241(02)00006-4) (cit. on p. 55).
- [53] M. Tröbs. *LOB-AEI-TN-005.1-Test of interferometry concept*. Tech. rep. Tech. rep. AEI Hannover, 2012 (cit. on pp. 36, 37, 138).
- [54] M. Tröbs et al. “Reducing tilt-to-length coupling for the LISA test mass interferometer”. In: *Classical and Quantum Gravity* Vol. 35, No. 10 (Apr. 2018), p. 105001. DOI: 10.1088/1361-6382/aab86c. URL: <https://doi.org/10.1088/1361-6382/aab86c> (cit. on pp. 7, 36, 38, 40, 148).
- [55] I. Velicogna. “Increasing rates of ice mass loss from the Greenland and Antarctic ice sheets revealed by GRACE”. In: *Geophysical Research Letters* Vol. 36, No. 19 (Oct. 2009). DOI: 10.1029/2009gl040222. URL: <https://doi.org/10.1029/2009gl040222> (cit. on p. 6).
- [56] G. Wanner. “Complex optical systems in space: numerical modelling of the heterodyne interferometry of LISA Pathfinder and LISA”. PhD thesis. Gottfried Wilhelm Leibniz Universität Hannover, 2010 (cit. on pp. 7, 11, 13, 16, 23, 27, 28).
- [57] G. Wanner. “Space-based gravitational wave detection and how LISA Pathfinder successfully paved the way”. In: *Nature Physics* Vol. 15, No. 3 (2019), pp. 200–202 (cit. on p. 5).

- 
- [58] G. Wanner et al. “A brief comparison of optical pathlength difference and various definitions for the interferometric phase”. In: *Journal of Physics: Conference Series* Vol. 610 (May 2015), p. 012043. DOI: 10.1088/1742-6596/610/1/012043. URL: <https://doi.org/10.1088/1742-6596/610/1/012043> (cit. on p. 14).
- [59] G. Wanner et al. “Methods for simulating the readout of lengths and angles in laser interferometers with Gaussian beams”. In: *Optics Communications* Vol. 285, No. 24 (Nov. 2012), pp. 4831–4839. DOI: 10.1016/j.optcom.2012.07.123. URL: <https://doi.org/10.1016/j.optcom.2012.07.123> (cit. on pp. 11, 14, 16).
- [60] J. Weber. “Detection and generation of gravitational waves”. In: *Physical Review* Vol. 117, No. 1 (1960), p. 306 (cit. on p. 2).
- [61] J. Weber. “Evidence for discovery of gravitational radiation”. In: *Physical Review Letters* Vol. 22, No. 24 (1969), p. 1320 (cit. on p. 2).
- [62] J. Weber. *General Relativity and gravitational waves*. Courier Corporation, 2004 (cit. on p. 1).
- [63] H. Wegener et al. “Tilt-to-Length Coupling in the GRACE Follow-On Laser Ranging Interferometer”. In: *Journal of Spacecraft and Rockets* Vol. 57, No. 6 (2020), pp. 1362–1372 (cit. on pp. 1, 22, 23).





# Acknowledgment

During my PhD research works at the AEI Hannover, time being with outstanding and fabulous colleagues would be remained as an unforgettable opportunity in my life. I would like to thank Karsten Danzmann for his extraordinary efforts to take care of institute members and establish and improve our excellent research conditions. I am grateful to my supervisor, Gerhard Heinzl, for guiding me in the direction of my research whenever I was wandering through research difficulties during my PhD at the space laser interferometer group of AEI. With your vast and deep knowledge and keen insight, your care for our group members enables us to face up the scientific challenge via your advice. I do express my appreciation to Benno Willke and Claus Braxmaier for your willingness to be my referees.

Thanks to Gudrun Wanner, I cannot imagine my PhD works without your advice with logical views. If I had not got your vast support in proofreading my thesis, I would not have completed my thesis. Also, thanks to Sönke, a former member of AEI, for many advices and supports on building experimental setups. I am grateful to my colleagues who were directly involved in my experiment. Thanks to Nils, a former member of AEI, for preparing the phasemeter for my experiment, Thomas for preparing ATA's feedback loop control, and Germán for preparing the transimpedance amplifier.

To Michael Tröbs and Daniel Schütze, owing to your kind answers to my frequent stupid questions, I could manage to build my experimental setups. With much gratitude to Moritz for not only scientific advice and supports but also sharing joys outside, time being with you is kind of adding Vitamin into my body. Great thanks to Axel, I could not imagine my life in Germany without your enormous supports and drinking beers after works. Alexander Koch, I really appreciate your warmth and kindness and managing experimental stuff together. To Henry, sharing our PhD life at AEI could make me feel a sense of comradeship.

For proofreading my PhD thesis, Miguel, Marie, Vitali, Moritz, and Gudrun, I cannot conceive finalising my PhD thesis without your great feedback, I sincerely appreciate your tremendous efforts on my PhD thesis.

I gratefully acknowledge fundings from the Sonderforschungsbereich (SFB) 1128 Relativistic Geodesy and Gravimetry with Quantum Sensors (geo-Q), as well as the International Max Planck Research School (IMPRS) on Gravitational-Wave Astronomy, allowing me to work on my researches.

Lastly, I am grateful to my Family for waiting and supporting me to get through my PhD.



## Curriculum Vitae

### PERSONAL

**Name** : Yongho Lee  
**Birth** : 06. Apr. 1981  
**Nationality** : South Korea

### EDUCATION

**Bachelor of Physics** 2000. Mar - 2008. Feb  
Kookmin University in South Korea

**Masters of Physics-Optics** 2010. Mar - 2012. Feb  
Inha University in South Korea, Thin Film Optics Laboratory

**Phd Candidate** 2014. Nov - Now  
Institut für Gravitationsphysik, Leibniz Universität Hannover and Max-Planck-Institut für Gravitationsphysik (Albert-Einstein-Institut)

## Publiations

### CONFERENACE TALKS

Yong Ho Lee, Sönke Schuster, Gudrun Wanner, Michael Tröbs, Daniel Schütze, Gerhard Heinzl, '*Experimental research on tilt-to-length coupling for future geodesy mission*', DPG-Frühjahrstagungen 2016

Yongho Lee, Gudrun Wanner, Thomas S. Schwarze, Germán Fernández Baranco, Gerhard Heinzl, '*Development of three-degrees-of-freedom interferometer for tilt-to-length coupling investigation*', LISA symposium 2020

## Supervision

Chittoori SaiSandesh '*Investigation of Tilt-to-Length (TTL) coupling using Advanced Tilt Actuator (ATA)*', Mater thesis, Leibniz Universität Hannover, 2018